

# **Study of the role of plant nuclear envelope and lamina-like components in nuclear and chromatin organisation using 3D imaging**

**Axel Poulet**

A thesis submitted in partial fulfilment of the requirements of Oxford Brookes University for the degree of Doctor of Philosophy

1 April 2016



*ECOLE DOCTORALE SCIENCES DE LA VIE, SANTE, AGRONOMIE et ENVIRONNEMENT*

Thèse présentée à l'Université Blaise Pascal pour l'obtention du grade de Docteur  
d'Université  
(Spécialité : Bioinformatique)

## **Study of the role of plant nuclear envelope and lamina-like components in nuclear and chromatin organisation using 3D imaging**

**Présentée par Axel Poulet**

Thèse dirigé par Pr Christophe Tatout et Pr David E. Evans

Soutenance prévue le 6 Juin 2016 devant le jury composé de :

Pr Paul Fransz, Université d'Amsterdam (Rapporteur)

Pr Chris Hawes, Université d'Oxford Brookes (Rapporteur)

Pr Philippe Andrey, INRA, Institut Jean-Pierre Bourgin, Versailles (Examineur)

Pr Rémy Malgouyres: LIMOS Aubière (Examineur)

Pr David Evans: co-superviseur, Université d'Oxford Brookes (co-directeur)

Pr Christophe Tatout: co-superviseur, GReD Aubière (co-directeur)



## Abstract

The linker of nucleoskeleton and cytoskeleton (LINC) complex is an evolutionarily well-conserved protein bridge connecting the cytoplasmic and nuclear compartments across the nuclear membrane. While recent data supports its function in nuclear morphology and meiosis, its implication for chromatin organisation has been less studied in plants. The first aim of this work was to develop *NucleusJ* a simple and user-friendly ImageJ plugin dedicated to the characterisation of nuclear morphology and chromatin organisation in 3D. *NucleusJ* quantifies 15 parameters including shape and size of nuclei as well as intra-nuclear objects and their position within the nucleus. A step-by-step documentation is available for self-training, together with data sets of nuclei with different nuclear organisation. Several improvements are ongoing to release a new version of this plugin. In a second part of this work, 3D imaging methods have been used to investigate nuclear morphology and chromatin organisation in interphase nuclei of the plant model *Arabidopsis thaliana* in which heterochromatin domains cluster in conspicuous chromatin regions called chromocentres. Chromocentres form a repressive chromatin environment contributing to the transcriptional silencing of repeated sequences a general mechanism needed for genome stability. Quantitative measurements of 3D position of chromocentres in the nucleus indicate that most chromocentres are situated in close proximity to the periphery of the nucleus but that this distance can be altered according to nuclear volume or in specific mutants affecting the LINC complex. Finally, the LINC complex is proposed to contribute to the proper chromatin organisation and positioning since its alteration is associated with the release of transcriptional silencing as well as decompaction of heterochromatic sequences. The last part of this work takes advantage of available genomic sequences and RNA-seq data to explore the evolution of NE proteins in plants and propose a minimal requirement to build the simplest functional NE. Altogether, work achieved in this thesis associates genetics, molecular biology, bioinformatics and imaging to better understand the contribution of the nuclear envelope in nuclear morphology and chromatin organisation and suggests the functional implication of the LINC complex in these processes.

## Acknowledgement

I would like thank my supervisors, Professor David Evans and Professor Christophe Tatout, who gave me the opportunity to do my thesis in co-tutelle. I am very grateful to David for his patience and his kindness, his great help during my last year of my PhD, and his availability to discuss on this project. For me, it was very challenging to finish my PhD in Oxford without speaking very well English and finish to write my thesis in English. I found in the Plant Cell biology group a lot of people to help each time when I was lost with my English or in my project or both in same time. I would also like to thank Dr Verena Kriechbaumer, Dr Maike Kittelmann and Dr Joseph Mckenna for, their help, the scientific discussions and to help me to write my manuscript.

Je tiens à remercier Christophe pour m'avoir proposé cette aventure de presque 4 ans qui a commencé par le stage en M2 sur quelque chose dont je n'avais jamais entendu parlé : l'imagerie. Je le remercie également pour la confiance qu'il a mis en moi, pour son aide et sa disponibilité. Je le remercie de m'avoir fait progressé scientifiquement, grâce aux nombreuses discussions durant ces 4 années.

I would also like to thank all the PhD student and post doc of the S208a office to follow me in my madness (Alex). I would specially thank Anish, Vidya, Alessandra, Frances, Vanessa, Jirka, Brittany, Rob, Scott and Aladin for their support, couple of pints, friday football, taste and test indian food, picture of cats, "I'am sorry, je suis bionformaticien" and again a lot of things... Now I change language and write in French.

Merci à Aline pour toutes les discussions scientifiques, toutes ses idées pertinentes et son aide.

Ce n'est pas merci, mais un grand ou énorme merci à Céline, pour à peu près tout. Merci de s'être impliquée, de m'avoir aidé à chaque étape de ce projet, qui sans son aide honnêtement se résumerait seulement à des développements bioinformatiques avec de pâles données biologiques. Merci pour les discussions que nous avons eu que ce soit scientifique ou pas.

Je tiens également à remercier les autres personnes qui se sont impliquées sur ce projet. Philippe sans qui ce projet en imagerie ne serait pas vraiment ce qu'il est actuellement. Je le remercie pour sa patience et son calme afin de me transmettre



un peu de son savoir. Je le remercie également pour son accueil durant les semaines que j'ai passé à Versailles. Rémy qui m'a permis de progresser en mathématiques et en informatique durant les deux dernières années.

Merci à tous les personnes présentes ou passées dans l'équipe et le labo qui m'ont supporté de près ou de loin.

Ensuite dans le désordre (je préfère), je tiens remercier Nicolas Kaspric, pour toutes les apremgs glandechichaBBTthéBD, les repas à base de soupe au fromage ou de gras arrosés de bières et aussi pour tout ce qui ne s'écrit pas. Matthias et Mélanie (papa et maman thèse SECPA) pour toute l'aide qu'ils m'ont apportée n'importe quand, n'importe où et pour n'importe quoi. Et aussi pour toutes les pâtisseries payées pour des sous-entendus plus ou moins douteux. Pour tous les surnoms donnés et les bières bues, pour tous les repas faits ensemble etc... Merci à eux et aussi à Romain, Armand et Emi. Merci aussi à Lauriane pour toutes les discussions plus ou moins constructives et d'avoir fait la nounou du chat. Merci à tous les autres thésards. Merci Tristan qui m'a montré que je n'étais pas seul. Et ensuite tout les potes du chorus et d'ailleurs (Polo, Max, Flo, Pif, Galette, Bruce, Seb, la beusse, Bud, DJ, Pierre et tous les autres (je n'ai plus de place)), qui ont toujours été présents et le seront encore.

Merci à toutes les personnes qui m'ont formé ou embauché ou aidé (François, Yannick, Maude, Sandrine, Gisèle ...).

Merci aussi à Fred, Fabien et tout le staff d'Esprit BD pour leur nourriture intellectuelle.

Merci à Django, Caouet, Decibel, Lisa et feu Fidji.

Et on termine par le plus important, merci aux personnes qui ont fait ce que je suis, ma famille (femme, parents, frère, grand-parents, belles soeurs, Maël, beau-frère (pas tant que ça) et beaux-parents (je ne me permets pas de juger), cousins, cousines, oncles, tantes ... ). Merci à mes parents de m'avoir montré que tout est possible et de m'avoir encouragé et permis de faire ce que je voulais , et aussi merci à mon frère pour tout et n'importe quoi.

# Contents

<b>1</b>	<b>Introduction</b>	<b>1</b>
1.1	Overview of the nucleus	1
1.1.1	Nuclear envelope and nuclear function	1
1.1.2	The nucleus is a dynamic structure	2
1.2	Chromatin organisation	4
1.2.1	Historic classification: Euchromatin/Heterochromatin	4
1.2.2	Chromatin organisation in the interphase nucleus	5
1.3	Nuclear and chromatin organisation	10
1.3.1	Chromatin position and genome size in the nucleus	10
1.3.2	Modelling of nuclear and chromatin organisation	11
1.4	Nuclear envelope anchored proteins	16
1.4.1	Nuclear Pore Complex	16
1.4.2	Linker of nucleoskeleton and cytoskeleton complex	17
1.4.3	Lamins	22
1.5	Nuclear morphology	25
1.5.1	Nuclear shape	25
1.5.2	Nuclear size	27
1.6	Objectives	30
<b>2</b>	<b>Quantitative analysis of nuclear parameters using 3D images</b>	<b>32</b>
2.1	Imaging : state of the art	32
2.1.1	Sample preparation	32
2.1.2	3D Light microscopy technologies	33
2.1.3	Digital image	34
2.1.4	3D image processing and analysis	39
2.2	Aims	46
2.3	Material and methods	47
2.3.1	Plant material	47
2.3.2	Whole mount preparation	47
2.3.3	3D image acquisition	47
2.3.4	Imaging process and analysis and statistical methods	48
2.4	Results and discussion	49
2.4.1	<i>NucleusJ</i> platform as a phenotyping tool for nuclear organisation	49
2.4.2	Improvement of the computing of the area	55
2.4.3	Improvements of 3D nuclear segmentation	57
2.4.4	Comparative studies of 3D nuclei acquired with SIM and con-	

	focal microscope.....	64
2.5	Conclusion.....	69
<b>3</b>	<b>Infl of nuclear morphology on chromocentre organisation in</b>	
	<i>Arabidopsis thaliana</i> .....	<b>70</b>
3.1	Introduction .....	70
3.2	Aim.....	73
3.3	Material and methods.....	74
	3.3.1 Plant material.....	74
	3.3.2 RNA extraction and RT-PCR.....	75
	3.3.3 Fluorescent in situ hybridisation in 2D .....	75
	3.3.4 Sample preparation, Hoechst staining and 3D-FISH .....	75
	3.3.5 3D image acquisition.....	76
	3.3.6 RNA-Seq analysis.....	76
	3.3.7 Statistical methods.....	77
3.4	Results .....	78
	3.4.1 Quantitative variations in nuclear organisation occur in wild- type cells. ....	78
	3.4.2 Chromocentres are positioned at the nuclear periphery.....	82
	3.4.3 Analysis of nuclear morphology of mutants of the nuclear en- velope and chromatin organisation .....	84
	3.4.4 Alterations of chromocentre compaction and alleviation of si- lencing in mutants.....	87
3.5	Conclusion.....	95
<b>4</b>	<b>Exploring the proteins of the plant nuclear envelope</b>	<b>98</b>
4.1	Introduction .....	98
4.2	Aim.....	102
4.3	Material and methods.....	103
	4.3.1 Homologous LINC complex and lamin-like protein detection .	103
	4.3.2 Phylogenetic reconstruction .....	104
	4.3.3 RNA sequencing data .....	104
	4.3.4 RNA sequencing processing and analysis .....	105
4.4	Results and discussion.....	107
	4.4.1 KASH protein homologues .....	107
	4.4.2 Inner nuclear membrane proteins and lamin-like homologues detection .....	110
	4.4.3 Phylogenetic analysis of the inner nuclear membrane proteins	113
	4.4.4 Phylogenetic analysis of the outer nuclear membrane proteins	115
	4.4.5 Phylogenetic analysis of the putative nuclear lamina proteins .	118
4.5	Conclusion.....	123
<b>5</b>	<b>Discussion and perspectives</b>	<b>125</b>
5.1	<i>NucleusJ</i> a user friendly ImageJ plugin for 3D images of nucleus . . .	126
	5.1.1 <i>NucleusJ</i> validation.....	126
	5.1.2 <i>NucleusJ</i> limitations .....	127

5.1.3	Future improvement of <i>NucleusJ</i> .....	128
5.2	Heterochromatin organisation and chromocentre positioning in wild-type plants .....	129
5.3	NE-anchored proteins disrupt nuclear morphology as well as chromatin organisation .....	130
5.4	Chromatin and histone chaperone mutants disrupt chromatin organisation but not nuclear morphology .....	132
5.5	Future work .....	132
5.5.1	Chromatin organisation of the NE-anchored mutants .....	132
5.5.2	Chromatin organisation of the natural ecotype of <i>Arabidopsis thaliana</i> .....	133
5.5.3	Length and number of cells in cotyledon epidermis .....	133
5.5.4	Impact of stress conditions on the nuclear shape and chromatin organisation .....	133
<b>References</b>		<b>134</b>
<b>A Quantitative analysis of nuclear parameters using 3D images</b>		<b>162</b>
A.1	NucleusJ: an ImageJ plugin for quantifying 3D images of interphase nuclei. ....	162
A.2	NucleusJ documentation .....	166
<b>B Infl of nuclear morphology on chromocentre organisation in <i>Arabidopsis thaliana</i></b>		<b>179</b>
B.1	Primers for genotyping and RT-qPCR .....	180
B.2	Results of statistical test between mutant and wild type .....	181
B.3	Nuclear morphology of the chromatin mutants .....	184
B.4	FISH-3D .....	185
B.5	Quantitative RT-PCR analysis of the chromatin mutants .....	186
<b>C Exploring of the proteins of the plant nuclear envelope</b>		<b>187</b>
C.1	KASH proteins detected with the Perl script .....	188
C.1.1	Results of finding KASH homologues .....	188
C.1.2	KASH proteins clustered using Perl script results .....	189
C.2	Homologue protein results obtain with BLASTp .....	190
C.2.1	CRWN homologue results .....	190
C.2.2	NEAP homologue results .....	191
C.2.3	KAKU4 homologue results .....	191
C.2.4	SINE homologue results .....	192
C.2.5	WIP homologue results .....	192
C.2.6	TIK homologues results .....	193
C.2.7	Cter SUN homologue results .....	193
C.2.8	MidSUN homologue results .....	194
C.3	Tissue expression of the LINC complex protein homologues .....	195
C.3.1	Eudicot expression results .....	195
C.3.2	Monocot expression results .....	197
C.3.3	Basal angiosperm and moss expression results .....	198

# List of Figures

1.1	Nucleus organisation at interphase. ....	2
1.2	Nucleus of mouse and <i>Arabidopsis thaliana</i> at interphase. ....	3
1.3	Chromatin organisation at interphase. ....	6
1.4	Rosette model and chromatin organisation in an <i>Arabidopsis thaliana</i> interphase nucleus. ....	8
1.5	Analysis of the radial position of the centromeres in 2D images. ....	12
1.6	Chromatin organisation modelling at the interphase. ....	13
1.7	Spatial point patterns within the nucleus and distance functions. ....	15
1.8	Protein components of the plant NE. ....	25
2.1	Structured illumination microscopy technique. ....	34
2.2	Histogram of 8 bits image in grey levels. ....	36
2.3	Resolution and Airy disks defi. ....	37
2.4	Shannon Nyquist theorem for the sampling signal. ....	39
2.5	Principles of deconvolution. ....	40
2.6	Comparison of deconvolution method between Iterative Deconvolve 3D and Huygens. ....	41
2.7	Mathematical morphology erosion and dilation. ....	43
2.8	Limits of nuclear segmentation. ....	44
2.9	<i>NucleusJ</i> processing. ....	49
2.10	Results of the Otsu and optimised Otsu method. ....	50
2.11	<i>NucleusJ</i> validation using plant cell nuclei. ....	54
2.12	Comparison of optimised Otsu method with the two estimations of the area. ....	58
2.13	Results of the three segmentations methods. ....	60
2.14	3D nuclear segmentation of a nucleus using three new segmentation methods. ....	64
2.15	3D morphological analysis of wild type nuclei from guard cells, pavement cells acquire by confocal and SIM microscopes. ....	65
2.16	Chromatin organisation analysis of wild type nuclei from guard cells, pavement cells acquire by confocal and SIM microscopes. ....	66
2.17	Distance of chromocentres analysis of wild type nuclei from guard cells, pavement cells acquire by confocal and SIM microscopes. ....	67
3.1	3D segmentation of nuclei and chromocentres using <i>NucleusJ</i> . ....	79
3.2	Wild type nuclei from guard cells, pavement cells and root hair cells can be distinguished by <i>NucleusJ</i> phenotyping. ....	81
3.3	Chromocentres are located close to the nuclear periphery. ....	83

3.4	RNA expression of candidate genes in epidermis, guard cells and roots.	85
3.5	Alteration of nuclear morphology in LINC complex mutants nuclei from guard cells, pavement cells and root cells.	86
3.6	Alteration of chromatin organisation in LINC complex mutant nuclei from guard cells, pavement cells and root cells.	88
3.7	Alteration of chromocentres distance on the chromatin and LINC complex mutant nuclei.	89
3.8	Alteration of chromatin organisation in heterochromatin mutant nuclei from guard cells, pavement cells and root cells.	91
3.9	Alteration of heterochromatin condensation in whole cotyledon analysed by 2D-FISH.	92
3.10	Alteration of transcriptional repression of heterochromatic markers in mutant backgrounds.	94
4.1	Overview of plant phylogeny	100
4.2	Phylogenetic tree of Cter-SUN proteins.	114
4.3	Phylogenetic tree of Mid-SUN proteins.	115
4.4	Phylogenetic tree of WIP proteins.	116
4.5	Phylogenetic tree of SINE1, SINE2 proteins.	118
4.6	Phylogenetic tree of KAKU4 proteins.	119
4.7	Phylogenetic tree of NEAP proteins.	120
4.8	Phylogenetic tree of CRWN proteins.	121
5.1	Image of <i>Arabidopsis thaliana</i> root with electron microscope SBF SEM.	128
B.1	Alteration of nuclear morphology in heterochromatin mutants nuclei from guard cells, pavement cells and root cells.	184
B.2	Quantitative RT-PCR analysis of TSI expression in WT and chromatin mutant.	186
C.1	KASH protein clustering	189
C.2	<i>Arabidopsis thaliana</i> results	195
C.3	<i>Arabidopsis lyrata</i> results	195
C.4	<i>Solanum lycopersicum</i> results	196
C.5	<i>Glycine max</i> results	196
C.6	<i>Oryza sativa</i> results	197
C.7	<i>Zea mays</i> results	197
C.8	<i>Amborella trichopoda</i> results	198
C.9	<i>Physcomitrella patens</i> results	198

# List of Tables

2.1	Parameters computed by <i>NucleusJ</i> .....	53
2.2	Comparison of two methods of area computing using theoretical objects. .	57
2.3	Mean morphologic parameters computed with the new algorithms and compared to the original Otsu segmentation procedure.....	63
2.4	Numbers of nuclei acquire by SIM and confocal microscopes. ....	64
3.1	Mutants used in this study .....	74
3.2	Number of nuclei of all genetic backgrounds.....	80
4.1	Species for the phylogenetic analysis of the NE proteins.....	101
4.2	Reference genes.....	104
4.3	SRA or fastq fi used for RNA sequencing analysis.....	105
4.4	Accession numbers of the SAND genes in all the species of interest. .	106
4.5	KASH homologous proteins.....	109
4.6	Sequences selected for the phylogenetic and expression analysis.....	112
B.1	Primers for the RT-qPCR. ....	180
B.2	Guard cell comparison between wild type and LINC complex mutants.	181
B.3	Pavement cell comparison between wild type and LINC complex mu- tants.....	181
B.4	Root hair cell comparison between wild type and LINC complex mu- tants.....	182
B.5	Guard cell comparison between wild type and chromatin mutants. . .	182
B.6	Pavement cell comparison between wild type and chromatin mutants.	183
B.7	Root hair cell comparison between wild type and chromatin mutants.	183
B.8	Sample of nuclei in GC and PC.....	185
B.9	Proportion of condensed nuclei in GC and PC.....	185
C.1	KASH results from the Perl script. ....	188
C.2	CRWN results.....	190
C.3	NEAP results.....	191
C.4	KAKU4 results. ....	191
C.5	SINE results. ....	192
C.6	WIP results.....	192
C.7	NEAP results.....	193
C.8	Cter-SUN results.....	193
C.9	Mid-SUN results.....	194

# List of Abbreviations

µm micrometers

nm nanometers

2D two Dimension

3D Three Dimensions

AtPSS1 Arabidopsis Pollen Semi-Sterility1

BAF Barrier-to-Autointegration Factor

BLASTp Basic Local Alignment Search Tool protein

bp base pairs

CC ChromoCentres

CCD Charge Coupled Device

CDK1 Cyclin-Dependant Kinase 1

CFP Cyan Fluorescent Protein

CRWN CRoWded Nuclei

CT Chromosome Territories

Cter-SUN C-terminal SUN

dag days after germination

DAPI 4', 6'-DiAmidino-2-PhenylIndole

DMSO DiMethyl SulfOxide

DNA DeoxyriboNucleic Acid

ER Endoplasmic Reticulum

FISH Fluorescence In Situ Hybridiation

FRAP Fluorescence Recovery After Photobleaching



ftp File Transfer Protocol  
GC Guard Cells  
GDP Guanosine DiPhosphate  
GTP Guanosine TriPhosphate  
HGPS Hutchinson-Gilford Progeria Syndrome  
HP1 Heterochromatin Protein 1  
IF Intermediate Filaments  
IHI Interactive Heterochromatic Island  
INM Inner Nuclear Membrane  
KASH Klarsicht/Anc/Syne-1 Homology  
KEE KNOT Engaged Element  
LAC Loop Arm and Chromocentre  
LAD Lamin Associated Domains  
LAP Lamina-associated polypeptides  
LBR Lamin B Receptor  
LCC Linear Chain and Chromocentre  
LEM LAP1beta, Emerin, Man  
LINC Linker of Nucleoskeleton and Cytoskeleton  
LNA Locked Nucleic Acid  
LRMP Lymphoid-Restricted Membrane Protein  
Mb Mega base  
Mlp1 Myosin-like protein 1  
MM Mathematical Morphology  
mRNA messenger RNA  
MT MicroTubules  
MTOC MicroTubule Organising Centres  
N/C nuclear-to-cytoplasmic  
NA Numerical Aperture

NE Nuclear Envelope  
NEAP Nuclear envelope anchored protein  
NEBD Nuclear Envelope Breaks Down  
Nesprins NEspectrin repeat  
NLS Nuclear Localisation Signals  
NOR Nucleolar Organiser Regions  
NPC Nuclear Matrix Constituent Proteins  
NPC Nuclear Pore Complex  
NUP NUcleoProteins  
ONM Outer Nuclear Membrane  
PBS Phosphate-Buffered Saline  
PC Pavement Cells  
PCA Principal component analysis  
PMT PhotoMultiplier Tube  
PNS PeriNuclear Space  
PSF Point Spread Function  
RanGAP GTP-binding protein Ran  
RC Root Crown Cells  
rDNA ribosomal DNA  
rER rough Endoplasmic Reticulum  
RHF Relative Heterochromatin Fraction  
RNA RiboNucleic Acid  
RNA-seq RNAsequencing  
RPKM Reads Per base Kilo per Million mapped reads  
rRNA ribosomal RiboNucleic Acid  
RT-qPCR quantitative Reverse transcription polymerase chain reaction  
RTN reticulon proteins  
SEM Standard Error of a Mean

SIM Structured Illumination Microscopy  
SINE SUN-Interacting Nuclear Envelope  
SLP1 Sun-Like Protein 1  
SUN SAD1/UNC84  
SWI2/SNF2 SWItch/Sucrose Non-Fermentable  
TAD Topologically Associating Domains  
TIK TIR Toll-Interleukin-Resistance-KASH protein  
TM Trans-Membrane  
TSI Transcriptional Silent Information  
UV UltraViolet  
WGD Whole-Genome Duplication  
WIPs WPP domain-interacting proteins  
WIT WPP domain-Interacting Tail-anchored proteins  
YFP Yellow Fluorescent Protein

# Chapter 1

## Introduction

### 1.1 Overview of the nucleus

Introducing the nucleus is not a simple task since it has multiple functions and properties. The nucleus is frequently the biggest organelle of the eukaryotic cell and its presence marks a major evolutionary transition between prokaryotes and eukaryotes. The nucleus is surrounded by the nuclear envelope (NE), consisting of two membranes and it contains most of the cellular genetic information organised in chromosomes (Figure 1.1).

#### 1.1.1 Nuclear envelope and nuclear function

The fi key component of the nucleus and a major focus of this thesis is the NE (Figure 1.1). The NE is a physical barrier between the genetic material and the cytoplasm providing protection against external damage (UV, free radical, viruses). It is constituted of an outer nuclear membrane (ONM) and inner nuclear membrane (INM), forming a double lipid bilayer separated by the periplasm (Figure 1.1).

In plants, the ONM binds microtubules (MT) and can act as a nucleation centre for microtubules, which then organise at microtubule organising centres (MTOC). These MTOC form the basis of the mitotic spindle needed for chromosome segregation during cell division [Zhang and Dawe, 2011, Masoud et al., 2013]. The NE regulates communication between the nucleus and the rest of the cell, mostly through the Nuclear Pore Complex (NPC), which controls trafficking of molecules inside and outside the nucleus (Figure 1.1). The NE is connected with the cytoskeleton and the endoplasmic reticulum (ER), which is continuous with the ONM. In addition, the NE is connected to the cyto- and nucleoskeleton by the Linker of Nucleoskeleton and Cytoskeleton (LINC) complex [Webster et al., 2009, Tapley and Starr, 2013].

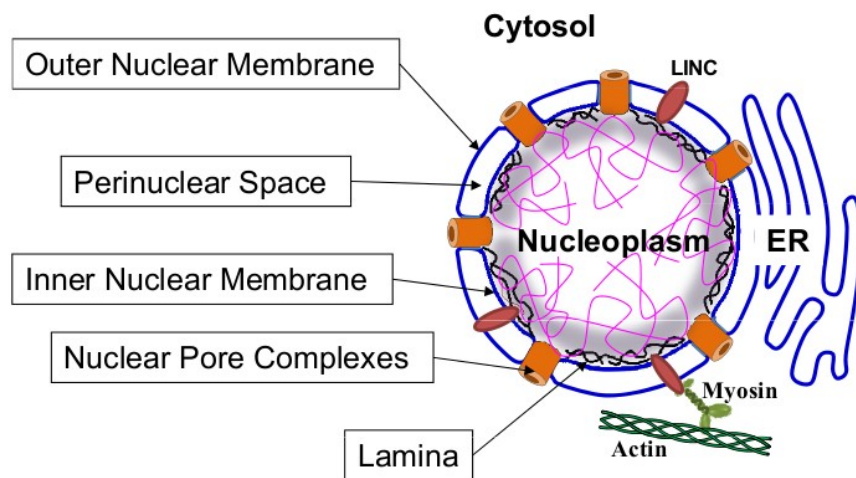


**Figure 1.1: Nucleus organisation at interphase.** Main NE structures seen at interphase. NE is made of membranes (blue) including Outer Nuclear Membrane (ONM), Inner Nuclear Membrane (INM) separated by the PeriNuclear Space (PNS), interrupted by numerous nuclear pore complex (NPCs; orange) and is connected with the Endoplasmic Reticulum (ER). The Linker of Nucleoskeleton and Cytoskeleton (LINC; red) complex is made of KASH and SUN domain proteins anchored in the NE. In many species, NE, LINC complex, NPCs and lamina (in black) interact with chromatin (purple). Adapted from [Tatout et al., 2014].

In metazoans, the nucleoskeleton is composed of a lamina made of intermediate filaments at the nuclear periphery. These lamin filaments interact with chromosomes and with the LINC complex (Figure 1.1).

### 1.1.2 The nucleus is a dynamic structure

The nucleus is not a static organelle but a dynamic structure [Jevtić et al., 2014]. During cell division, Nuclear Envelope Breaks Down (NEBD) occurs and the NE is then reassembled to surround the two daughter nuclei [Graumann and Evans, 2010, Jevtić et al., 2014]. The nucleus is also dynamic during chromosome condensation, segregation and cell division. The nucleus can be mobile in various cells and the migration occurs through the interactions of the nucleo- and cytoskeleton [Tamura and Hara-Nishimura, 2013]. Many examples of nuclear migration have been well documented: in the budding yeast, nucleus mobility is important as nuclei move into the bud neck during cell division so that each daughter cell can receive one nucleus [Pearson and Bloom, 2004, Xiang and Fischer, 2004]. In *Drosophila*, nuclei show basal then apical movements which permit establishment of the characteristic

cell arrangement of the developing optic epithelium. In the large one-cell zygote of animals, the two pronuclei (male and female) move towards one another by the action of microtubules [Reinsch and Gonczy, 1998]. Nuclear migration is involved in cell division of the pseudostratified neural epithelium. In these cells, the nucleus migrates from the apical surface to the basal surface and back to the apical surface for mitosis [Sauer, 1935, Baye and Link, 2008].

In plants, nuclear movement is essential for plant fertility, specifically during pollen tube growth [Zhou and Meier, 2014]. The two sperm nuclei are transported by the growth of the pollen tube for fertilisation to take place. Furthermore, nuclear positioning is a biological process involved in development (*e.g.* in cell cycle progression and cell growth) [Ketelaar et al., 2002]. In response to several stress factors, nuclei are relocated and this process is followed by changes in gene expression [Iwabuchi and Takagi, 2008, Nagai, 1993].

Finally, morphology of the nucleus, such as its size and shape, seems to play a functional role in cell differentiation and development as well as in disease resistance [Starr, 2009, Webster et al., 2009]. Variation of nuclear size and shape may affect gene expression, possibly by altering the position of a locus relative to the nuclear envelope. The size and shape of nuclei as well as possible effects on chromatin structure are addressed as part of the work described in this thesis.

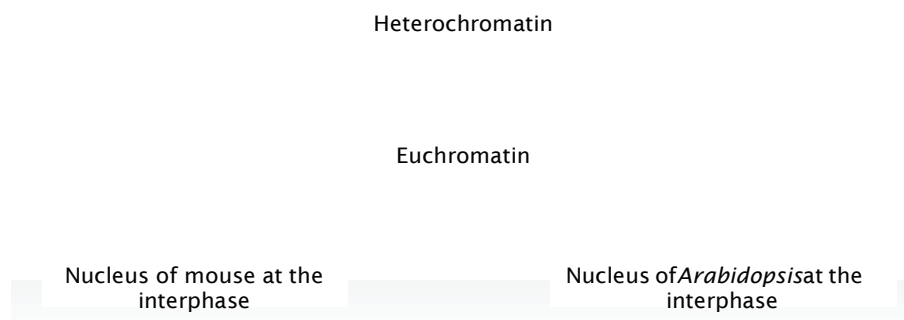


**Figure 1.2: Nucleus of mouse and *Arabidopsis thaliana* at interphase.** The nuclei are stained with 4', 6'-diamidino-2-phenylindole (DAPI). The high intensity regions are heterochromatin, the condensed state of chromatin. These regions are named chromocentres. The less intense regions are the euchromatin. Adapted from [Probst et al., 2009, Benoit et al., 2013].

## 1.2 Chromatin organisation

In eukaryotes, DNA is not naked but organised into chromatin. DNA winds around an octamer of histone proteins to form the nucleosome, the basic subunit of chromatin. Organisation in chromatin allows DNA to be compacted so that it can be contained in the nucleus of a cell, and plays an important role in the transcriptional regulation of the genome. Chromatin carries "epigenetic marks" defined as modifications that induce heritable changes in gene expression independent of the genetic code itself. The information encoded by each or the combination of these different epigenetic marks can affect gene expression, and modifications of these marks can impact genome expression [Turner, 2000]. Combinations of specific marks called permissive marks are found at transcriptionally active or competent loci, while specific combinations of repressive marks are found at transcriptionally repressed euchromatin or constitutive heterochromatin respectively [Roudier et al., 2009, Sequeira-Mendes and Gutierrez, 2015]

### 1.2.1 Historic classification: Euchromatin/Heterochromatin

The chromatin studies by E. Heitz more than 80 years ago allowed the first distinction of euchromatin and heterochromatin on the basis of cytological observations [Heitz, 1928]. The nucleus can be easily stained with 4, 6-diamidino-2-phenylindole (DAPI), a DNA intercalating agent capable of fluorescing under UV light to visualise the organisation of chromatin within the nucleus. Such a method used on interphase nuclei of mouse or *Arabidopsis thaliana* (*A. thaliana*) reveals different regions of different fluorescence intensity (Figure 1.2). The regions of high intensity correspond to compact chromatin, called heterochromatin. The more different intensity regions correspond to relaxed chromatin, called euchromatin [Probst et al., 2009, Benoit et al., 2013, Vanrobays et al., 2013]. Euchromatin and heterochromatin are not distributed randomly along the chromosomes.

In *A. thaliana*, euchromatin is localised on the chromosome arms while heterochromatin is concentrated in several genomic regions [Simon et al., 2015]. Heterochromatin constitutes centromeric regions made of repeated elements such as the satellite 180bp sequences and the repeated sequence elements called 106B while pericentromeric regions are mainly constituted of transposable elements and, on some chromosomes, of tandem repeats of 5S ribosomal RNA genes (rRNA). Heterochromatin is also found on chromosome arms between two euchromatic regions (heterochromatic knobs), at the Nucleolar Organiser Regions (NORs), consisting of tandem repeats of 45S rRNA genes [Fransz et al., 2000].

Molecular characterisation of these two chromatin states defines euchromatin as rich in genes and associated with permissive histone marks for transcription. On the contrary, the heterochromatin is highly condensed, rich in DNA methylated cytosines, enriched in repressive histone marks and has low transcriptional activity.

Heterochromatin, which constitutes about 10% of the *A. thaliana* genome (ie: 15Mb), plays key structural roles in centromere function, regulation of 5S and 45S rDNA expression and the transcriptional repression of repeated sequences such as transposable elements. Different studies in yeast, plants, *Drosophila* and mammals have brought insight into the molecular mechanisms involved in heterochromatin formation and maintenance [Saksouk et al., 2015]. One additional hypothesis proposed by nuclear architecture studies is that the positioning of chromatin in relation to the periphery of the nucleus is an important parameter in heterochromatin formation [Towbin et al., 2013].

In summary, the definition of the two principal chromatin states can be based on cytological and molecular criteria as well as the transcription level of the sequences that compose it. The implication of the plant nuclear periphery in heterochromatin organisation is one of the central questions addressed in this thesis.

### **1.2.2 Chromatin organisation in the interphase nucleus**

Different compaction levels of DNA into chromatin have been described. At the level of the basic subunit of chromatin, the nucleosomes, around one hundred and forty seven base pairs (bp) of the DNA double helix (with an estimated diameter of 2 nm) wrap around a histone octamer to form the nucleosome. The histone octamer comprises two molecules of each histone H2A, H2B, H3 and H4 [Luger et al., 1997]. All histones, except histone H4, exist in several forms (histone variants) encoded by different genes.

The arrays of nucleosomes form a pearl necklace like structure with a 10 nm diameter. These nucleosome arrays can wrap to form a fibre of higher organisation of 30 nm in diameter (Figure 1.3). The formation of the fibre needs other proteins including the linker H1 histone. This 30 nm fibre has only been observed in specific cell types or after nuclear swelling and disruption, or in isolated nuclei. However the 30 nm fibre is not always associated with transcriptional repression and its existence *in vivo* is still under debate [Even-Faitelson et al., 2015]. Recent data also suggest that condensed heterochromatin structures are facilitated by the presence of specific histone variants such as H2A.W, which promotes fibre to fibre contacts between 10 nm fibres [Yelagandula et al., 2014]



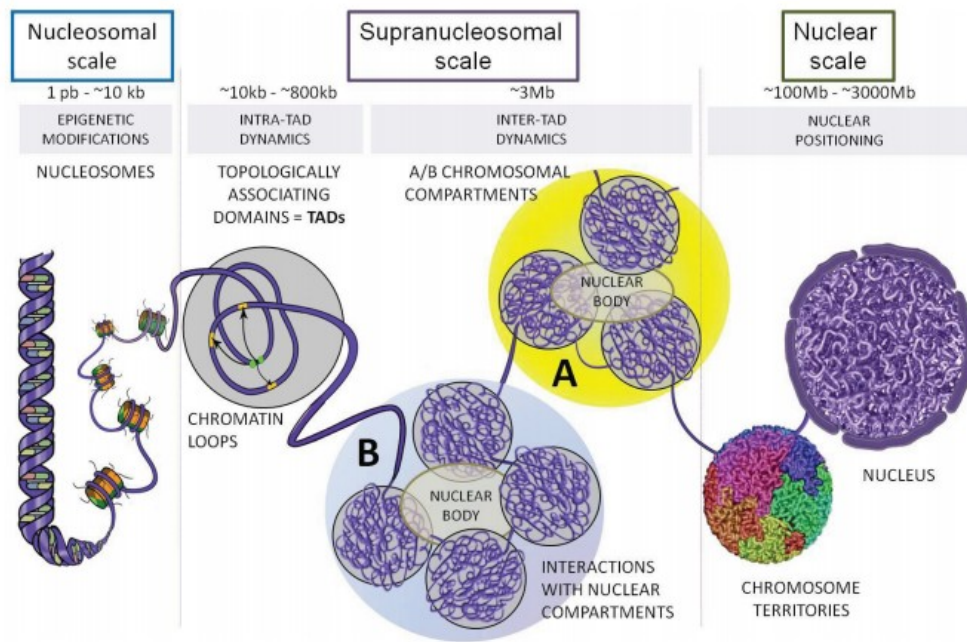


**Figure 1.3: Chromatin organisation at interphase.** Organisation of the DNA between the nucleosomal (nucleofilament) and the nuclear scale (chromosome territories). Beyond the transcriptionally active (A) or inactive (B) chromosomal compartments, Topologically Associating Domains (TADs) and chromatin loops are two essential determinants of eukaryotic genome organisation (Source: [Ea et al., 2015], Creative Commons Attribution License).

Using a chromatin conformation capture (3C) technique which detects interaction between chromatin regions, Dixon et al. (2012) have identified a specific chromatin organisation in animals named Topologically Associated Domains (TADs, Figure 1.3). These domains are chromosomal regions which interact within the domain, but the interaction can occur between adjacent and other more distal TADs although less frequently [Dixon et al., 2012, Nora et al., 2012]. Chromatin, by its conformation and organisation permits interaction between different chromosomal regions which form the TADs [Dekker et al., 2013] (Figure 1.3). This chromosome organisation is conserved in yeast as well as in animal. In *A. thaliana*, chromatin is organised through contacts with pericentromeric regions [Fransz and de Jong, 2002], and no obvious TADs structures could be identified [Feng et al., 2014, Grob et al., 2014, Mizuguchi et al., 2014]. The chromosomes are localised to subnuclear domains called chromosome territories initially shown in animal cells by Carl Rabl (Figure 1.3) [Rabl, 1885].

Chromatin fibres may undergo a higher level of compaction in fibres of 300 nm, which form chromatin loops attached to the nuclear matrix (three dimensional

fi tous protein network which provides a structural framework for organising chromatin). These loops could also participate in defi higher order chromatin domains. A fi condensation can form a 700 nm fi found only in metaphase chromosomes. This is the highest level of compaction known to date [Fussner et al., 2011, Bian and Belmont, 2012].

### **Chromosome organisation in the interphase nucleus**

Chromosome structure is not randomly organised in the nucleus. It is organised by several parameters dependent on the species studied, the stage of the cell cycle, the type of cell, ploidy level, chromosome size, distribution of heterochromatin on the chromosome, cell size, size and position of nucleolus or gene activity [Fransz and de Jong, 2011].

In all organisms 45S rDNA genes are organised in tandem repeats NORs. In *A. thaliana*, these 45S rDNA genes are clustered into thousands of copies in two NOR loci of about 3.5 to 4.0 Mb [Layat et al., 2012] localised in a sub-telomeric position on the short arms of chromosomes 2 and 4. Not all 45S rDNA genes of the NOR loci are transcriptionally active and according to their activity, the NOR region is organised in two parts. On the one hand, it forms a highly condensed heterochromatic region without transcriptional activity and forms chromocentres. On the other hand, it is organised into chromatin loops that are actively transcribed within the nucleolus [Fransz and de Jong, 2002]. The nucleolus is a structure that can represent up to 30% of the nuclear volume and is easily viewable by negative staining with DAPI. Apart from NOR loci, heterochromatin also includes centromeres and peri-centromeric regions (on either side of the centromere) also organised in chromocentres [Fransz and de Jong, 2002].

Fransz and De Jong (2002) propose that euchromatic loops of around 0.2-2 Mb gene rich regions emanate from chromocentres (Figure 1.4). This model is known as the rosette model [Fransz and de Jong, 2002]. One possible mechanism for loop assembly relies on peri-centromeric heterochromatin rich in transposable elements that recruit homologous sequences scattered on chromosome arms. In a diploid somatic cell of *A. thaliana* at the interphase, six to ten chromocentres can be identified [Fransz and de Jong, 2002, Fang, 2005, Berr and Schubert, 2007].

Given the organisation of the *A. thaliana* genome into fi e chromosomes and the presence of two NORs, this suggests that some heterochromatin domains from the same or diff t chromosomes reunite into a single chromocentre. Those chromocentres that contain NOR regions also contain centromeric sequences, indicating

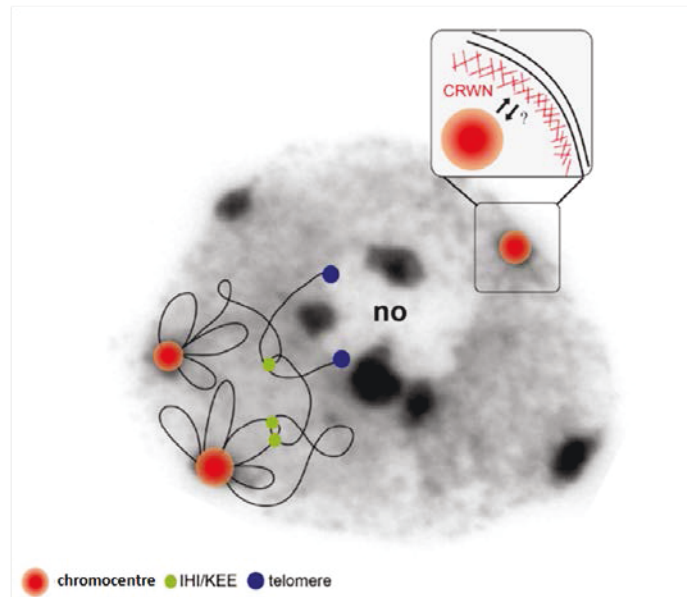


**Figure 1.4: Rosette model and chromatin organisation in an *Arabidopsis thaliana* interphase nucleus.** Model of the organisation of a chromosome in nuclear space overlaid on a DAPI stained image of an *A. thaliana* leaf nucleus. Centromeric and pericentromeric regions of the five *A. thaliana* chromosomes are tightly packed into chromocentre (red/orange). Chromocentres structure the chromosome in nuclear space by anchoring proximal euchromatic loops, while distal chromosomal regions tend to cluster with telomeres (blue) next to the nucleolus (no). Interactive heterochromatic island (IHI)/KNOT engaged element (KEE) regions, identified in Hi-C maps, form additional intra- and inter-chromosomal contacts (green). Enlargement at the top right shows the nuclear envelope coated internally by a lamina-like structure, which includes the CRoWned Nuclei proteins (CRWN) (see Section 1.4.3). Chromocentres tend to localise at the nuclear periphery, but the physical link between nuclear envelope components or the nuclear lamina-like components remains to be identified (Source: [Simon et al., 2015], Creative Commons Attribution License).

that in interphase, NORs and centromeres co-localise with or are physically close to the chromosomes 2 and 4 [Fransz and de Jong, 2002].

Finally, part of the condensed chromatin carries repressive epigenetic marks (DNA methylation, H3K9 type histone methylation) whereas euchromatin loops are rich in acetylated histones and poor in methylated cytosines. This last point illustrates the two states of chromatin, the condensed heterochromatin grouped in chromocentres and more released euchromatin, which forms loops that emanate from the chromocentres. The clustering of heterochromatin in chromocentres could have an important functional role, as the rosette model shows that chromocentres could organise the rest of the chromosome.

The rosette model revealed by cytological analyses, has been refined by a new sequencing method of chromosome conformation capture applied genome-wide (Hi-C). This method permits the visualisation and quantification of the physical interaction between all regions of the genome [Feng et al., 2014, Grob et al., 2014, Liu and Weigel, 2015]. The principal interactions detected by this method are among pericentromeric regions. These regions interact within or between chromosomes and the centromere-proximal half of the euchromatic chromosomal regions [Feng et al., 2014]. The distal halves of the chromosomes however, interact with each other, to form a pattern potentially driven by telomere interactions [Feng et al., 2014]. Furthermore, the high-resolution studies also revealed that euchromatic loops also contain repetitive sequences called interactive heterochromatic islands (IHIs) [Feng et al., 2014] or knot-engaged elements (KEEs) [Grob et al., 2014], which group together in heterochromatic islands through intra- and inter-chromosomal interactions [Grob et al., 2014] (Figure 1.4).

### **Chromosome territories**

A territorial organisation of the chromosome in interphase was first suggested for animal cell nuclei by Carl Rabl during the 19th century (Figure 1.3). In animals, a radial distribution of chromosome territories has been observed, which depends on gene density. The more a chromosomal region is rich in genes, the more it will be internally localised, away from the nuclear periphery. Reciprocally gene poor regions tend to localise closer to the periphery. Such a radial pattern was confirmed in several animal species (*e.g.* human and yeast) [Cremer et al., 2001, Habermann et al., 2001, Bolzer et al., 2005]. The position of chromosome territories is determined by the specific relationships between different chromosomal regions (Figure 1.3). The global gene organisation (called synteny) studies between human and pri-

mates [Tanabe et al., 2002], and human and mouse [Mahy et al., 2002] indicate that the chromosome territories positions in the nucleus are conserved during evolution. In *A. thaliana*, chromosome territories were also described [Pecinka et al., 2004] but to date plant chromosome territories are poorly described apart from this early pioneer work.

## 1.3 Nuclear and chromatin organisation

In the small genome of *A. thaliana*, which has chromosome arms of around 10 Mb, expression levels do not correlate well with gene positioning within the nucleus [Rosin et al., 2008]. However, it has been shown that genes are not randomly organised on chromosomes [Rosa et al., 2013]. In the nucleus, elements (transcriptional enhancers, genes, promoters), which are physically separated on the linear chromosome, can be brought close together by the 3D conformations of the chromatin to form chromatin loops. Chromatin loops were discovered first in maize with pigmentation gene *b1* using the 3C method and have also been shown in *A. thaliana* for several genes involved in flowering and hormone signalling [Louwers et al., 2009, Ariel et al., 2014]. The nuclear organisation of chromatin can be analysed by conformation capture techniques and by cytology or mathematical modelling. All these methods permit a better understanding of the spatial organisation of chromatin in the nucleus.

### 1.3.1 Chromatin position and genome size in the nucleus

The organisation of chromatin in nuclei differs depending on the size of the genome. According to literature, three types of genomes are suggested [van Driel and Fransz, 2004]. Small genomes, which have a size of less than 500 Mb, such as *A. thaliana* and *Drosophila*, medium-sized genomes, between 500 and 3000 Mb (mouse, human, tomato, maize and sorghum) and large genomes larger than 3000 Mb as for example wheat or barley.

In a small genome as the one of *A. thaliana*, the fraction rich in transposable elements and poor in genes represents 10% of the genome and is localised mainly in the centromeric, telomeric and pericentromeric regions. In sorghum and mouse, heterochromatic regions are present at the centromeric and pericentromeric level but also scattered along chromosomes. As in *A. thaliana*, heterochromatic regions for these two organisms are visible in DAPI staining and form chromocentres, but there are more chromocentres and the contrast between condensed and decondensed regions is less marked [Cheng et al., 2001, She et al., 2007].

In humans and mice, the gene poor regions and repressed genes are associated with the nuclear periphery and co-localise with heterochromatin [van Driel and Fransz, 2004, Geyer et al., 2011]. Finally, for large genomes, such as wheat or barley, regions rich in repeated elements and gene clusters are present all along the chromosome. These two species show the organisation called "Rabl" [Jasencakova et al., 2001, Santos and Shaw, 2004, She et al., 2007], the chromosome arms are aligned and centromeres and telomeres are at the nuclear periphery but at opposite poles. However, in the small genomes of *Saccharomyces cerevisiae* or in some rice tissues, chromosomes also adopt this configuration [Santos and Shaw, 2004, Sáez-Vásquez and Gadal, 2010]. Therefore chromosome size cannot explain why an organism or cell type adopts this type of conformation.

In summary, in small and medium genomes, centromeric heterochromatin is focused mostly in a pericentromeric position. In larger genomes, where repeated items appear to have "colonised" the entire chromosome, it is more difficult to clearly define eu- and heterochromatic regions.

### **1.3.2 Modelling of nuclear and chromatin organisation**

To study the position of the heterochromatin in *A. thaliana*, Fang and Spector (2005) combined two histone proteins fused to fluorescent proteins in the same transgenic line (HTR12-YFP and H2B-CFP). HTR12 is a specific centromeric histone while H2B is found at all regions thus marking centromeres and chromatin [Fang, 2005]. The nuclei of these plants were observed by confocal microscopy and an analysis of the radial position of centromeres was performed (Figure 1.5). The radial position was determined by the position of the centromere depending on the distance to the nuclear envelope. In their study, the initial 3D information was lost as the radial position was determined in 2D. This analysis in living cells has shown that centromeres of different cell types with diploid nuclei are close to the nuclear periphery or near to the nucleolus in all tissues that have been observed [Fang, 2005].

Other studies have attempted to model the distribution of chromocentres in *A. thaliana* to determine if the distribution is random or otherwise constrained by other factors such as the number of chromocentres, interaction or repulsion between chromocentres, the presence of chromatin loops, or the presence of the nucleolus which co-localises with NOR regions. Thus, two fundamental questions were addressed [de Nooijer et al., 2009, Andrey et al., 2010]: how are the chromocentres organised in the nucleus and what are the mechanisms responsible for this organisation?

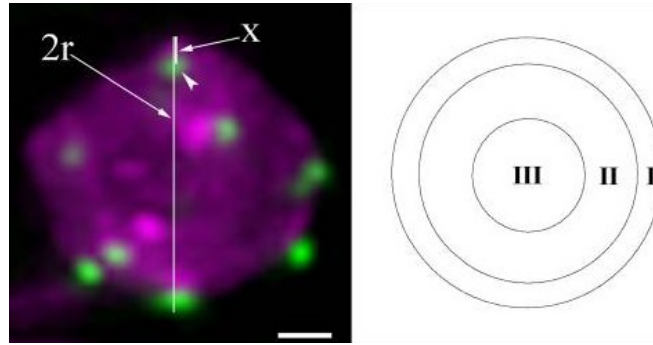


**Figure 1.5: Analysis of the radial position of the centromeres in 2D images.** The centromeres were labeled by HTR12-Venus (green), and the nucleus was labeled by HTB1-CFP (magenta). The nucleus is acquired in 3D and projected in 2D before the radial position analysis. The radial distance of the centromere of interest to the nuclear periphery ( $x$ ) is divided by the nuclear radius ( $r$ ). Centromere position can be mapped to three concentric zones of equal surface (I, II, and III) right scheme. The analysis shows a preferential distribution of the centromere in zone I, the most peripheral. Scale bar 1  $\mu\text{m}$ . (Source: [Fang, 2005], MBoC licence).

In 2009, De Nooijer et al. (2009) determined different mechanistic models of chromocentre distribution in *A. thaliana*, based on data acquired by confocal microscopy on nuclei of leaf cells [de Nooijer et al., 2009]. The three models generated predict a peripheral location of chromocentres. But two of these models (LCC: Linear Chain and Chromocentre and LAC: Loop Arm and Chromocentre) also predict a very high association between chromocentres which group them in four clusters. This is not in agreement with the biological observations of six to ten well-individualised chromocentres.

Instead, the Rosette model, based on the model defined by Fransz et al. (2002), seems to simulate a more realistic distribution of chromocentres. To improve their modelling, the nucleolus, which forms a large volume that had been excluded, was integrated into the model (the volume of the nucleolus is estimated at 30% of the nuclear volume). The nucleolus is positioned in the periphery for the LCC model, but still positioned centrally in the pattern of rosettes.

With the introduction of NOR regions of chromosomes 2 and 4, the LAC model involves no significant alteration in the positioning of the other chromocentres. The rosette model remains the most robust and offers a peripheral distribution of chromocentres through nonspecific interactions. Only chromocentres for chromosomes 2 and 4 are close to the nucleolus, hence, presenting a central position in the nucleus. These models have only been compared to a few biological datasets for validation [de Nooijer et al., 2009]. Furthermore, chromocentre modelling as a sphere could promote their peripheral location and would lead to a bias.

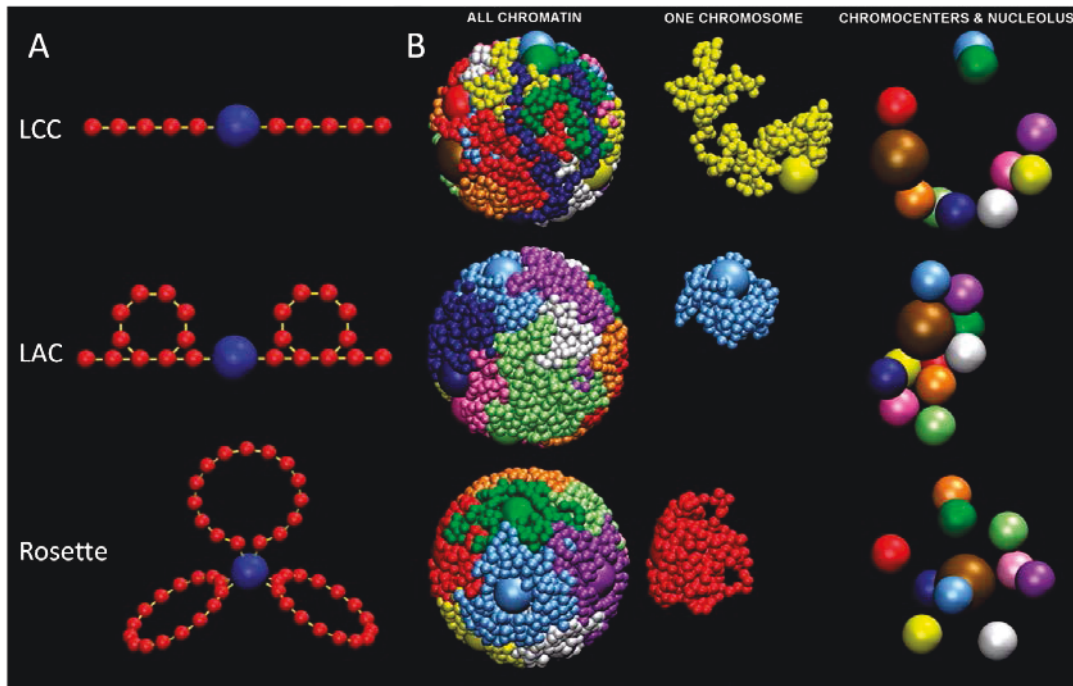


**Figure 1.6: Chromatin organisation modelling at the interphase. A):** Each chromosome is modelled by a monomer of 65 kb of DNA (red ball) and linkers (yellow line). The LCC model (Linear Chain and Chromocentre) includes the chromocentre represented by a blue sphere. The LAC model (Loop Arm and Chromocentre) is based on the LCC model but loops are added on the chromosome arms. The Rosette model based on the model of Fransz et al. (2002), shows the chromosome arms organised in loops around the chromocentre. **B):** Simulation results for the 3 chromatin models from left to right: a whole nucleus with each chromosome with different colour (chromocentres are represented by a sphere with the same colour as its chromosome); one chromosome; and a set of spheres with different colours representing the chromocentre (10 spheres) and the nucleolus (brown sphere). The results obtained with the LCC and LAC models show a clustering of the chromocentres. The Rosette model shows a chromocentre dispersion (Source: [deNooijer et al., 2009]).



Andrey et al. (2010) have recently proposed an approach based on statistical models useful for nuclear architecture [Andrey et al., 2010]. This work is based on the study of spatial distribution of chromocentres using spatial functions termed F and G (Figure 1.7) and using DAPI-stained nuclei. The distributions obtained for each nucleus were compared to a random distribution model and a statistical test at the population scale of nuclei was performed. These approaches show that the distribution of heterochromatin domains would not be random and would tend to form regular distribution patterns with respect to the complete random pattern. It is therefore possible that repulsion mechanisms between chromocentre can generate this distribution. This method makes it possible to observe the distribution of the chromocentre taking into account the possible interactions between them.

Note, however, that analyses are based on images of isolated nuclei; that is to say in a context where the cell is not constrained by other cells of the tissue to which it belongs. It will be interesting to achieve the same approach in living cells or in tissue.

In summary, our knowledge on nuclear organisation of chromocentre structures in *A. thaliana* nuclei is still limited and is based on four founding papers defining the organisation of chromatin according to the rosette model [Fransz and de Jong, 2002]; radial positioning of chromocentre in 2D nuclei [Fang, 2005] and random distribution of the chromocentre to the nuclear periphery [de Nooijer et al., 2009] or a repulsion between chromocentre could explain their distinct distribution relative to each other [Andrey et al., 2010].

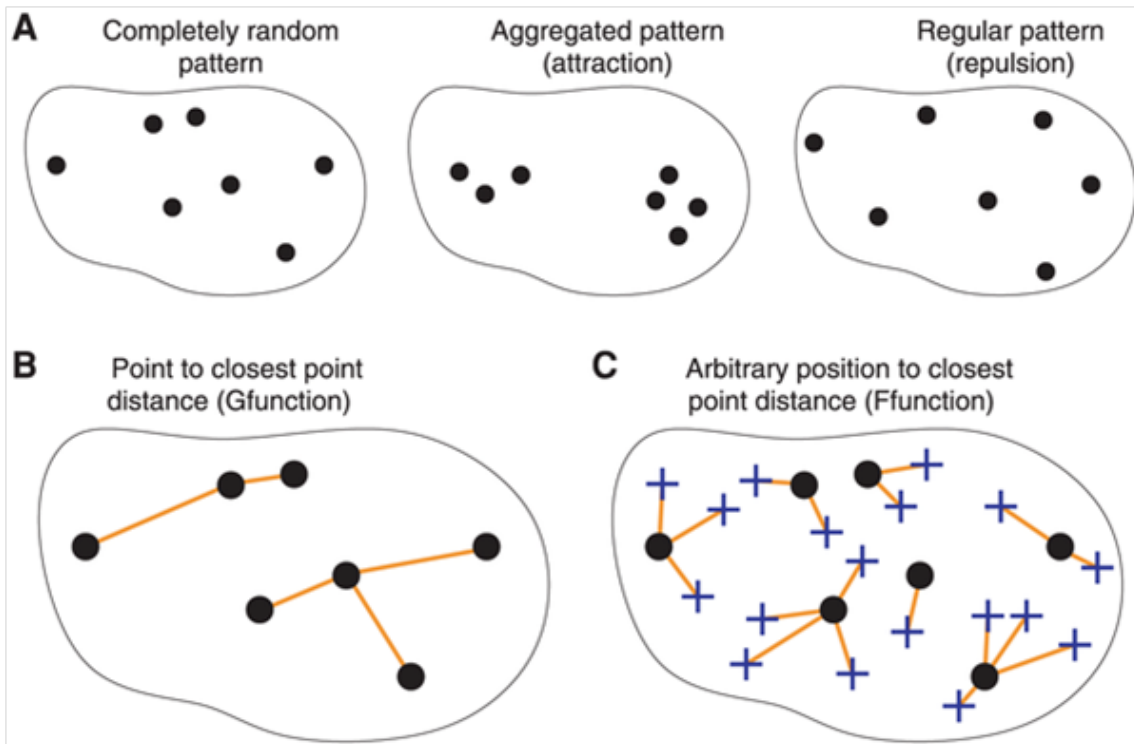


**Figure 1.7: Spatial point patterns within the nucleus and distance functions.** Centromere/chromocentre positions are represented as dots within nuclear contours. **(A)** Various types of spatial distribution. Positions can be uniformly and independently distributed (completely random pattern), or exhibit mutual attraction (aggregated pattern) or mutual repulsion (regular pattern). **(B)** The G-function is the cumulative distribution function of the distance between each centromere/chromocentre and its nearest neighbour (orange lines). This distance tends to be small for aggregated patterns and large for regular patterns. **(C)** The F-function is the cumulative distribution function of the distance between typical nuclear positions (blue crosses) and their nearest centromere/chromocentre (orange lines). This distance tends to be large for aggregated patterns and small for regular patterns (Source: [Andrey et al., 2010], Creative Commons Attribution License).

## **1.4 Nuclear envelope anchored proteins**

As briefly mentioned above, NPC and NE-anchored proteins are major components of the NE and extensive description of these key components will help to better understand their roles in chromatin organisation and expression.

### **1.4.1 Nuclear Pore Complex**

The NPC is a large protein complex composed of at least 35-40 proteins termed nucleoporins (NUPs). This complex makes a channel, in the NE of around 90-120 nm in diameter in all organism. The NPC is conserved in all eukaryotes and allows nucleo-cytoplasmic transport and exchange (molecule, protein, mRNA...) between the nucleus and cytoplasm [DeGrasse et al., 2009]. NUPs are formed of several sub-complexes, with overlapping as well as specific cellular roles [Alber et al., 2007]. Although NUP complex proteins are conserved, their sequences vary between species [Baptiste et al., 2005, Tamura et al., 2010]. Furthermore, these proteins are essential for growth, and despite their sequence variations, their function seems to be well conserved. The major function of the NPC is the directional transport of molecules in and out of the nucleus.

In plants, active transport through the NPC applies for proteins larger than 40 kDa while below this threshold proteins diff freely. The NPC transport function involves a small GTP-binding protein Ran (RanGAP) [Görlich and Kutay, 1999]. RanGAP interacts directly with a protein of the NPC, Nup358, and is localised to the outer basket of the nuclear pore in animal cells. The RanGAP protein is conserved in plants for which nuclear localisation is permitted by an N-terminal WPP domain [Rose and Meier, 2001]. The NPC is also involved in other processes including chromatin interaction, gene regulation, and nuclear morphology (see Part 1.5).

It has been shown by chromatin immunoprecipitation that there are direct or indirect interactions between nucleoporins and genomic sequences. In yeast, the NPC can be associated with promoters, or specific NUPs (Nup157) can interact with double-stranded DNA [Luthra et al., 2007, Seo et al., 2013]. The mammalian Nup93 protein interacts preferentially with heterochromatin marks such as a trimethyl group on the lysine 9 on the histone 3 (H3K9me3), but also H3K27me3 and H3K79me3 [Brown et al., 2008]. In a similar manner, in yeast, Nup170 interacts with centromeric and subtelomeric regions (which constitute heterochromatin regions) [Van de Vosse et al., 2013]. In addition, it has also been shown that NUP

proteins can be transcriptional activators. For example, the human Nup98 protein interacts with proteins via its histone acetylase domain (histone acetylation in general being associated with transcriptional activity), and in yeast, the nuclear basket protein Mlp1 (myosin-like protein 1) interacts indirectly with various promoters [Kasper et al., 1999, Luthra et al., 2007].

Loss of Nup136, a plant specific nucleoporin, causes changes in nuclear morphology, pollen development and flowering time. Nuclei of the *nup136* mutant present a more circular shape in comparison to wild type while overexpression of the same protein causes shape changes where the nuclei becomes more elongated than wild type nuclei [Tamura et al., 2010, Tamura and Hara-Nishimura, 2011].

#### **1.4.2 Linker of nucleoskeleton and cytoskeleton complex**

The LINC complex is a conserved complex of the NE among eukaryotes and is composed of two protein families: the SAD1/UNC84 (SUN) domain proteins of the INM and the Klarsicht/Anc/Syne-1 homology (KASH) domain proteins of the ONM [Crisp et al., 2006]. SUN and KASH proteins connect to each other through interactions of the SUN and KASH domains located at the C-terminus of the respective proteins. In animals, SUN-domain proteins also interact directly with proteins of the nucleoskeleton and with chromatin, whereas KASH-domain proteins interact with cytoskeletal proteins [Crisp et al., 2006]. These complexes are involved in various cellular and nuclear processes such as nuclear shape and migration, chromatin organisation and chromosome segregation [Starr, 2009, Tatout et al., 2014].

Over the years, many components of the plant nuclear envelope have been discovered. It is now assumed that plants have their own LINC complex consisting of SUN [Graumann et al., 2010, Graumann et al., 2014] and KASH proteins including WIPs (WPP domain-interacting proteins) and SINE (SUN-interacting nuclear envelope) proteins [Zhou et al., 2012, Graumann et al., 2014, Zhou et al., 2015a].

#### **SUN domain proteins**

In eukaryotes, two sub families of SUN domain proteins are known so far, the C-terminal SUN domain (Cter-SUN) proteins and the mid-SUNs proteins that can be distinguished by the position of the SUN domain within the protein. These two sub-families diverged early during evolution before the emergence of the plant and animal kingdoms and are now forming two distinct monophyletic groups. Most species have Cter-SUN and mid-SUN proteins, suggesting that both groups have been conserved through evolution [Field et al., 2012, Graumann et al., 2014]. Crystal structure of

the human SUN2 organised in homotrimers and the KASH protein Nesprin2 have been obtained [Sosa et al., 2012]. Their study showed that SUN domain proteins form homotrimers within the INM and interact with three KASH domain proteins with which they form the LINC complex.

In mammals, Cter-SUN proteins are involved in a large range of cellular processes such as chromosome organisation, decondensation of mitotic chromosomes, nuclear pore distribution, telomere maintenance and regulation of cellular death [Tzur et al., 2006, Chi et al., 2007, Fridkin et al., 2009]. Cter-SUN proteins can immobilise proteins of the nuclear membrane such as the Lamin B receptor, by interaction with chromatin and nuclear lamins [Ellenberg et al., 1997]. In mouse, a knock out of the *SUN1* gene disrupts the production of piRNAs and causes a misregulation of several genes involved in meiosis [Chi et al., 2009]. Furthermore disturbance of the *SUN1* gene in the murine model leads to several defects in chromosome organisation such as telomere-NE association during meiosis, pairing, synapsis and recombination. Interaction with telomeres is also well documented in yeast where the sole Cter-SUN protein called Mps3 interacts with telomeres and plays a role in nuclear organisation [Bupp et al., 2007]. Interestingly, Mps3 directly binds to the histone variant H2A.Z and this interaction is needed to localise Mps3 in the INM suggesting a new chaperone function for H2A.Z [Gardner et al., 2011]. These phenotypes are similar to maize and *A. thaliana sun* mutants that display defects in synapsis suggesting a redundancy of the Cter-SUN activity [Bass et al., 2003, Ding et al., 2007, Varas et al., 2015].

In *A. thaliana*, the two Cter-SUN proteins (AtSUN1 and AtSUN2) localise to the NE, form homomers and heteromers and interact with the ONM KASH-domain proteins [Graumann et al., 2010, Graumann and Evans, 2010, Oda and Fukuda, 2011]. In *Zea mays*, two Cter-SUN proteins ZmSUN1 and ZmSUN2 have been identified and as in *A. thaliana* localise to the NE [Murphy et al., 2010]. In the mitotic prophase, AtSUN1 and AtSUN2 accumulate at the nuclear envelope; after NEBD, they associate with the mitotic ER membranes and rapidly aggregate around chromatin during the post-mitotic NE reassembly, suggesting a role of NE-anchored proteins in chromatin organisation during mitosis [Graumann and Evans, 2011]. Furthermore, Varas et al. (2015) showed a delayed meiotic progression and incomplete synapsis in the double mutant *atsun1 atsun2* leading to reduced plant fertility suggesting a connection between SUN domain protein and chromatin during meiosis. These defects are only found in the *atsun1 atsun2* double mutant and are

not detectable from in the single mutants [Varas et al., 2015].

The Cter-SUN proteins also regulate migration and shaping of the nucleus. In *Caenorhabditis elegans*, the SUN-domain protein UNC-84 is involved in nuclear migration regulation during embryo development [Malone et al., 1999]. In human cells, expression of SUN1 without the Cter-SUN domain changes nuclear morphology. This suggests the importance of this domain in the establishment of the LINC complex by interaction with the KASH protein complex that maintains nuclear morphology [Haque et al., 2010]. In *A. thaliana*, Cter-SUN mutants also impact nuclear morphology. Their nuclei are more circular than wild type nuclei (see Section 1.5, [Graumann et al., 2010, Graumann and Evans, 2010, Oda and Fukuda, 2011]).

Several studies on mid-SUN proteins in mouse, yeast and fungi showed that these proteins are localised to the ER [Sohaskey et al., 2010, Friederichs et al., 2012, Vasnier et al., 2014]. In mouse, the mid-SUN protein named *Osteopotentia* is a membrane protein of the rough ER (rER). This protein is involved in the production of type I collagen, rER expansion, and terminal osteoblast differentiation [Sohaskey et al., 2010]. Analysis of the *Saccharomyces cerevisiae* mid-SUN protein SLP1 (Sun-Like Protein 1) revealed its interaction with the Cter-SUN protein Mps3 for its transport to NE [Friederichs et al., 2012], suggesting that this mid-SUN protein functions as a Cter-SUN chaperone as H2A.W. SLP1 was also identified in *Sordaria* and is involved in localisation of the ER and NE during the sexual cycle [Vasnier et al., 2014].

The mid-SUN proteins in plants were first described in maize by Murphy and Bass [Murphy et al., 2010], who detected three mid-SUN proteins. In *A. thaliana*, three mid-Sun proteins have also been identified (AtSUN3, AtSUN4 and AtSUN5) [Graumann et al., 2014]. AtSUN3 and AtSUN4 are expressed in most tissues at low to medium levels, where they localise to the ER and NE. AtSUN5 is expressed predominantly in pollen, anthers and the endosperm. The mobility of the mid-SUN proteins was studied by microscopy with the Fluorescence Recovery After Photobleaching (FRAP) technique [Graumann et al., 2007]. AtSUN3 and AtSUN4 do not have the same mobility characteristics. AtSUN4 is more mobile in the ER than in the NE whereas AtSUN3 is less mobile than AtSUN4 generally. AtSUN4 therefore could be a protein chaperone that carries proteins between ER and the nucleus. The triple mid-SUN mutant is lethal suggesting that mid-SUN proteins are necessary for plant survival [Graumann et al., 2014]. Like the Cter-SUN proteins, the mid-SUN

proteins interact with the KASH-domain proteins, such as AtWIP1 and AtTIK which will be detailed below, and are components of the *A. thaliana* LINC complex [Graumann et al., 2014]. AtSUN3 and AtSUN4 both interact with AtSUN1 and AtSUN2, in a yeast-two-hybrid system while AtSUN5 does not. AtSUN3 also interacts with AtSUN4. AtSUN5 interacts with itself and with AtSUN3. For AtSUN1 and AtSUN2 it has been demonstrated in yeast and in planta that the coiled-coil domain of AtSUN1 and AtSUN2 are necessary for this interaction. In summary, the mid-SUNs can organise into homo or hetero-polymers as can the Cter-SUN proteins, localised in the ER and NE and all the SUN proteins play a role in LINC complex structure [Graumann et al., 2014].

### **KASH domain protein**

KASH domain proteins are ONM-specific and highly conserved in vertebrates and yeast. The characteristic KASH domain that defines the family interacts with the SUN domain, an interaction essential for the ONM localisation of KASH domain proteins. In mammals, six KASH-domain proteins have been identified [Rothballer and Kutay, 2013, Sosa et al., 2013]. Four of these KASH proteins are called NE spectrin repeat (Nesprins). The spectrin repeat is a 3D conformation involved in the structure of the cytoskeleton. The other two are KASH5, which interacts with SUN1 in germinal line cells, and the lymphoid-restricted membrane protein (LRMP) [Lindeman and Pelegri, 2012]. These KASH proteins in vertebrate cells can impact the architecture of the cell and the nucleus [Chambliss et al., 2013].

Zhou et al. (2012) identified a previously described protein family, WIPs as the first KASH domain proteins in plants (Figure 1.8). WIPs can bridge the ONM and the INM by interacting with the SUN domain proteins through a C-terminal VVPT motif. WIPs also interact with WITs (WPP domain-interacting tail-anchored proteins) [Zhao et al., 2008]. Mutants for WIPs or WITs impact nuclear morphology in root hair cells as do the Cter-SUN mutants [Zhou et al., 2012, Tamura and Hara-Nishimura, 2013, Zhou and Meier, 2014]. Together, these data showed the first functional plant SUN-KASH complex at the nuclear envelope. More recently in *A. thaliana*, the importance of AtWIPs and AtWITs for migration of the pollen vegetative nucleus and successful pollen tube elongation during fertilisation has been shown [Zhou and Meier, 2014]. Furthermore, AtWIP and AtWIT proteins target plant specific Ran GTPase activating protein (RanGAP) to the plant NE, as this protein has an N-terminal WPP domain in the plant [Rose and Meier, 2001, Jeong et al., 2005]. The RanGAP aids Ran in hydrolysis of GTP to GDP, driving biological

processes in mitotic spindle assembly, including nuclear transport and post-mitotic nuclear envelope reassembly.

Another KASH domain protein AtTIK (TIR Toll-Interleukin-Resistance-KASH protein) has been identified by yeast two-hybrid using Cter-SUN as bait [Graumann et al., 2014]. AtTIK contains a putative TIR domain [Mitcham et al., 1996] and a C-terminal PPS amino acid motif characteristic of a KASH domain. The *Attik* mutant displays alteration of nuclear morphology reminiscent of phenotypes observed in other KASH mutants, as well as shorter roots [Graumann et al., 2014].

Use of the DORY computer program [Zhou and Meier, 2014] has allowed the detection of additional putative KASH domain proteins in genome databases. This *in silico* analysis detected five putative plant KASH domain proteins named SUN-Interacting Nuclear Envelope1-5 (SINE1-5) [Zhou and Meier, 2014]. SINE1 and SINE2 are conserved across all land plants while SINE3 homologues are only present in eudicots. The SINE4 and SINE5 families are more restricted to a few closely related species, suggesting rather specific functions [Zhou and Meier, 2014]. Zhou et al. (2014) localised the SINE proteins at the NE and showed interaction with the Cter-SUN. The meaning of this interaction is discussed in Section 1.4.2.

### **SUN-KASH interaction**

SUN-KASH interactions allow a link between cyto- and nucleoskeleton (Figure 1.8). This LINC complex involved in nuclear movement and chromosome tethering at the NE is found from yeast to human [Crisp et al., 2006]. In *Caenorhabditis elegans*, the LINC complex is involved in nuclear anchorage via the interaction between the SUN protein UNC-84 and the KASH protein UNC-83. UNC-83 protein recruits kinesin-1 protein (a microtubule-associated force-producing protein) and permits the transfer of forces for the migration of nuclei [Horvitz and Sulston, 1980, Sulston and Horvitz, 1981, Malone et al., 1999]. The same process has been reported in mouse and human and a defective LINC complex causes several developmental defects [Rothballer and Kutay, 2013].

In *A. thaliana*, the LINC complex is involved in establishing the elongated shape of nuclei in trichomes, root cells and leaf epidermal cells [Oda and Fukuda, 2011, Zhou et al., 2012]. In root hairs of *A. thaliana*, nuclei have been observed to be more spherical for *atwip1 atwip2 atwip3* (KASH), *atsun1 atsun2* (Cter-SUN), *kaku1* (AtMyosin XI-i mutants) and *atwit1-1 atwit2-1* [Oda and Fukuda, 2011, Zhou



et al., 2012, Tamura et al., 2013]. Tamura et al. (2013) hypothesised that the two AtWIT proteins recruit KAKU1 to the NE and together transfer motive forces from myosin to the nuclear envelope generating nuclei with elongated shape. AtMyosin XI-i KAKU1 is also needed for nuclear movement in *A. thaliana* [Tamura et al., 2013]. This movement is bidirectional in mature *A. thaliana* root hair cells. It is slowed down in *atwit1-1 atwit2-1* and *kaku1* mutants [Tamura et al., 2013]. Finally, mutants of the LINC complex components, WITs and KAKU1 display similar nuclear shape alterations in agreement with the protein interaction described for them [Goto et al., 2014]. These proteins may be part of a complex involved in the establishment of nuclear shape but are also needed for nuclear migration [Zhou et al., 2015a].

The LINC complex also plays a role in meiotic crossovers in *A. thaliana*. The double mutant *atsun1 atsun2* (Cter-SUNs) causes defects in the distribution of crossover sites if absent [Duroc et al., 2014, Varas et al., 2015]. Another protein, AtPSS1 (Arabidopsis Pollen Semi-Sterility1), also named AtKin-1, encodes a kinesin1-like protein and its mutant has the same defect [Duroc et al., 2014, Wang et al., 2014]. AtPSS1 interacts with AtWIP1 and AtWIP2. Therefore SUN, WIP and AtPSS1 were proposed to mediate chromosome synapsis during meiotic prophase I [Duroc et al., 2014].

### 1.4.3 Lamins

Lamins are conserved in protozoa and metazoa in which they constitute a meshwork layer underneath the nuclear periphery that can be observed by electron microscopy [Burke and Stewart, 2013]. The lamins are classified in two groups, type-A and type-B. In vertebrates, there are two major isoforms of type-A lamins, lamins A and C; the two protein isoforms resulting from alternative splicing of transcripts made from the same gene (LMNA) [Lin and Worman, 1993]. Expression of these two isoforms of type-A lamins is regulated during development, whereas B-types lamins are expressed during development in all cells [Benavente et al., 1985, Schatten et al., 1985, Lehner et al., 1987]. In the early mouse embryo, lamins A and C are not vital and for example, cells of the hematopoietic lineage express only B-type lamins [Guilly et al., 1990, Röber et al., 1990]. Lamins have a central alpha helical coiled-coil rod domain between non-helical head and tail domains typical of Intermediate Filaments (IF) structure [Dechat et al., 2010]. Two conserved cyclin-dependant kinase 1 (CDK1) domains fl the rod domain, which is responsible for dimerisation and higher order assembly of lamins permitting interaction between

lamins monomers [Dechat et al., 2010].

The lamin proteins form polymers giving rise to filaments of about 10 nm in diameter named the nuclear lamina, which is the major component of the nucleoskeleton [Simon and Wilson, 2011]. The nuclear lamina is directly connected with the NE and the NPC [Goldberg et al., 2008a, Goldberg et al., 2008b, Gerace and Huber, 2012]. In metazoans, this complex is made of several layers of lamin polymers, which form filaments and interact with INM lamin-binding proteins such as the Lamin B receptor (LBR) or with proteins associated with chromatin such as the Barrier-to-Autointegration Factor (BAF) or Heterochromatin Protein 1 (HP1) anchoring the chromatin to the lamina [Ho and Lammerding, 2012, Simon and Wilson, 2013]. HP1 and BAF proteins interact with histones, and participate in gene regulation and chromatin organisation [Margalit et al., 2007].

The nuclear lamina has key functions in nuclear morphology. The lamina meshwork possesses compressibility and elastic properties and plays a role as a molecular shock absorber with biophysical characteristic of a solid-elastic shell, which permits a dynamic change of nuclear morphology [Dahl et al., 2004, Dahl et al., 2005]. Studies conducted in human cells have shown the importance of lamins A and C for the rigidity and shape of the nucleus [Lammerding et al., 2006, Ferrera et al., 2014]. Indeed, in lamin A mutant cells, nuclei are less rigid. Mutation of lamin B1 seems to have only little effect and does not cause a general defect in nuclear organisation [Lammerding et al., 2006], although Ferrera et al. (2014) showed that overexpression of lamin B increases the rigidity of the nucleus and changes the biophysical properties of nuclear lamina. The authors hypothesise that this overexpression changes the organisation of nuclear proteins and impacts protein and chromatin position. The two groups of lamins are required for nuclear movement and migration via the LINC complex [Folker et al., 2011, Bone et al., 2014]. Finally, because of all these central functions in nuclear organisation and because mutations in lamins and their associated proteins are involved in developmental and progeria (ageing related diseases in human), called nuclear envelopathies and laminopathies, the nuclear lamina has been well studied in metazoans.

Aside from the mammalian systems, filamentous structures reminiscent of the metazoan lamina have been observed in the plant species *Nicotiana tabacum* and *Allium cepa* by electron microscopy [Minguez and Espina, 1993, Fiserova et al., 2009]. Direct lamin homologues are not found in plants and unicellular organisms [Cohen et al., 2001, Fiserova et al., 2009]. Main candidates involved in the formation of

these structures are Nuclear Matrix Constituent Proteins (NMCPs), which are specific to the plant kingdom [Ciska and Moreno Diaz de la Espina, 2013]. NMCPs are subdivided into two groups, NMCP type1 and 2 and a total of 71 NMCP genes have been recorded in flowering plants. In *A. thaliana*, four NMCP homologues called Crowded Nuclei (CRWN) have been identified [Dittmer et al., 2007]. The NMCP proteins contain four domains, two coiled-coil domains flanked by a short head and a long tail domain [Ciska and Moreno Diaz de la Espina, 2014]. The rod domain includes highly conserved regions at both ends involved in head to tail association of lamin dimers.

The four CRWN proteins do not possess the same spatial distribution in the nucleoplasm and display distinct patterns of expression [Dittmer et al., 2007, Sakamoto and Takagi, 2013]. Single, double and triple mutants are viable but show alterations in chromatin organisation and reduced nuclear size. In contrast, the quadruple mutant *crwn1 crwn2 crwn3 crwn4* is lethal indicating that CRWN proteins are key components of the nucleus [Dittmer et al., 2007, Sakamoto and Takagi, 2013]. It has emerged that CRWN1 and CRWN4 are located at the nuclear periphery while CRWN2 and CRWN3 are more nucleoplasmic. During NEBD and from prometaphase to anaphase, CRWN1 is always associated with chromatin while CRWN2, CRWN3 and CRWN4 are localised in the nucleus only at telophase [Sakamoto and Takagi, 2013]. The co-localisation of CRWN proteins with chromatin, their enrichment at the NE, and their similarities with lamins (coiled coil and rod domains), suggest their involvement in chromatin organisation and segregation and that they are functional homologues of lamins in *A. thaliana* (Figure 1.8). The function of CRWNs has been investigated by several groups and the current picture proposes that CRWN4 may play an important role in the maintenance of chromocentre integrity and organisation during interphase, whereas CRWN1 would be more involved in nuclear morphology regulation [Grob et al., 2014, Wang et al., 2014].

Recently, KAKU4 has been proposed as a new putative lamin binding protein in plants [Goto et al., 2014] (Figure 1.8). KAKU4 also localises to the nuclear periphery and interacts with CRWN1 and 4. As with most mutants of the NE and nuclear periphery, the *kaku4-2* mutant displays altered nuclear shape and size. This *kaku4-2* mutant is not lethal, which suggests that plants might have acquired non-essential components of the lamina-like structure.

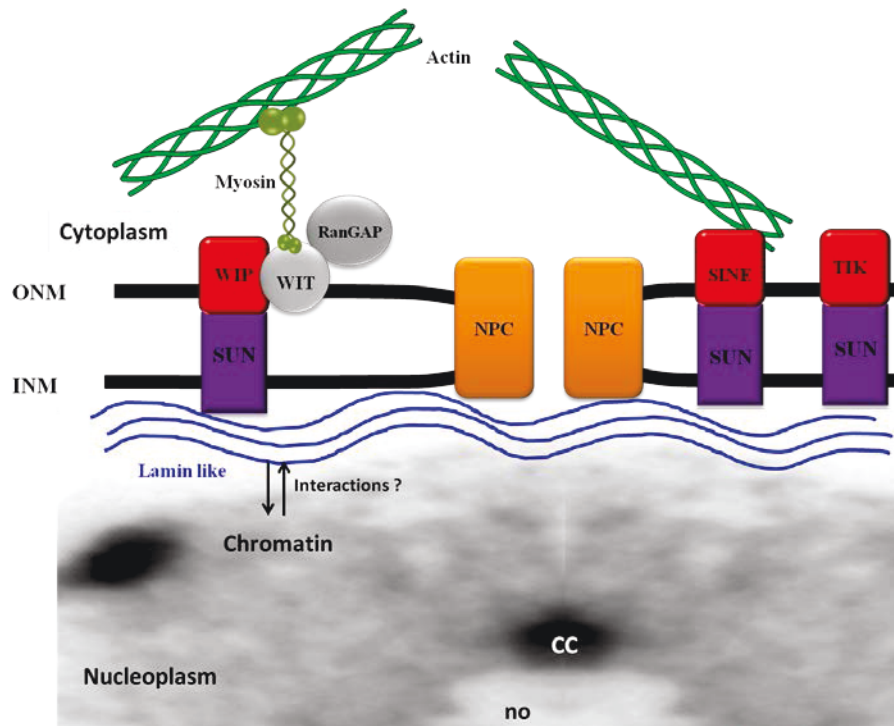


Figure 1.8: **Protein components of the plant NE.** The SUN and KASH (WIP, SINE, and TIK) proteins that form the LINC complex appear functionally in plant and animals (see Section 1.4). WIPs interact with WITs and are associated with actin by their interaction with myosin XI-i. SINEs interact directly with actin and TIK interacts only with SUN proteins. As in mammals putative nuclear lamina was detected (KAKU4 and CRWN), but no interaction between these proteins and chromatin was found. (CC: chromocentre, no: nucleolus).

## 1.5 Nuclear morphology

### 1.5.1 Nuclear shape

The NE is an elastic structure and can expand or retract upon physical constraints within the nucleus or outside of it [Dahl et al., 2004]. Natural variations in nuclear shape are involved in different cell fates. As an example, nuclear morphology is frequently modified in human cancer cells. The exact consequences of these nuclear shape alterations are not well understood but are suggested to change chromatin organisation and gene expression [Chow et al., 2012, Jevtić and Levy, 2014]. In breast cancer or in invasive ductal carcinoma the cancer cells feature enlarged nuclei. Other cancer cells possess atypical nuclear invaginations. Finally cancer cells have generally misshapen nuclei [Dey, 2010, True and Jordan, 2008]. Variations in cell size and morphology is also observed in plants. In *A. thaliana*, variations in nuclear morphology have been observed in various tissues such as epidermis, trichomes, root hairs [Traas et al., 1998, Qian et al., 2009] or during seed formation [van Zanten et al.,

2011] and cotyledon development [Bourbousse et al., 2015]. Two main hypotheses have been proposed to explain how the nuclear shape is regulated and how this impacts nuclear function. First, nuclear reshaping may modify the nuclear rigidity needed for nuclear movement. Second, nuclear reshaping may induce chromatin reorganisation, which in turn modifies gene expression [Webster et al., 2009].

### **Cytoskeleton components**

Actin, myosin and microtubules actively participate in the regulation of nuclear shape [Gerlitz and Bustin, 2011]. In humans, actomyosin and actin filaments mediate changes of nuclear shape respectively in neural cells and chondrocytes [Guilak, 1995, Martini and Valdeolmillos, 2010]. Another well-known example comes from *Drosophila*, in which nuclei elongate during cellularisation in the course of embryogenesis. The elongation process is dependent on microtubules and INM proteins such as the Kuk/Char protein [Brandt et al., 2006, Pilot et al., 2006]. This protein possesses three domains: a coiled-coil domain, a nuclear localisation signal (NLS) and a CaaX motif. This motif facilitates the localisation of proteins in the NE. The Kuk/Char protein is known to play a role in the regulation of positioning and morphology nuclei in *Drosophila* blastoderm cells [Brandt et al., 2006, Pilot et al., 2006]. The microtubules produce forces transmitted through the LINC complex, which in turn alter nuclear shape. In *A. thaliana*, Kaku1 interacts with WIT which interacts with the KASH counterpart of the Plant LINC complex, thus connecting microtubules and the LINC complex (Figure 1.8). Mutations in KAKU1 encoding MYOSIN-XI-i impact nuclear shape in root hair cells [Tamura et al., 2013].

### **Lamins**

Lamins (see Section 1.4.3) are major actors for nuclear shape maintenance. For example the neutrophils, which can migrate to reach infected tissues, display multi-lobed nuclei connected by a thin layer of chromatin filaments. This process of migration is affected in a Lamin B Receptor (LBR) mutant, which is associated with the Pelger-Huet anomaly (defect of terminal neutrophil differentiation) and leads to the simultaneous loss of the multi-lobed phenotype and of nuclear migration [Hoffmann et al., 2007]. Lamin mutants such as those identified in the premature aging Hutchinson-Gilford progeria syndrome (HGPS) display ghost-like instead of spherical nuclei [Shumaker et al., 2006].

In *A. thaliana*, *crwn* (lamin-like protein) and *kaku4* (lamin-binding protein) mutants exhibit altered nuclear shape [Dittmer et al., 2007, Sakamoto and Takagi,

2013, Goto et al., 2014] and in the case of *kaku4-2* mutant, nuclear mobility is affected [Goto et al., 2014].

### **NE-anchored proteins**

Examples of NE proteins, which alter nuclear shape include the LBR, members of the LEM (LAP1beta, Emerin, Man) domain family, and SUN and KASH domain proteins. LBR is required for the differentiation of granulocytes to obtain the final nuclear shape (lobulated or ring-shaped). A defect in LBR impacts the NE morphology and chromatin organisation of granulocytes. Their nuclei, which are normally lobulated, ovoid and the heterochromatin classically located at the nuclear periphery is redistributed to the nuclear centre [Lammerding et al., 2006, Hoffmann et al., 2007, Olins et al., 2008]. Lem2 is a conserved transmembrane protein, which interacts with Lamins. A *lem2* human mutant cell line has altered nuclear shape, with nuclei having a large invagination and lobulation [Ulbert et al., 2006]. To date LBR and LEM were not identified in plants.

In mice and human Nesprin (a KASH domain protein) has been shown to function in the shape regulation of the nucleus [Lu et al., 2012, Lüke et al., 2008]. Absence of the giant Nesprin in mouse results in a severe defect in nuclear shape, while expression of Nesprin2 without the N-terminal actin-binding domain restores a normal nuclear shape phenotype [Lu et al., 2012, Lüke et al., 2008]. Finally, the shape of the nucleus is not only dependent of cytoskeleton interactions but also of the other component of the LINC complex, the SUN domain proteins. In the HGPS syndrome, caused by a mutation of the lamin A, nuclei show several shape defects [Sullivan et al., 1999, Shumaker et al., 2006]. Mutation of SUN1 in HGPS cells restores nuclear morphology and chromatin organisation [Chen et al., 2012]. In plants SUN and KASH domains proteins which are components of the LINC complex display defects in nuclear shape [Zhou et al., 2012, Graumann et al., 2014].

## **1.5.2 Nuclear size**

### **Theory of nuclear-to-cytoplasmic ratio**

Within a given species, nuclear size can display a great range of variability. In the 19th century, Conklin (1912) showed a correlation between nuclear and cellular sizes and defined the nuclear-to-cytoplasmic (N/C) ratio [Conklin, 1912]. This ratio remains constant with nuclear volume being  $\approx 7\%$  of the cell volume. This ratio is conserved even with the variation of cellular size occurring in yeast cell cycle mutants

[Jorgensen et al., 2007, Neumann and Nurse, 2007]. The regulation of nuclear size appears to be essential as a variation of the N/C ratio was found in cancer cells but relationships and mechanisms between cell volume and nuclear volume remain unclear [Zink et al., 2004, Chow et al., 2012].

### **Theory of the karyoplasmic ratio**

Nuclear size does not only correlate with cell size but also with the volume of cytoplasm, thus define the karyoplasmic ratio [Cavalier-Smith, 2005, Gregory, 2005]. Cavalier-Smith (2005) proposed a theory to explain this relationship between nuclear size and DNA content. He suggested that natural selection results in the optimum karyoplasmic ratio [Cavalier-Smith, 2005]. This theory includes that nuclear size depends on DNA content and that DNA content or chromatin condensation affect nuclear size.

### **Functions of NPC and endoplasmic reticulum membranes in nuclear size**

The theory of Cavalier-Smith is controversial, and other authors propose a third theory proposing that the NPC and/or ER membrane availability determine nuclear size [Webster et al., 2009]. This theory states that DNA content would not be the most important parameter for nuclear size regulation [Webster et al., 2009, Edens et al., 2013]. It is best illustrated by the fact that nuclear size changes when it is implanted into a new cellular environment and this does not involve any change in DNA content [Harris, 1967]. Evidence for the involvement of the ER comes from the reticulon proteins (RTN), a family of proteins specific to the ER involved shaping and maintaining of the tubular ER [Voeltz et al., 2006]. In *Xenopus*, over-expression of RTN induces growth of the nucleus whereas a lack of these proteins accelerates nuclear re-assembly [Kiseleva et al., 2007, Anderson and Hetzer, 2008]. This shows that the availability of the sheet ER membranes can be limiting for nuclear growth.

A function of NPC in regulating nuclear size was suggested by the observation that when NPC function is blocked, the volume of the nucleus increases [Jorgensen et al., 2007, Neumann and Nurse, 2007]. In *A. thaliana* the *nup136* mutant has a decreased nuclear size while NUP136 over-expression induces nuclear elongation that can be linked to increased nuclear volume [Tamura et al., 2010, Tamura and Hara-Nishimura, 2011]. Thus the amount of Nup136 protein in the NE affects nuclear morphology suggesting the involvement of this protein in the maintenance of nuclear structure [Tamura et al., 2010, Tamura and Hara-Nishimura, 2011]. Alternatively, changes in nuclear morphology may be due to alteration in the nucleocytoplasmic transport of molecules by the nuclear pore (nuclear component and/or mRNA), as

the *nup136* mutant shows abnormal mRNA export [Tamura et al., 2010, Tamura and Hara-Nishimura, 2011].

### **Other proteins of the NE and the nuclear periphery are involved in nuclear size**

The LINC complex, which permits physical interactions between the inside and the outside of the nucleus, can also regulate nuclear size thanks to these interactions [Shumaker et al., 2005, Lu et al., 2012]. In *A. thaliana*, mutation in the KASH domain protein AtTIK decreases nuclear size whereas the murine knockout of the KASH protein *nesprin-2* increases the nuclear size [Lu et al., 2012, Graumann et al., 2014]. Mis-regulation of lamin production (by under- or over-expression) through lamina-associated polypeptides (LAPs) has been shown to cause a disruption of nucleus size regulation [Gant et al., 1999, Prüfert et al., 2004, Levy and Heald, 2010]. In *A. thaliana* mutations of lamin-like proteins (CRWN) decrease nuclear size [Dittmer et al., 2007].

In summary, nuclear size and shape have important implications for cellular functions and their alterations characterised by an altered karyoplasmic ratio is associated with alteration of basic functions of the cell [Zink et al., 2004, Slater et al., 2005]. For instance, these two parameters have also been associated with the variations in transcription levels, maintenance of the nucleolus and DNA polymerase activity [Hancock, 2004, Sasaki et al., 2006, Miyoshi and Sugimoto, 2008]. Nuclear size and shape are suggested to be important parameters correlated with optimal nuclear activity. Methods to quantify nuclear shape and size in plant cells has been a major part of the work undertaken in this thesis.



## 1.6 Objectives

This research focusses on the role of the LINC complex in nuclear morphology and chromatin organisation in *A. thaliana*. The LINC complex is a well conserved evolutionary protein bridge connecting the nuclear and cytoplasmic compartments across the NE. While its alteration affects nuclear morphology in most species, its implication for chromatin organisation has been less studied in plants. Genes involved in chromatin organisation and maintenance (histone chaperone, chromatin remodeller) are also included in this analysis, to study the impact of chromatin disorganisation on the nuclear morphology. To achieve this aim 3D imaging methods have been developed to investigate nuclear morphology and chromatin organisation of the plant model species *A. thaliana* in which chromosomes are organised in rosette-like structures leading to the formation of conspicuous chromatin domains called chromocentres.

Firstly, a semi-automatic informatic programme termed *NucleusJ* was developed [Poulet et al., 2015]. *NucleusJ* allows the analysis of a large data set from 3D images gained from light microscopy. Several improvements have then been added to the original version of *NucleusJ*. Informatic and mathematic developments were undertaken in collaboration with Professor Philippe Andrey (Institut Jean-Pierre Bourgin, UMR1318 INRA-AgroParisTech) and with Professor Rémy Malgouyres (LIMOS UMR 6158 CNRS, Clermont-Ferrand). This tool was developed as a phenotyping tool to analyse nuclear morphology and heterochromatin organisation. *NucleusJ* was also used to investigate the position of chromocentres in the 3D nucleus.

Using *NucleusJ*, 3D images of nuclei from root and cotyledon of wild type, mutants in the LINC complex and mutants in chromatin organisation were analysed. To determine the impact of the alteration of nuclear morphology on transcription, RT-qPCR was performed in collaboration with Doctor Céline Duc (GReD) to analyse the transcriptional reactivation of heterochromatic targets. Chromocentre decompaction was evaluated using Fluorescence In Situ Hybridation (FISH) 2D (undertaken by Doctor Matthias Benoit) and by FISH 3D (undertaken by Doctor Sophie Desset and Professor Christophe Tatout, GReD).

Finally this work explore the evolution of the LINC complex in green plants, using RNA sequencing (RNA-seq) expression data and phylogenetic analyses. The LINC complex has been well studied in *A. thaliana*; but in many cases, there is evidence of gene duplication and complexity in this species leading to redundancy

and diffi in functional assays. The phylogenetic and RNA-seq analysis of the LINC complex provides a better understanding of potential redundancy and specialised function of the LINC complex members and lamina-like proteins. This analysis was applied to make predictions about the composition of the simplest functional LINC complex in green plants.

# Chapter 2

## Quantitative analysis of nuclear parameters using 3D images

### 2.1 Imaging : state of the art

#### 2.1.1 Sample preparation

As introduced in Chapter 1, organisation and positioning of chromatin domains within the nuclear space, such as chromocentres may be one of the important mechanisms needed for transcriptional regulation of the eukaryotic genome [Fransz and de Jong, 2002, Bickmore and van Steensel, 2013]. To comprehend nuclear structure and function, imaging tools are needed to quantify nuclear morphology, positioning and organisation of chromatin domains in three dimensions. To achieve this goal two strategies can be developed: *in vivo* or *in vitro* living cells. These two approaches have advantages and disadvantages. Live cell imaging allows visualisation of chromatin organisation as well as nuclear morphology by using fluorescent fusion proteins. However overexpression of a fusion protein may lead to its mislocalisation, competition with the endogenous protein, induce steric hindrance or may affect structures of interest. Depending on the time needed to perform image acquisition photobleaching may also occur. As an alternative, *in vitro* tissue can be used and the structures of interest detected by fluorescent *in situ* hybridisation (FISH). In the FISH technique the nucleus is stained by an intercalating agent (DAPI or Hoechst) which binds DNA. FISH uses cryogenically or chemically *in vitro* tissue and these steps can also affect nuclear shape and chromatin organisation [Ronneberger et al., 2008, Tirichine et al., 2009]. The FISH method has advantages when studying multiple mutants, because it avoids the time needed to establish a transgenic line expressing the fusion protein. Furthermore, *in vitro* methods that immobilise

the nucleus are useful as it avoids movements during image acquisition. The FISH technique can be used on fixed isolated nuclei [Tirichine et al., 2009] or whole mount preparations [Bauwens et al., 1994]. Artefacts may occur in isolated nuclei since the cellular environment strongly influences nuclear morphology and chromatin organisation [Versaevel et al., 2012] and is absent in this type of preparation. Whole-mount preparation would then be the preferred method of investigation in this work.

### **2.1.2 3D Light microscopy technologies**

The majority of 3D microscopy technologies are based on optical sample sectioning, which results in a stack of images which are then used to produce 3D representations of the object of interest. For this study, confocal microscopy and Structured Illumination Microscopy (SIM) were used to acquire 3D images of nuclei.

Fluorescent 3D microscopy techniques are frequently based on photon emission after excitation by a laser which is specifically located in the sample. The photon is captured by a detector, which permits the detection of the fluorescently tagged object of interest. The aim is to capture only the photons emitted in a specific focal plane. The focal plane in confocal microscopy is obtained by a pinhole aperture that is situated in a conjugate plane (confocal) with a scanning point on the sample. A second pinhole is positioned in front of the detector (a photomultiplier tube (PMT)). The fluorescence emitted by the sample, which is excited by a scanning laser, is focused as a confocal point at the detector pinhole aperture [Pawley, 2006].

The technique of SIM is used in wide-field microscopes. To obtain images of the focal plane, first raw images are acquired with an optical grid in different positions and with different angles relative to the axis of the microscope (Figure 2.1). These images are then combined in real-time to form an optical section at the focal plane (Figure 2.1) [Lukosz and Marchand, 1963, Neil et al., 1997].

In the both cases, the sectioning of the sample is achieved by vertical movement of the sample which permits changes in the focal plane. For the purpose of this study, the image data obtained, with the two methods (confocal and SIM), is similar. The nucleus is stained and the rest of the cell remains black and defined as background. The limit of detection and of analysis of the data sets obtained with the two types of microscope are therefore the very similar.

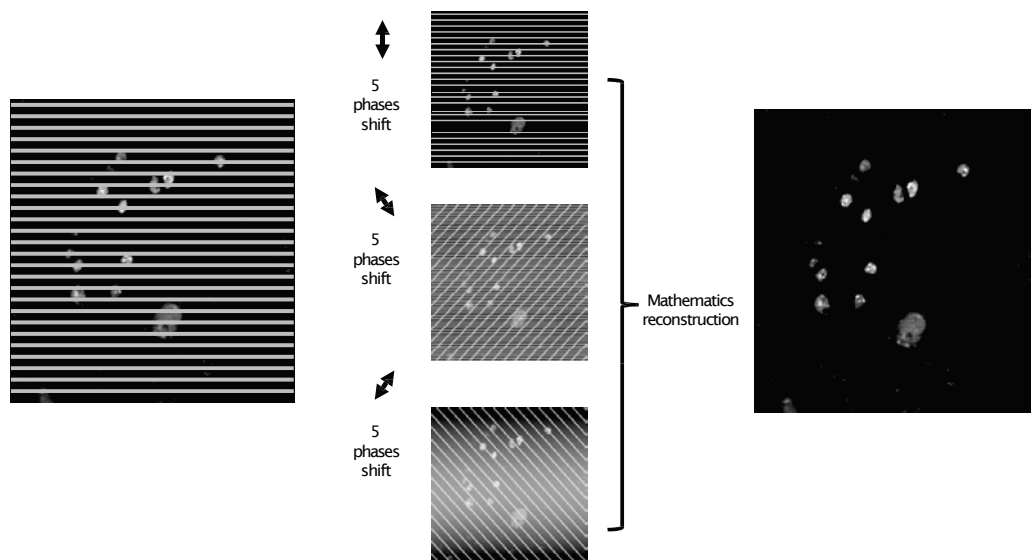


**Figure 2.1: Structured illumination microscopy technique.** The optical grid is located between the laser light and the sample, which involved a stripe-shaped sinusoidal interference pattern. The Charge Coupled Device (CCD) camera detects the light intensity emitted, and an algorithm reconstructs a 3D image from a series of 15 raw images per slice (adapted from [Schermelleh et al., 2010]).

### 2.1.3 Digital image

An image represents a spatial distribution of visual information, which is a 2D digital signal in computer science. An image can be interpreted as a 2D matrix of values which represents the light or the color intensity. This representation defines the image as a set of pixels (contraction of picture elements) in 2D or voxels (contraction of volumetric pixel) in 3D.

#### What is a digital image?

In general, the image initially obtained by microscopy is continuous and must be digitised as discrete data before further analysis [Wu et al., 2008]. The detector system (e.g. CCD camera or PMT) detects the continuous distribution of the light intensity on a 2D surface. The optical information is sampled to create the digital image. The loss of information in this sampling process and the resulting limitations will be considered in this chapter.

The digitisation is therefore dependent on the detector system. A CCD camera is used on the SIM microscope. This type of camera, due to the small square area

of the sensor surface detects the quantity of photons emitted by the sample and converts it into a voltage proportional to the number of electrons absorbed by the square during exposure. This small square area on the CCD defines a pixel size in association with the magnification [Janesick, 2001, Pawley, 2006, Wright et al., 2015].

The confocal microscope used in this study uses a PMT as detector. The photocathode of the PMT produces a single photoelectron, resulting from the striking of small parts of photons (emitted by the sample). The PMT then amplifies the photoelectron by charge multiplication [Pawley, 2006]. The continuous output signal of the PMT is digitised under the control of a pixel clock. This clock divides the time taken to scan one line into the appropriate number of intervals, so that each time interval represents a pixel of the total image.

In summary, to obtain the digital image, a continuous optical image is sampled, to produce an array of pixels of integer values which represent the light intensity at each coordinate by a non-negative integer. Finally the sampling of the continuous signal can affect the resolution because poor sampling has a direct impact on the ability to detect two closely positioned objects as being distinct. Resolution is an important parameter to develop tools for the 3D characterisation of nuclei since objects like chromocentres can be located close to each other.

### **The different types of digital image**

Three different types of image exist; black and white, monochrome or in color. The black and white image is simplest, as there are only two possibilities of value: 0 for black and 1 for white, this type of image are named binary images. The most commonly used format is the 8 bit monochrome image (grey level image), which displays  $2^8 = 256$  possibilities of pixel values between 0 (black) and 255 (white). Monochrome images can also be encoded in 16 bits ( $2^{16} = 65536$  possibilities), or 32 bits ( $2^{32} = 4294967296$  possibilities), these two formats however significantly increase the weight of the image, and the time for processing. It is easy to obtain a black and white image from a monochrome grey scale, by finding a threshold value  $S$ , which allows the detection of object of interest:

$$\text{If } (I(x, y) \geq S) \text{ } IB(x, y) = 1 \text{ Else } IB(x, y) = 0 \quad (2.1)$$

With  $IB$  the binary version of the raw grey level image  $I$ .

The distribution of the values of one image is represented by the histogram of this im-

age (Figure 2.2). The image histogram is the representation of the discrete function  $v(C)$  which at each colour  $C$  of the image associates the number  $v(C)$  of pixel (population) having the same color (Figure 2.2). Histogram computation is frequently used between image acquisition and image processing, with several pre-processing, segmentation or statistical methods needed.

Operations on the histogram allow improvement of the image. The equalisation of the histogram homogenises the repartition of the grey values to obtain a better distribution of the pixel for each class of the histogram. The dynamic of the histogram value can be expanded to allow a better pixels repartition on the grey value scale. This operation improves the contrast of the image.

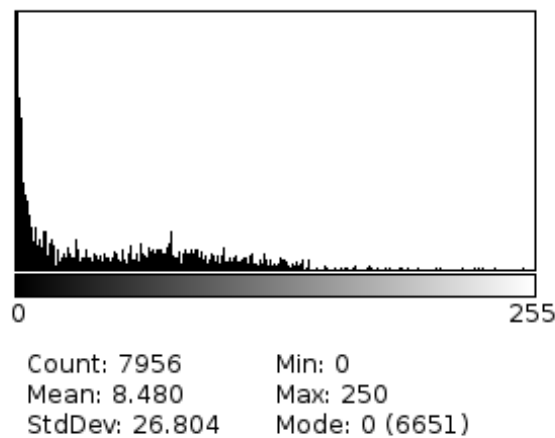


**Figure 2.2: Histogram of 8 bits image in grey levels.** A histogram represents the grey intensity level on the abscissa from black (left) to white (right). A 256 grey level image will be represented by a histogram with 256 values in the abscissa and in the ordinate the number of pixels for the image for each grey level.

### How is image resolution defined?

Resolution is defined as the shortest distance between two points that can still be distinguished on a specimen. The Rayleigh criterion is defined as the minimum distance separating two adjacent Airy disks (Figure 2.3). These Airy disks are produced by an optical system with circular apertures which are limited by the diffraction pattern. This diffraction pattern results from the passage of light through a small circular aperture, and this pattern is surrounded by concentric circular rings. The point sources of light emitted by a specimen is represented by Airy diffraction patterns at the microscope intermediate image plane (Figure 2.3) [Airy, 1835].

Finally the image of the sample is constituted by a set of closely spaced point light sources that form Airy patterns. The resolution is then defined by the spatial

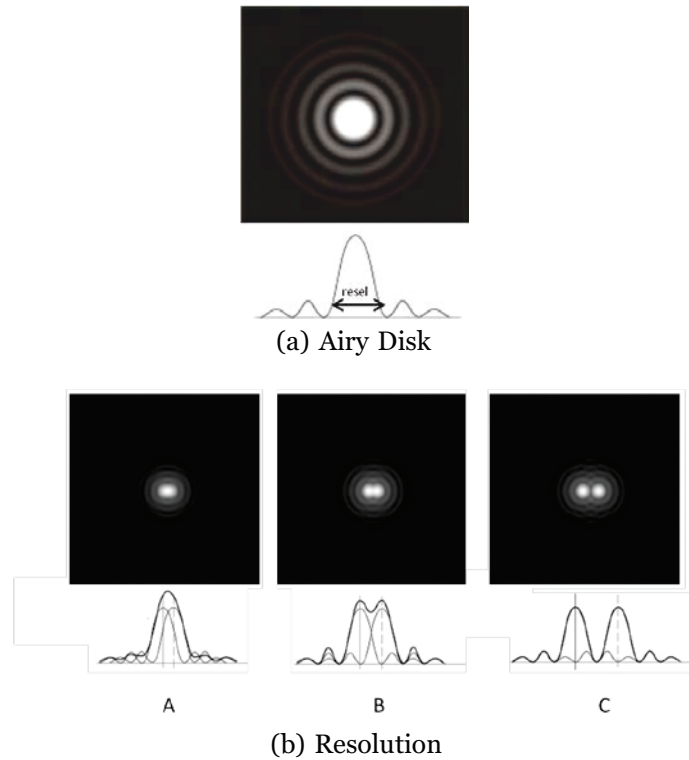


**Figure 2.3: Resolution and Airy disks definition.** **a)** The Airy disks are produced by an optical system with circular apertures which are limited by the diffraction. This diffraction pattern results of the passage from light through a small circular aperture, and this pattern is surrounded by concentric circular rings. Airy disks define the optical system resolution and is dependant on the wave length used, the numerical aperture (NA), and the focal distance. **b)** Two objects are well resolved, if their Airy disks are sufficiently far apart and if they respect the Rayleigh criterion. This criterion that two closely spaced Airy disks are distinct if they are farther apart than the distance at which the principal maximum of one Airy disk coincides with the first minimum of the second Airy disk. If the diffraction pattern of these two objects are totally overlapping, the two objects are not distinguishable (A). The Rayleigh criterion limit is just respected in (B) whereas in C there are two elements resolvable.

sampling which corresponds to the frequency of sampling of the continuous signal, and this frequency is equal to the pixel/voxel length [Wu et al., 2008]. The quality and fi analysis of the image is therefore dependent on the sampling of the continuous signal. To defi the resolution of the image the fi step is to defi the maximal theoretical resolution and this resolution is dependent on the characteristics of the microscope [Abbe, 1873, Pawley, 2006, Wu et al., 2008]. These characteristics are described by the point spread function (PSF). On "perfect" optical systems, the PSF is not a point but is represented by the Airy Disk (Figure 2.3a). Finally, the lateral and axial resolution are defi by two formulae.

The lateral resolution (x and y axes) is deduced from the Abbe diffraction limit [Abbe, 1873] and is defi in the image plane as the distance between the central maximum and the fi minimum in the Airy disk:



$$r_{xy} = \frac{0.6\lambda}{NA} \quad (2.2)$$

Where NA is the objective numerical aperture and  $\lambda$  is the emitted light wavelength. The lateral resolution of the confocal microscope is improved by 30% compared to that in the widefield microscope because the PSF is improved by this percentage [Pawley, 2006]. This increases the maximal theoretical resolution by:

$$r_{xy} = \frac{0.4\lambda}{NA} \quad (2.3)$$

The axial resolution in confocal microscopy is proportional to the refractive index of the specimen medium ( $n$ ) and the wave length ( $\lambda$ ) and is inversely proportional to the square of the NA (Formula 1.3) [Pawley, 2006].

$$r_z = \frac{1.4\lambda n}{NA^2} \quad (2.4)$$

As seen above, the resolution is equivalent to the frequency of sampling of the continuous signal detected by the microscope to obtain the digital image. The Nyquist-Shannon sampling theorem establishes that when sampling a signal (e.g., converting from an analog signal to digital), the sampling frequency must be greater than twice the band width of the input signal in order to be able to reconstruct the original perfectly from the sampled version [Nyquist, 1928, Shannon, 1949]. The implication of this theorem states that the sampling interval has to be less than half of the smallest object to be resolved (Figure 2.4). So, if there are less than two pixels by resolution element (resel), it is not possible to describe the signal reliably. From three pixels per resel, the signal can describe the specimen with the greatest resolution possible (Figure 2.4). This criterion permits the definition of the voxel calibration to obtain the optimal resolution. In the Handbook of biological confocal microscopy, the factor advised is 2.3 pixel per resel. The factor applied to define the calibration of the voxel in the formulae 1.2 and 1.3 is then divided by 2.3 [Pawley, 2006].

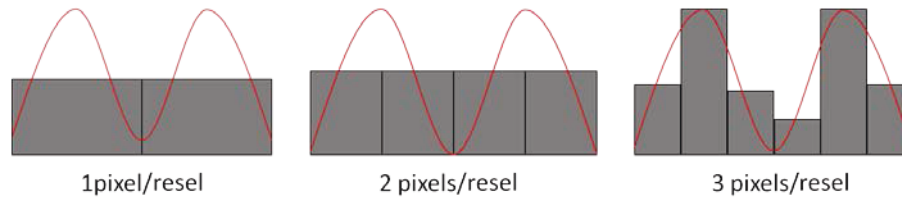


Figure 2.4: **Shannon Nyquist theorem for the sampling signal.** Below two pixels by resolution element (resel), the signal cannot be described reliably. Above three pixels by resels, the sample is described with higher resolution and better reliability.

### 2.1.4 3D image processing and analysis

Image processing is an important step in imaging when the problem is the quantification or detection of an object in the image. This step enhances the quality of the image and permits the extraction of information from the image. Three different approaches exist to process the 3D image. The first is to process a 2D image for each slice of the stack of the 3D volume, the second is to use 3D processing on the 3D volume and the third is to project the 3D volume onto a 2D image and use 2D processing (with the loss of information content). In this PhD project, algorithms have been developed for 3D analysis. Using different methods, it is possible to restore an image, detect an object, decrease the blur of the image, or improve image contrast. But the image information content cannot be increased.

#### Image restoration

Image restoration methods are used to correct the alterations generated by the acquisition system. The 3D image is the result of the convolution operation applied to the specimen through the acquisition system. Each point of the specimen is represented on the image by a blurred point with a value proportional to the intensity of that point in the specimen. The PSF which characterised the acquisition systems, models the blur of each specimen point to obtain the final image (Figure 2.5). With the deconvolution algorithm, it is theoretically possible to do the reverse: with the help of the PSF, to attempt to obtain an image closest to the initial specimen.

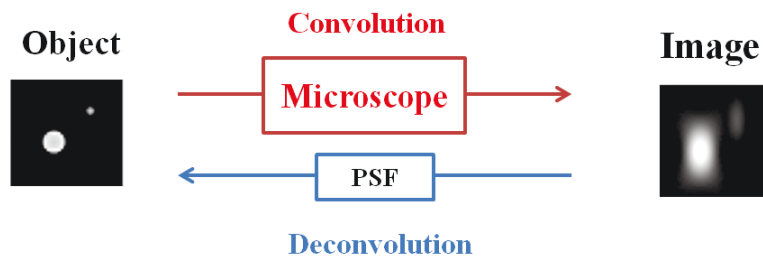
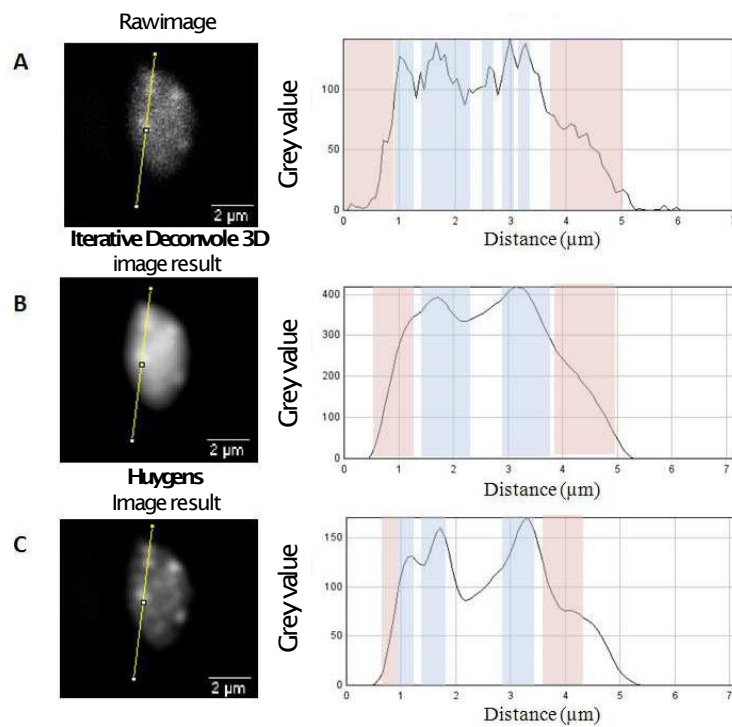


Figure 2.5: Principles of deconvolution.

Deconvolution algorithms can decrease or remove the noise and the blur of an image. To achieve this aim, the algorithm removes out-of-focus blur from the specimen plane located above and below the plane of focus. In deconvolution methods, there are two types of algorithms, deblurring and image restoration. In deblurring methods, the PSF is not needed. The restoration algorithm works on each voxel in a 3D image: these types of algorithms need to use the PSF of the image. Restoration algorithms can take as input the PSF (*e.g.* : Wiener deconvolution, Tikhonov-Miller regularisation, Maximum-Likelihood Restoration), or the algorithm can estimate the PSF from a 3D image (blind deconvolution) [Wu et al., 2008].

Deconvolution methods as Iterative 3D Deconvolve are available freely as plugins for ImageJ [Schneider et al., 2012], a free imaging platform. However a suitable deconvolution algorithm is the commercial software known as Huygens Software Suite commercialised by SVI (<https://svi.nl/HuygensSuite>). When these two softwares were tested, the boundaries were clearer after deconvolution in comparison to the raw image. The result show the value of using a deconvolution method before the detection of the object for noisy images. However, only the Huygens software allow the detection of the chromocentres, and an enhancement of the chromocentres constrast in the nucleus (Figure 2.6).



**Figure 2.6: Comparison of deconvolution method between Iterative Deconvolve 3D and Huygens.** The three images (A, B and C) correspond to the same slice of the same nucleus. The graphs on the right hand side display the intensity voxel value (grey value) on the yellow line on the image. Three chromocentres are on the yellow line. The nuclear boundaries (in pink) and the chromocentres (in blue) help to position the object limits. **A)** Raw image of the nucleus. The graphic is very irregular and the maximal value is lower than 150. The nucleus is blurry and weakly contrasted. The pink zone to position the nuclear boundary is very large. Five chromocentres can be detected (blue area) while only three are on the yellow line. **B)** Deconvolved image obtained with *Iterative Deconvolve 3D*. The deconvolved image is smoother than the raw image, the maximal intensity value is increased to 400. The detection of the nucleus seems more simple than in the raw image but the image is not sufficiently contrasted to obtain optimal chromocentre detection. **C)** Deconvolved image obtained with *Huygens*. The nuclear boundary is similar to the result of *Iterative Deconvolve 3D* but the chromocentres (in blue) are well defined. *Huygens* increases the contrast inside the nucleus allowing the detection of the three chromocentres.

## Image filtering

Studies requiring analyses using signal intensity need to reduce noise due to the acquisition system as far as possible. As mentioned above, it is possible to use the deconvolution algorithm for this purpose. Another solution is to process the image with a filter. One of the aims of filtering methods is to "clean" the signal, eliminating as much noise as possible while preserving the information available in the image. The filter computes a new value for each voxel as a function of the neighbourhood value of the same voxel in the input image. Filters may be linear or nonlinear. This classification depends on whether the voxel value between input and output image

are linear or not; for example the median filter is a nonlinear filter which replaces the initial voxel value by the median of the voxel values in a specified neighborhood [Wu et al., 2008]. This filter reduces noise without damaging the edges in the image. As an example the low-pass filter is a linear filter, which keeps low value voxels and attenuates high value voxels. This filter therefore smooths the image [Wu et al., 2008].

## Morphological operators

Mathematical morphology (MM) is a set of methods created to process binary images or grey level images through filtering, segmentation, and pattern recognition [Serra, 1983, Serra and Soille, 1994]. One part of MM is to compare the image against a structuring element with a known geometrical shape (cube, triangle) to highlight some image characteristics. This part of MM is based on set theory [Serra, 1983, Serra and Soille, 1994]. It uses a structuring element with known geometry and size. Binary images are composed of several regions with value 1 (set of connected pixels/voxels) which define objects of interest, and the regions with value 0 corresponding to the image background. The structuring element is moved so that its centre  $x$  passes through all pixel/voxel of the binary image. For each  $x$  position, the method queries the union<sup>1</sup> or intersection<sup>2</sup> between the object and the structuring element. The combination of pixels/voxels which give a positive response permit the creation of the processed image.

The MM possesses basic operators named erosion and dilation [Serra, 1983, Serra and Soille, 1994]. Erosion erodes the boundaries of the object of interest (Figure 2.7). This operator removes objects smaller than the structuring element, so other objects will erode based on the size of the structuring element. Objects which are connected will be separated, and the hole in the object will increase in size.

Dilation is the inverse operator of erosion (Figure 2.7). The entire object will increase in size equivalent to the structuring element, therefore the hole in the object can be filled, and objects which are separated by a distance smaller or equal to the structuring element will be fused.

It is possible to combine these two operators, to obtain opening or closing. Opening (erosion+dilation) permits the removal of all the parts of objects which cannot contain the structuring element. Closing (dilation+erosion) permits to fill all spaces which are smaller than the structuring element.

---

<sup>1</sup>The union of two sets is a new set that contains all of the elements that are in at least one of the two sets. The union is written as  $A \cup B$ .

<sup>2</sup>The intersection of two sets is a new set that contains all of the elements that are in both sets. The intersection is written as  $A \cap B$ .

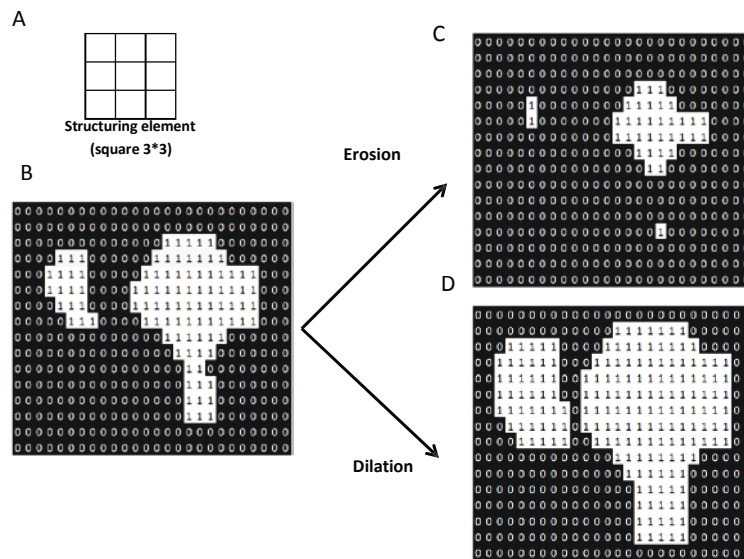


**Figure 2.7: Mathematical morphology erosion and dilation. A)** Structuring element 3\*3 used for this MM process. **B)** Initial binary image. **C)** Results of erosion with the structuring element on the initial image. Pixels which do not intersect the structuring element and the initial shape are set to zero, whereas the others stay at one. **D)** Results of dilation with structuring element on the initial image. Pixels which are contained in the union with the structuring element are set to one.

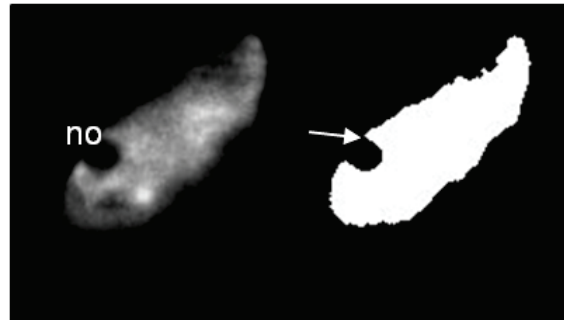
### Object detection in 3D image

The most difficult step in image analysis and therefore a key step in the study of nucleus size and shape from images collected from microscopy is to delimit the nucleus from the background, a process called segmentation. There is no universal segmentation technique that will work for all images, and therefore no segmentation technique is perfect.

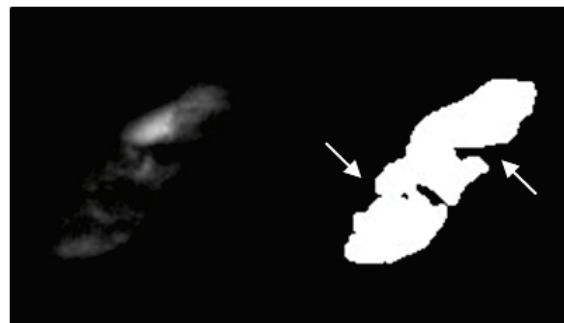
Several segmentation methods have been developed to achieve this goal. Threshold methods applied in the original method developed by Otsu [Otsu, 1979] yield a binary image thanks to the distribution of pixels in two categories (0 for the background and 1 for the object) according to their range of grey scale values. The difficulty is to define the best threshold value to apply and Otsu proposed to select a threshold which minimises the intraclass variance of pixels from the background and the object [Otsu, 1979].

An alternative to the threshold method is to define pixels delimiting the border of

the object. The so-called boundary-based segmentation applies  $f_i$  (e.g. gradient based  $f_i$ ) to the image. Pixels are then classified as edge or non-edge depending on the  $f_i$  output and pixels, which are not separated by an edge, are allocated to the same category [Castleman, 1996]. Many broadly used region-based segmentation algorithms in the field rely on the watershed concept which operates iteratively by grouping together pixels which are neighbours and have similar values, eventually distinguishing groups of pixels with distinct values [Gonzalez and Woods, 1992].



(a) Artifactual hole created by a nucleolus (*no*) close to the boundary (*white arrow*).



(b) Artifactual stripes due to non-homogeneous staining (*white arrow*).

**Figure 2.8: Limits of nuclear segmentation.** Raw (left) and segmented (right) images of a 3D nucleus exemplified some of the difficulties encountered during the segmentation processing with the original Otsu method.

Generally, the drawback of all these methods intrinsically based on grey scale values, is that there are some structures such as the nucleolus inside the nucleus, for which the grey scale value is closer to the background than to other parts of the nucleus (Figure 2.8). Attempts have been made to use active contour approaches, which can involve regularisation as well as data attachment terms. However, active contours are difficult to initialise and the balance between the data attachment term and regularisation is difficult to tune, especially to design robust acquisition modality independent segmentation algorithms.

### **Three dimensional image analysis**

Three dimensional image analysis includes several operations and transformations to extract the object of interest from the image and achieve quantitative measures. Image analysis can permit the characterisation of object morphology or structure by the measurement of several parameters such as volume, area and intensity, but also permits discrimination between objects by comparison of the computed parameters. According to the analysis required, the objects of interest can be analysed as grey-level objects or as binary objects or both. Finally it is possible to compute geometric measures, or parameters based on the intensity of the object.

### **Tools in image processing and analysis**

Several softwares exist for 3D processing and analysis of images. Proprietary software (AMIRA, IMARIS and Metamorph), require financial investment; open source programs such as ImageJ are also available. ImageJ is a Java image processing platform, developed for scientific images of several dimensions. ImageJ is collaborative and highly extensible to perform different tasks [Schneider et al., 2012]. It is possible for the user to develop a plugin or macros for a new task or a new algorithm and to release it to the ImageJ community for its open source improvement [Schneider et al., 2012].



## 2.2 Aims

The 3D nucleus is a good model for the development of methods such as the spatial analysis of 3D images. It is a structure often described as a sphere and alteration of its size and shape have been shown in specific tissues (placental trophoblast in human, root hair cells in plants), affected by ploidy levels (guard cells and pavement cells in plant epidermis) and to be linked to human diseases [Bickmore and van Steensel, 2013] or increased sensitivity to DNA damage [Makova and Hardison, 2015]. SIM 3D microscopy technology has been chosen for the acquisition of the image and the creation of the dataset to permit the development and improvement of 3D tools for nuclear morphology and chromatin organisation analysis. The work described in this section aims to show the development and the validation with biological data of an ImageJ plugin named *NucleusJ* [Poulet et al., 2015]. *NucleusJ* has been developed for 3D light microscopy and improvements have been realised for a better detection of the nucleus and a better precision of the computing parameters.

## **2.3 Material and methods**

### **2.3.1 Plant material**

All mutants and wild type *A. thaliana* plants are from the Columbia-0 ecotype. T-DNA accession numbers were as follows *crwn1-1* (SALK-023383), *crwn2-1* (SALK-041774). T-DNA insertions were obtained from Eric Richards (Cornell University, USA). Seed batches from all genotypes used in this study were propagated together in the greenhouse under long day conditions. Phenotypic evaluations were performed on *A. thaliana* seedlings grown from sterilised seeds sown on germination medium containing 0.8% w/v agar, 1% w/v sucrose and Murashige & Skoog salts (MO255; Duchefa Biochemie, Netherlands). After 2 days of stratification at 4°C in the dark, seedlings were grown under 16 h light / 8 h dark cycles at 23°C, cotyledons were harvested 14 days after germination (dag).

### **2.3.2 Whole mount preparation**

To collect 3D images from cells in their original tissue environment, the method of Bauwens et al., 1994 was adapted to obtain whole mount preparations of 14 dag cotyledons and crown roots. Plant tissues were collected and fixed using 1% formaldehyde, 10% DMSO in PBS 1X, EGTA 6.7 mM pH7.5, subjected to vacuum for 5 min and incubated for 25 min at room temperature. Tissues were then washed 3 times with methanol and several ethanol washes were performed to obtain transparent tissue preparation. Tissue can then either be used for 3D analysis or for 3D-FISH. For standard 3D analysis, tissues were stained overnight at 4°C in a solution of Hoechst at 0.1 mg/ml in PBS. Samples were then washed 3 times with PBS 1X, excess water removed with paper tissue and placed on a slide in PBS/glycerol (20:80) solution and covered with a cover slip for microscopic observations.

### **2.3.3 3D image acquisition**

#### **3D image acquisition with SIM microscope**

Three dimensional light microscopy was performed on fixed whole mount cotyledons and roots. Images were acquired with a structured illumination microscope (Leica MAAF) using a X63 oil objective with the voxel calibration equal at  $xy = 0.103 \mu\text{m}$  and  $z = 0.2 \mu\text{m}$ . These parameters of the calibration are used by the microscope software according to the sampling theory of Shannon and Nyquist [Nyquist, 1928, Shannon, 1949].

### **3D image acquisition with confocal microscope**

Three dimensional light microscopy was performed on *fi* whole mount cotyledons and roots. Images were acquired with Zeiss LSM 510 META confocal microscope using a X63 oil objective with the voxel calibration equal at  $xy = 0.075 \mu\text{m}$  and  $z = 0.29 \mu\text{m}$ . These parameters of the calibration were chosen to follow the sampling theory of Shannon and Nyquist [Nyquist, 1928, Shannon, 1949].

### **2.3.4 Imaging process and analysis and statistical methods**

#### **Imaging processing, analysis and process**

The processing and analysis of the images of nuclei were performed with the *NucleusJ* plugin [Poulet et al., 2015] using the ImageJ platform. Several steps are required before using this plugin. *NucleusJ* can only analyse images containing a single nucleus in the raw image. SIM and confocal contain several nuclei per image, and each nucleus has to be cropped using ImageJ or other softwares to obtain a single nucleus per 3D raw image.

#### **Statistical methods**

Statistical analyses were performed using R [R Core Team, 2013]. Principal component analysis (PCA) was carried out with the FactoMineR package, an extension of R [Husson et al., 2009]. R scripts were developed to undertake automatically undertake statistical tests (Student's T test and correlation), Principal component analysis (PCA), and boxplots on the data obtained after 3D image analysis.

## 2.4 Results and discussion

### 2.4.1 *NucleusJ* platform as a phenotyping tool for nuclear organisation

*NucleusJ* is a simple and user-friendly ImageJ plugin dedicated to the characterisation of nuclear morphology and chromatin organisation in 3D [Poulet et al., 2015]. Starting from image stacks, the nuclear boundary is delimited by a modified Otsu segmentation method [Otsu, 1979] developed based on the definition of a threshold which was during the work undertaken in this thesis (Figure 2.9). Chromocentres are segmented by partitioning the nucleus using a 3D watershed algorithm [Gonzalez and Woods, 1992] and by manual thresholding a contrast measure over the resulting regions. As output, *NucleusJ* quantifies parameters including shape and size of nuclei as well as intra-nuclear objects such as chromocentres and their position in the nucleus (Figure 2.9).

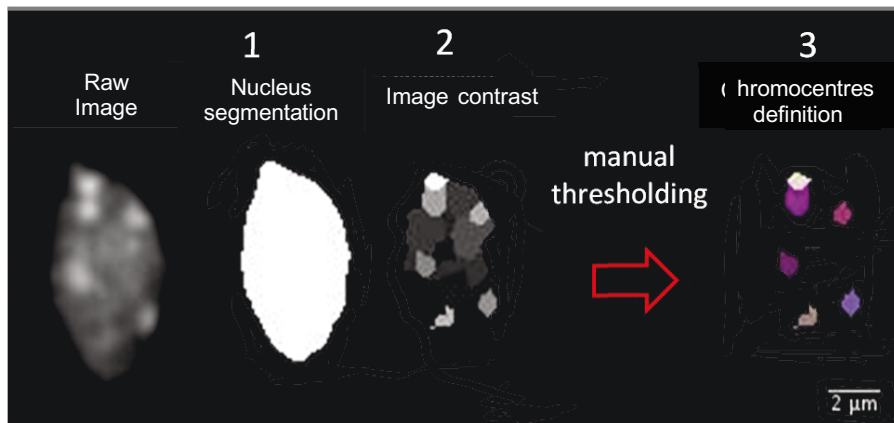


Figure 2.9: ***NucleusJ* processing.** *NucleusJ* combines four steps. **(1)** Nucleus segmentation produces segmented images automatically. **(2)** Domains of variable intensities are defined by a 3D watershed and **(3)** finally chromocentres are delimited by applying a manual threshold to the contrasted image.

#### ***NucleusJ* nuclear segmentation process**

To detect the nucleus in the raw image, the Otsu method was associated with a parameter of the nuclear morphology called sphericity (see formula 2.5, [Andrey et al., 2010]). This optimisation of the Otsu method permitted determination of the best threshold value of a 3D image stack.

During this process, the sphericity was computed for each given threshold value and the highest value retained to select the best threshold. Finally, mathematical

morphology operators were applied to the image. The aim of these operators was to fix invaginations and holes in the detected shape.

---

**Algorithm 1:** Optimised Otsu method for 3D segmentation algorithm.

---

```

Data: 3D rawImage
Result: 3D binaryImage
1 Threshold value initialisation:  $t \leftarrow \text{OtsuMethod}(\text{rawImage})$ ;
2 Research interval  $I \leftarrow ]t - \text{stdv}(\text{rawImage}) * 2 ; t + \text{stdv}(\text{rawImage}) * 2]$  (With stdv, the standard deviation of the voxels value);
3 for each value of  $I[i]$  do
4   binaryImage  $\leftarrow \text{binarisation}(\text{rawImage}, I[i])$ ;
5   sphericity  $\leftarrow \text{computeSphericity}(\text{binaryImage})$ ;
6   if sphericity > sphericityMax then
7     bestThreshold  $\leftarrow I[i]$ ;
8     sphericityMax  $\leftarrow \text{sphericity}$ ;
9     bestBinaryImage  $\leftarrow \text{binaryImage}$ ;
10 morphologicalCorrection(bestBinaryImage);

```

---

Indeed the optimised Otsu method improves the detection of the boundary (Figure 2.10), in most cases includes the nucleolus as part of the nucleus and removes several artifactual indentations or voxels not connected to the boundary. This leads to a more regular and uniform shape of the boundary.

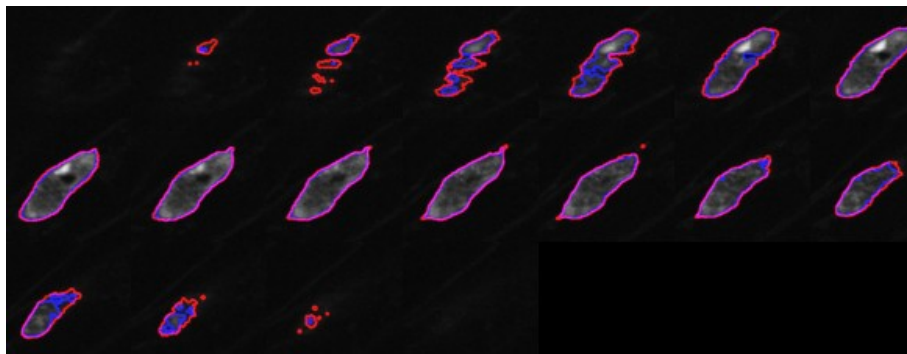


**Figure 2.10: Results of the Otsu and optimised Otsu method.** Nucleus stain with Hoechst. Selected z slices of a raw image of nucleus, the blue edge is the result of the segmentation of the Otsu method and the optimised method is shown in red.

The following step after nuclear segmentation is the detection of chromocentres to analyse the position of these structures in the boundaries of the nucleus.

### Chromocentre segmentation process

In *A. thaliana*, when the chromatin is stained with DAPI or Hoechst, chromocentres can easily be detected as regions of high intensity. Therefore, the first aim is to

detect the region with highest intensity. This work starting from an already available algorithm developed in Pr Philippe Andrey's lab [Andrey et al., 2010], but this this procedure had not been adapted and developed as an ImageJ plugin. The 3D image of the nucleus is used by the watershed transformations (<https://github.com/ijpb/MorphoLibJ>) and each region was assigned mean intensity value of the voxel regions. The computation of the contrast between neighbouring region is strengthened by the volume of the neighbouring regions which decrease the impact of small region with low or high mean intensity. Image contrast was manually segmented to obtain the final image of the chromocentre (Figure 2.9).

### **Choice of parameters to describe nuclear morphology and chromatin organisation**

The aim of this study is to characterise the 3D of nuclear morphology and chromatin organisation in *A. thaliana*. Chromatin organisation is studied using chromocentre size and distribution. After detection of the nucleus and chromocentres, it is then necessary to choose appropriate parameters to characterise these objects (Table 2.1).

It is possible to define individual characteristics for the different 3D objects based on morphological parameters. The estimation of volume ( $Volume = \sum_{Voxel \in Object} 1$ ) and area ( $Area = \sum_{boundaries\ voxels\ facets \in Object} 1$ ) are often computed and represent the size of the object of interest. With these two parameters, it is possible to obtain a value for sphericity (formula 2.5) [Andrey et al., 2010]. Sphericity is a shape feature used to reflect the complexity of the object boundary. Sphericity take into account the regularity of the surface of the volume as well as its "roundness". An object with sphericity close to 1 has a shape similar to a sphere.

$$Sphericity = 36\pi \frac{Volume^2}{Area^3} \quad (2.5)$$

Other shape parameters can be defined, including flatness and elongation. An ellipsoid is defined by three distinct principal axis lengths x, y and z which are the major, intermediate and minor principal axes, respectively ( $x > y > z$ ). These parameters on any 3D object are defined by analogy with physics, using the theory of moments of inertia. Inertia moments measure how the object mass is distributed in space as a function at the rotation axis. The elongation and the flatness is defined by the following formulae:

$$Elongation = \frac{x}{y} = \frac{\text{major axis}}{\text{intermediate axis}} \quad (2.6)$$

$$Flatness = \frac{y}{z} = \frac{\text{intermediate axis}}{\text{minor axis}} \quad (2.7)$$

The morphology of the nucleus in this study will be characterised by five parameters (volume, area, sphericity, flatness and elongation) whereas for chromocentre morphology, which are much more smaller only the volume was relevant (Table 2.1). In addition, the distance of the chromocentre to the limit of DNA staining that was assumed to be representative to NE periphery is determined. Here it should be noticed that the limit of the DNA staining by the intercalating agent (DAPI or Hoechst) may not reflect exactly the NE boundary. However in this first attempt to define a spatial position of the chromocentre in the nucleus, this strategy was the easiest to be applied. This distance can be computed as a distance of the barycentre of the chromocentre to the NE or between the NE periphery and the closest point of the chromocentre periphery (Table 2.1). The measure of this distance is based on computing a distance map of the nucleus. The aim is to compute the distance between each voxel and the image background. A computation of the distance map by the Euclidean distance transformation [Saito and Toriwaki, 1994] is realised with the ImageJ plugin developed by Bob Dougherty ([http://www.optinav.com/download/LocalThickness\\_.jar](http://www.optinav.com/download/LocalThickness_.jar)). This Euclidean distance can be computed only on images with isotropic voxels (*i.e.* cubic voxels). The voxels obtained from SIM and confocal images are anisotropic (*i.e.* rectangular voxels), and a step of resampling is necessary to obtain images with isotropic voxels. This resampling is simply performed using an algorithm available in Imagej [Schneider et al., 2012].

Chromatin organisation within the nucleus was studied by the number of chromocentre, the mean or total volume of chromocentre, and the mean distance of the chromocentre (closest point, and barycentre) to the NE. This organisation was studied also by a parameter called the Relative Heterochromatin Volume ( $RHV = \frac{\text{total volume of chromocentres}}{\text{nuclear volume}}$ ), which is the ratio of the volume of the chromocentre by the total nuclear volume. The same compute is did on function the intensity, and named Relative Heterochromatin Intensity ( $RHI = \frac{\text{total inetnsity of chromocentres}}{\text{nuclear intensity}}$ ).

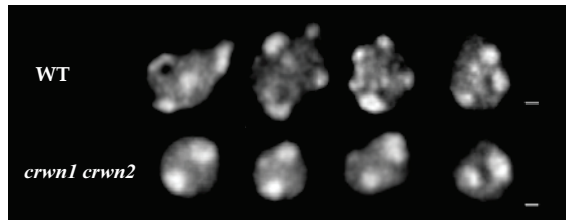
**Table 2.1: Parameters computed by *NucleusJ*.** Parameters are grouped according to three categories: nuclear size, shape and heterochromatin organisation. \* : Aspect ratio and circularity are 2D parameters widely used in 2D image analysis.

Parameters	Sub-parameters	Abbreviations	Characteristics	output files		
				3DNucleiParameters	2DNucleiParameters	CcParameters NucAndCcParameters
<b>Nuclear Size</b>	volume	Volume	Volume of the nucleus	x		x
	equivalent spheric radius	ESR	Radius of a sphere of equivalent volume	x		x
	Surface Area	SurfaceArea	Total surface of the nucleus	x		x
<b>Nuclear Shape</b>	elongation	Elongation	Length of longest axis / Length of intermediate axis	x		x
	sphericity	Sphericity	$36\pi \times \text{volume}^2 / \text{surface Area}^3$	x		x
	flatness	Flatness	Length of intermediate axis / Length of shortest axis	x		x
	Aspect Ratio*	AspectRatio	length of longest axis / Length of small axis		x	x
	Circularity*	Circularity	$4\pi \times \text{surface area} / \text{Perimeter}^2$		x	x
<b>Heterochromatin organization</b>	chromocenter (Cc)	NbCc	Number of Cc			x
		DistanceBorderToBorder	Distance between each Cc border and nuclear peiphery		x	
		DistanceBarycenterToBorder	Distance between each center and nuclear peiphery		x	
		DistanceBarycenterToBorderNucleus	Distance between each nucleus center and nuclear peiphery		x	
		Volume	Volume of Cc		x	
		DistanceBorderToBorderMean	Mean distance between Cc border and nuclear peiphery / nucleus			x
		DistanceBarycenterToBorderMean	Mean distance between of Cc centre and nuclear peiphery / nucleus			x
		VCcMean	Mean volume of chromcenter / nucleus			x
		VCcTotal	Total chromocenter volume / nucleus			x
		Relative heterochromatic compute	RHV	Computed from volume		
	RHI	Computed from intensity			x	

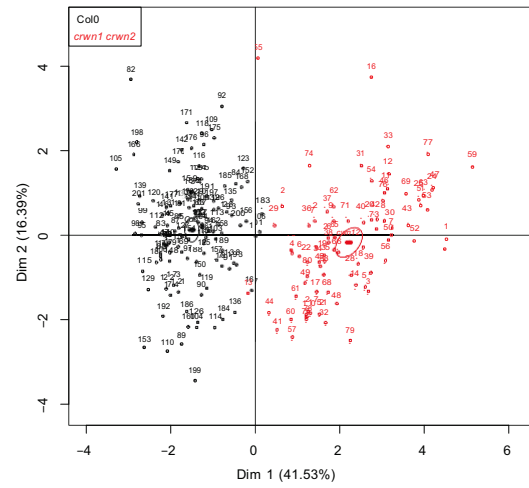
## Biological validation of *NucleusJ* plugin

*NucleusJ* was validated using an *A. thaliana* mutant line lacking CRWN1 and CRWN2 proteins, which are putative components of the plant nucleoskeleton [Dittmer et al., 2007, Wang et al., 2013]. Analysis of a set of 220 nuclei from wild type Col-0 and *crwn1 crwn2* mutant plants revealed nuclei of reduced volume and increased sphericity containing fewer chromocentres of increased size in the mutant compared to Col-0, in perfect agreement with previous report [Dittmer et al., 2007, Wang et al., 2013].

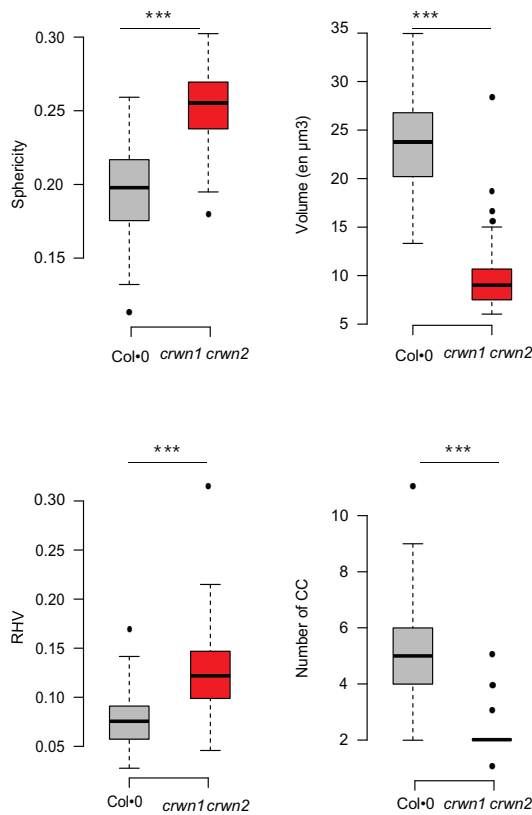




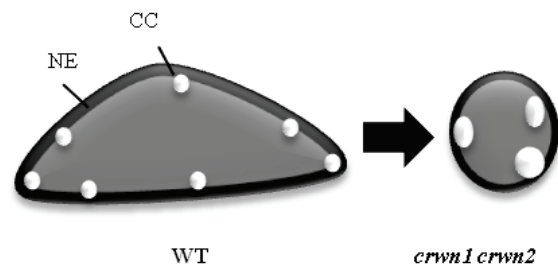
(a) Image of nuclei



(b) Data set Principal Component Analysis



(c) Statistical analysis



(d) Nucleus model from the quantitative data

**Figure 2.11: *NucleusJ* validation using plant cell nuclei.** **a)** Representative epidermis nuclei of wild type (top panel) and mutant (*crwn1 crwn2*; bottom panel) cotyledons. Scale bar (at the right): 2  $\mu\text{m}$ . **b)** PCA using nuclear volume, sphericity, elongation, flatness, RHV, number of chromocentre, size mean of chromocentres, total volume of chromocentres, and the two distances computed parameters and the whole set of Col-o (black) and *crwn1 crwn2* (red) pavement cell nuclei. **c)** Statistical analysis of four selected parameters (\*\*\* :  $P < 0.0001$ ). **d)** Model from the quantitative data: nucleus in grey is surrounded by the NE in dark grey, chromocentre (CC) in white. *crwn1 crwn2* nuclei are smaller and contain fewer but bigger chromocentres. Results are supported by a previous publications from Dittmer et al. 2007 and Wang et al. 2013.

## Conclusion of *NucleusJ* platform development

Computational image analysis provides precise, objective and reproducible quantitative data from images. The *NucleusJ* plugin developed as part of this study generates, within a few steps, 3D quantitative measurements from single images or large data sets, without requiring expertise in image analysis. The method developed for 3D segmentation (Algorithm 1) was included into *NucleusJ* during its development. Quantitative parameters were also included in this integrated tool to characterise nuclear morphology. Hence, this approach can be used by biologists, without requiring further knowledge than the use of ImageJ. 3D Nuclear segmentation of nuclei is a task that can be addressed in many species and nuclear domains visible with DNA dyes, such as chromocentres, are not specific to plants, but can also be identified other species such as mice. *NucleusJ* will therefore be useful for a large community of users interested in quantifying size, shape, and positioning of nuclei, nuclear objects or chromatin domains. The work was made available on the ImageJ and Fiji (an image processing package) web sites with documentation for the user ([http://imagejdocu.tudor.lu/doku.php?id=plugin:stacks:nuclear\\_analysis\\_plugin:start](http://imagejdocu.tudor.lu/doku.php?id=plugin:stacks:nuclear_analysis_plugin:start), see Appendix A.2) and an article was published to advertise about this new ImageJ plugin (see Appendix A.1) [Poulet et al., 2015].

### 2.4.2 Improvement of the computing of the area

The final *NucleusJ* version was finalised in 2013 and was used to analyse various mutant backgrounds affecting the nuclear envelope or chromatin organisation (Chapter 3). In the mean time, several improvements of *NucleusJ* have been implemented to correct known bias of the preliminary version. Efforts were focused to improve the definition of the 3D nuclear segmentation which impacts directly the sphericity. Indeed in the preliminary version sphericity was at best up to 0.29 while a perfect sphere as a sphericity of 1. These developments were developed in collaboration with Pr Rémy Malgouyres (LIMOS, Clermont-Ferrand).

### Method development

The first estimation developed of the area used previously was based on the total boundary surface of the voxels, and this method is used in the *NucleusJ* plugin [Poulet et al., 2015]. Here, the sphericity calculation has been improved and now takes into account the contribution of each surfel<sup>3</sup> area. The first step of the area

---

<sup>3</sup>Surfel is an abbreviation of "surface element".

calculation is to determine the image gradient  $\nabla f_{x,y,z}$  of the raw image  $f$ , which we estimate using finite differences in the anisotropic image.

$$\nabla f = \begin{pmatrix} \frac{\partial f}{\partial x} \\ \frac{\partial f}{\partial y} \\ \frac{\partial f}{\partial z} \end{pmatrix} \quad \text{and} \quad \begin{pmatrix} \frac{\partial v}{\partial x} \\ \frac{\partial v}{\partial y} \\ \frac{\partial v}{\partial z} \end{pmatrix} = \begin{pmatrix} \frac{1}{z_{calibration}} \cdot (v_{x+1,y,z} - v_{x-1,y,z}) \\ \frac{x_{calibration}}{1} \cdot (v_{x,y+1,z} - v_{x,y-1,z}) \\ \frac{y_{calibration}}{1} \cdot (v_{x,y,z+1} - v_{x,y,z-1}) \end{pmatrix}$$

Then the program determines the unitary normal vector  $\vec{N}$  for  $f$ ,  $\vec{N} = \frac{\nabla f}{\|\nabla f\|}$  with  $\|\nabla f\|$  norm of  $f$  [Fourey and Malgouyres, 2009, Gonzalez et al., 2013, Esbelin and Malgouyres, 2014]. The algorithm then browses each boundary voxel on the segmented image. For each boundary voxel, the contribution of each of the surfel to the total area is computed. The factor  $as$  is the unity of the surfel, which allows management of the problem of anisotropy. The resulting area is  $d(AS)$ , the area of boundary voxels.

---

**Algorithm 2:** Area computing algorithm

---

**Data:** 3D rawImage, 3D binaryImage

**Result:** area

- 1 UnitaryVectorTable  $\leftarrow$  computeUnitaryVector(gradient(rawImage));
  - 2 **for** each voxel boundary  $v$  in binaryImage **do**
  - 3     **for** each voxel neighbor  $v_n$  **do**
  - 4         **if**  $v$  value  $\neq$   $\frac{v_n \text{ value}}{NV + NV}$  **then**
  - 5              $d(AS) = \left| \frac{1}{2} \cdot |v - v_n| \cdot as \right|$ ;
  - 6             area  $\leftarrow$  area +  $d(AS)$ ;
- 

**Results of estimation on different shapes**

Here, the calculation procedure of the area is improved (Algorithm 2) and its effectiveness is tested on spheres and ellipsoids of various volumes and shapes in order to evaluate the deviation observed from theoretical values (Table 2.2). The area is strongly overestimated in the original method (*ratio* between observed and theoretical value = 1.55) while estimation is more accurate with the new method (*ratio* = 1.08). In both cases, variations in shape (ellipsoid or sphere) do not strongly impact the deviation from the theoretical values. Thus, the surface is computed more accurately and the binary images are more relevant to investigate irregularities at the object boundaries. This improvement is an important step to better define shape

parameters.

**Table 2.2: Comparison of two methods of area computing using theoretical objects.** Ellipsoid of various x, y and z axes in brackets and spheres of various radius (r) were analysed by the original method developed in [Poulet et al., 2015] (old method) and the new method. Surface is computed with each method and the ratios between the observed and theoretical values were calculated. Average values of the ratios are given at the bottom of the table.

Objects	Theoretical values Area	Old method Area		New method Area	
		Obs	Ratio	Obs	Ratio
<b>Ellipsoid (10,20,30)</b>	4 897	7 274	1.49	5 209	1.06
<b>Ellipsoid (15,5,10)</b>	1 224	1 902	1.55	1 376	1.12
<b>Ellipsoid (15,10,12)</b>	1 900	3 028	1.59	2 079	1.09
<b>Ellipsoid (20,35,10)</b>	5 624	9 984	1.78	7 054	1.25
<b>Ellipsoid (25,60,50)</b>	25 229	36 872	1.46	26 102	1.03
<b>Ellipsoid (40,20,50)</b>	16 716	24 514	1.47	17 328	1.04
<b>Ellipsoid (60,40,25)</b>	21 295	31 468	1.48	22 343	1.05
<b>Sphere : r = 5</b>	314	540	1.72	364	1.16
<b>Sphere : r = 10</b>	1 257	2 010	1.60	1 363	1.08
<b>Sphere : r = 20</b>	5 027	7 782	1.55	5 273	1.05
<b>Sphere : r = 30</b>	11 310	17 298	1.53	11 720	1.04
<b>Sphere : r = 40</b>	20 106	30 606	1.52	20 723	1.03
<b>Sphere : r = 50</b>	31 416	47 730	1.52	32 273	1.03
<b>Sphere : r = 60</b>	45 239	68 562	1.52	46 343	1.02
<b>AVERAGE VALUE</b>			<b>1.55</b>		<b>1.08</b>

## Conclusion of the improvement of the computing of the area

This new "optimised Otsu method" for the estimation of the area permits to obtain an accurate value of the real area of the object of interest, and with this method, the area is more relevant. This improvement involved an estimation of a more realistic sphericity as a value of sphericity of 1.0 is now obtained for a perfect sphere (the old value being 0.29).

### 2.4.3 Improvements of 3D nuclear segmentation

#### Limitation of the new optimised Otsu method

As the new optimised Otsu method is used by the two other methods described hereafter, it is important to illustrate the improvement it provides in respect to the original Otsu method used by *NucleusJ*.

There are few differences in the results of nuclear segmentation between the two methods (Figure 2.12). Here the improvement of the segmentation in comparison to the Otsu method are the same that as those already presented in Section 2.4.1 (Figure 2.13).

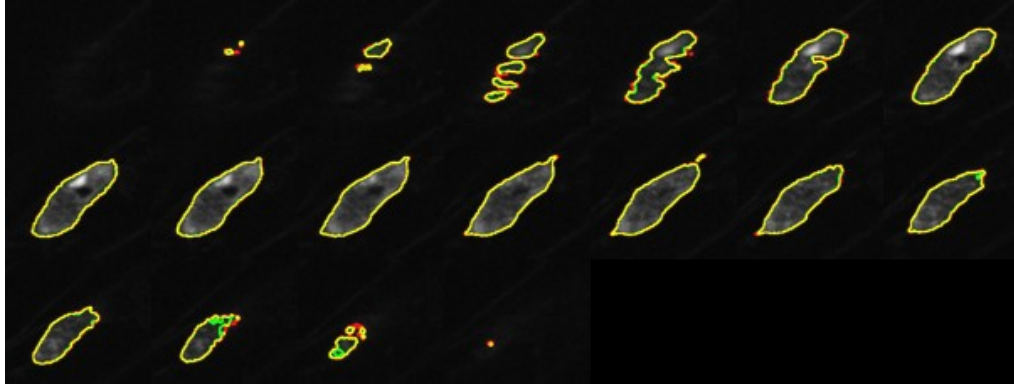


Figure 2.12: **Comparison of optimised Otsu method with the two estimations of the area.** Nucleus stain with Hoechst. Selected z slices of a raw image of nucleus are displayed, the red edge is the result of the segmentation with the old estimation of the area, the green is the results with the new estimation and the yellow when the two segmentations are overlapping.

While sphericity is improved (see Table 2.2), the major limit of the "new optimised Otsu method" is observed for non-uniform staining as described in Figure 2.13a. In this case, the method cannot efficiently remove indentations, because heterogeneity in voxel intensity avoid their classification as boundary voxels. Furthermore, if the nucleolus is closer to the boundary, it can still be considered as belonging to the background. These limitations highlight the need of further improvements of the 3D segmentation method of the nucleus.

### **Improvement of 3D segmentation using a mathematical morphology method**

In order to improve the 3D segmentation step, we have developed a novel method based on the definition of *deep kernel* to best fit the binary image. Binary nuclei may contain concave parts, holes, cavities or irregular boundaries generated through the thresholding step, in particular due to the presence of the nucleolus (Figure 2.8). Removing these artefacts is a critical step for high-quality segmentation.

To achieve this goal, mathematical morphology treatment was applied, the basic principle of which is based on concave parts fit to complete the object as fully as possible by moving a sphere of given radius within a delimited space. First the 3D segmented image obtained with optimised Otsu method should be made of isotropic voxels, and if it is not the case, the image has to be transformed to obtain cubic voxels with the algorithm available in ImageJ. An euclidean distance map is built to compute and store the distance between each voxel of the 3D segmented image which belongs to the object and the background [Saito and Toriwaki, 1994, Hildebrand and Rügsegger, 1997]. The maximum distance is used to define an initial distance threshold called  $s$  (where  $s = MaxDistance$ ) which is subsequently used to define a

sphere of radius  $s$ .

The initial threshold  $S$  was defined as  $S = \frac{r}{2}$ . The distance thresholding is performed on the distance map image and a *deep kernel* is defined by all the voxel with *value*  $\geq S$ . For each sphere of radius  $S$ , centred on the *deep kernel* voxels, each voxel which belongs to the sphere in the initial segmented image will take a value of 1. This step is then repeated but using  $S-1$  until  $S$  takes a higher value than the  $x$  calibration. Finally in order to remove the potential artefacts generated through the method the image is inverted to apply the same procedure to the image background but only with greatest threshold distance  $S$ .

---

**Algorithm 3:** Algorithm for 3D segmentation based on mathematical morphology method

---

**Data:**  $I$ : inputImage (binary)  
**Result:** 3D correctedBinaryImage

```

1  initRadius  $\leftarrow S$ ;
2  while  $S \geq 1$  do
3    map  $\leftarrow$  distanceMap( $I$ );
4     $I \leftarrow$  threshold(map,  $S$ );
5     $I \leftarrow \Delta_S(I)$ ;
6     $S \leftarrow S - 1$ ;
```

---

In this algorithm *distanceMap(I)* is the distance map for the Euclidean distance for the binary image  $I$ . Then, *threshold(map, S)* is the binary image obtained by applying the threshold value  $S$  on the gray level image map.  $\Delta_S(I)$  is the morphological dilation with an Euclidean sphere with radius  $S$  as structuring element.

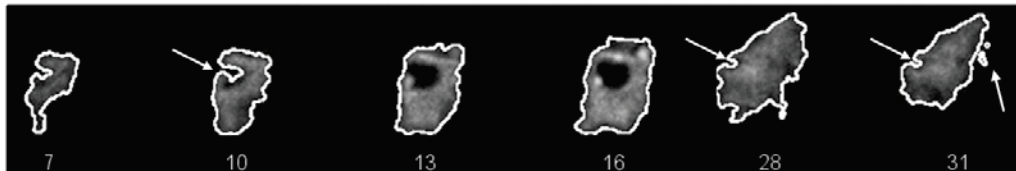
### Limitations of the mathematical morphology method results

The mathematical morphology method based on the definition of a deep kernel improves further the outcome observed with the optimised Otsu method and permits fitting of the majority of the observed indentations (Figure 2.13c). The algorithm performs an efficient segmentation and considers the nucleolus as part of the nucleus (Figure 2.13a and Figure 2.13a sections 7 and 10). However the algorithm still keeps some irregularities and as a major drawback overestimates the nuclear volume and the sphericity (Table 2.3). These overestimations are due to the method, which adds background voxels in the fitting nucleus because these voxels belong to the sphere used for the segmentation (Table 2.3). The overestimation of the volume without increase of the area results in sphericity value higher than 1 for several nuclei. This result shows the bias introduced by this method. As the mathematical morphology method enlarged the nuclear boundaries another strategy has been investigated to

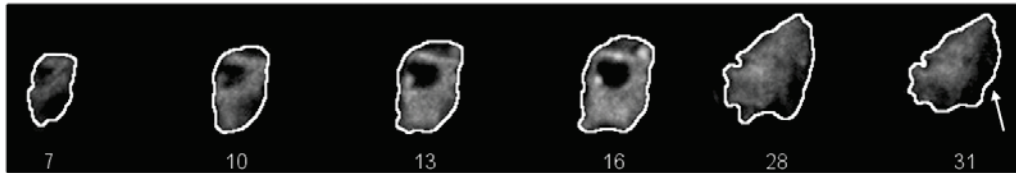
improve the 3D nuclear segmentation.



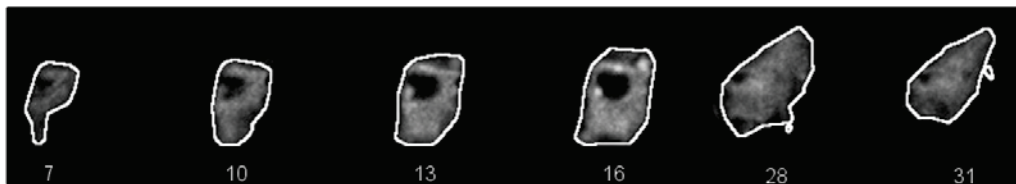
(a) Segmentation results for original Otsu method.



(b) Segmentation results for optimised Otsu method.



(c) Segmentation results for mathematical morphology method.



(d) Segmentation results for 3D gift wrapping method.

**Figure 2.13: Results of the three segmentations methods.** Selected z slices of a raw image of nucleus. Sections 13 and 31 of sub figure **b**) show respectively the nucleolus and voxels outside the boundary which are captured during the segmentation process (*white arrow*). Sections 31 of sub figure **c**) highlights in the overestimation of the nuclear volume observed with the mathematical morphology method, **d**) results of the *3D gift wrapping* algorithm.

### Improvement of 3D segmentation using a 3D gift wrapping algorithm

An alternative to the mathematical morphology method initiated within the object is to better define the edge of the object, and delete shape irregularities generated by the initial step of segmentation. To achieve this goal the *3D gift wrapping* method was used to define the limits of the object. Actually this new approach is neither a convex hull, nor an approximation of a convex hull, nor a simplified convex hull, but a new notion, which can be named *3D gift wrapping* of a set of voxels. The idea is that, due to a priori knowledge from biology, and due to the goal of this study which is to improve the geometric accuracy of the segmented nucleus, the nucleus cannot be considered as convex object. The shape is essentially non convex, but the aim is

to remove some artefactual concavities, while preserving the natural ones, using a relevant distance threshold in the *3D gift wrapping* algorithm.

For the sake of simplicity, this method was designed in 2D and then implemented slice by slice up to the 3D volume. Hence, depending on the axis used to decompose the volume into slices, three different volumes can be obtained. Then the union of the three volumes was built.

In each slice, in order to tune the *3D gift wrapping* algorithm, and to best fit the shape artifacts, a parameter of maximal threshold distance  $td$  was applied between two vertices which will define the boundary. This distance is determined experimentally and this parameter can, with generally good results whatever the size of the nucleus, be adaptively set to the following value:

$$td = \frac{\sqrt[3]{\frac{3 \text{Volume}}{4\pi}}}{2} \quad (2.8)$$

The method of threshold distance efficiently removes shape artifacts, although keeping real indentations occurring at the nuclear surface. The developed algorithm takes into account only one slice at once, in other words uses 2D objects. First of all, if several objects are detected on a given slice, the first problem is to label the connected components and then to use the *3D gift wrapping* algorithm for each label. During the distance thresholding, the aim is to minimise the outer-pointing normal to obtain the next vertex.



---

**Algorithm 4: Three dimension gift wrapping algorithm**


---

**Data:** list of the boundary voxel  
**Result:** list of the voxel vertices

- 1  $v_n \leftarrow$  voxel with  $v_n y$  maximal;
- 2 **while**  $anglesSum \leq 2 * \Pi$  **do**
- 3     whether  $v_n(v_n x, v_n y)$  the current point;
- 4     **if** *is the first lap* **then**
- 5          $\vec{V}_{test}(10, 0)$ ;
- 6     **else**
- 7          $\vec{V}_{test}(v_n x - v_{n-1} x, v_n y - v_{n-1} y)$ ;
- 8     **for each** voxel boundary  $v_b$  **do**
- 9          $\vec{V}_{current}(v_b x - v_n x, v_b y - v_n y)$ ;
- 10        **if**  $distance^b(v_n, v_b) \leq td$  **then**
- 11             $\alpha \leftarrow$  angle $[0, 2*\Pi]$  between  $\vec{V}_{test}$  and  $\vec{V}_{current}$ ;
- 12            outerPointingNormal  $\leftarrow \alpha + \Pi/2$  **if** outerPointingNormal  $\geq \Pi$  **then**
- 13                outerPointingNormal  $\leftarrow$  outerPointingNormal  $- 2 * \Pi$ ;
- 14            **if** outerPointingNormal  $\leq Min_{outerPointingNormal}$  **then**
- 15                **if** outerPointingNormal  $< Min_{outerPointingNormal}$  **then**
- 16                    angleMin  $\leftarrow \alpha$ ;
- 17                    voxelMin  $\leftarrow v_b$ ;
- 18                **else if** outerPointingNormal  $\leq Min_{outerPointingNormal}$  &&  
                  distance $(v_b, v_n)$  is max **then**
- 19                    angleMin  $\leftarrow \alpha$ ;
- 20                    voxelMin  $\leftarrow v_b$ ;
- 21
- 22     verticesList  $n+1 \leftarrow$  voxelMin;
- 23     anglesSum  $\leftarrow$  anglesSum + angleMin;
- 24      $v_n \leftarrow$  voxelmin;

---

The initialisation of the first voxel ( $v_n$ ) for the first lap is defined by the lowest voxel in the image plane. Then for each voxel boundary of the same plane, the *distance* between the voxel boundary ( $v_b$ ) and  $v_n$  was computed.

$$distance = \sqrt{\frac{\sum_x \vec{V}_{current}^2 + \sum_y \vec{V}_{current}^2}{2}} \quad (2.9)$$

$\vec{V}_{current}$  is defined by  $(v_b x - v_n x, v_b y - v_n y)$ .

If the *distance* is lower than  $td$ , the angle is computed between  $\vec{V}_{test}$  and  $\vec{V}_{current}$

(Algorithm 4). The  $\alpha$  angle is computed using  $\sin \alpha = \frac{vector\ product}{norm\ product}$  and  $\cos \alpha =$

$\frac{scalar\ product}{norm\ product}$ . The *arccos* function is used to determine  $\alpha$  angle taking into account the sign  $\sin \alpha$ . Then when the minimum angle is found, the current  $v_b$  becomes  $v_n$

and a new lap starts. When the sum of the angle equals  $2 * \Pi$ , the turn around of the shape is finished and all the vertices are defined for the 2D plane.

### 3D gift wrapping method results

Finally, the *3D gift wrapping* method, although more complex to set up, remains the most accurate (Figure 2.13). It nicely removes the artifactual indentations, considers the nucleolus as part of the nucleus and does not overestimate the nuclear volume. This geometric post-process preserves the significant angular features while removing noise, which is rather difficult to achieve with the active contours approach, in which regularisation terms will smooth out angular features, or by morphological operations. Morphological parameters such as sphericity, elongation or flatness can then be computed with great confidence from this last method (Table 2.3).

**Table 2.3: Mean morphologic parameters computed with the new algorithms and compared to the original Otsu segmentation procedure.** Here nuclei of guard cells (*GC*), pavement cells (*PC*), and root hair cells (*RHC*) were used which display distinct shape and size. The numbers in the Method column are 0: Otsu method, 1: optimised Otsu method, 2: mathematical morphology method and 3: *3D gift wrapping* method.

Nuclear Type	Method	Volume	Area	Sphericity
<b>GC</b>	0	17.21	38.63	0.59
	1	21.65	43.77	0.64
	2	23.16	39.06	1
	3	20.67	40.49	0.74
<b>PC</b>	0	117.50	180.74	0.27
	1	155.65	205.32	0.32
	2	184.17	162.72	0.88
	3	182.44	175.83	0.69
<b>RHC</b>	0	96.30	173.04	0.23
	1	130.42	196.60	0.27
	2	152.58	186.83	0.57
	3	140.44	183.08	0.44

### Conclusion of comparative studies of 3D nuclear segmentation

In this section, new 3D nuclear segmentation procedures have been developed and finally the *3D gift wrapping method* gave the best result very close to our expectation. This is a very important progress for nuclear segmentation as it improves the precision of the nuclear volume, remove artefactual indentations and nicely includes the nucleolus within the nucleus. Furthermore improving the boundary of the nucleus also benefits to the measurements of intranuclear objects as their positions are computed in respect to the boundaries of the nucleus. A comparison of all methods is provided on Figure 2.14 which is accessible online at <https://www.gred-clermont.fr/media/uploads/poulet-tatout.avi>.

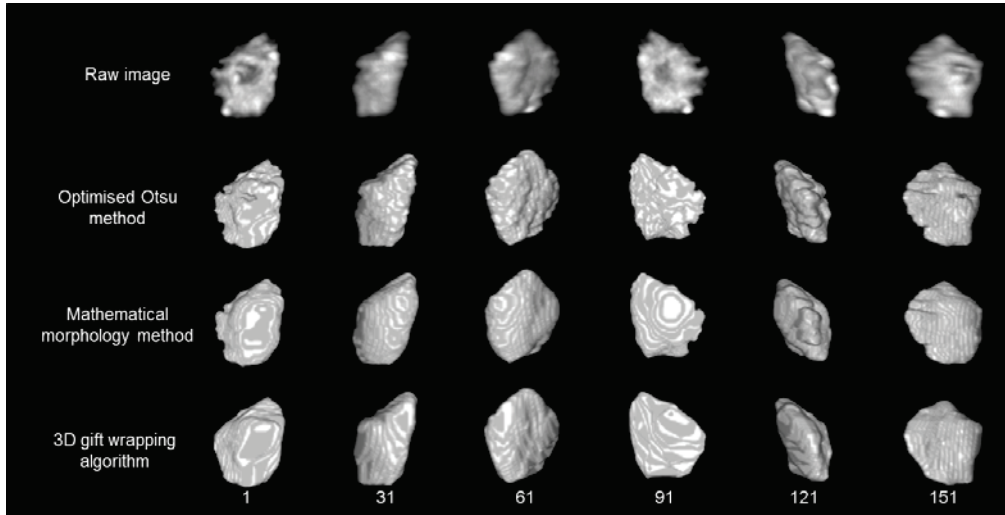


Figure 2.14: **3D nuclear segmentation of a nucleus using three new segmentation methods.** Selected z slices (numbers at the bottom) of a raw image of nucleus (top) have been selected for a raw image and for the three new methods indicated on the left.

#### 2.4.4 Comparative studies of 3D nuclei acquired with SIM and confocal microscope

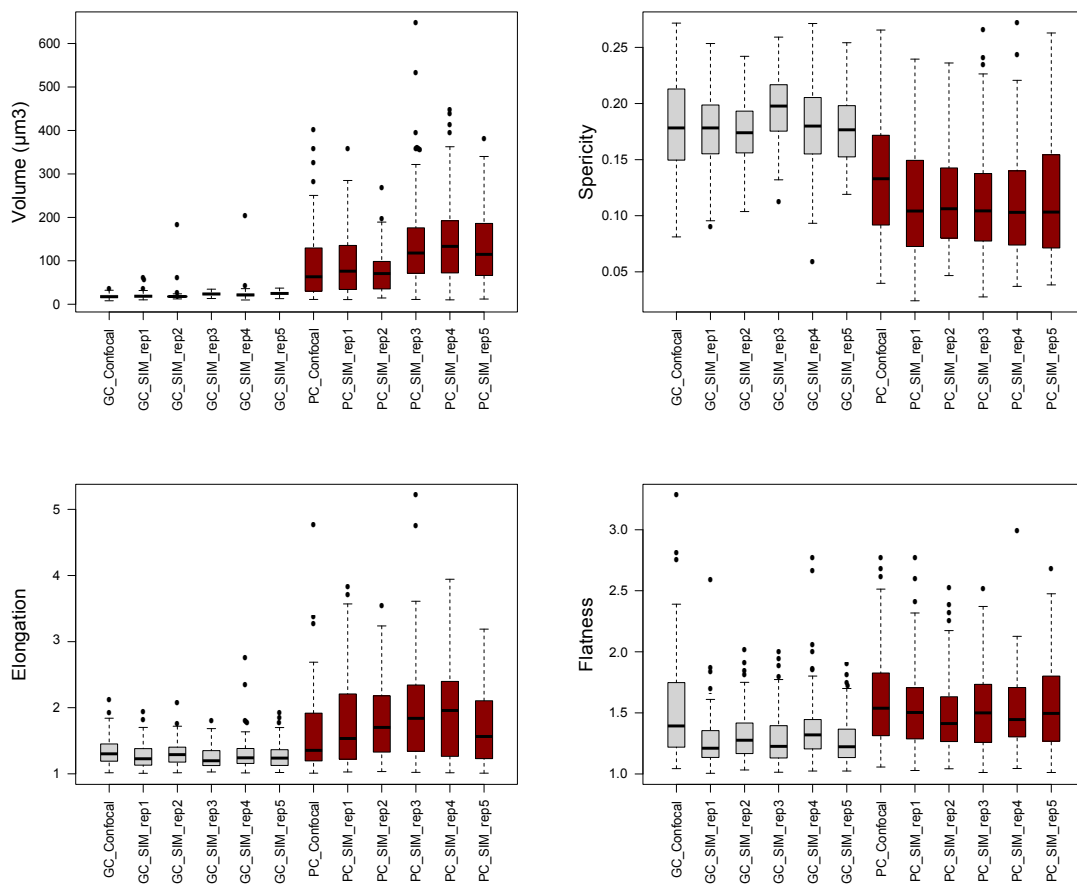
It is important to compare the parameters obtained using *NucleusJ* for 3D images obtained with the SIM and confocal microscopes to determine the reproducibility of data obtained using the two techniques and avoid dependency on one imaging system. Fixation and staining of *A. thaliana* cotyledons was carried out using both microscope systems, replicated five times for SIM and once for confocal. Nuclei of two cells type were acquired, guard cells (GC) and pavement cells (PC), to test different types of nucleus (Table 2.4). GCs have round nuclei while PC nuclei are more elongated. Furthermore the DNA content is not the same between this two cells type GC stay diploid whereas PCs are diploid or polyploid [Melaragno et al., 1993].

Table 2.4: **Samples of nuclei acquire by SIM and confocal microscopes.**

	<b>GC</b>	<b>PC</b>	<b>Total</b>
<b>Confocal</b>	94	74	168
<b>SIM rep1</b>	94	91	185
<b>SIM rep2</b>	154	126	280
<b>SIM rep3</b>	120	139	259
<b>SIM rep4</b>	202	114	316
<b>SIM rep5</b>	127	120	247

## Comparison of nuclear morphology parameters

In the GC samples the data within each experiment are homogeneous. Variability is low between SIM datasets, and between SIM and confocal experiments. The shape parameters (sphericity, elongation and flatness) also show homogeneity between experiments and very similar results were obtained for nuclear morphology between SIM and confocal data for diploid nuclei. The PC nuclei show more variability between experiments, but that is consistent with the fact that PC nuclei can be diploid or polyploid [Melaragno et al., 1993], but globally the observed variations are of similar range between SIM repetitions and between SIM and confocal.



**Figure 2.15: 3D morphological analysis of wild type nuclei from guard cells, pavement cells acquire by confocal and SIM microscopes.** Boxplots of nuclear morphology parameters generated by *NucleusJ* in two types of nuclei (GC in gray, PC in red) for 6 experiments of Col-o. Sample of nuclei is available in the Table 2.4.

## Comparison of the chromatin organisation parameter

As was the case for morphological parameters, in GCs the number of chromocentres detected by *NucleusJ* was around five for all the experiments. The other parameters are also homogeneous for the GCs. As with morphological parameters, the PCs have more intra-group variability than the GCs, except for the RHV which is always very low.

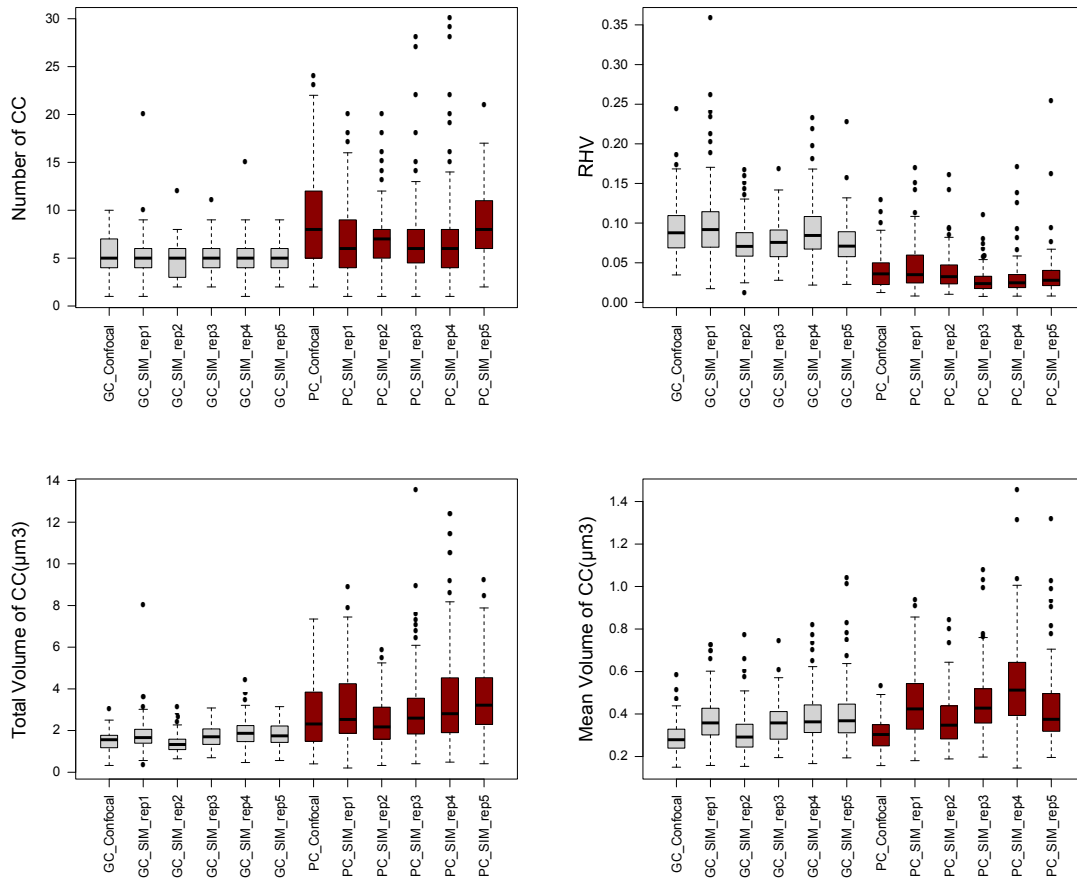


**Figure 2.16: Chromatin organisation analysis of wild type nuclei from guard cells, pavement cells acquire by confocal and SIM microscopes.** Boxplots of chromatin organisation parameters generated by *NucleusJ* in two types of nuclei (GC in gray, PC in red) for 6 experiments of Col-0. Sample of nuclei is available in the Table 2.4.

## Distance between chromocentres and nuclear periphery

The two distances computed between chromocentres and the nuclear periphery for the SIM data show less homogeneity than the other parameters analysed. But the majority of these data were overlapping with the same properties where GCs have

a shorter distance than PC. The comparison between SIM and confocal data for the distance of chromocentres from the NE were totally different, and a shorter distance was found for all the nuclei acquired by confocal in comparison to the SIM. The differences found are equivalent to the difference of the voxel resolution between both microscopes. The SIM images have voxel resolution equal to  $0.103 * 0.103 * 0.2 \mu\text{m}$  whereas the confocal voxel resolution is  $0.075 * 0.075 * 0.28 \mu\text{m}$ . The better resolution of the confocal microscope gave better precision in computing of the distance parameters.

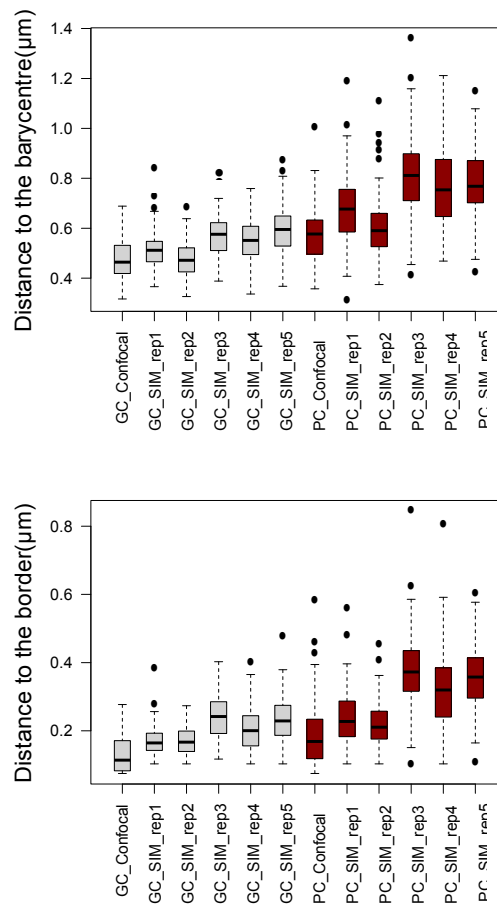


**Figure 2.17: Distance of chromocentres analysis of wild type nuclei from guard cells, pavement cells acquire by confocal and SIM microscopes.** Boxplots of the chromocentre distance generated by *NucleusJ* in two types of nuclei (GC in gray, PC in red) for 6 experiments of Col-o. Sample of nuclei is available in the Table 2.4.

## Conclusion

The results show similar results between 6 independent experiments and between two different microscopes on two types of cells. These results show the repeatability

of this experiment, and the power of this method, which can be carried out on different types of light microscopy while generating similar results for the same genetic background.

## 2.5 Conclusion

The development of *NucleusJ* allows the generation, within a few steps, of 3D quantitative parameters from single images or large data sets, without requiring expertise in image analysis. This plugin will be useful for a large community of users interested in quantifying size and shape of nuclei, nuclear objects or chromatin domains as well as positioning of the latter in nuclear space.

To improve the nuclear detection three different algorithms were developed. The first method is initialised by an Otsu threshold, but computes a new threshold, which is not related to the Otsu threshold, but is based on maximisation of sphericity and is already used in *NucleusJ*. Through this, estimation of sphericity was improved and now based on area estimation based on discrete geometry. The second is an iterated process of morphological openings and closings. The third method is a meaningful generalisation of a convex hull called *3D gift wrapping*.

This is an improvement of 3D segmentation procedures because measurements of intranuclear objects in respect to the boundaries of the nucleus benefit from a better segmentation. The *3D gift wrapping* method seems the most reliable procedure to perform the 3D segmentation of the nucleus (Figure 2.14). Note that some a priori knowledge from biology was required to tune the parameters. This method clearly shows the interest in combining colour and geometric information to improve segmentation, and also shows some advantages with respect to active contours, where regularisation terms, which are also difficult to tune, tend to smooth out angular features.

Finally, comparison of six experiments created using confocal and SIM microscopy shows a similarity in the results obtained with *NucleusJ*. But in these experiments there is variability between computed parameters which can be due to the growing conditions as the SIM experiments were carried out in Clermont Ferrand and the confocal experiments in Oxford Brookes University, though using the same seed lots and set growing conditions. The comparison shows a good reproducibility of the experiments between the two labs and two different microscopes.



# Chapter 3

## Influence of nuclear morphology on chromocentre organisation in *Arabidopsis thaliana*

### 3.1 Introduction

In *A. thaliana*, natural variations in nuclear shape and size are observed in various tissues such as epidermis, trichomes, root hairs [Traas et al., 1998, Qian et al., 2009] or during seed formation [van Zanten et al., 2011] and also in mutants altering the nuclear envelope [Dittmer et al., 2007, Tamura and Hara-Nishimura, 2011, Janski et al., 2012, Zhou et al., 2012, Goto et al., 2014].

Over the years, many components of the plant nuclear envelope have been discovered. It is now assumed that plants have their own LINC complex consisting of SUN (SAD1-UNC-84 HOMOLOGY) [Graumann et al., 2010, Graumann, 2014] and KASH (Klarsicht/Anc-1/Syne homology) proteins including WIP (WPP domain-interacting proteins) and SINE (SUN-interacting nuclear envelope) [Zhou et al., 2012, Graumann, 2014, Zhou et al., 2014]. The WIP proteins interact with the WITs (WPP domain-Interacting Tail-anchored proteins) and connect the LINC complex to the cytoskeleton [Zhao et al., 2008] (see Section 1.4). Furthermore, possible candidates for nuclear lamina proteins have been identified and are known as CRWN [Dittmer et al., 2007, Wang et al., 2013] and KAKU4 [Goto et al., 2014]. Strikingly, 2D nuclear morphology analysis of *sun*, *wip*, *kaku* and *crwn* mutants display nuclear shape and/or nuclear size modification suggesting that mechanical constraints such as those applied by the cytoskeleton at the NE may be released in mutant backgrounds [Dittmer et al., 2007, Graumann et al., 2010, Graumann, 2014, Goto et al., 2014]. Finally, the SUN-WIP-WIT-myosin XI-i complex and CRWN1 were pro-

posed to independently determine an elongated shape of the nucleus, highlighting the function of cytoskeleton and nucleoskeleton in nuclear morphology [Zhou et al., 2015b]. If nuclear morphology impacts chromatin organisation, it is also possible that chromatin organisation affects nuclear morphology.

Chromatin in eukaryotes is a complex structure in which DNA associates with histone proteins and a variety of other histone-associated proteins (see Chapter 1 Section 1.2). Modifications such as DNA or histone methylations taking place on chromatin named epigenetic modifications are associated with euchromatin and heterochromatin formation or maintenance [Li et al., 2007]. In *A. thaliana*, chromocentres are constituted by pericentromeric repeats, transposons and ribosomal DNA genes (see Chapter 1 Section 1.2) [Maluszynska and Heslop-Harrison, 1991]. Chromocentres are enriched in epigenetic marks such as DNA methylation at CG, CHG and CHH (H represents A, T or C) sites, as well as histone modifications (dimethylation at histone H3 Lys9 (H3K9me2) and monomethylation at histone H3 Lys27 (H3K27me1)) [Cao and Jacobsen, 2002, Tariq et al., 2003, Probst et al., 2003, Zhang et al., 2007, Cokus et al., 2008].

Heterochromatin maintenance is performed by proteins such as chromatin remodeling factors like the ATXR proteins (*Arabidopsis* Trithorax-Related Protein) or DDM1 (Decrease in DNA Methylation1) or by the incorporation of histone variants. Indeed, some histone variants are specific for some epigenetic marks. For example, only the canonical histone H3.1 can be modified by the *A. thaliana* proteins ATXR5 and ATXR6 which are H3K27 monomethyltransferases involved in the chromatin condensation and gene silencing. The *atxr5 atxr6* double mutants show reduced H3K27me1 at chromocentres and a partial heterochromatin decondensation [Jacob et al., 2009]. DDM1 is an ATP-dependent SWI2/SNF2 (SWITCH/Sucrose Non-Fermentable) chromatin remodeling factor necessary for normal patterns of DNA methylation in the *A. thaliana* genome [Hirochika et al., 2000]. Loss of DDM1 function impacts chromatin organisation and triggers DNA decondensation at the heterochromatic regions [Hirochika et al., 2000, Soppe et al., 2002, Franz et al., 2003, Probst et al., 2003].

The histone H3 possesses several variants which are enriched in different parts of the genome. For example, H3.1, H3.3, CENH3 are respectively enriched in chromocentres, 3' end of active genes, and centromeres [Otero et al., 2014]. The deposition by specific histone chaperones of these variants allow the maintenance or the formation of heterochromatin. Several histone H3 chaperones have been described in various organisms. For examples, ASF1 and ATRX have been described as H3 chap-

erone in *A. thaliana* [Otero et al., 2014]. Mutation of these chaperones impacts the incorporation of histone H3 (Doctor Céline Duc personal communication and [Otero et al., 2014]). However, no studies have been performed so far to analyse the effect of chaperone loss on heterochromatin organisation in 3D imaging and on the volume and positioning of chromocentres.

## 3.2 Aim

The aim of the analysis undertaken was to investigate the potential impact of nuclear reshaping on chromatin organisation and vice versa. Using *NucleusJ*, a quantitative analysis of 3D images of nuclei of mutants of the NE envelope and chromatin were carried out to investigate the potential link between NE and chromatin organisation on the plant. Whole mount preparations in three contrasted cell types (guard cells (GC), pavement cells (PC) and root hair cells (RC)) known to display distinct nuclear organisation in *A. thaliana* were analysed for all mutants. To determine the impact of the alteration of nuclear morphology on silencing, maintenance of heterochromatin, qRT-PCR was performed (undertaken by Dr Celine Duc) to analyse the reactivation of these targets. The decompaction of heterochromatic sequences was then studied using 2D FISH (undertaken by Dr Matthias Benoit) and 3D FISH (undertaken by Dr Sophie Desset and Prof. Christophe Tatout) with 180bp probes.

## 3.3 Material and methods

### 3.3.1 Plant material

All mutants and wild type *A. thaliana* plants were from the Columbia-o ecotype. T-DNA insertions were obtained from The European Arabidopsis Stock Centre (NASC, <http://arabidopsis.info/>). T-DNA accession numbers and genes used in this study are described in Table 3.1. Seed batches from all genotypes used in this study were propagated together in the green house under long day conditions. Phenotypic evaluations were performed on *A. thaliana* seedlings grown from sterilized seeds sown on germination medium containing 0.8% w/v agar, 1% w/v sucrose and Murashige & Skoog salts (MO255; Duchefa Biochemie, Netherlands). After 2 days of stratification at 4°C in the dark, seedlings were grown under 16 h light/8 h dark cycles at 23°C, cotyledons were harvested 14 days after germination. For each biological replicate, a typical experimental plan always included Col-o as a control along with one or several mutants. For each genotype, 3 cotyledons are used to confirm genotype, 8-10 for 3D image analysis, 4-6 for 3D in situ hybridisation and 30 for RT-qPCR analysis.

**Table 3.1: Mutants used in this study.** Mutant descriptions can be found in Zhou and Meier 2014 for *wifi*, Dittmer et al. for *crwn1 crwn2*, Goto et al. 2014 for *kaku4-2*, Jordan et al. 2007 for *dcm1-10* and Jacobs et al. 2009 for *atrx5 atrx6*. *sun1 sun4 sun5* has been evaluated for the first time in this study.

Mutant names	Alleles	T-DNA	Gene Name	Acc Number	Family	Mutant class
<i>wifi</i>	<i>wit1-1</i>	GABI-Kat_470E06	<i>WIT1</i>	At5g11390	KASH interacting	Nuclear periphery
	<i>wit2-1</i>	SALK_CS39986	<i>WIT2</i>	At1g68910		
	<i>wip1-1</i>	SAIL_390_A08	<i>WIP1</i>	At4g26455	KASH	
	<i>wip2-1</i>	SALK_052226	<i>WIP2</i>	At5g56210		
	<i>wip3-1</i>	GABI-Kat_459H07	<i>WIP3</i>	At3g13360		
<i>sun1 sun4 sun5</i>	<i>sun1-1</i>	SAIL_84_G10	<i>SUN1</i>	At5g04990	SUN	
	<i>sun4-1</i>	SALK_022028	<i>SUN4</i>	At1g71360		
	<i>sun5-1</i>	SALK_126070	<i>SUN5</i>	At4g23950		
<i>crwn1 crwn2</i>	<i>crwn1-1</i>	SALK_023383	<i>CRWN1</i>	At1g67230	Lamin-like	
	<i>crwn2-1</i>	SALK_090952	<i>CRWN2</i>	At1g13220		
<i>kaku4</i>	<i>kaku4.2</i>	SALK_076754	<i>KAKU4</i>	AT4G31430		
<i>dcm1</i>	<i>dcm1-10</i>	SALK_000590	<i>DDM1</i>	At5g66750		
<i>atrx5 atrx6</i>	<i>atrx5-1</i>	SALK_130607	<i>CATXR5</i>	At5g09790	Heterochromatin	Chromatin
	<i>atrx6-1</i>	SAIL_240_H01	<i>ATXR6</i>	At5g24340		
<i>asf1a asf1b atrx</i>	<i>asf1a-1</i>	GABI_200G05	<i>ASF1A</i>	At1g66740	Heterochromatin	Histone Chaperone
	<i>asf1b-1</i>	SALK_105822	<i>ASF1B</i>	At5g38110		
	<i>atrx-1</i>	SALK_025687	<i>ATRX</i>	At1g08600		
<i>atrx-2</i>	SAIL_861_B04					

### 3.3.2 RNA extraction and RT-PCR

Total RNAs were extracted from 30 cotyledons using Tri-Reagent (Euromedex), further treated with RQ1 DNase I (Promega) and purified using phenol-chloroform extraction. Reverse transcription was primed either with oligo(dT)<sub>15</sub> or with random hexamers using M-MLV reverse transcriptase (Promega). The resulting cDNAs were used further in quantitative PCR with the LightCycler<sup>®</sup> 480 SYBR Green I Master kit on the Roche LightCycler<sup>®</sup> 480. Transcript levels for the target of interest were normalised to *AtSAND* [Czechowski et al., 2005] using the comparative threshold cycle method.

### 3.3.3 Fluorescent in situ hybridisation in 2D

Cotyledons were fixed in ethanol-acetic acid (3:1 v/v) and Fluorescence in situ hybridization (FISH), was performed essentially as described [Probst et al., 2003, Bowler et al., 2004]. Biotin labelled probes complementary to the 180 bp repeats region were generated by PCR from the pSK180bp plasmid [Douet et al., 2008]. The Biotin labelled probe was detected with Texas Red-conjugated Avidin (5 µg/mL, Vector Laboratories) followed by a biotinylated goat anti-Avidin antibody (5 µg/mL, Vector Laboratories) followed by Texas Red-conjugated Avidin. Slides were analysed with a Zeiss Axio Imager Z.1 microscope equipped with a Zeiss AxioCamMRm camera system and images processed with ImageJ and Adobe Photoshop. More than 200 nuclei were scored per condition using a double blind experimental setup. Only nuclei in which all 180 bp are clustered in chromocentres are scored as clustered. Differences were compared using a frequencies test (R function: *prop.test*).

### 3.3.4 Sample preparation, Hoechst staining and 3D-FISH

3D images were collected from cells in their original tissue environment using a method described by Bauwens et al. (1994) to obtain whole mount preparations of 14 day cotyledons and crown roots. Briefly, plant tissues were collected and fixed using 1% formaldehyde, 10% DMSO in PBS 1X, EGTA 6.7 mM pH7.5 under vacuum for 5 min and incubated for 25 min at room temperature. Tissues were then washed 3 times with methanol and several ethanol washes to obtain transparent tissue preparations. Whole mount preparations were then used either for a simple Hoechst-staining procedure or for 3D-Fluorescent In Situ Hybridization (3D-FISH) after progressive rehydration with PBS-Tween 0.1%.

For Hoechst-staining, tissues were stained overnight at 4°C in a solution of Hoechst 33258 (SIGMA) at 25 µg/ml in PBS. Samples were then washed three

times with PBS 1X, excess water removed with paper tissue and placed on a slide in PBS/glycerol (20:80) solution and covered with a cover slip for microscopic observations.

For 3D-FISH hydrated tissues were washed twice in 2xSSC then incubated for 30 min in 2xSSC:HB50 (1:1) (50% formamide, 2xSSC, 50 mM sodium phosphate pH7) and finally 30 min in HB50. Tissues were directly immersed in HB50 containing 1  $\mu$ M of centromeric Locked Nucleic Acid (LNA) probe (Exiqon 180 pb centromeric repeats sequence is TEX615: GTATGATTGAGTATAAGAACT-TAAACC) and incubated 2 hrs at 37°C, boiled 5 min and then rapidly cooled on ice, tissues were hybridized overnight at 37°C. Then were rinsed twice for 30 min at 42°C in SF50 (50% formamide, 2xSSC) and incubated overnight with 0.25  $\mu$ g/ml Hoechst 33258 in PBS at 4°C. Samples are rinsed twice in 2xSSC and 2 twice in PBS and mounted in PBS:glycerol (20:80) as described above. 3D FISH experiments were performed as previously [Bauwens et al., 1994] when standard probes were used (*i.e.* not LNA probe). Labelling was performed by nick translation (Roche) using the 45S rDNA probe from *Triticum aestivum* [Gerlach and Bedbrook, 1979] using Cy3-dUTP (GE healthcare) and the 180 pb probe from *A. thaliana* [Martinez-Zapater et al., 1986] using Cy5-dUTP.

### 3.3.5 3D image acquisition

Microscopic observations were performed by structured illumination microscopy to produce confocal-like images using an Optigrid module (Leica-microsystems MAAF DM 16000B). All images were acquired using a X63 oil objective at optimal resolution; lateral and axial resolution were respectively  $xy = 0.103$  and  $z = 0.2$   $\mu$ m. The ImageJ plugin, *NucleusJ*, was used to characterise nuclear morphology and chromatin organisation [Poulet et al., 2015]. Description of the quantitative parameters generated by *NucleusJ* can be found in supplemental materials of Poulet et al. (2015) and in the Section 2.4.1.

### 3.3.6 RNA-Seq analysis

Already published RNA-seq datasets from wild type Col-0 ecotype were used in order to determine the expression of candidate genes investigated in this study. The Illumina RNA-seq data are available at the NCBI Sequence Read Archive (<http://www.ncbi.nlm.nih.gov/Traces/sra/sra.cgi>) under accession number SRR1463334, SRR1463335, SRR826283 for guard cells from 10 dag cotyledons, SRR1463325, SRR1463326 for epidermis from 10 dag cotyledons and SRR1042766,

SRR1042767, SRR656215 for roots from 7 day-old seedlings. Reads from RNA-Seq libraries were mapped onto the candidate gene sequences allowing no mismatches using TOPHAT v 2.0.14 [Kim et al., 2013] using standard settings and maximum of multihits set at 1, minimum intron length set at 15 bp, and maximum-intron length set as 6000 bp. Reads were summed for each gene using HTseq-count with the overlap resolution mode set as intersection-non empty and with no strand-specific protocol [Anders et al., 2015].

A Perl script was developed to parse the HTseq output file and recover only the results of the genes of interest. The script computed the Reads Per base Kilo per Million mapped reads (RPKM) on the non-overlapping gene region. The RPKM formula normalises the reads per gene in each dataset and relative to the length of the gene to allow comparison of gene coverage values.

$$RPKM = \frac{10^9 * Read\ number}{Gene\ Length * Total\ Reads} \quad (3.1)$$

Transcription levels were normalized to *AtSAND* as for RT-qPCR and expressed in Fragments per Kilobase of Exon Model (FPKM) per million mapped reads. *SAND* was chosen due to its gene expression stability across different tissues at different developmental stages [Czechowski et al., 2005].

### 3.3.7 Statistical methods

Statistical analyses were performed using R [R Core Team, 2013]. Principal component analysis (PCA) was carried out with the FactoMineR package, an extension of R software [Husson et al., 2009]. R scripts were developed to undertake statistical tests automatically (Student's T test and correlation) as well as PCA, and boxplots of the data were drawn from analysis of 3D images. A Student's T test was used to compare means for quantitative PCR. A proportion test was used to compare the proportion of nuclei with condensed chromocentre.



## 3.4 Results

### 3.4.1 Quantitative variations in nuclear organisation occur in wild-type cells.

In *A. thaliana*, hypocotyls and trichomes [Traas et al., 1998], root hairs [Sugimoto-Shirasu et al., 2005], epidermis [Guimil and Dunand, 2007] and pollen tubes [Zhou et al., 2014] may be used to illustrate variations in cell and nuclear morphogenesis. To assess nuclear size, shape and chromocentre organisation, a simple DNA staining procedure was applied on whole mount tissue using Hoechst intercalating agent. Three different cell types displaying distinct nuclear features were characterised (Figure 3.1A). On the one hand, epidermal cells from cotyledons are made of two main cell types: guard cells (GC), which are bean shaped cells with round nuclei, and pavement cells, which are lobed and display elongated nuclei. Pavement cells (PC) have undergone one or several rounds of endoreplication, *i.e.* DNA replication without cell division. As a consequence, while GC have mostly 2C content, the DNA content varies between 2C and 16C in PC and their cell size expands roughly in proportion to the amount of DNA [Melaragno et al., 1993]. Nuclei from root hair epidermis (RC) were investigated from the easily accessible crown roots which display elongated nuclei [Ketelaar et al., 2002].

Nuclear shape, in these different cell types in WT Columbia (Col-0) plants was first quantified using *NucleusJ*, which permits segmentation of the nucleus as well as the chromocentres (Figure 3.1B). Upon 3D segmentation, large datasets can be investigated through 3D quantitative parameters relative to nuclear morphology and heterochromatin organisation. In order to confirm that segmented objects within the nucleus are indeed chromocentres, Hoechst DNA-staining and 3D-Fluorescence in situ Hybridisation (3D-FISH) was done simultaneously on whole mount tissue. 180bp satellite repeats and 45S rDNA repeats, which are the main repetitive sequences enriched in chromosome regions forming chromocentres, were used as probes. Most of the intranuclear objects segmented using *NucleusJ* overlap with 180bp and 45S signals indicating that they are true chromocentres (Figure 3.1C).

The use of a large dataset of 1,500 nuclei obtained from five biological repetitions (Table 3.2) allowed the characterisation of nuclear morphology and heterochromatin organisation in the three cell types. The quantitative parameters produced by *NucleusJ* explain up to 60% of the phenotypic variation across the two main axes of a Principal Component Analysis (PCA) analysis (Figure 3.2a, 3.2b) clearly divid-

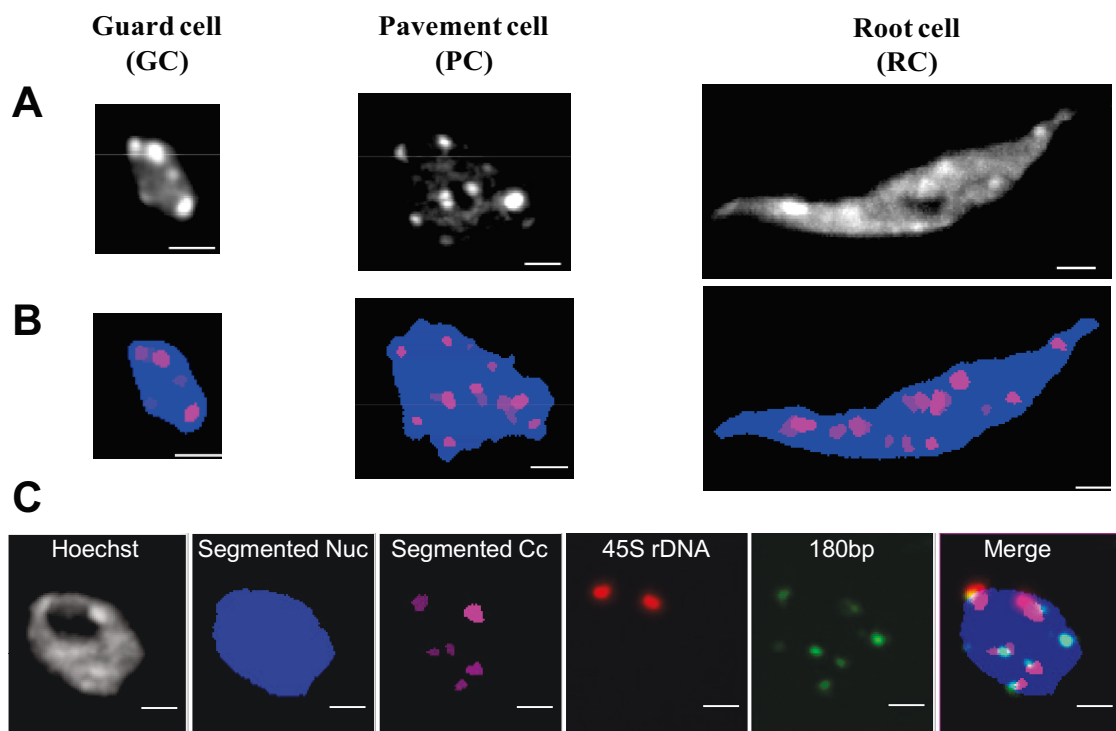


**Figure 3.1: 3D segmentation of nuclei and chromocentres using *NucleusJ*.** **A)** Raw images of representative nuclei from GC, PC and RC stained with Hoechst DNA intercalating-agent. Chromocentres corresponds to bright nuclear foci. **B)** 3D segmentation of nucleus (blue) and chromocentres (pink) are achieved by an ImageJ plugin called *NucleusJ* which keeps 3D information along the segmentation processes and generates quantitative parameters relative to the nuclear morphology and chromatin organisation. **C)** Image of the same nucleus stained with Hoechst, the segmented nucleus (blue) and the segmented chromocentres (pink) through *NucleusJ* and hybridised with centromeric 180bp satellite repeats (green) and 45SrDNA (red) from 3D-FISH. An overlay of the four channels is also given (merge) indicating that most dense nuclear foci recorded by *NucleusJ* co-localise with chromocentres. Scale bar = 2  $\mu\text{m}$ .

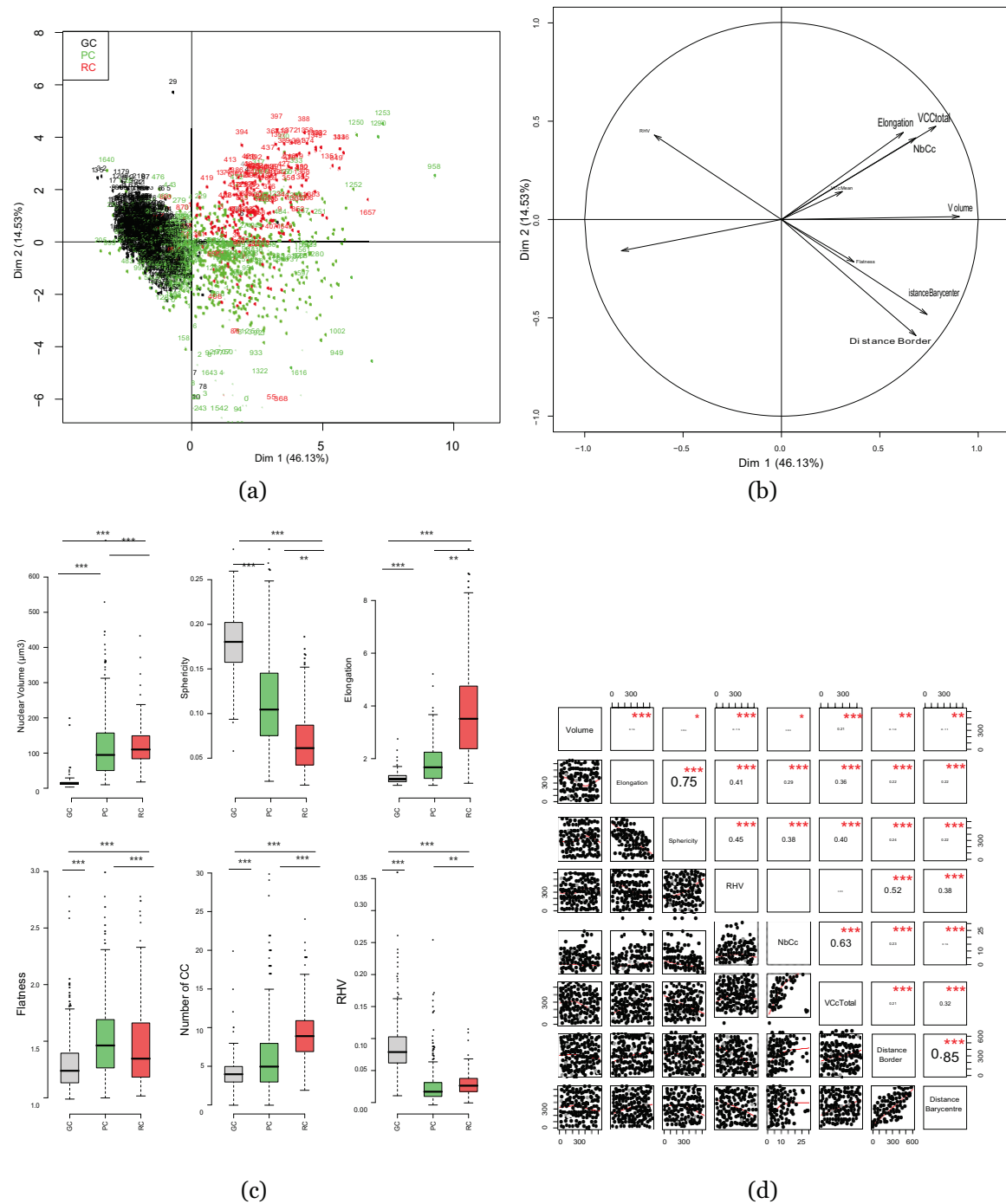
ing the nuclei belonging to the three different cell types in three different clouds. Pavement cells display the greatest variability, root hair nuclei an intermediate variability whereas guard cell nuclei are easily grouped together in PCA analysis (Figure 3.2a). GCs exhibit nuclei of small volume ( $21.8 \pm 0.4 \mu\text{m}^3$ ) with elevated sphericity, but reduced elongation (Figure 3.2c) suggesting that small nuclei tend to be rounder and to show a smoother nuclear shape. On the contrary, in PC and RC, nuclear volumes are larger (respectively  $115.2 \pm 3.4$  and  $123.3 \pm 3.9 \mu\text{m}^3$ ) and nuclei are more elongated suggesting that increased nuclear size is associated with nuclear

Table 3.2: Number of nuclei of all genetic background.

Genetic background	GC	PC	RC
Col-0_rep1	94	91	26
Col-0_rep2	154	126	59
Col-0_rep3	120	139	44
Col-0_rep4	202	114	59
Col-0_rep5	127	120	25
<i>asf1a</i>	119	124	20
<i>asf1b</i>	114	140	35
<i>asf1a asf1b</i>	162	173	47
<i>atrX-1</i>	96	130	26
<i>atrX-2</i>	103	138	49
<i>atr5 atr6</i>	107	132	38
<i>ddm1-10</i>	108	127	48
<i>crwn1 crwn2</i>	82	119	39
<i>kaku4-2</i>	109	123	34
<i>sun1 sun4 sun5</i>	112	124	27
<i>wip1 wip2 wip3</i>	100	130	45
<i>wit1 wit2</i>	114	128	53
<i>wifi</i>	190	174	57
<b>TOTAL</b>	<b>2213</b>	<b>2352</b>	<b>731</b>
<b>MOYENNE</b>	<b>123</b>	<b>131</b>	<b>41</b>

shape alterations in these two cell types. The PCA analysis revealed that elongation and sphericity display a strong negative correlation ( $r^2 = 0.75$ ,  $p < 0.0001$ ) and are among the best parameters to discriminate the three nuclear types (Figure 3.2b and 3.2d). To the contrary, *fl* another morphological parameter computed by *NucleusJ*, only poorly discriminates the three populations of nuclei. Whole mount tissue preparations associated with Hoechst staining also gave the opportunity to better describe chromocentre organisation. GC contain fewer chromocentres than larger nuclei such as PC and RC. RHV, determined as volumes of chromocentres relative to the volume of the nucleus, was higher due to smaller nuclear volume, despite the fact that chromocentre number was lower in these cells (Figure 3.2c). The RHV decreases in larger nuclei, which have undergone endoreplication. Finally, a strong positive correlation was observed between the number of chromocentres and the total amount of heterochromatin ( $r^2 = 0.63$ ,  $p < 0.0001$ ) indicating that either parameter can be used to discriminate the three cell types.

Taken together, *NucleusJ* phenotyping easily distinguishes the three contrasted nuclear types chosen in this study. Variability among the three nuclear types is best explained by two nuclear shape parameters namely elongation and sphericity and the number of chromocentres.



**Figure 3.2: Wild type nuclei from guard cells, pavement cells and root hair cells can be distinguished by *NucleusJ* phenotyping.** PCA of **a)** individual nuclei from guard cells (GC,  $n=799$ , black), pavement cells (PC,  $n=614$ , green) and root hair cells (RC,  $n=230$ , red) and **b)** quantitative parameters generated by *NucleusJ* are depicted in two main axis. Nuclear volume (Vnuc), total volume of all chromocentres (VCCtotal), number of chromocentres (NbCC). Statistical differences performed with Student's T test are indicated above box-plots. **c)** Selected *NucleusJ* parameters highlight the phenotypic variations among the three types of nuclei. **d)** Scatter plot matrix and absolute correlation between pairs of variables. The two major correlations are between elongation and sphericity ( $r^2 = 0.75$ ) and NbCC and VCCtotal ( $r^2 = 0.63$ ) are highlighted in color. (\*:  $p \leq 0.01$ , \*\*:  $p \leq 0.001$ , \*\*\*:  $p \leq 0.0001$ ).

### 3.4.2 Chromocentres are positioned at the nuclear periphery

Radial position, a widely used 2D parameter to characterise object position, was used to describe chromocentre position in living cells of various *A. thaliana* tissues expressing HTR12 and H2B fused to fluorescent proteins. These experiments highlighted the peripheral position of chromocentres next to the nuclear periphery and the nucleolus [Fang, 2005]. Furthermore, modelling also predicted that chromocentres would tend to be located at the nuclear periphery [de Nooijer et al., 2009] (see Chapter 1 Section 1.2).

Here, Hoechst-stained nuclei allow quantification of the position of each chromocentre of a given nucleus to the limit of the DNA staining and computation of two distinct distances (see Chapter 2 Section 2.4.1). The first was the distance between the two closest voxels from the chromocentre and the limit of the DNA staining in GC, PC and RC, which are respectively of  $0.20 \pm 0.06$ ,  $0.30 \pm 0.11$  and  $0.27 \pm 0.09 \mu\text{m}$  (Figure 3.3A, 3.3B). Secondly, the distance from the centre of each chromocentre (barycentre) was computed, which are respectively of  $0.54 \pm 0.09$ ,  $0.72 \pm 0.16$ ,  $0.68 \pm 0.11 \mu\text{m}$  (Figure 3.3A, 3.3C). These data suggest that chromocentres are not at the most external position of the segmented nuclei. In other words they are not completely bound to the nuclear envelope but instead there may be a space in between. Surprisingly, almost all of the chromocentres are close to the periphery including those usually linked to the nucleolus, which are easy to identify thanks to their larger size suggesting that the nucleolus may also be close to the nuclear periphery in interphase nuclei. These data also suggest that chromocentres are at a greater distance from the nuclear periphery in the larger nuclei of PC and RC (Figure 3.3B). Finally, the two distance parameters describing the position of chromocentres are strongly correlated ( $r^2 = 0.85$ ,  $p < 0.0001$ ).

Taken together, the results show that chromocentres are localised at a small distance from the nuclear periphery.

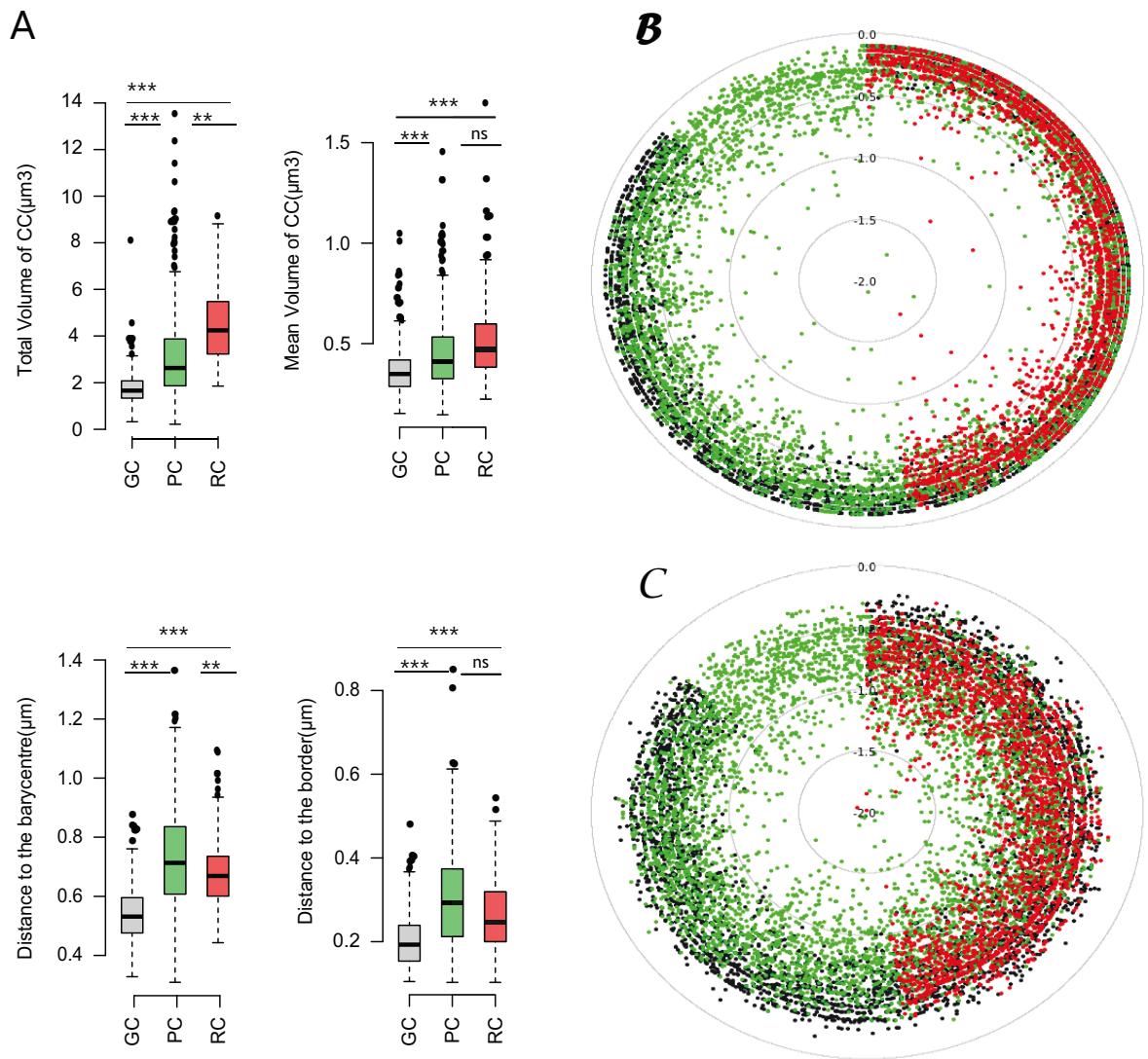


**Figure 3.3: Chromocentres are located close to the nuclear periphery.** **A)** Selected *NucleusJ* parameters describing the phenotypic variations relative to chromocentre organisation among the three types of nuclei. Statistical differences performed with Student's T test are indicated above box-plots. **B)** Graphical representation of chromocentres distribution of the distance between the two closest voxels from the chromocentres and the limit of the DNA staining among the three cell types. GC: guard cells (black), PC: pavement cells (green), RC: root hair cells (red) or **C)** the distance from the centre of each chromocentre to the limit of the DNA staining among the three cell types. GC: guard cells (black), PC: pavement cells (green), RC: root hair cells (red). (\*:  $p \leq 0.01$ , \*\*:  $p \leq 0.001$ , \*\*\*:  $p \leq 0.0001$  and ns: not significant).

### 3.4.3 Analysis of nuclear morphology of mutants of the nuclear envelope and chromatin organisation

The fact that chromocentres are situated close to the NE, suggests that alterations of components of the LINC and lamina complexes might perturb position, compaction or even formation of chromocentres. Previous studies highlighted that chromatin organisation is different in distinct genetic backgrounds [Tessadori et al., 2009], environmental changes such as light [Tessadori et al., 2007b], cellular context [Tessadori et al., 2007a] or growth medium conditions [Vaillant et al., 2008]. For these reasons, experimental procedures were standardised to reduce phenotypic variability within and across repetitions of a given genotype and our mutant datasets normalised against mutant plants grown in the same conditions within the same experiment (see Section 3.3).

In all, a set of thirteen mutants all in Col-o genetic background disrupting the expression of seventeen genes were studied (Table 3.1). Mutants altering components of the LINC complex chosen were *wifi*, *wip1 wip2 wip3*, *wit1 wit2*, *sun1 sun4 sun5*, *crwn1 crwn2* and *kaku4-2* such as KASH domain proteins [Zhou et al., 2014], SUN domain proteins [Graumann, 2014] and putative components of the plant lamina [Dittmer et al., 2007, Goto et al., 2014]. Mutants for chromatin remodelling factors such as *DDM1* and histone methyltransferases such as *ATXR5* and *ATXR6* were chosen as they show different heterochromatin organisation [Probst et al., 2003, Jacob et al., 2009] as well as two histone chaperones ASF1 and ATRX. The quintuple *wifi* and triple *sun1 sun4 sun5* mutants as well as chromatin mutants were evaluated for the first time in this study.

It was important to first analyse whether the genes altered in the mutants (Table 3.1) are expressed in the GC, PC and RC and whether they are differentially expressed. For that purpose, a survey of available RNA-Seq data was performed and 8 Col-o datasets were selected. Tissues include whole seedling roots, whole cotyledon epidermis and guard cells gained from FACS-sorted protoplasts. As GC and epidermis were investigated, pavement cell expression can be deduced from comparison of these two datasets. All genes are expressed in GC, PC and RC although at different expression levels (Figure 3.4). Data do not show strong bias between cell types except for *SUN4*, *CRWN1*, and *ASF1A* which are strongly expressed respectively in PC and GC (Figure 3.4). As expected from previous work [Baubec et al., 2014], *DDM1* and *ATXR5* and *ATXR6* are weakly expressed in these early stage tissues.

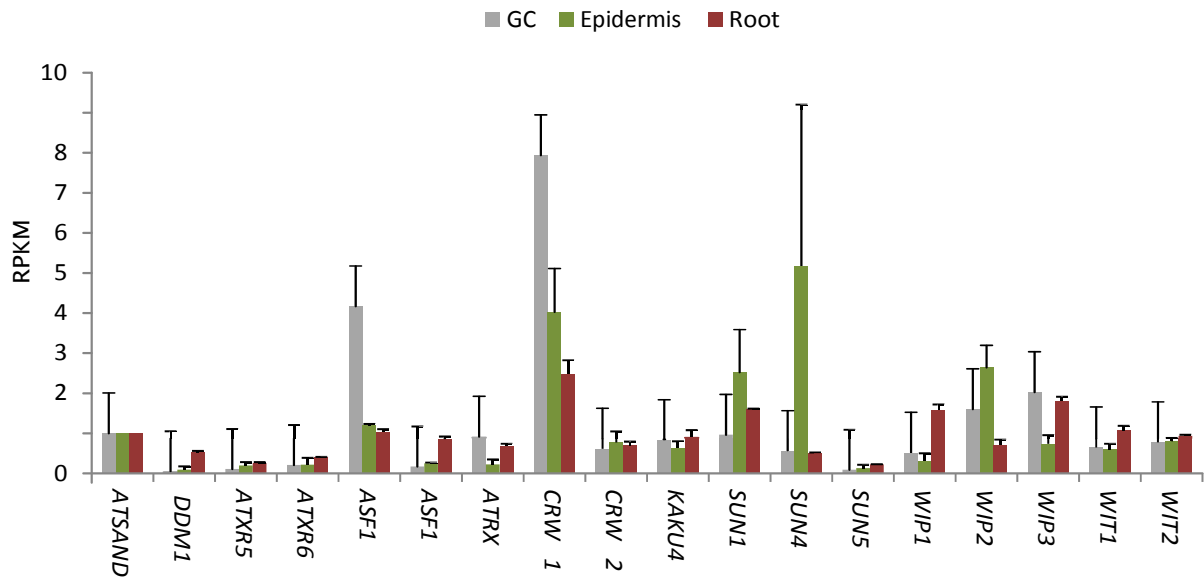


**Figure 3.4: RNA expression of candidate genes in epidermis, guard cells and roots.** RNA-seq datasets from wild type Col-o ecotype from guard cells (GC) at 10 day-old cotyledons (SRR1463334, SRR1463335, SRR826283), epidermis at 10 day-old cotyledon (SRR1463325, SRR1463326) and roots at 7 day-old cotyledons (SRR1463334, SRR1463335, SRR826283) were used in order to monitor the expression of candidate genes investigated in this study. Histograms show means of transcript levels expressed in RPKM  $\pm$  SEM (standard error of a mean). *At2g28390* (*AtSAND*) gene was used as a reference and set at 1 RPKM.

### Alterations of nuclear shape parameters in LINC complex and lamina mutants

The mutants deficient in nuclear periphery components (*wifi*, *wit1 wit2*, *wip1 wip2 wip3*, *sun1 sun4 sun5*, *kaku4-2*, *crwn1 crwn2*) display similar profiles especially in RC, the strongest effects being observed for the putative nuclear lamina mutants, *crwn1 crwn2* and *kaku4-2* (Figure 3.5 and see Appendix B.2). The six mutants show reduced nuclear size, increased sphericity and decreased elongation compared to Col-o (see Appendix B.2). It is however the first time that these mutants have been analysed in a single experiment which allows a quantitative comparison of the mutant effects. These data are in good agreement with previous work performed in 2D image analysis for *wip1 wip2 wip3* [Zhou et al., 2012], *wit1 wit2* [Tamura et al., 2013], *sun1 sun2* [Oda and Fukuda, 2011], *kaku4-2* [Goto et al., 2014] and *crwn1 crwn2* [Wang et al., 2013].



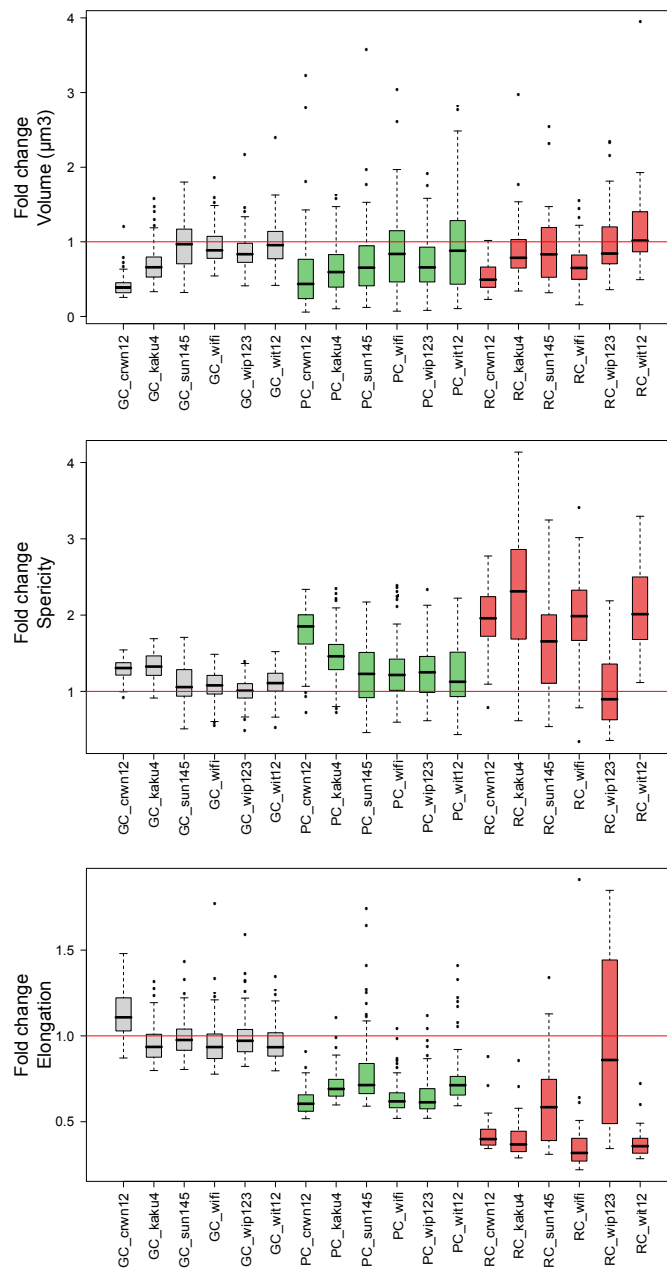


**Figure 3.5: Alteration of nuclear morphology in LINC complex mutant nuclei from guard cells, pavement cells and root cells.** Boxplots of nuclear morphology parameters generated by *NucleusJ* highlighting the phenotypic variations in three types of nuclei (GC in gray, PC in green and RC in red) for seven mutant backgrounds are shown. Samples and Statistical analysis are available respectively in Table 3.2 and Appendix B.2. All parameters recorded for mutant backgrounds were standardised using Col-0 (WT) set as 1 (red line).

### **Alterations of nuclear shape parameters in histone chaperones and chromatin mutants**

All the chromatin mutants display the same profile with a high variability of nuclear shape parameters especially for elongation in RC but these variations were not significantly different from the Col-0 (see Appendix B.3 and B.2). The exact significance of this higher phenotypic variation remains speculative but as it is mainly observed in PCs and RCs it can be hypothesised that it reflects an altered distribution of ploidy levels.

### 3.4.4 Alterations of chromocentre compaction and alleviation of silencing in mutants

#### Analysis of chromatin organisation by the *NucleusJ* parameters

Differences in heterochromatic parameters were less pronounced between Col-0 and mutants (Figure 3.6 and 3.7b and see Appendix B.2) except for the *crwn1 crwn2* double mutant, which displays a significant reduction in the number of chromocentres ( $p < 0.0001$ , Figure 3.6) as previously described [Dittmer et al., 2007, Wang et al., 2013]. In the *crwn1 crwn2* mutant there is also an increase of the mean volume of each chromocentre and of the RHV on all cell types ( $p < 0.0001$ , and see Appendix B.2). The significant increase of the RHV is also observed for *kaku4-2* in GC and PC ( $p < 0.001$ , Figure 3.6 and see Appendix B.2). The mutant *wip1 wip2 wip3* and *sun1 sun4 sun5* in the GC show a decrease of the mean volume of chromocentre and of the total volume of chromocentre ( $p < 0.001$ , Figure 3.6 and see Appendix B.2), furthermore in the same cell type, *wifi* presents a decrease of total volume of chromocentre and *wit1 wit2* a decrease of the mean size of the chromocentre ( $p < 0.001$ , Figure 3.6 and see Appendix B.2). The impacts of the *wip1 wip2 wip3* mutation were also found in the PC ( $p < 0.001$ , Figure 3.6 and see Appendix B.2).

The distance between the border of chromocentres and the nuclear periphery is increased in *sun1 sun4 sun5* and *wip1 wip2 wip3* with a statistically significant difference in GC and PC ( $p < 0.0001$ ) (Figure 3.7b and see Appendix B.2). Despite the strong effect observed in nuclear morphology for the LINC complex and lamin-mutant (Figure 3.5), 3D image analysis allows the detection of heterochromatin disorders on the total volume of chromocentre and the mean size of chromocentre (Figure 3.7b and see Appendix B.2). The RHV was affected in the lamin-like mutant, this shows a global disorder of the nucleus on these proteins. The distance of the chromocentre to the NE was affected by *sun1 sun4 sun5* and *wip1 wip2 wip3* mutants.

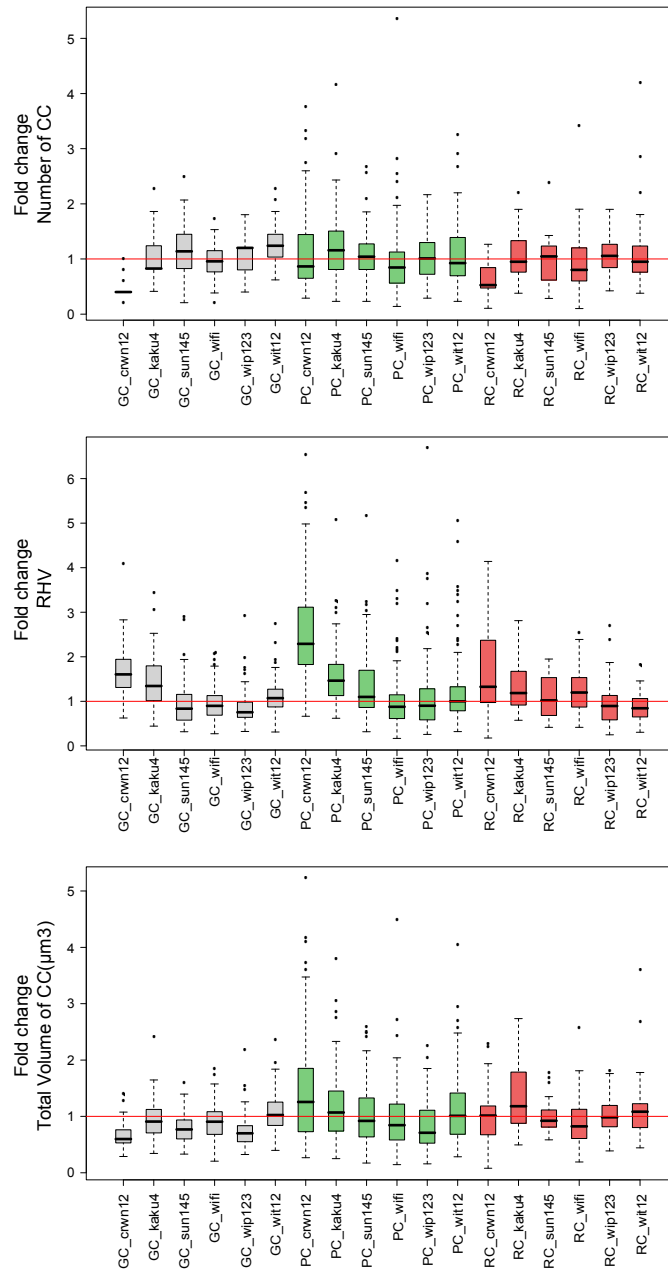
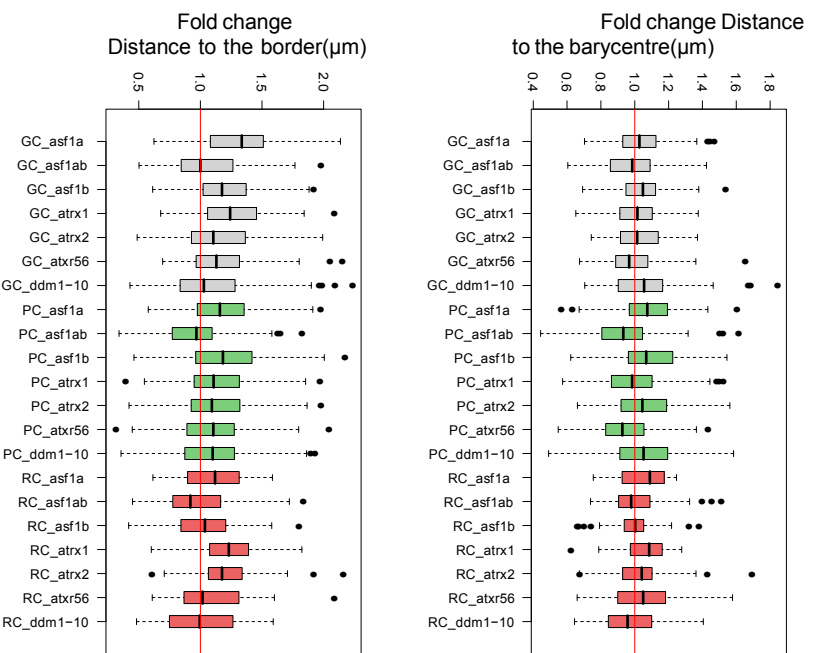
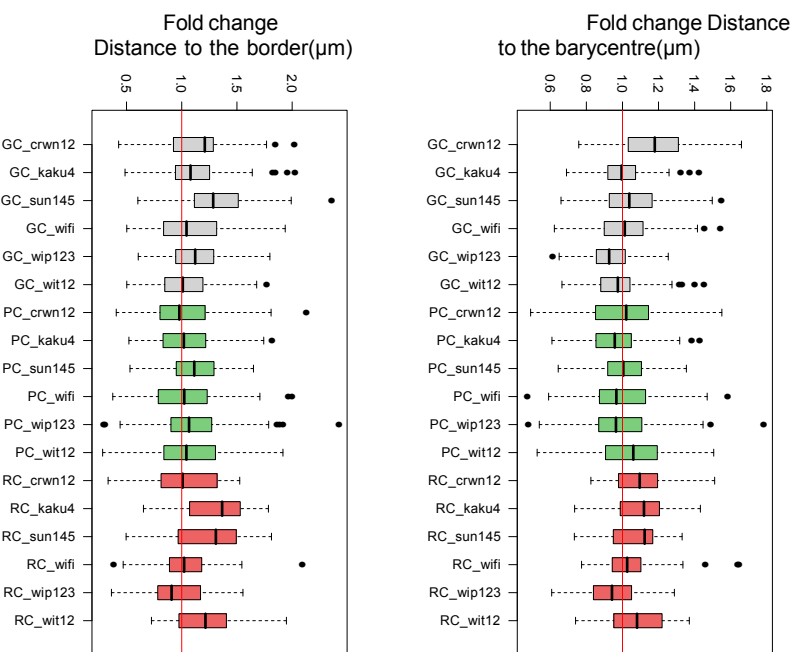


**Figure 3.6: Alteration of chromatin organisation in LINC complex mutant nuclei from guard cells, pavement cells and root cells.** Boxplots of chromatin organisation parameters generated by *NucleusJ* highlighting the phenotypic variations in three types of nuclei (GC in gray, PC in green and RC in red) of six mutants. Samples and statistical analysis are available respectively in Table 3.2 and Appendix B.2. All parameters recorded for mutant backgrounds were standardised using Col-o (WT) set as 1 (red line).



(a) Chromatin mutants



(b) LINC complex mutant.

**Figure 3.7: Alteration of chromocentres distance on the chromatin and LINC complex mutant nuclei.** Boxplots of the chromocentre distance generated by *NucleusJ* highlighting the phenotypic variations in three types of nuclei (GC in gray, PC in green and RC in red). Samples and statistical analysis are available respectively in Table 3.2 and Appendix B.2. All parameters recorded for mutant backgrounds were standardized using Col0 (WT) set as 1 (red line).

Chromatin mutants display globally the same phenotypes with a decrease in the RHV, the mean size of the chromocentre and of the total volume of the chromocentre, the histone chaperone mutants also show an increase of the number of chromocentre in the GC. The *ddm1-10* mutant does not show diff from the Col-o (Figure 3.8). The *atxr5 atxr6* mutant shows a strong phenotype in the PC with an increase of the RHV, of the number of chromocentre and in total volume on chromocentre, but the size of chromocentre decrease (Figure 3.8). The chromatin mutants increase the distance between the border of the chromocentre to the NE in the GC and PC. For the RC, few differences were observed (Figure 3.7a).

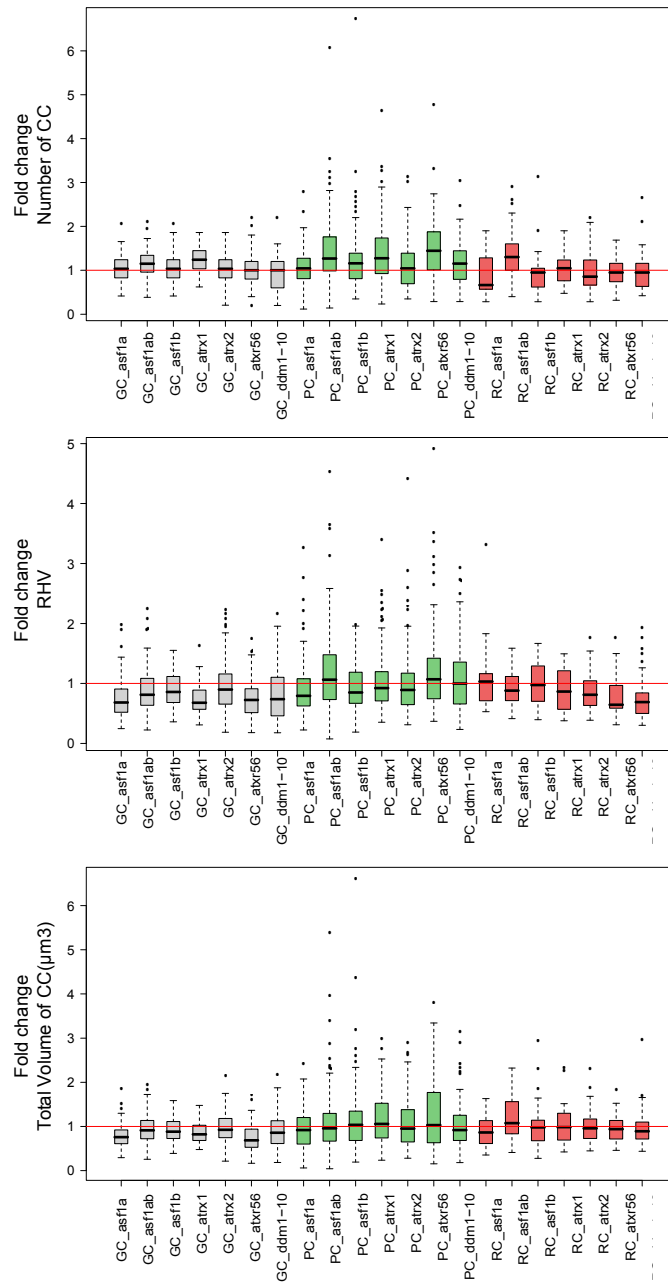


**Figure 3.8: Alteration of chromatin organisation in heterochromatin mutant nuclei from guard cells, pavement cells and root cells.** Boxplots of chromatin organisation parameters generated by *NucleusJ* highlighting the phenotypic variations in three types of nuclei (GC in gray, PC in green and RC in red) of seven mutants. Samples and statistical analysis are available respectively in Table 3.2 and Appendix B.2. All parameters recorded for mutant backgrounds were standardised using Col-o (WT) set as 1 (red line).

### Analysis of chromocentre compaction and its impact on alleviation of silencing

Chromocentre decompaction has previously been observed by 2D FISH in different mutants including *ddm1-10* and *atrx5 atrx6* [Soppe et al., 2002, Probst et al.,

2003, Jacob et al., 2009]. The 2D FISH experiments used whole cotyledon spreads with the 180bp probe, with small and large nuclei removed from the analysis to keep only nuclei with intermediary size. Then nuclei were divided into two classes, condensed or decondensed. For this 2D analysis mutants of the LINC complex (*wip1 wip2 wip3*), of lamin-like protein (*crwn1 crwn2*) and of chromatin organisation were included (all the mutants of interest), and a decompaction of the chromocentres was detected in *ddm1-10* and *atr5 atr6* as previously described [Probst et al., 2003, Jacob et al., 2009]. The lamin-like mutant *crwn1 crwn2* showed less effect on chromocentre decompaction in comparison to Col-0 (Figure 3.9), but the nuclear morphology and the parameters of chromatin detected by *NucleusJ* were totally changed. The chaperone histone *asf1a asf1b* and *atr-1* also contained more nuclei with chromocentres decompacted in comparison to Col-0 (Figure 3.9). Interestingly, the volume of the chromocentres for these mutants decreased at the epidermis, with a parallel decrease in RHV. However, the decompaction of the chromocentre did not have the same effect on the silencing of TS1, for which a significant reactivation is found for *ddm1-10*, *atr5 atr6* and *asf1a asf1b* ( $p < 0.05$ ) and not for *atr-1* (Appendix B.5).

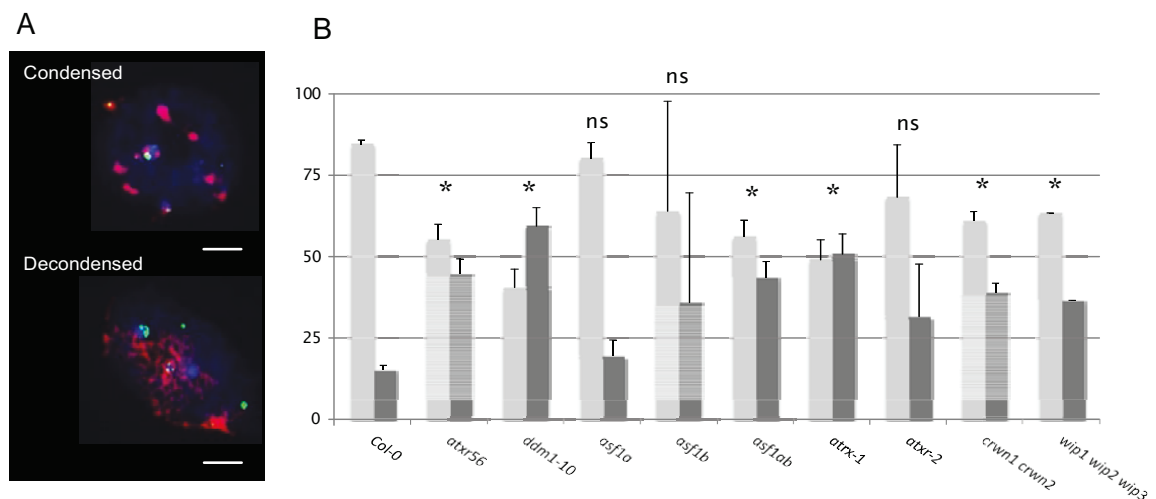


**Figure 3.9: Alteration of heterochromatin condensation in whole cotyledons analysed by 2D-FISH.** **A)** Representative nuclei collected from 2D-FISH experiments on nuclei counter-stained with DAPI (grey) of spread whole cotyledon using a fluorescent probe against 180bp repeats (red) and 45s rDNA (green). **B)** Quantification of condensed and decondensed 180bp hybridisation signals recorded by 2D-FISH obtained from 2 independent experiments. Average  $\pm$  SEM. Number of nuclei ranging from  $n = 180$  to 220. (\*:  $p \leq 0.0001$  and ns: not significant).

To test more specifically the decompaction on the cotyledon epidermis, 3D-FISH was applied to whole mount tissues in order to specifically investigate cotyledon epidermis. Thus GC and PC chromatin decompaction were examined using a short LNA-DNA (Locked Nucleic Acid) oligonucleotide probe generated to specifically recognise the 180bp centromeric repeats (Figure 3.10A). Each 3D nucleus was classed into the condensed type (Figure 3.10, top) or the decondensed type (Figure 3.10, bottom). Firstly, for Col-0 cotyledon nuclei at this developmental stage, a significant fraction from the epidermis were of the decondensed type ( $65 \pm 4\%$ , Figure 3.10B), with an equal distribution between GC and PC, except for *kaku4-2* (Appendix Table B.9). The number of decondensed nuclei significantly increases in the cotyledon epidermis of *ddm1-10* mutant ( $p < 0.05$ ), and a not significant increase was observed in the *atxr5 atxr6* mutant. Interestingly also a significant decompaction was recorded in *wifi*, *sun1 sun4 sun5* mutants ( $p < 0.05$ ), while *crwn1 crwn2* double mutants have the reverse effect and show a higher compaction of the 180bp repeats (Figure 3.10B).

As chromatin decompaction can be associated with release in transcriptional gene silencing (TGS) at centromeric and pericentromeric repeats [Probst et al., 2003, Jacob et al., 2009, Yelagandula et al., 2014], TGS release was investigated in the diff t mutants. Using RT-qPCR, transcript levels of the 180bp centromeric repeats [Nagaki et al., 2003], 106B [Thompson et al., 1996] and Transcriptional Silent Information (TSI) [Steimer et al., 2000] pericentromeric repeats were quantified (Figure 3.10C & D). TGS as expected is alleviated in *ddm1-10* and *atxr5 atxr6* with the significant effect observed for TSI ( $p < 0.05$ , Figure 3.10D). Interestingly, in accordance with the increased number of nuclei with decondensed heterochromatin type, derepression was also observed for TSI, 106B and 180bp repeats in *wifi*, *sun1 sun4 sun5* and *kaku4-2* but not in *crwn1 crwn2* mutants (Figure 3.10C).

Taken together, the functional analysis of the evolutionary conserved LINC complex strengthens its implication in nuclear morphology but also revealed its contribution in chromocentre positioning, heterochromatin compaction and maintenance of TGS. Whether heterochromatin alteration is a consequence of nuclear morphology alteration or intrinsic function of the LINC complex remains speculative.



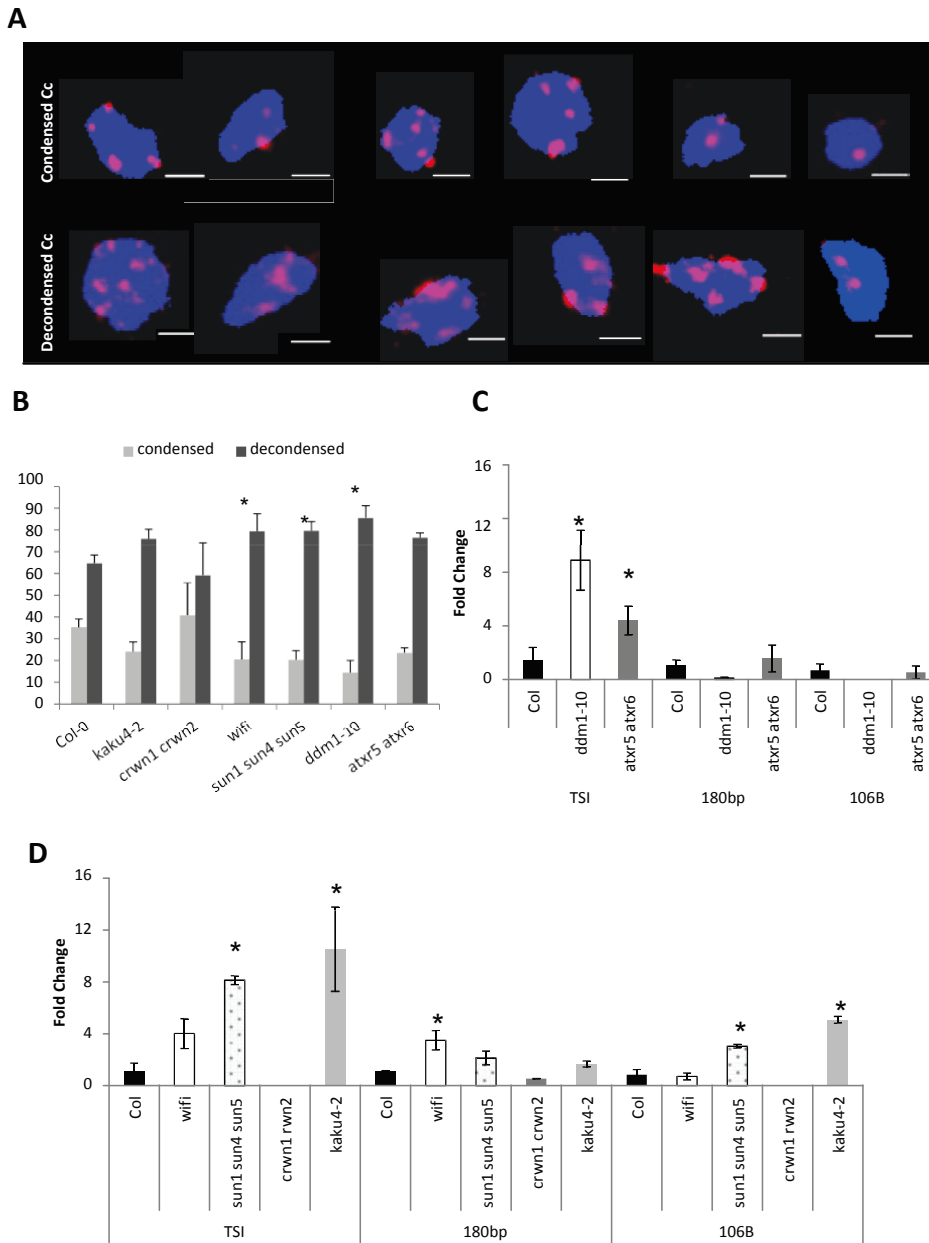


**Figure 3.10: Alteration of transcriptional repression of heterochromatic markers in mutant backgrounds.** **A)** Representative nuclei shown as maximal z projection collected from 3D-FISH experiments on nuclei counterstained with Hoechst (blue) of cotyledon epidermis using a fluorescent probe against 180bp satellite repeats (red). **B)** Quantification of condensed and decondensed 180bp hybridisation signals recorded by 3D-FISH obtained from 4 independent cotyledons. Average  $\pm$  SEM. Number of nuclei ranging from  $n = 60$  to  $100$  are available in Appendix Table B.8. **C & D)** Transcription level of TSI, 106B and 180bp scored by RT-qPCR. Histograms show means of transcript level  $\pm$  SEM obtained for two independent PCR amplifications of three biological replicates. The y axis shows the fold change relative to WT (WT set to 1) after normalisation to expression of *At2g28390* (*AtSAND*). (\*:  $p \leq 0.05$ ).

### 3.5 Conclusion

Here 3D imaging methods have been used to investigate nuclear morphology and chromatin organisation in interphase nuclei of the model plant *A. thaliana* in chromatin organisation (*ddm1-10*, *atxr5 atxr6*, *asf1a asf1b*, *asf1a*, *asf1b*, *atrx-1* and *atrx-2*) or NE mutants (*wifi*, *wit1 wit2*, *wifi*, *wip1 wip2 wip3*, *kaku4-2* and *crwn1 crwn2*). These NE genes have been shown to be involved in the regulation of nuclear shape and size (see Section 1.5) [Dittmer et al., 2007, Tamura and Hara-Nishimura, 2011, Janski et al., 2012, Zhou et al., 2012, Goto et al., 2014]. 3D imaging analysis of these mutants makes it possible to test whether disturbing the organisation of the NE can disturb chromatin organisation. Furthermore the inclusion of chromatin mutants which change chromatin organisation permits testing of the reverse- whether chromatin organisation affects organisation of the nuclear envelope [Hirochika et al., 2000, Fransz et al., 2003, Probst et al., 2003, Jacob et al., 2009]. The experiment was conducted in three cell types from the cotyledon and root hair epidermis (see Section 3.3). A survey of diff t RNA-seq data shows that all the genes analysed are expressed in the tissues of interest (Figure 3.4).

In *A. thaliana* the nucleus was not a homogenous structure and nuclear morphological variation was observed in diff t tissues [Traas et al., 1998, Qian et al., 2009, van Zanten et al., 2011]. In order to establish a baseline of this variability, 3D Col-0 nuclei were analysed with *NucleusJ*. The analysis by PCA of the nuclear parameters obtained, allows the clustering of GC, PC and RC nuclei, the most important parameters for this clustering are the sphericity, elongation and nuclear volume for the morphological parameters (Figure 3.2). Chromatin parameters are also important for this clustering as are the number of the chromocentres and their distance to the NE, and the RHV (Figure 3.2). Finally GC, PC and RC can be detected as a function of their shape and quantity of heterochromatin (Figure 3.2). The analysis of the distribution of the radial distance of the chromocentre to nuclear periphery, suggests a preferential positioning close to the nuclear periphery and by deduction also suggests the nucleolus is close to the nuclear periphery in interphase nuclei. The distance of the chromocentre to the NE periphery was greater in the larger nuclei of PC and RC in comparison to the GC (Figure 3.3). Finally the chromocentres are not organised randomly in the nucleus, and are positioned at a small distance from the nuclear periphery.

The analysis of the morphological impact of the mutants of the NE and putative lamina show similar patterns of morphological disruption for all the cell types. The

nucleus of these mutants are smaller and more spherical than the Col-o nucleus. These characteristics are found to be stronger in putative nuclear lamina mutants (*crwn1 crwn2* and *kaku4-2*). The chromatin organisation parameters of these mutants are more impacted in GC in comparison the two other cell types. It may be that the polyploidisation of the nucleus tends to decrease the impact of mutations on the chromatin parameters computed. No specific impact of the LINC complex or lamin-like mutants was detected on these parameters. However, the *crwn1 crwn2* mutant was the only one where an effect was observed for all the cell types studied, with a global disruption of chromatin organisation (chromocentre volume mean or total, position, and RHV). The analysis of the same mutants with FISH 2D or 3D and RT-qPCR shows a strong similarity between mutants of the LINC complex, with an increase of chromocentre decompactions linked with the reactivation of silenced transposable elements (Figure 3.9, 3.10). For putative nuclear lamina functional homologues, the two show the inverse defect with an increase of condensed chromocentre correlated with a decrease of the expression of the transposable element in *crwn1 crwn2*, and the inverse for *kaku4-2* with an decreased of the condensed chromocentre correlated with an increase of expression of silenced targets. The morphological changes in the NE and for the lamin-like mutants may have been due to a loss of specific protein interactions and physical constraint between nucleoskeleton and cytoskeleton and that can lead to chromatin disorganisation. Alternatively, chromatin organisation involves adaptation of nuclear morphology.

In contrast with the NE/nuclear lamina-like mutants, only few changes were detected for chromatin and histone chaperone mutants on nuclear morphology parameters (see Appendix Figure B.3 and B.2). Histone chaperone shows a global change in chromatin organisation with a decrease in the RHV, the mean size of the chromocentre and of the total volume of the chromocentre and increase of the number of chromocentres (Figure 3.8 and see Appendix B.2). *atr1-1* and *atr1-2* are two alleles of the same genes, and globally show the same pattern of the parameters, but for *atr1-2* differences are less pronounced, this is consistent with the fact that this allele of *ATRX* is leaky and *atr1-1* is a complete knock-out. This result shows the capacity of *NucleusJ* to phenotype two different alleles of the same gene. The condensation of the chromocentres of the histone chaperone mutants show decrease in the number of the nuclei condensed for *asf1ab* and *atr1-1*, but correlate only for *asf1ab* at a change in the expression level of TSI.

Chromatin mutants *ddm1-10* and *atr5 atr6* mutants have different effects on chromatin parameters, the first does not differ from Col-o (Figure 3.8 and see Appendix B.2), and the second mutant possesses a strong phenotype in GC and PC

with an increase of the RHV, of the number of chromocentre and in total volume of chromocentre, but the size of individual chromocentre decreases (Figure 3.8 and see Appendix B.2). However, both show an increase of nuclei which possess decondensed chromocentres, and a reactivation of the TSI transposable element.

# Chapter 4

## Exploring the proteins of the plant nuclear envelope

### 4.1 Introduction

Following the first description of classical SUN-domain proteins in plants, groups associated with the International Plant Nucleus Consortium (<http://bms.brookes.ac.uk/ipnc>) and others have made significant progress in describing novel plant nuclear envelope proteins [Parry, 2015, Tamura et al., 2015, Zhou et al., 2015a]. In *A. thaliana*, these include novel Cter-SUN [Graumann et al., 2010, Graumann and Evans, 2010, Oda and Fukuda, 2011] and mid-SUN domain proteins [Graumann et al., 2014], according to the position of the mid-SUN domain; KASH domain proteins (WIPs, SINEs and TIK) [Zhou et al., 2012, Zhou and Meier, 2014, Graumann et al., 2014] and plant proteins proposed to form the nuclear lamina (CRWNs, KAKU4 and NEAPs) [Dittmer et al., 2007, Wang et al., 2013, Goto et al., 2014, Pawar, 2015]. All these proteins constitute or interact with the LINC complex and have been described in *A. thaliana*. Sequence data now available for many other species permit comparison of components of the LINC complex between species such as rice, maize, with the well characterised components of the *A. thaliana* NE. While several functional analyses have already been performed in *A. thaliana* it remains challenging because of gene redundancy due to gene or whole-genome duplication (WGD) creating several paralogues [Gaut and Ross-Ibarra, 2008]. Three mechanisms explain the increased size and the complexity of plant genome: whole genome duplication, tandem duplication and transposable elements [Gaut and Ross-Ibarra, 2008]. Hence it is necessary to explore the pattern of paralogues within the gene families in order to better understand their interactions.

One way to explore gene redundancy is to retrace the history of genome dynamics starting from the most ancestral species. One of the candidate species to achieve this aim is *Amborella trichopoda* (*A. trichopoda*), a dioecious New Caledonian shrub, as its genome has been recently sequenced [Project et al., 2013]. *A. trichopoda* shows very limited evidence of transposable element activity, has not undergone a recent whole genome duplication and is therefore, in evolutionary terms, suggested to be the most primitive basal angiosperm described [Project et al., 2013]. Analysing genes encoding nuclear envelope proteins in *A. trichopoda* and in other species (Table 4.1) provides opportunities to explore protein interaction networks function as well as to speculate on origins. Including *A. trichopoda*, the moss *Physcomitrella patens*, the lycophytes *Selaginella moellendorffii* and single cell algae with eudicots and monocots in the phylogenetic analysis allows assessment of nuclear envelope organisation in less complex genomes of photosynthetic organisms. This study will help to address questions about the minimal/initial functional LINC complex and the lamin-like proteins, and retrace their evolutionary history to more complex species.

Whole-genome duplication has long been recognised as an important evolutionary force in animals, plants and fungi. Following WGD, gene loss can occur restoring the diploid state for each duplicated locus. Previous analyses of plant genomes have shown that all seed plants share an ancient WGD called zeta (Figure 4.1) [Jiao et al., 2011]. A second WGD called epsilon has been detected shortly before the diversification of all living angiosperms. These two WGDs seem to play a crucial role in the origin and rapid diversification of the angiosperms [Jiao et al., 2011]. Finally, a gamma WGD occurred after the eudicot/monocot diversification (Figure 4.1), followed by several partial or complete duplication events during evolution as indicated on Figure 4.1. Species included in this study of the plant nuclear envelope proteins have been chosen to relate to the evolutionary history of plants, and to include the known WGD (Table 4.1).

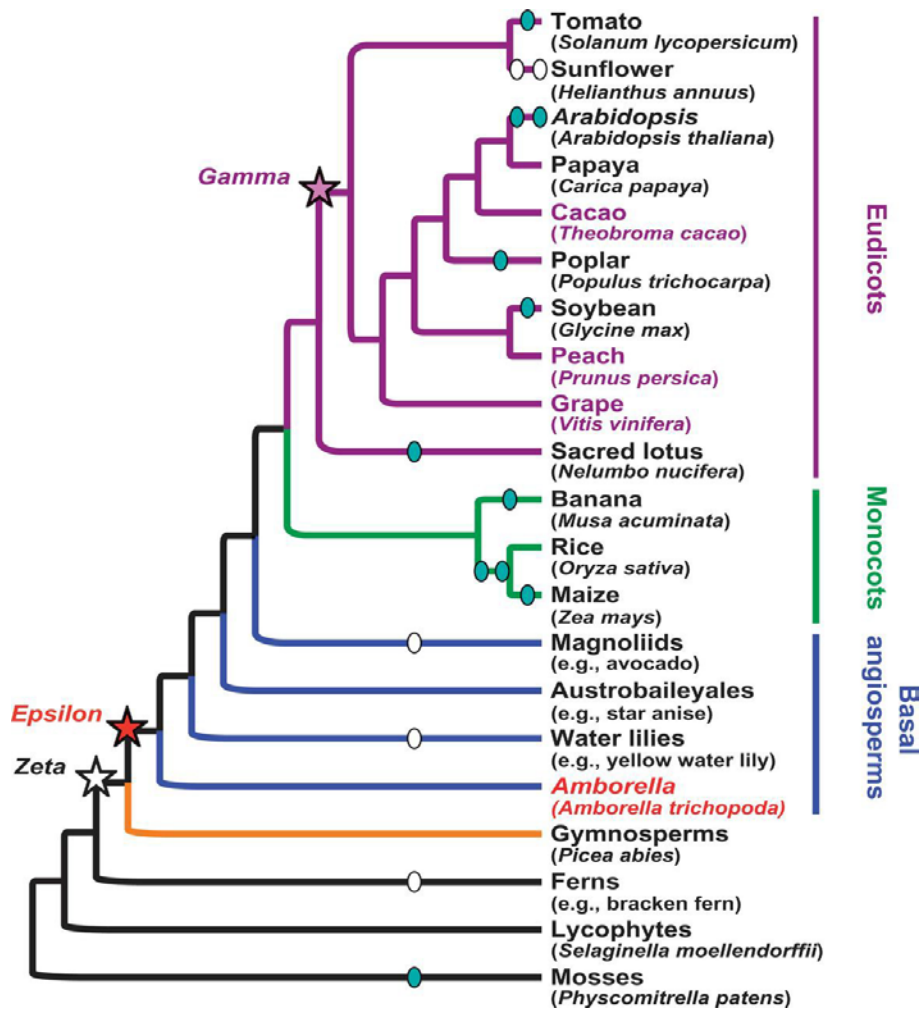


**Figure 4.1: Overview of plant phylogeny.** Representatives with sequenced genomes are shown for most lineages (scientific names in parentheses); basal angiosperms and non-flowering plant lineages are indicated by their larger group names. Hypothesised polyploidy events in land plant evolution are overlaid on the phylogeny with symbols. The red star indicates the common ancestor of angiosperms and the evolutionary timing of the epsilon WGD [Jiao et al., 2011]. The evolutionary timing of zeta [Jiao et al., 2011] and gamma [Jaillon et al., 2007, Jiao et al., 2012, Ming et al., 2013] polyploidy events are shown with empty and purple stars, respectively. Additional polyploidy events are indicated with ellipses. Symbols for events supported by genome-scale gene organisation analyses are filled, whereas those supported only with frequency distributions of paralogous gene pairs or phylogenomic analyses are empty. (Source: [Project et al., 2013])

Table 4-1: **Species for the phylogenetic analysis of the LINC complex proteins.** The species abbreviation is used in all the following phylogenetic and expression analyses (Figures 4-2, 4-3, 4-3, 4-4, 4-5, 4-6, 4-7, 4-8 and in Appendix C.1)

Species	Abbreviation	Group	Phylogeny	RNAseq	Genome	Reference
<i>Arabidopsis thaliana</i>	At	eudicots	yes	yes	150Mb	[Initiative, 2000].
<i>Arabidopsis lyrata</i>	Aly	eudicots	yes	yes	206.7Mb	[Hu et al., 2011].
<i>Brassica rapa</i>	Bra	eudicots	yes	no	283.8Mb	[rapa Genome Sequencing Project Consortium, 2011].
<i>Prunus persica</i>	Ppe	eudicots	yes	no	224.6Mb	[The International Peach Genome Initiative et al., 2013].
<i>Glycine max</i>	Gma	eudicots	yes	yes	950Mb	[Schmutz et al., 2010].
<i>Carica papaya</i>	Cpa	eudicots	yes	no	372Mb	[Ming et al., 2008].
<i>Theobroma cacao</i>	Tca	eudicots	yes	no	326.9Mb	[Argout et al., 2011].
<i>Nelumbo nucifera</i>	Nnu	eudicots	yes	no	804 Mb	[Ming et al., 2013].
<i>Vitis vinifera</i>	Vvi	eudicots	yes	yes	487Mb	[Jaillon et al., 2007].
<i>Populus trichocarpa</i>	Ptr	eudicots	yes	no	485Mb	[Tuskan et al., 2006].
<i>Solanum lycopersicum</i>	Sly	eudicots	yes	yes	900Mb	[Consortium, 2012].
<i>Zea mays</i>	Zma	monocots	yes	yes	2.3Gb	[Schnable et al., 2009].
<i>Oryza sativa</i>	Osa	monocots	yes	yes	372Mb	[International Rice Genome Sequencing Project, 2005].
<i>Musa acuminata</i>	Mac	monocots	yes	no	472Mb	[Droc et al., 2013]
<i>Amborella trichopoda</i>	Atr	basal angiosperm	yes	yes	706Mb	[Project et al., 2013].
<i>Picea abies</i>	Pab	gymnosper	yes	no	19.6Gb	[Nystedt et al., 2013].
<i>Physcomitrella patens</i>	Ppa	moss	yes	yes	473Mb	[Rensing et al., 2008].
<i>Selaginella moellendorffii</i>	Smo	lycophytes	yes	yes	212.5Mb	[Banks et al., 2011].
<i>Chlamydomonas reinhardtii</i>	Cre	single cell green alga	yes	no	473Mb	[Merchant et al., 2007].
<i>Ostreococcus lucimarinus</i>	Olu	single cell green alga	yes	no	13.2 Mb	[Palenik et al., 2007].



## **4.2 Aim**

The aim of this work was to use genomic and available RNA-seq data to explore the evolution of the NE proteins in uni and multicellular plants and to provide evidence for the composition of the simplest functional NE. Expression of LINC components and the lamins-like genes was explored using RNA-seq data to demonstrate gene activity and when possible tissue specific expression. Finally, this study is a prerequisite for mutant analyses and other functional studies by identifying potential redundancy and specialised functions.

## 4.3 Material and methods

### 4.3.1 Homologous LINC complex and lamin-like protein detection

#### KASH protein homologue detection

KASH domain protein homologues have previously been identified using the program Dory [Zhou and Meier, 2014]. This program is a java tool, which detects the KASH domain. Here a new Perl script based on the same strategy as Dory has been developed but applied to proteomic data. The program tests the presence of the trans-membrane (TM) domain and four specific amino acids at the C-terminal which are characteristic for KASH proteins. The position of the TM domain is variable and the script searches this TM domain up to 40 amino acids away from the KASH-specific C-terminal motif detected in *A. thaliana* (VIPT or VVPT or AVPT or PLPT or TVPT or LVPT or PPPS) [Graumann et al., 2014, Zhou et al., 2015a]. The identification of the TM domain is based on a matrix of the Kyte-Doolittle, a hydrophobicity scale which gives a score for each amino acid [Kyte and Doolittle, 1982]. Only proteins which possess a TM domain and the four KASH specific amino acids in the C-terminus of the protein were selected.

#### Detection of the LINC complex and lamin-like protein homologues

The Basic Local Alignment Search Tool protein (BLASTp) was used with default parameters. The best hits for the BLASTp results were retained and used for the following phylogenetic analysis [Altschul et al., 1990]. The proteome of each species was used as reference for the BLASTp (Table 4.1), and the protein sequences of the LINC complex as well as the putative lamina of *A. thaliana* as queries (Table 4.2).

Table 4.2: Reference genes.

Name	Description	Localisation	IdGene	Reference
AtSINE1	KASH	ONM	AT1G54385	[Zhou et al., 2015a]
AtSINE2	KASH	ONM	AT3G03970	[Zhou et al., 2015a]
AtSINE3	KASH	ONM	AT3G06600	[Zhou et al., 2015a]
AtSINE4	KASH	ONM	AT4G24950	[Zhou et al., 2015a]
AtTIK	KASH	ONM	AT5G44920	[Graumann et al., 2014]
AtWIP1	KASH	ONM	AT4G26455	[Zhou et al., 2012]
AtWIP2	KASH	ONM	AT5G56210	[Zhou et al., 2012]
AtWIP3	KASH	ONM	AT3G13360	[Zhou et al., 2012]
AtCRWN1	Lamin-like	nucleoplasm-NE	AT1G67230	[Dittmer et al., 2007]
AtCRWN2	Lamin-like	nucleoplasm-NE	AT1G13220	[Dittmer et al., 2007]
AtCRWN3	Lamin-like	nucleoplasm-NE	AT1G68790	[Dittmer et al., 2007]
AtCRWN4	Lamin-like	nucleoplasm-NE	AT5G65770	[Dittmer et al., 2007]
AtKAKU4	Lamin-like	nucleoplasm-NE	AT4G31430	[Pawar, 2015]
AtNEAP1	Lamin-like	nucleoplasm-NE	AT3G05830	[Pawar, 2015]
AtNEAP2	Lamin-like	nucleoplasm-NE	AT5G26770	[Pawar, 2015]
AtNEAP3	Lamin-like	nucleoplasm-NE	AT1G09470	[Pawar, 2015]
AtNEAP4	Lamin-like	nucleoplasm-NE	AT1G09483	[Pawar, 2015]
AtSUN1	Cter-SUN	INM	AT5G04990	[Graumann et al., 2010]
AtSUN2	Cter-SUN	INM	AT3G10730	[Graumann et al., 2010]
AtSUN3	Mid-SUN	INM	AT1G22882	[Graumann et al., 2014]
AtSUN4	Mid-SUN	INM	AT1G71360	[Graumann et al., 2014]
AtSUN5	Mid-SUN	INM	AT4G23950	[Graumann et al., 2014]

### 4.3.2 Phylogenetic reconstruction

Selected sequences were first aligned with MUSCLE a multiple sequence alignment tool [Edgar, 2004], using default parameters. Then the alignment was refined using Gblocks [Talavera and Castresana, 2007]. FastTree was then applied with default parameters, for the construction of the phylogenetic tree [Price et al., 2010]. Fast-Tree infers approximately-maximum-likelihood phylogenetic trees from alignments. Finally, phylogenetic trees were drawn using the Interactive Tree Of Life ITOL [Letunic and Bork, 2011].

### 4.3.3 RNA sequencing data

Data used for the RNA-seq analysis were obtained from the NCBI (site <http://www.ncbi.nlm.nih.gov/geo/browse/>) or from the Amborella Genome Database, respectively (site <http://amborella.huck.psu.edu/>). Five different tissues (leaves, roots, flowers, bud flowers, and seeds/siliques) as well as total seedling were chosen for the analysis of the expression patterns of the genes of interest (Table 4.3). The expression was analysed for ten species (Table 4.1).

**Table 4.3: SRA or fastq files used for RNA sequencing analysis.** All files named SR-Rxxxxx were downloaded from site <http://www.ncbi.nlm.nih.gov/geo/browse/> and the data for *A. trichopoda* are available at site <http://amborella.huck.psu.edu/>.

	Seedling	Leaf	Root	Flower	Flower bud	Seed/Silique
<i>Arabidopsis thaliana</i>	SRR346552 SRR346553	SRR1159821 SRR1159827 SRR1159831 SRR1159837 SRR1030234 SRR1030235 SRR656216	SRR656215	SRR656217	SRR314815 SRR800753 SRR800754	SRR656218
<i>Arabidopsis lyrata</i>	na	SRR2033954 SRR2033955 SRR2039795 SRR2039796	na	na	SRR800644 SRR800645	na
<i>Solanum lycopersicum</i>	SRR786602 SRR786603 SRR786605 SRR786607	SRR404309 SRR404310	SRR404311 SRR404312	SRR404313 SRR404314	SRR404315 SRR404316	na
<i>Vitis vinifera</i>	na	SRR2845695	na	na	na	na
<i>Zea mays</i>	SRR1198847	SRR029177 SRR029178 SRR029179 SRR029180 SRR029181 SRR029182 SRR029183 SRR029184 SRR1124756 SRR2080978	SRR640264	SRR1017566 SRR1017567 SRR1017568	na	na
<i>Oryza sativa</i>	SRR358791 SRR358792 SRR358793 SRR358794	SRR1213692 SRR1213693 SRR1761530	SRR1213694 SRR1213695	SRR1213691	SRR1213690	SRR1213697
<i>Amborella trichopoda</i>	AmborellaWPN-1_s_7_1 AmborellaWPN-1_s_7_2 AmborellaWPN-2_s_8_1 AmborellaWPN-2_s_8_2	na	na	2006-2975_flower_R1 2006-2975_flower_R2 2008-1967_flower_R1 2008-1967_flower_R2 2008-1968_flower_R1 2008-1968_flower_R2	2006-2975_bud_R1 2006-2975_bud_R2 2008-1967_bud_R1 2008-1967_bud_R2 2008-1968_bud_R1 2008-1968_bud_R2	na
<i>Physcomitrella patens</i>	SRR060806	na	SRR072918	na	na	na
<i>Selaginella moellendorffii</i>	na	SRR042532	na	na	na	na

#### 4.3.4 RNA sequencing processing and analysis

The data was downloaded using the File Transfer Protocol (ftp) from the NCBI database as .sra fi Then *fastq dump* tool was used to decompress the fi and obtained the fastq fi Reads of the fastq fi were trimmed for quality using *fastq quality trimmer* with a minimal quality score for the sequence of 20. Trimmed reads were then mapped to the genome of interest and its annotation fi (.gff3) using the same programs and parameters explain in the Chapter 3 Section 3.3.6.

For each species, *SAND* gene was used as reference gene and the expression value of the gene of interest was normalised by the expression value of the *SAND* gene of

all species (Table 4.4).

Table 4.4: Accession numbers of the SAND genes in all the species of interest.

<b>Gene id</b>	<b>Species</b>
AT2G28390	<i>Arabidopsis thaliana</i>
481666.v1	<i>Arabidopsis lyrata</i>
Solyco3g115810.2	<i>Solanum lycopersicum</i>
Glyma.12G172200	<i>Glycine max</i>
GSVIVT01025191001	<i>Vitis vinifera</i>
LOC Os01g74460	<i>Oryza sativa</i>
GRMZM2G179732.v6a	<i>Zea mays</i>
evm_27.TU.AmTr v1.0 scaffold00145.30	<i>Amborella trichopoda</i>
Phpat.010G053700.v3.0	<i>Physcomitrella patens</i>
438801.v1	<i>Selaginella moellendorffii</i>

## 4.4 Results and discussion

### 4.4.1 KASH protein homologues

For the detection of the KASH domain protein homologues, two strategies were used. The first was a BLASTp analysis based on the *A. thaliana* KASH proteins (Table 4.2). This analysis permitted a first detection of KASH protein homologues in all the organisms studied, except for the unicellular algae where no KASH protein was detected (see Appendix Tables C.6, C.5 and C.7). As previously described (Chapter 1 Section 1.4), the KASH domain proteins have been divided into the following groups; SINEs, WIPs and TIKs.

Using this method, 32 SINE homologues were found (see Appendix Table C.5), whereas WIP (see Appendix Table C.6) and TIK proteins (see Appendix Table C.7) were much less common and were found mainly in eudicots. An exception is *Brassicaceae*, where several WIPs (3 in *A. lyrata*, 4 in *Brassica rapa*) and TIKs (2 in *A. lyrata* and 1 in *Brassica rapa*) were identified, these two types of protein are detected in *Glycine max* (2 WIP, 1 TIK), *Prunus persica* (1 TIK), *Carica papaya* (1 WIP), *Musa acuminata* (1 WIP), *A. trichopoda* (1 TIK) and the gymnosperm *Picea abies* (1 TIK) (Table 4.5). The SINE proteins are well conserved across monocots and eudicots, while WIPs and SINEs were not detected in *Zea mays* and *Oryza sativa*, although one WIP was detected in the monocot *Musa acuminata*.

KASH proteins are known to be diverse in sequence and structure [Zhou and Meier, 2014] but possess a conserved C-terminal region with a TM domain and a conserved motif of four amino acids at the extreme C-terminus which interacts with the SUN domain (Chapter 1 Section 1.4). As an alternative to detect KASH proteins, a script was developed to detect proteins with the TM domain and C-terminal motif modelled using the motif detected in *A. thaliana* (see Section 4.3.1). The aim of this script was to increase the number of homologues of KASH proteins detected by BLASTp. This script analysed the C-terminal region of each protein present in the proteomic data. The script was tested first on the *A. thaliana* proteome in which it detected all the KASH proteins described so far. This script was then used on all the proteomes of interest, and the proteins identified were aligned to generate a phylogenetic tree which allows the clustering of similar proteins. The script detected several proteins already identified using BLASTp, validating this approach.

Six KASH protein clusters were revealed (Appendix Figure C.1). One cluster

includes WIP proteins detected in the monocotyledons and the basal angiosperms (Table 4.5), as well as seven new putative WIP proteins to those detected previously by BLASTp. For SINE proteins, three clusters were detected, one for each cluster (SINE1/2, SINE3 and SINE4) which added respectively two, six and twelve SINE proteins to those already identified by BLASTp. The high number of proteins in the SINE3 and SINE4 cluster found only by the script and not by BLASTp was due to weak conservation of these proteins. One much smaller cluster includes TIK but few proteins belong to it and only four proteins were added to the TIK putative homologues already detected. The last cluster detected, which has a low sequence similarity, could not be attached to specific KASH domain proteins already known in *A. thaliana*, was not used in the following analysis.

To confirm that the TM domain and C-terminal motif are present in the proteins identified a protein alignment was carried out. This analysis eliminated all the additional homologues detected for TIK; these having either the TIR domain or the C-terminal TM domain and motif but not both. The data suggests that the TIK protein described by Graumann et al. (2014) as encoded by the *A. thaliana* genome is not present, or difficult to detect in other genomes. Hence, this protein may be unique to *A. thaliana*.

The three WIP proteins in *A. thaliana* showed a similar cytoplasmic domain at the N-terminus, with AtWIP1 and AtWIP2 featuring three coiled coil domains but AtWIP3 featuring only one. The C-terminal region is well conserved and the coiled coil domains aligned correctly, with all proteins detected as homologues having a C-terminal TM domain and KASH motif, except AlyWIP1, which lacks homology at the C-terminal region but is well conserved at the N-terminus.

The SINE gene family comprises four genes in *A. thaliana*. The alignment of these four proteins shows similarity between AtSINE1 and AtSINE2 and between AtSINE3 and AtSINE4. AtSINE1 and AtSINE2 are characterised by the presence of an Armadillo repeat domain near the N-terminus. AtSINE3 and AtSINE4 do not possess such a domain but feature a cytoplasmic domain and a typical KASH TM domain and the amino acid motif at the C-terminus [Zhou et al., 2015a]. The new Perl script identified only two sequences in the SINE1/SINE2 group not detected by the BLASTp analysis. The SINE3/SINE4 cluster contains 17 proteins, which possess the typical C-terminus of the KASH proteins. However this group is heterogeneous due to the absence of well conserved domains in the N-terminal region and

**Table 4.5: KASH homologous proteins.** The number of homologues of KASH proteins detected by each method is presented for each species, along with the number detected by both methods and by the combination of both methods. The "Putative homologues detected" column is the number of putative KASH proteins confirmed by domain verification.

Species	BLASTp results	Script results	Results share	Putative homologues Detected
<i>Arabidopsis thaliana</i>		SINE: 4 WIP: 3 TIK: 1		SINE: 4 WIP: 3 TIK: 1
<i>Arabidopsis lyrata</i>	SINE: 3 WIP: 3 TIK: 2	SINE: 3 WIP: 1 TIK: 1	SINE: 2 WIP: 1 TIK: 0	SINE: 4 WIP: 3 TIK: 3
<i>Brassica rapa</i>	SINE: 4 WIP: 4 TIK: 1	SINE: 7 WIP: 3 TIK: 0	SINE: 4 WIP: 3 TIK: 0	SINE: 7 WIP: 3 TIK: 1
<i>Prunus persica</i>	SINE: 1 WIP: 0 TIK: 1	SINE: 3 WIP: 1 TIK: 0 Other : 2	SINE: 0 WIP: 0 TIK: 0	SINE: 4 WIP: 1 TIK: 1
<i>Glycine max</i>	SINE: 4 WIP: 2 TIK: 1	SINE: 5 WIP: 2 TIK: 1	SINE: 4 WIP: 1 TIK: 0	SINE: 5 WIP: 3 TIK: 2
<i>Carica papaya</i>	SINE: 1 WIP: 1 TIK: 0	SINE: 2 WIP: 1 TIK: 0 Other : 1	SINE: 1 WIP: 1 TIK: 0	SINE: 2 WIP: 1 TIK: 1
<i>Theobroma cacao</i>	SINE: 1 WIP: 1 TIK: 1	SINE: 1 WIP: 1 TIK: 0 Other : 1	SINE: 1 WIP: 1 TIK: 0	SINE: 1 WIP: 1 TIK: 1
<i>Nelumbo nucifera</i>	SINE: 2 WIP: 1 TIK: 1	SINE: 2 WIP: 0 TIK: 0	SINE: 2 WIP: 0 TIK: 0	SINE: 2 WIP: 1 TIK: 1
<i>Vitis vinifera</i>	SINE: 1 WIP: 1 TIK: 1	SINE: 1 WIP: 1 TIK: 0	SINE: 1 WIP: 1 TIK: 0	SINE: 1 WIP: 1 TIK: 1
<i>Populus trichocarpa</i>	SINE: 2 WIP: 2 TIK: 1	SINE: 2 WIP: 1 TIK: 1	SINE: 0 WIP: 1 TIK: 0	SINE: 4 WIP: 2 TIK: 2
<i>Solanum lycopersicum</i>	SINE: 1 WIP: 0 TIK: 1	SINE: 4 WIP: 1 TIK: 0 Other : 1	SINE: 1 WIP: 0 TIK: 0	SINE: 4 WIP: 1 TIK: 1
<i>Zea mays</i>	SINE: 1 WIP: 0 TIK: 0	SINE: 4 WIP: 2 TIK: 0 Other : 1	SINE: 1 WIP: 0 TIK: 0	SINE: 4 WIP: 2 TIK: 0
<i>Oryza sativa</i>	SINE: 1 WIP: 0 TIK: 0	SINE: 4 WIP: 1 TIK: 0	SINE: 1 WIP: 0 TIK: 0	SINE: 4 WIP: 1 TIK: 0
<i>Musa acuminata</i>	SINE: 2 WIP: 1 TIK: 0	SINE: 1 WIP: 0 TIK: 0	SINE: 1 WIP: 0 TIK: 0	SINE: 2 WIP: 1 TIK: 0
<i>Amborella trichopoda</i>	SINE: 1 WIP: 0 TIK: 1	SINE: 1 WIP: 1 TIK: 1 Other : 1	SINE: 1 WIP: 0 TIK: 0	SINE: 1 WIP: 1 TIK: 2
<i>Picea abies</i>	SINE: 3 WIP: 0 TIK: 1	SINE: 1 WIP: 0 TIK: 0	SINE: 1 WIP: 0 TIK: 0	SINE: 3 WIP: 0 TIK: 1
<i>Physcomitrella patens</i>	SINE: 3 WIP: 0 TIK: 0	SINE: 6 WIP: 0 TIK: 0 Other : 1	SINE: 2 WIP: 0 TIK: 0	SINE: 7 WIP: 0 TIK: 0
<i>Selaginella moellendorffii</i>	SINE: 1 WIP: 0 TIK: 0	SINE: 0 WIP: 0 TIK: 0 Other : 1	SINE: 0 WIP: 0 TIK: 0	SINE: 1 WIP: 0 TIK: 0
<i>Chlamydomonas reinhardtii</i>		0	0	0
<i>Ostreococcus lucimarinus</i>		0	0	0



few proteins in this cluster are detected by BLASTp (3 proteins), the majority only being detected by the script (13 proteins).

After deletion of sequences with the lowest similarity or without the conserved domain, SINE1/SINE2 proteins are present in all species except the unicellular algae and club moss, while SINE3/SINE4 display fewer protein homologues, and are not present in all species.

In summary, SINE especially the SINE1/SINE2 cluster and WIP proteins are detected in basal angiosperms whereas the TIK protein is detected only in *A. thaliana* (Table 4.6).

#### **4.4.2 Inner nuclear membrane proteins and lamin-like homologues detection**

##### **Cter-SUN and mid-SUN homologues**

The Cter-SUN and mid-SUN homologues were found in species studied, though no Cter-SUN protein was detected for *Chlamydomonas reinhardtii* (4.6 and see Appendix Table C.9 and Table C.8). Thirty-three Cter-SUN and fifty mid-SUN homologues were found (Table 4.6, and also Appendix Table C.8 and C.9). The majority of the species possess at least two mid-SUN and one Cter-SUN proteins except for *Solanum lycopersicum*, *Picea abies*, and the two unicellular algae which have only one mid-SUN. These results are in good agreement with previous studies that have highlighted the conservation of both Cter- and mid-SUN proteins in most eukaryotes [Graumann et al., 2014]. Mid-SUN homologues and Cter-SUN were detected in all species suggesting that SUN emergence pre-dates the evolution of multicellularity (Figure 4.3 and Figure 4.2 and see Appendix Table C.9 and C.8).

##### **Putative nuclear lamina homologues**

Two protein families have been suggested to be components of the putative "lamina" in *A. thaliana*, CRWN and KAKU4 (Chapter 1 Section 1.4) and the new protein family NEAP discovered by the Evans and Graumann group is also proposed to be part of the plant lamina [Pawar, 2015]. These three components of the nuclear lamina structure are investigated in this section.

The NEAP proteins are characterised by a TM at the C-terminus, a functional NLS and extensive coiled coil domains [Pawar, 2015]. There are four NEAP genes in *A. thaliana*, and the analysis of the evolution rate shows an increased accumulation

of non-synonymous mutations in AtNEAP4 suggesting its evolution as a pseudogene. The three other NEAPs are localised inside the nucleus around the INM [Pawar, 2015]. The results of BLASTp show a conservation of NEAP1, NEAP2, and NEAP3 in gymnosperms and angiosperms and 28 proteins were detected (Table 4.6 and also Appendix Table C.3).

KAKU4 homologues are only detected in angiosperms. Only one KAKU4 homologue is detected in each species except for *Glycine max* and *Brassica rapa* (Table 4.6 and also Appendix Table C.4)).

The CRWN gene family, characterised by a NLS and extensive coiled coil domains has four members in *A. thaliana*. CRWN proteins were detected by BLASTp in all multicellular plants, and homologues have been detected in moss, club moss, gymnosperm and angiosperm. Ciska and Moreno Diaz de la Espina (2013) defined two groups of plant CRWNs. The first group combines AtCRWN1, AtCRWN2 and AtCRWN3, and the second group is made up of the homologues of AtCRWN4. This work was done with few species. For the present analysis, twenty species were included, adding more diversity. AtCRWN protein homologues were detected in all species except unicellular algae. At least two homologues were detected for each species except for *Selaginella moellendorffii* for which only one homologous protein is detected (Table 4.6 and Appendix Table C.2).

**Table 4.6: Sequence selected for the phylogenetic and expression analysis.** Each grey shading represent the plant lineage, from light grey to dark grey, respectively Eudicots, Monocots, Basal Angiosperms, Gymnosperm, Moss, Club Moss, Unicells Algae.

	WIP	TIK	SINE <sub>1 2</sub>	SINE <sub>3 4</sub>	Other KASH	Cter-SUN	Mid-SUN	CRWN	NEAP	KAKU <sub>4</sub>
<i>Arabidopsis thaliana</i>	3	1	2	2	0	2	3	4	4	1
<i>Arabidopsis lyrata</i>	3	0	3	2	2	3	3	2	3	1
<i>Brassica rapa</i>	3	0	3	3	3	2	4	5	4	2
<i>Prunus persica</i>	1	0	1	0	5	1	2	3	2	1
<i>Glycine max</i>	3	0	4	0	3	2	6	7	2	2
<i>Carica papaya</i>	1	0	1	0	2	1	3	3	1	1
<i>Theobroma cacao</i>	1	0	1	0	1	1	2	3	1	1
<i>Nelumbo nucifera</i>	1	0	2	0	0	1	2	3	2	1
<i>Vitis vinifera</i>	1	0	1	0	0	1	2	3	2	1
<i>Populus trichocarpa</i>	2	0	2	0	3	2	3	3	2	1
<i>Solanum lycopersicum</i>	1	0	1	0	5	1	1	3	1	1
<i>Zea mays</i>	2	0	2	0	6	2	2	2	2	0
<i>Oryza sativa</i>	1	0	2	0	4	2	2	2	1	0
<i>Musa acuminata</i>	1	0	2	0	0	3	2	4	2	1
<i>Amborella trichopoda</i>	1	0	1	0	3	1	2	2	1	0
<i>Picea abies</i>	0	0	3	0	0	2	1	2	2	0
<i>Physcomitrella patens</i>	0	0	2	0	5	2	2	2	0	0
<i>Selaginella moellendorffii</i>	0	0	0	0	1	4	6	1	0	0
<i>Chlamydomonas reinhardtii</i>	0	0	0	0	0	0	1	0	0	0
<i>Ostreococcus lucimarinus</i>	0	0	0	0	0	1	1	0	0	0

### 4.4.3 Phylogenetic analysis of the inner nuclear membrane proteins

Cter-SUNs are the classical "core" of the LINC complex. Their coding genes are expressed in all tissues. The monocots and the eudicots form two paraphyletic<sup>1</sup> groups, because the homologue detected for *Vitis vinifera* is more similar to the monocot Cter-SUN sequence. The *Brassicaceae* group made of *A. thaliana*, *A. lyrata* and *Brassica rapa* form a monophyletic<sup>2</sup> group and the duplication of the Cter-SUN gene seems to occur late during plant evolution because duplicated Cter-SUNs remain grouped within a given species (Figure 4.2). In some cases, one of the two Cter-SUNs is more strongly expressed in the seedling (e.g.: *AtSUN1* more strongly expressed than *AtSUN2*; *OsaSUN-a* more strongly expressed than *OsaSUN-b*) (Figure 4.2).

The expression data for different tissues shows a similar level of expression for all the tissue analysed in different species (see Appendix C.3). *A. trichopoda* encodes only one Cter-SUN that is highly expressed in all tissues. This suggests the simplest functional LINC complex may be based on a single Cter-SUN, and strengthens the suggestion that duplication of the Cter-SUN gene occurred after speciation.

One or two Cter-SUN proteins were identified in most plants, moss and club moss. In *A. thaliana*, the Cter-SUN proteins share almost the same activity and localisation [Graumann et al., 2010]. This is in contrast to mammals, where different Cter-SUN orthologues have clearly differentiated functions. It appears that the gene duplication resulting in these orthologues occurred earlier in the evolution of mammals with many species possessing them. One likely consequence is the lack of specificity of function of plant Cter-SUN homologues in contrast to mammals. For example, a disruption of a single SUN gene results in an infertility phenotype in animals [Ding et al., 2007], but in *A. thaliana*, a single Cter-SUN deletion does not affect meiosis or fertility whereas a double mutant *atsun1*, *atsun2* impacts fertility and cell division [Varas et al., 2015]. This result suggests a significant redundancy in Cter-SUN function in plants and that double knock-out or knock-down mutants are required for recognisable phenotypes to be obtained.

The mid-SUN homologous proteins of the of angiosperms in the tree are clustered in two groups, the SUN3/SUN4 homologues and the SUN5 homologues. In each mid-SUN homologous group, the basal angiosperm, monocots and eudicots form

---

<sup>1</sup>Paraphyletic group contains an ancestor but only some of its descendants

<sup>2</sup>Monophyletic group contains an ancestor and all of its descendants

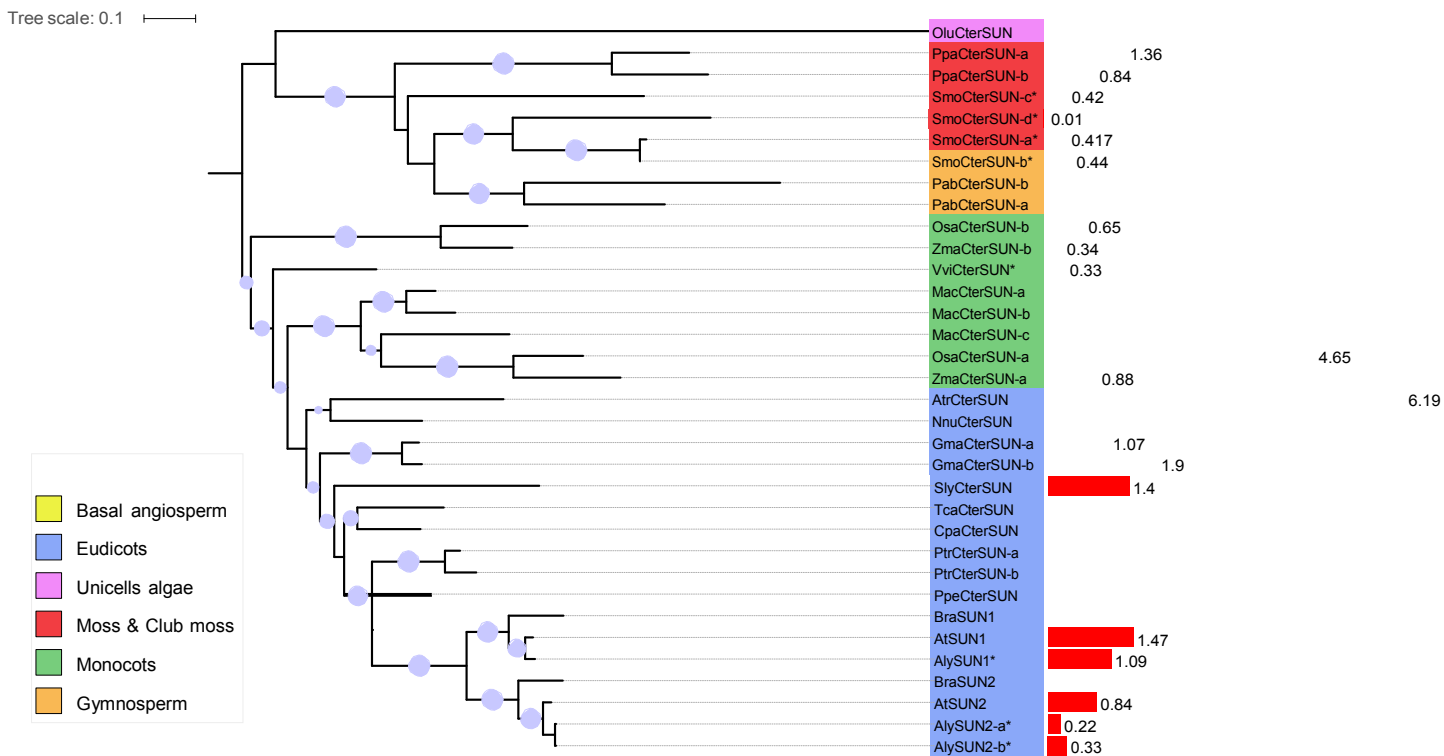


**Figure 4.2: Phylogenetic tree of Cter-SUN proteins.** **Left:** maximum likelihood tree of Cter-SUN protein homologues constructed from an alignment. Bootstrap values are represented by the diameter of the pale blue circle. Bootstrap value below 0.5 the bootstrap are not indicated. The colour of the label shows the lineage of the plant. The gene label is constructed with the three letters from the species name (see Table 4.1) and the gene name of the *A. thaliana* homologues. **Right:** red bar represents the value of the transcription level in seedlings, except for species indicated by \*, the RNA-seq data was obtained from leaf tissue (Table 4.3).

monophyletic groups. These results suggest that mid-SUN gene duplication occurred after speciation between angiosperms and gymnosperms (Figure 4.3). In all tissue analysed the *SUN3/SUN4* group tends to be more highly expressed than the *SUN5* group (see Appendix C.3).

It has been suggested that *AtSUN5* has a meiotic function [Graumann et al., 2014] and this is also true for maize with *ZmaSUN5* [Murphy et al., 2010]. *A. trichopoda* has two mid-SUN proteins, one *SUN3/SUN4* homologue and a *SUN5* homologue. In *A. trichopoda*, *AtrSUN3/SUN4* is more highly expressed than *AtrSUN5*. This suggests that the simplest LINC complex has two mid-SUNs with each a specific function as in *A. thaliana*.

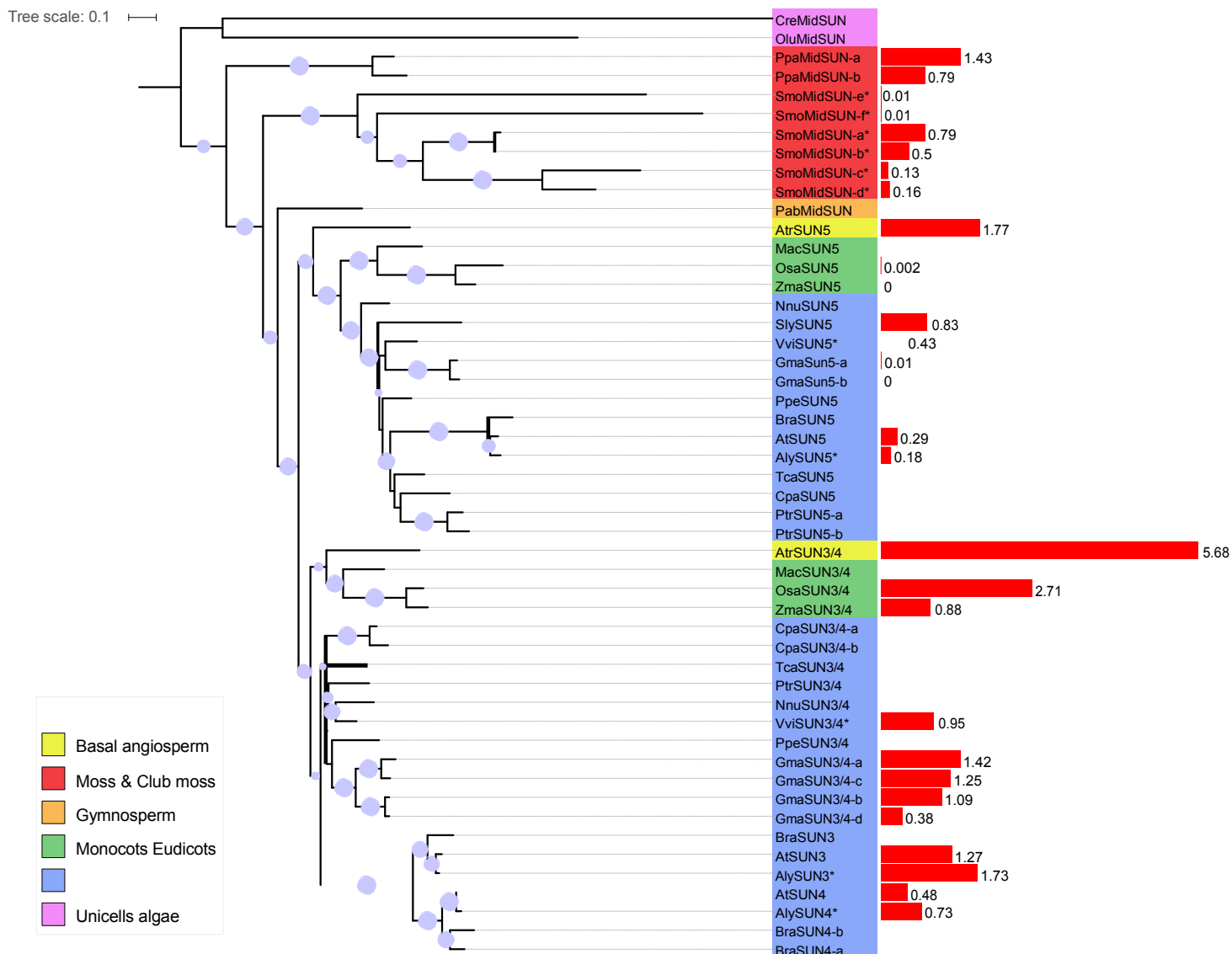


**Figure 4.3: Phylogenetic tree of Mid-SUN proteins.** **Left:** maximum likelihood tree of mid-SUN protein homologues constructed from an alignment. Bootstrap values are represented by the diameter of the pale blue circle. Bootstrap value below 0.5 the bootstrap are not indicated. The colour of the label shows the lineage of the plant. The gene label is constructed with the three letters from the species name (see Table 4.1) and the gene name of the *A. thaliana* homologues. **Right:** red bar represents the value of the transcription level in seedlings, except for species indicated by \*, the RNA-seq data was obtained from leaf tissue (Table 4.3).

#### 4.4.4 Phylogenetic analysis of the outer nuclear membrane proteins

The WIP protein family was the first KASH protein family detected in *A. thaliana*, and consists of three genes; these three KASH proteins interact with the SUN domain protein. Homologues of WIP proteins were not detected in unicellular algae, moss, club moss or gymnosperms (Table 4.6); suggesting that they are angiosperm specific

proteins. Within angiosperms one WIP homologue was detected for *A. trichopoda*. The monocots form a monophyletic group, with one protein for *Musa acuminata* and rice, and two for maize suggesting a gene duplication in maize (Figure 4.4).

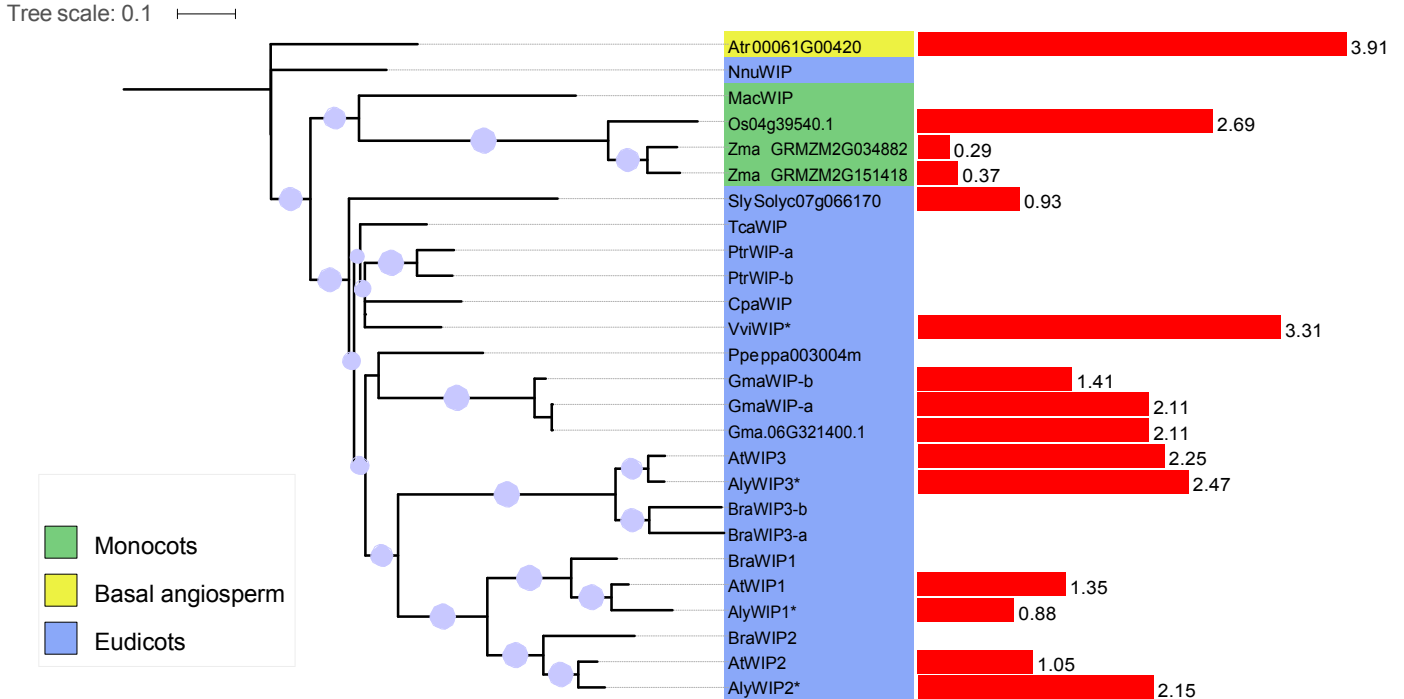


**Figure 4.4: Phylogenetic tree of WIP proteins.** **Left:** maximum likelihood tree of WIP protein homologues constructed from an alignment. Bootstrap values are represented by the diameter of the pale blue circle. Bootstrap value below 0.5 the bootstrap are not indicated. The colour of the label shows the lineage of the plant. The gene label is constructed with the three letters from the species name (see Table 4.1) and the gene name of the *A. thaliana* homologues. The labels without the homologue name were detected with the Perl script (eg: Atr 00061G00420). **Right:** red bar represents the value of the transcription level in seedlings, except for species indicated by \*, the RNA-seq data was obtained from leaf tissue (Table 4.3).

The eudicots form a paraphyletic group because the WIP homologue of *Nelumbo nucifera* diff from the WIPs of eudicots and monocots and is positioned outside of these two groups. The *Brassicaceae* form a monophyletic group (Figure 4.4). This suggests that an ancestral duplication in the *Brassicaceae* ancestor gave rise to WIP1/WIP2 and WIP3, and then WIP1 and WIP2 resulted from a more recent gene duplication. These results are consistent with Figure 4.1, in which two partial genome duplications were positioned on the *Brassicaceae* branch. Expression of the three genes is found in all the tissues analysed. In *A. thaliana* *AtWIP3* is more expressed than *AtWIP1* and *AtWIP2* in all tissues. This diff may be due to the redundancy in *AtWIP1* and *AtWIP2* activities, and in *A. trichopoda*, the *WIP* homologue is highly expressed (see Appendix C.3). This result suggests that *WIP3* can be the functional homologue of *A. trichopoda* WIP.

SINEs were characterised in *A. thaliana* [Zhou and Meier, 2014] in two groups SINE1/SINE2 and SINE3/SINE4. These proteins interact with the SUN domain proteins, and are positioned at the NE. *AtSINE1* is more expressed in guard cells, and the Armadillo domain of *AtSINE1* forms F-actin-associated filaments which are involved in nuclear positioning in the guard cell [Zhou and Meier, 2014]. *AtSINE2* seems to be involved in the immune response of leaves [Zhou and Meier, 2014]. No expression and activity information is available for *AtSINE3* and *AtSINE4*.

The phylogenetic analysis of SINE3 and SINE4 is not possible due to the low similarity between sequences and a lack of real conserved domains. Although SINE3 and SINE4 are detected in the *Brassicaceae* group, the other sequences are divergent. So these two proteins seem to be conserved in *Brassicaceae* but not in other species.

SINE1/SINE2 proteins were not found in unicellular algae and in club moss but, in contrast to WIPs, two and three SINE homologues were found in moss and gymnosperms, respectively. Of the three SINE1/SINE2 detected in the gymnosperms, two members are very similar (PabSINE-a and PabSINE-b). This can be due to recent gene duplication, or an error in the protein prediction in the proteome data (Figure 4.5). The angiosperms form a monophyletic group (Figure 4.5) and one SINE1/SINE2 homologue was detected for *A. trichopoda* and positioned at the base of the angiosperm group. The angiosperm group is therefore separated into two monophyletic groups (monocots and eudicots) (Figure 4.5).

In the monocots two protein homologues were detected for each species: *Musa acuminata*, *Oryza sativa* and *Zea mays*. However, the phylogeny suggests the presence of recent gene duplication in *Musa acuminata* (Figure 4.5). In contrast, the gene duplication between the two other monocots seems to have occurred before their speciation. All the eudicots possess at least one SINE1/SINE2 homologue. Four homologues that group together were found in *Glycine max*. This suggests a recent gene duplication during the evolutionary history of the *Glycine max* genome. As for WIPs, *Brassicaceae* proteins cluster together, and one group of homologues is detected for each gene *SINE1* and *SINE2*. The organisation between the two groups suggests a gene duplication in *Brassicaceae* ancestral gene to form *SINE1* and *SINE2*.

SINE expression is very interesting in *A. thaliana*: *AtSINE1* and *AtSINE2* are expressed at the same level in all tissues, but at a higher level than *AtSINE3* and



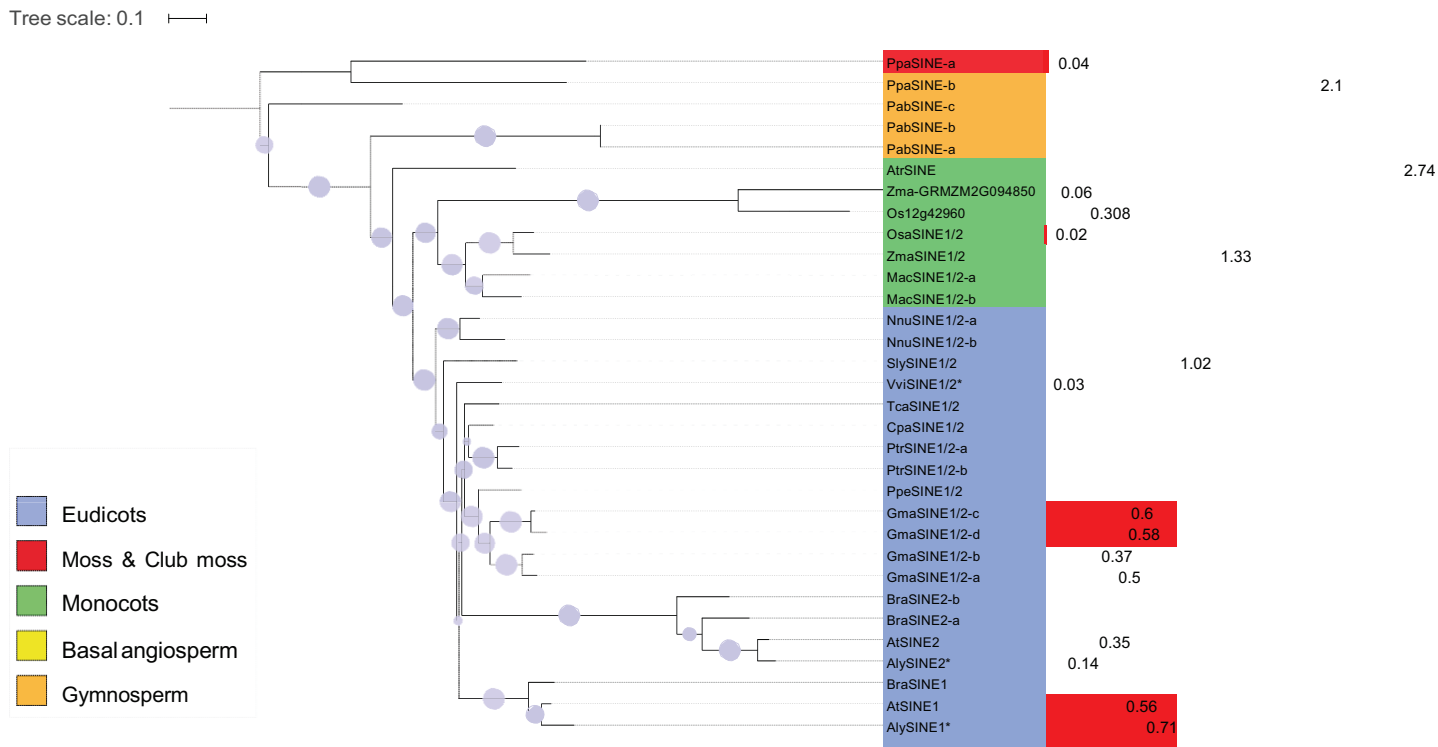


**Figure 4.5: Phylogenetic tree of SINE1, SINE2 homologues proteins.** **Left:** maximum likelihood tree of SINE protein homologues constructed from an alignment. Bootstrap values are represented by the diameter of the pale blue circle. Bootstrap value below 0.5 the bootstrap are not indicated. The colour of the label shows the lineage of the plant. The gene label is constructed with the three letters from the species name (see Table 4.1) and the gene name of the *A. thaliana* homologues. The labels without the homologue name were detected with the Perl script (eg: Zma-GRMZM2G094850). **Right:** red bar represents the value of the transcription level in seedlings, except for species indicated by \*, the RNA-seq data was obtained from leaf tissue (Table 4.3).

*AtSINE4*. However, SINE1/SINE2 homologues in other species show lowest level of expression for for all KASH proteins for all tissues analysed expect for maize, rice, *A. trichopoda* and *Physcomitrella patens* (see Appendix C.3). In these species *WIP* and *SINE* expression is at the same level for all tissues and this suggests there may be redundancy between KASH families. In *A. thaliana*, *AtWIPs* are more expressed than *AtSINE*; this suggests a new expression pattern of KASH protein genes in specific tissue in *Brassicaceae* [Zhou and Meier, 2014].

#### 4.4.5 Phylogenetic analysis of the putative nuclear lamina proteins

The analysis of the *KAKU4* phylogeny, shows two monophyletic groups, for the monocot and eudicot homologues (Figure4.6). The *KAKU4* gene is expressed at a level similar to the reference gene *SAND* in all species analysed. The protein was not detected in basal angiosperms, gymnosperms, moss, club moss and unicellular

algae. Either KAKU4 is a protein with specific function in angiosperms, or was not detected due to a high variability between species. The pattern of expression of *KAKU4* homologues shows a basal expression in all tissues (see Appendix C.3).

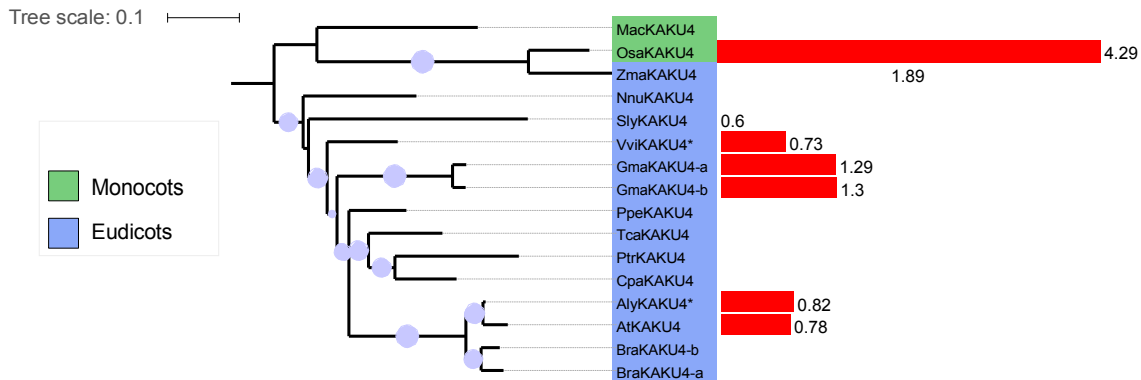


**Figure 4.6: Phylogenetic tree of KAKU4 proteins.** **Left:** maximum likelihood tree of KAKU4 protein homologues constructed from an alignment. Bootstrap values are represented by the diameter of the pale blue circle. Bootstrap value below 0.5 the bootstrap are not indicated. The colour of the label shows the lineage of the plant. The gene label is constructed with the three letters from the species name (see Table 4.1) and the gene name of the *A. thaliana* homologues. **Right:** red bar represents the value of the transcription level in seedlings, except for species indicated by \*, the RNA-seq data was obtained from leaf tissue (Table 4.3).

Two NEAPs were detected in gymnosperms, and one in *A. trichopoda*. The monocots form a monophyletic group with two potential specific gene duplications for *Musa acuminata* and *Zea mays* (Figure 4.7). As for monocots, the eudicots form a monophyletic group (Figure 4.7), and the gene duplication seems specific to species. So the three NEAP genes in *Brassicaceae* appear to result from a duplication event during the speciation of *Brassicaceae*.

The *NEAP* gene in *A. trichopoda* is expressed at very high level, *AtNEAP4* does not have protein homologues and is not expressed, implying that it is a pseudogene. The other *NEAP* genes are expressed in seedlings and in the other tissues but at a low level (see Appendix C.3).

The two clusters defi in the previous publication [Ciska and Moreno Diaz de la Espina, 2013] are found in this tree, but gymnosperm homologues seem to have only one type of CRWN protein, CRWN4 (Figure 4.8). The cluster of CRWN4 homologues constitute monophyletic groups found for monocots and eudicots, and one *A. trichopoda* homologous protein is detected (Figure 4.8). Only one protein was found for all species except for *Glycine max*. Surprisingly, no CRWN4 homologue was detected for *A. lyrata*, maybe due to the loss of this gene during its evolution.

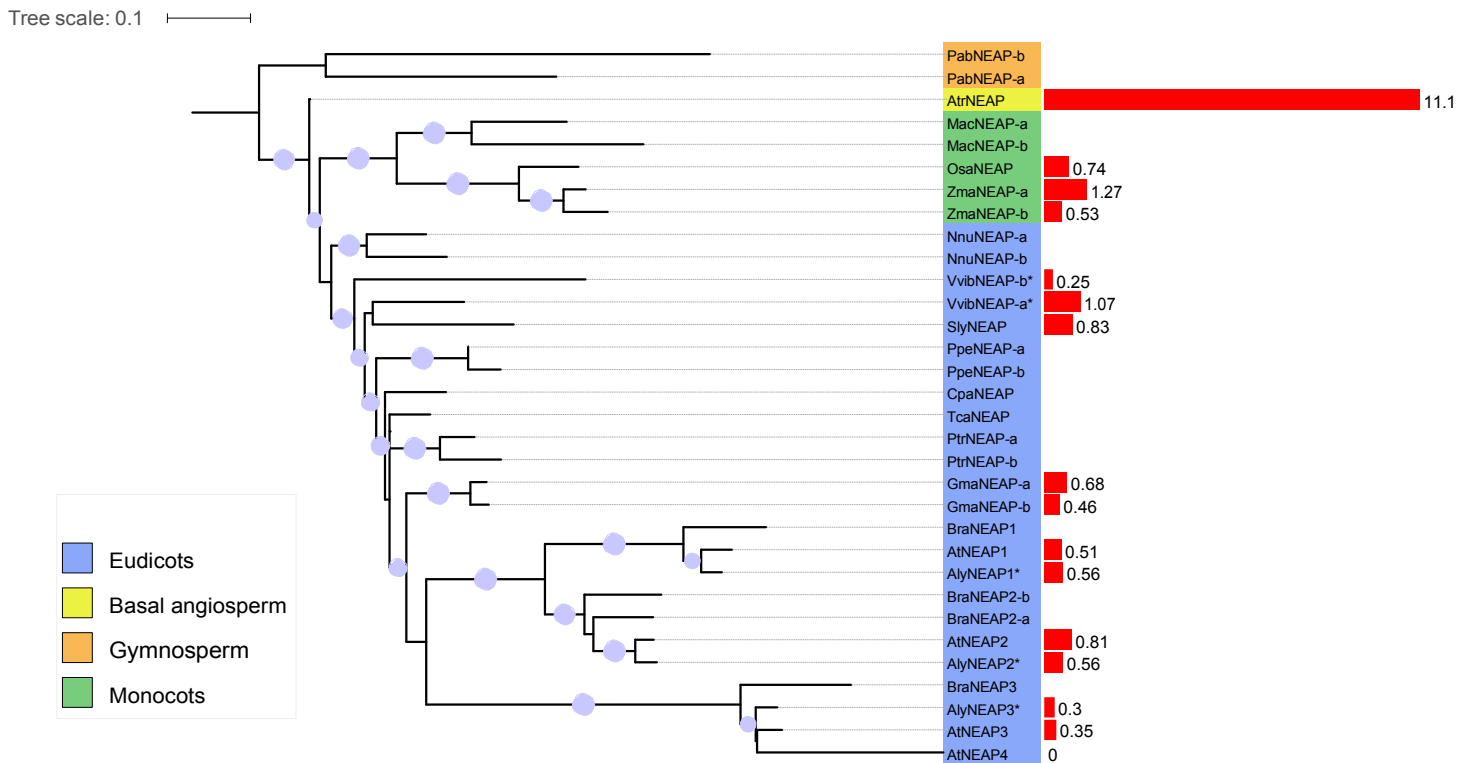


**Figure 4.7: Phylogenetic tree of NEAP proteins.** **Left:** maximum likelihood tree of NEAP protein homologues constructed from an alignment. Bootstrap values are represented by the diameter of the pale blue circle. Bootstrap value below 0.5 the bootstrap are not indicated. The colour of the label shows the lineage of the plant. The gene label is constructed with the three letters from the species name (see Table 4.1) and the gene name of the *A. thaliana* homologues. **Right:** red bar represents the value of the transcription level in seedlings, except for species indicated by \*, the RNA-seq data was obtained from leaf tissue (Table 4.3).

For the second group made up of the homologues of the three other CRWN proteins, the same organisation was found, with a monophyletic group for monocots and eudicots, and the detection of only one homologue in the *A. trichopoda* proteome (Figure 4.8). In the monocot group, only *Musa acuminata* possess three homologues, the other monocots possessing only one (Figure 4.8). In the eudicot group, two clusters can be distinguished; one for the homologues of AtCRWN1 and the other for AtCRWN2/AtCRWN3 and this reveals a gene duplication which occurred after speciation between monocots and eudicots. The other speciation, which gave rise to CRWN2 and CRWN3, occurred after the *Brassicaceae* speciation and formed a monophyletic group.

The genes belonging to the cluster *CRWN1/CRWN2/CRWN3* show higher expression in comparison of *CRWN4*. Other than in the *Brassicaceae*, *CRWN2* is less expressed than *CRWN1* and *CRWN3* for all the tissues analysed. The CRWN genes seem more highly expressed in all tissues in comparison to the other genes of this

analysis (Figure 4.8 and see Appendix C.3).

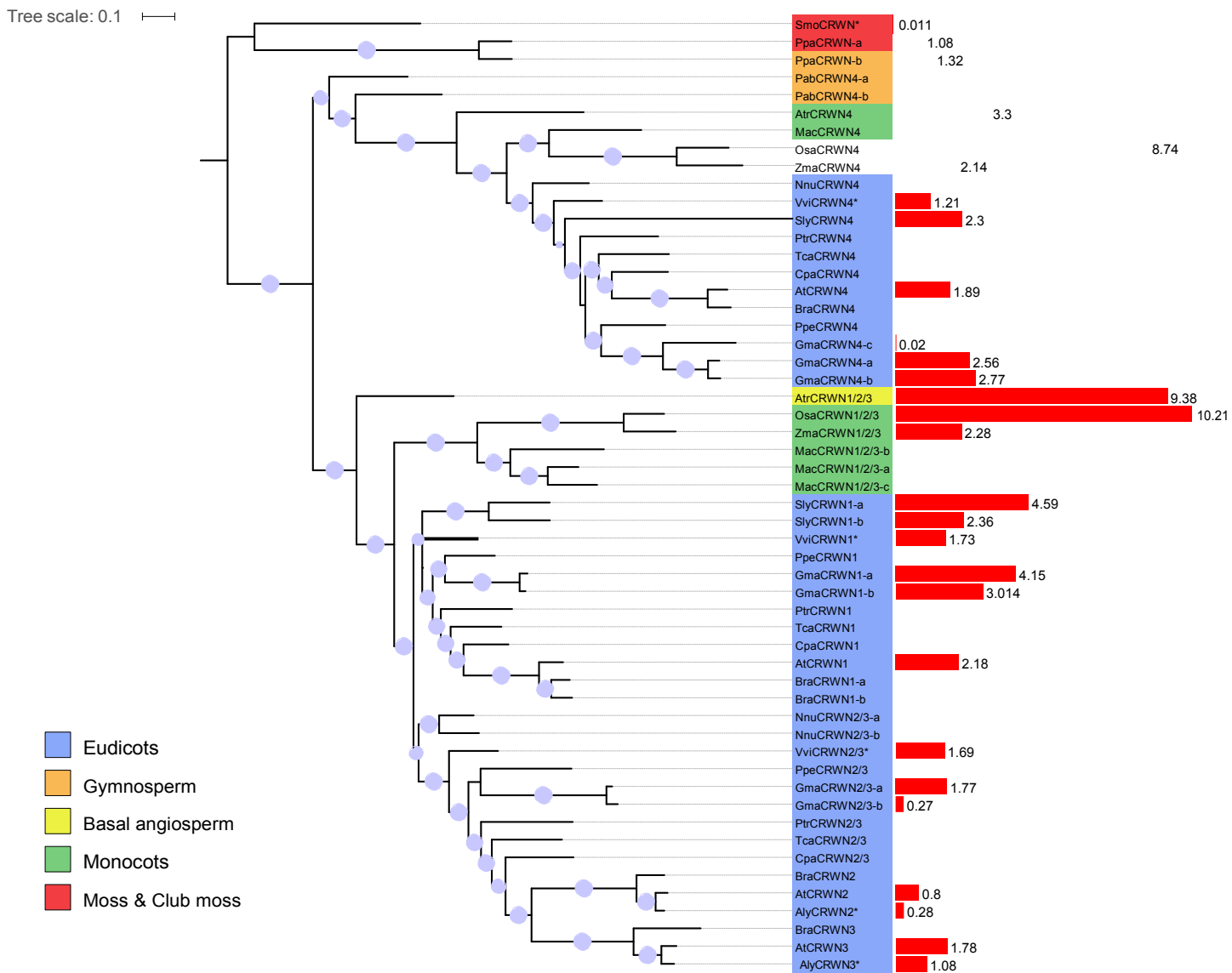


**Figure 4.8: Phylogenetic tree of CRWN proteins.** **Left:** maximum likelihood tree of CRWN protein homologues constructed from an alignment. Bootstrap values are represented by the diameter of the pale blue circle. If the bootstrap is below 0.5 the bootstrap is not indicated. The colour of the label shows the lineage of the plant. The gene label is constructed with the three letters from the species name (see Table 4.1) and the gene name of the *A.thaliana* homologues. **Right:** red bar represents the value of the transcription level in seedlings, except for species indicated by \*, the RNA-seq data was obtained from leaf tissue (Table 4.3).

Surprisingly, no lamin-like proteins were detected in unicellular algae (Table 4.6). However, NE81 and NUP1, two lamin-like proteins have already been described in unicellular organisms [Krüger et al., 2012, DuBois et al., 2012], but are not present in higher plants. It remains possible that lamin-like proteins exist in unicellular algae,

but while their sequences are not conserved, their functions are. Alternatively, it may be that these proteins evolved as part of the development of multicellularity and may have a function related to cellular interactions in tissues and organs.

## 4.5 Conclusion

This approach has permitted for the first time the detection of homologous proteins for the LINC complex and some of its interactors in twenty species. The detection of homologues was based on the *a priori* knowledge of the nuclear proteome in *A. thaliana* (Table 4.2). The sequence queries for BLASTp were *A. thaliana* sequences, and the motifs in the Perl script for KASH protein detection were defined only with motifs known in *A. thaliana*. Basing the analysis only on the knowledge of *A. thaliana* restrains outcomes to the most probable results; but this stringency may lead to omission of putative homologues. This choice of stringency is based on the fact that the majority of the proteomes were constructed only by bioinformatics predictions, and several errors or interpretation problems can be caused by these predictions. For example the high number of orthologues detected in *Glycine max* species may be due to the protein prediction or real gene duplication.

One major limitation of research to better describe the LINC complex and its interactors results from the lack of strong morphological phenotypes. Only *atcrwn* mutants display reduced plant growth which is an easily recognisable phenotype, whilst all other T-DNA insertion lines require microscopic analysis to investigate nuclear size and shape [Dittmer et al., 2007, Graumann et al., 2010, Graumann et al., 2014, Goto et al., 2014] or careful characterisation of meiotic foci [Varas et al., 2015]. The presence of multiple copies of KASH and SUN genes in *A. thaliana* and the lack of strong phenotypes in single mutants suggests the presence of gene redundancy due to gene duplication. This is further supported by lack of tissue-specific expression of most of the proteins investigated in this study. Whilst T-DNA insertion lines have predominantly been used, it is likely that in most cases combinations of mutations in several genes are needed for further functional analysis such as the double mutant *atsun1/atsun2* [Zhou et al., 2012] or the quintuple mutant *wifi (atwip1 atwip2 atwip3 atwit1 atwit2)* [Zhou et al., 2015b]. The research presented here will inform future mutant strategies both for *A. thaliana* and other species in enabling researchers to identify combinations of genes to be knocked out to overcome redundancy and will also suggest the tissues in which effects are most likely to be observed.

The simple *A. trichopoda* model may represent the minimal requirement with only two KASH proteins (one WIP and one SINE), three SUN proteins (one Cter-SUN and two mid-SUNs) and three lamin-like proteins (two CRWNs and one NEAP). Therefore, studying the LINC complex and its interactors in this plant model seems promising, given that it can be cultivated in a controlled environment, and also

easier in comparison to the complexity of the situation in *A. thaliana*. However, difficulties in its cultivation mean that alternative experimental models would be more promising. Many other species were shown to have simpler LINC complexes than *A. thaliana*; for instance, *Physcomitrella patens* and *Solanum lycopersicum* with respectively 4 SUNs, 2 KASHs, 2 putative nuclear lamina proteins and 2 SUNs, 2 KASHs, 5 putative nuclear lamina proteins. This information will also be of use to plant breeders as they develop strategies based on increased knowledge of epigenetics and chromatin positioning.

# Chapter 5

## Discussion and perspectives

The work described in this thesis provides new insights into the role of NE anchored proteins in chromatin organisation and nuclear morphology in *A. thaliana*. This role was investigated using 3D images of nuclei of three cell types (root epidermis (RC) or cotyledon epidermis (GC and PC)) (see Chapter 3). For this purpose, *NucleusJ*, an ImageJ plugin, was developed to segment the nucleus and the chromocentres in the initial 3D image from light microscopy. *NucleusJ* then computes 3D quantitative parameters from single images or large data sets of the two types of detected objects (Table 2.1) [Poulet et al., 2015].

Before studying NE-anchored or chromatin mutants it was important to analyse the three cell types of interest in wild-type plants, to determine variability and organisation of the wild type. Analysis of *NucleusJ* parameters permits to distinguish nuclei of the three cell types of interest which exhibit different nuclear morphology and chromatin organisation (see Chapter 3 Section 3.4.1). Furthermore, the analysis of the chromocentre distance to the nuclear periphery shows a preferential position of the chromocentre in interphase nuclei at a small distance from the nuclear periphery (see Chapter 3 Section 3.4.2).

The analysis of the link between nuclear morphology and chromatin was analysed with three types of mutants, NE-anchored, chromatin and histone chaperones mutants. A phylogenetic analysis carried out for the NE-anchored protein families (lamin-like, KASH and SUN) revealed several gene duplications specific to the *Brassicaceae* group (see Chapter 4). Among this group, my model plant *A. thaliana* possesses 8 lamin-like, 5 SUN and 8 KASH proteins suggesting some functional redundancy. This organisation complicates research on these proteins, and multiple mutants are needed to obtain strong phenotype. Analysis of 3D nuclear morphology of several NE-anchored mutants (SUN: *sun1 sun4 sun5*, KASH: *wifi* and *wip1 wip2 wip3* and lamin-like: *crwn1 crwn2* and lamin-binding: *emphkaku4-2*) was carried



out and shows a decrease in nuclear volume correlated with an increase in sphericity compared to wild type (see Chapter 3 Section 3.4.3). These changes were found to be stronger in lamin-like mutants. Nuclear morphology changes involve new chromatin organisation, but specific mis-organisation of the NE-anchored proteins remained difficult to be detected using only *NucleusJ* parameters, whereas analysis with 2D and 3D FISH, for chromocentre condensation and transcriptional reactivation analysis at heterochromatic loci shows the impact of mutations of the LINC complex proteins in chromatin organisation (see Chapter 3 Section 3.4.4). In contrast to the proteins of the LINC, mutants for the two proteins associated with the plant lamina, *crwn1 crwn2* and *kaku4-2*, show the exact opposite effect, *crwn1 crwn2* possesses more condensed chromocentres, correlated with a decrease in the expression of the normally silent repetitive sequences, and the converse for *kaku4-2*. Finally, these two lamina components do not play the same role in the nucleus, CRWN1 and CRWN2 proteins seem to be more involved in shape regulation whereas KAKU4 seems to possess a role more strongly related to chromatin organisation and may be involved in the organisation of silenced domains. We hypothesise that the impact of NE associated mutations on chromatin organisation may have been due to the release of specific interactions between cytoskeleton and nucleoskeleton (Figure 1.4), which can lead to chromatin disorganisation (see Chapter 1 section 1.2).

The chromatin mutants (*atxr5 atxr6* and *ddm1-10*) and histone chaperone mutants (*atrx-1*, *atrx-2*, *asf1a*, and *asf1b*) do not appear to have a great effect on nuclear morphology but, as expected, histone chaperone and *atxr5 atxr6* mutants globally impact the chromatin organisation parameters of *NucleusJ*, except *ddm1-10* (see Chapter 3 Section 3.4.4). Condensation of chromocentre in these mutants is generally reduced and correlated with an increase of TSI expression. Finally, it is not clear from the mutants that chromatin disorganisation leads to changes in nuclear morphology. Before the role of NE-anchored and chromatin and histone chaperone mutants can be discussed, validation and limitations of the imaging method will be considered (see Section 5.1 and 5.3 below).

## **5.1 *NucleusJ* a user friendly ImageJ plugin for 3D images of nucleus**

### **5.1.1 *NucleusJ* validation**

*NucleusJ* was developed as an ImageJ plugin and published in the Bioinformatics journal [Poulet et al., 2015]. The first version of *NucleusJ* was released as an ImageJ

plugin and is also available on the Fiji platform. Documentation was written and is available on the wiki of ImageJ ([http://imagejdocu.tudor.lu/doku.php?id=plugin:stacks:nuclear\\_analysis\\_plugin:start](http://imagejdocu.tudor.lu/doku.php?id=plugin:stacks:nuclear_analysis_plugin:start)). *NucleusJ* has been presented in several scientific congresses (IPNC 2013, 2015, JOBIM 2015, and the one day doctoral school in Clermont Ferrand in 2014). We had several contacts with end-users during the past year; however our Bioinformatics paper has been cited only twice (Source: web of Science, Thompson Reuters) and it will be important in the coming years to continue publishing new analyses performed with *NucleusJ* as well as to inform users about new improvements such as the new 3D segmentation processes developed during this thesis.

### 5.1.2 *NucleusJ* limitations

Several limitations exist in *NucleusJ*. The main limitation in the 3D image processing and analysis tool used in this study is the manual step of 3D segmentation of the chromocentres. This manual step is a well known drawback of the contrast map calculated on the region obtained with the watershed method. To finish the segmentation of the contrast map, it is needed to apply a manual threshold, this last step increases the time taken for the analysis. A method based on a histogram distribution could be developed to automatically detect chromocentres. Two dependencies, the Java library (morpholib.jar, imagescience.jar) and the plugin containing of the Euclidean distance map (See Chapter 2 Section 2.4.1) used by *NucleusJ* limit the development of the plugin and increase the risk of errors through the updating of these plugins. The Euclidean distance map method used during the computing of chromocentre distance increases the time of analysis. It would be interesting to implement the Euclidean distance method for *NucleusJ* to facilitate source code homogeneity in the next modification of *NucleusJ*.

Radial distance, defined as concentric circles from the nucleus centre is frequently used to compute position within the nucleus. While this strategy applies well to round nuclei, it is more complicated to define the nucleus centre when the nuclei adopt ellipsoid or elongated shapes. Here, spatial positioning was used to compute the radial distance within a nucleus, but with radial distance, all the 3D information was lost, and transformed into unidimensional information. To keep and analyse the current distribution of position of the chromocentres, it would be advantageous to implement the distribution method of Andrey et al. (2010) (Figure 1.7). With the radial distance information and the distribution function information, it would then be possible to identify specific chromocentre distribution phenotypes in the mutants of interest.

Hoechst or chromatin staining/markings used for the images analysed by *NucleusJ* also provides a limitation. These types of staining are limited by the fact that only chromatin and not the nuclear envelope is stained. As part of the work for this thesis, a nuclear envelope stain (FM4-64FX) was tested but the method needs to be improved before its use. As an alternative, several transgenic constructs for expression of tagged proteins targeted to the different types of membranes already exist, but fusion proteins can disorganise the morphology of the NE. One drawback of this approach is that each construct needs to be introduced in the mutant of interest. To establish possible bias produced by Hoechst staining and preparation for light microscopy, alternative methods, for instance 3D electron microscopy (serial block-face scanning electron microscopy (SBFSEM)) should be undertaken with osmium staining which permits the detection of NE (Figure 5.1). Indeed, this work was initiated during my stay at Oxford Brookes and images of plant nuclei were collected from Col-0 cotyledon, using SBFSEM. I also started to adapt *NucleusJ* to process such images. However this will require further developments in the future in order to be able to perform 3D segmentation on SBFSEM, the main difficulties being the presence of many other structures stained during the osmium treatment including ER and mitochondria while chromatin remains poorly contrasted (Figure 5.1).

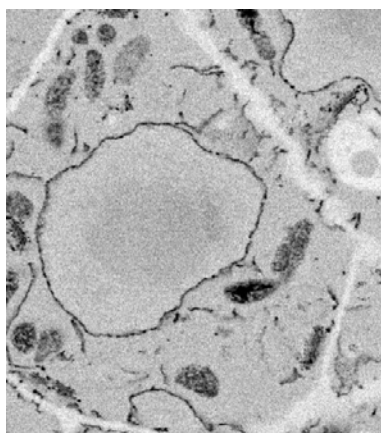


**Figure 5.1: Image of *Arabidopsis thaliana* root with electron microscope SBF SEM.** Fixed tissue observed after osmium staining and observed by SBF SEM: organelles and membranes are well stained, but chromatin within the nucleus is not well contrasted. (Source: Image obtained from Dr Louise Hughes, Oxford Brookes University)

### **5.1.3 Future improvement of *NucleusJ***

New developments are ongoing, and algorithms presented in Chapter 2 Section 2.4.2 and Section 2.4.3 need to be integrated into a new version of *NucleusJ*. The new version will have a new program architecture, to easily perform modifications or to

implement the improvements of the code using Unified Modelling Language (UML). This work is currently done in collaboration with Pr R. Malgouyres. Furthermore, a method for analysis of 3D electron microscope images will be developed to segment the nucleus. This method will be integrated in the new version of *NucleusJ* to permit the comparison of the parameters obtained with the NE staining and chromatin methods. Other methods can be added to *NucleusJ* to permit automatic segmentation of the chromocentre in order to decrease the time of computation. To complete the *NucleusJ* plugin, it will be interesting to test if the segmentation of the nucleolus is possible in images stained with Hoechst or with other techniques to specifically stain the nucleolus, to get new insights about the position of the nucleolus within the nucleus. To continue to analyse the position of DNA sequences or chromatin domains, methods for 3D FISH should be integrated, and then integration of distribution function used to analyse the distribution in the nucleus of these domains or sequences. All these new developments would actively promote the efficiency and relevance of *NucleusJ* as a useful tool to analyse the 3D organisation of chromatin.

## **5.2 Heterochromatin organisation and chromocentre positioning in wild-type plants**

One aim was to determine whether nuclear structure would impact chromatin decompaction and genome. First, we showed that the positioning of chromocentre is closed to the nuclear periphery. Endoreplicated PC and RC nuclei have more internal chromocentres than diploid GC suggesting that chromocentres formed by the 45S rDNA clusters are also located at the nuclear periphery. This suggests that the nucleolus position is also close to the nuclear periphery. This remains to be demonstrated by specifically labelling the nucleolus, using for instance nucleolin or fi antibodies. The data produced, also support the fact that larger nuclei tend to have a reduced heterochromatic content. One hypothesis can be that endoreplicated nuclei contain uncompleted chromosome replication at heterochromatic regions maybe due to its late replicating properties. However this is not well supported by previous data [Jacob et al., 2010]. Another hypothesis is that endoreplicated nuclei may have a more decondensed heterochromatic organisation which reduced chromocentre detection as previously proposed [Schubert et al., 2012]

### 5.3 NE-anchored proteins disrupt nuclear morphology as well as chromatin organisation

Here, effects of alteration of NE-anchored proteins were investigated on nuclear morphology and chromatin organisation. All the mutants analysed (*wip1 wip2 wip3*, *wit1 wit2*, *wifi*, *sun1 sun4 sun5*, *crwn1 crwn2* and *kaku4-2*) present a more spherical nucleus and for the majority, a smaller nucleus in comparison with the wild-type. In previous studies, all the defects have already been shown, but these analyses had been carried out by analysis of 2D parameters, and it is the first time that effects of all these NE-anchored proteins have been investigated in 3D and analysed together in a single set of experiments with standardised procedures [Dittmer et al., 2007, Graumann et al., 2010, Zhou et al., 2012, Graumann, 2014, Goto et al., 2014, Zhou et al., 2015b]. Finally, we hypothesise that mutations of NE-anchored protein proteins impact interaction between cyto- and nucleoskeleton, and lead to a decrease of the constraint force applied to the nucleus resulting in the increase of sphericity and decrease of nuclear volume [Alam et al., 2014].

The analysis of chromatin organisation was motivated by previous results in other species such as in yeast in which Mps3p a Cter-SUN homologue of AtSUN1 and AtSUN2 is involved in the recruitment of telomeric repeats at the nuclear envelope, an essential process needed for telomeric silencing [Friederichs et al., 2012]. In plants and animals, Cter-SUN proteins also interact with telomeres although the molecular mechanisms of this interaction remain elusive [Murphy and Bass, 2012, Varas et al., 2015]. To date, only the Dictyostelium SUN-1 has been described to directly bind DNA through its N-terminal domain [Xiong et al., 2008] and this function does not seem to be conserved in other species. AtSUNs do not contain any Zinc finger or other conserved domains in the N-terminal part of the protein [Graumann et al., 2010, Graumann, 2014]. The analysis of the NE-anchored proteins revealed that the triple *sun1 sun4 sun5* mutant increases the distance of chromocentres from the nuclear boundary, induces chromocentre decompaction as well as transcriptional derepression at heterochromatic repeats. Alteration of heterochromatic markers can be the result of a global disorganisation of the transcriptional machinery due to modification of nuclear morphology. Thus the transcriptional status of euchromatic sequences was thus investigated. To test this hypothesis three genes were chosen with high, middle and low transcription levels [Duc et al., 2015] and located at euchromatic sites. Transcription level at those genes is very similar in wild type and mutants (data not shown) suggesting that transcriptional alteration specifically affect heterochromatic sequences. In summary, we propose that SUN proteins are

important to keep chromocentres at the nuclear periphery and that altering this function affect the transcriptional repression of heterochromatic sequences which are enriched in chromocentres.

Interestingly, this does not imply that the nuclear periphery is a required environment to achieve heterochromatin repression. This is well illustrated by the lamin-like mutant *crwn1 crwn2* in which chromocentres are fused together and are at a more internal position. In that case, neither decompaction nor transcriptional release for repetitive sequence silencing was observed, but instead a more repressed state occurred. The *crwn* phenotype recalls *Sir4* overexpression in yeast in which telomeric repeats are delocated from the periphery and became more central. In the *sir4* mutant, repression becomes higher in this new central repressive chromatin domain [Taddei et al., 2004]. The nuclear periphery may contain all the required repressive complexes needed to insure transcriptional repression. CRWN may be a key component of the nuclear periphery which recruits some of these repressive factors.

The analysis of KASH5 in mice shows also a decrease in the mutant of the associations between telomere and NE [Morimoto et al., 2012]. Horn et al. (2013) hypothesise that the absence of KASH5 impacts SUN1 organisation in the NE reducing the efficiency or stability of telomere attachment to the NE [Horn et al., 2013]. The three types of mutants analysed (*wip1 wip2 wip3*, *wit1 wit2*, *wifi*) do not exhibit a disturbance of the chromocentre distance as for the triple mutant *sun*, while only the triple *wip* mutants show a weak increase of this distance. These three mutants show a decompaction of the chromocentres but only for *wifi* decompaction was correlated with transcriptional derepression at heterochromatic repeats. The activity and functional redundancy shown in the phylogenetic analysis (Chapter 4), can explain the weak phenotype of these mutants. *A. thaliana* has 8 KASH proteins which interact with SUN proteins and with the cytoskeleton and it is likely that other KASH proteins can complement the *wip* mutation, explaining why *wip1 wip2 wip3* conserves a certain order in the chromatin organisation.

From this initial set of mutants, we have now set up standardised procedures that can be now extended to other mutations such as *nup136* [Tamura and Hara-Nishimura, 2011], *gip1 gip2* [Janski et al., 2012], *kaku1* [Tamura and Hara-Nishimura, 2013] that have been described to alter nuclear morphology.

## 5.4 Chromatin and histone chaperone mutants disrupt chromatin organisation but not nuclear morphology

Chromatin and histone chaperone mutants were included in this study to test the impact of chromatin misorganisation on nuclear shape. In this case, these mutants impact chromatin organisation as expected but show no effect on nuclear morphology. However, this may be due to mutations used, for example the weak *ddm1* allele. Other alternatives would be to include the H3.1 quintuple mutant, since the H3.1 histone has been shown to be enriched in heterochromatin and may involve a loss of connection between heterochromatin and the NE. Interestingly, the defects in chromatin organisation found for the NE-anchored proteins are stronger than those for the chromatin and histone chaperone mutants and show the importance of the NE on chromatin organisation and regulation. It will be also probably very interesting to evaluate histone variants specific of pericentromeric sequences such as H2AW which have been shown to affect chromocentre compaction [Yelagandula et al., 2014].

## 5.5 Future work

### 5.5.1 Chromatin organisation of the NE-anchored mutants

To continue the analysis of NE organisation on chromatin, it would be interesting to use several sequencing techniques. RNA sequencing of the NE-anchored mutants allows the analysis of the expression of genes, and a change of their regulation in these mutants. The technique of Chromatin Conformation Capture sequencing can complete the analysis of chromatin organisation in these mutants, and allow understanding of how chromatin is organised and would maybe help to explain the heterochromatin derepression we observed in the analysed mutants. This technique has already been successfully applied to *crwn1* and *crwn4* mutants and revealed their implication in heterochromatic sequence interaction [Grob et al., 2014].

Then, as already discussed in the Section 5.3, other mutants can be analysed with the same methods. Preliminary experiments have already been carried out on the NEAP mutants (*neap1*, *neap3* and *neap1 neap3*). The results for these mutants show that they impact chromatin organisation and the phenotype observed is closed to that of *kaku4-2*. We hope that the analysis of more mutants will increase of the understanding of the link between the NE and chromatin organisation.

### **5.5.2 Chromatin organisation of the natural ecotype of *Arabidopsis thaliana***

Tessadori et al. (2009) showed that chromatin compaction is correlated with geographic latitude of the ecotype [Tessadori et al., 2009]. This fact is interesting since it shows natural variation in 3D organisation in chromatin and nuclear morphology. Preliminary results of the comparison with *NucleusJ* between three different ecotypes (Cape Verde Islands, Wassilewskija and Columbia) show different nuclear morphology and chromatin organisation. To pursue these experiments, it would be interesting to add more ecotypes and also to control the growing conditions of each ecotype to avoid introducing a bias due to these conditions.

### **5.5.3 Length and number of cells in cotyledon epidermis**

Several studies in mammals have shown that nuclear morphology is correlated with the cellular morphology and an elongated cell typically exhibits an elongated nucleus [Weiss and Garber, 1952, Khatau et al., 2009, Versaevel et al., 2012]. It is interesting to replace the nucleus analysis in the context of the cell with the context of the vacuole, a compartment which can represent up to 90% of the cellular volume in plant, and to establish whether N/C ratio is conserved for various vacuolar volumes. In addition, it would be useful to explore whether mutations altering nuclear volume or shape also alter the shape or volume of cells. This could be achieved by analysing cell shape and size for many cells in the epidermis of the cotyledon.

### **5.5.4 Impact of stress conditions on the nuclear shape and chromatin organisation**

*In vivo*, the nucleus is typically spherical or ellipsoidal in mammals; dramatic morphological changes of the nucleus can occur in response to physical or environmental stresses [Kim et al., 2015]. Vigouroux et al. (2001) demonstrated an increase in sensitivity to heat stress of nuclei from laminopathy cells [Vigouroux et al., 2001]. Furthermore in *A. thaliana*, stress conditions involve changes in chromatin organisation [Pecinka and Mittelsten Scheid, 2012]. It will be interesting to do the same 3D analysis on wild-type and NE-anchored mutants to know the impact of NE mutation on stress sensitivity and the capacity to react to stress.



# References

Abbe, E. (1873). Beiträge zur theorie des mikroskops und der mikroskopischen wahrnehmung. *Archiv für mikroskopische Anatomie*, 9(1):413–418.

Airy, G. B. (1835). On the diffraction of an object-glass with circular aperture. *Transactions of the Cambridge Philosophical Society*, Vol. 5, 1835, p. 283-291.

Alam, S., Lovett, D. B., Dickinson, R. B., Roux, K. J., and Lele, T. P. (2014). Nuclear forces and cell mechanosensing. *Progress in Molecular Biology and Translational Science*, 126:205–215.

Alber, F., Dokudovskaya, S., Veenhoff, L. M., Zhang, W., Kipper, J., Devos, D., Suprpto, A., Karni-Schmidt, O., Williams, R., Chait, B. T., Sali, A., and Rout, M. P. (2007). The molecular architecture of the nuclear pore complex. *Nature*, 450(7170):695–701.

Altschul, S. F., Gish, W., Miller, W., Myers, E. W., and Lipman, D. J. (1990). Basic local alignment search tool. *Journal of Molecular Biology*, 215(3):403–410.

Anders, S., Pyl, P. T., and Huber, W. (2015). HTSeqa Python framework to work with high-throughput sequencing data. *Bioinformatics*, 31(2):166–169.

Anderson, D. J. and Hetzer, M. W. (2008). Reshaping of the endoplasmic reticulum limits the rate for nuclear envelope formation. *The Journal of Cell Biology*, 182(5):911–924.

Andrey, P., Kiu, K., Kress, C., Lehmann, G., Tirichine, L., Liu, Z., Biot, E., Adenot, P.-G., Hue-Beauvais, C., Houba-Hrin, N., Duranthon, V., Devinoy, E., Beaujean, N., Gaudin, V., Maurin, Y., and Debey, P. (2010). Statistical analysis of 3d images detects regular spatial distributions of centromeres and chromocenters in animal and plant nuclei. *PLoS Comput Biol*, 6(7):e1000853.

Argout, X., Salse, J., Aury, J.-M., Gultinan, M. J., Droc, G., Gouzy, J., Allegre, M., Chaparro, C., Legavre, T., Maximova, S. N., Abrouk, M., Murat, F., Fouet, O., Poulain, J., Ruiz, M., Roguet, Y., Rodier-Goud, M., Barbosa-Neto, J. F., Sabot, F., Kudrna, D., Ammiraju, J. S. S., Schuster, S. C., Carlson, J. E., Sallet, E., Schiex, T., Dievart, A., Kramer, M., Gelley, L., Shi, Z., Brard, A., Viot, C., Boccara, M., Risterucci, A. M., Guignon, V., Sabau, X., Axtell, M. J., Ma, Z., Zhang, Y., Brown, S., Bourge, M., Golser, W., Song, X., Clement, D., Rivallan, R., Tahiri, M., Akaza, J. M., Pitollat, B., Gramacho, K., D'Hont, A., Brunel, D., Infante, D., Kebe, I., Costet, P., Wing, R., McCombie, W. R., Guiderdoni, E., Quetier, F., Panaud, O.,

Wincker, P., Bocs, S., and Lanaud, C. (2011). The genome of *Theobroma cacao*. *Nature Genetics*, 43(2):101–108.

Ariel, F., Jegu, T., Latrasse, D., Romero-Barrios, N., Christ, A., Benhamed, M., and Crespi, M. (2014). Noncoding transcription by alternative RNA polymerases dynamically regulates an auxin-driven chromatin loop. *Molecular Cell*, 55(3):383–396.

Banks, J. A., Nishiyama, T., Hasebe, M., Bowman, J. L., Gribskov, M., dePamphilis, C., Albert, V. A., Aono, N., Aoyama, T., Ambrose, B. A., Ashton, N. W., Axtell, M. J., Barker, E., Barker, M. S., Bennetzen, J. L., Bonawitz, N. D., Chapple, C., Cheng, C., Correa, L. G. G., Dacre, M., DeBarry, J., Dreyer, I., Elias, M., Engstrom, E. M., Estelle, M., Feng, L., Finet, C., Floyd, S. K., Frommer, W. B., Fujita, T., Gramzow, L., Gutensohn, M., Harholt, J., Hattori, M., Heyl, A., Hirai, T., Hiwatashi, Y., Ishikawa, M., Iwata, M., Karol, K. G., Koehler, B., Kolukisaoglu, U., Kubo, M., Kurata, T., Lalonde, S., Li, K., Li, Y., Litt, A., Lyons, E., Manning, G., Maruyama, T., Michael, T. P., Mikami, K., Miyazaki, S., Morinaga, S.-i., Murata, T., Mueller-Roeber, B., Nelson, D. R., Obara, M., Oguri, Y., Olmstead, R. G., Onodera, N., Petersen, B. L., Pils, B., Prigge, M., Rensing, S. A., Riaño-Pachón, D. M., Roberts, A. W., Sato, Y., Scheller, H. V., Schulz, B., Schulz, C., Shakhov, E. V., Shibagaki, N., Shinohara, N., Shippen, D. E., Sorensen, I., Sotooka, R., Sugimoto, N., Sugita, M., Sumikawa, N., Tanurdzic, M., Theien, G., Ulvskov, P., Wakazuki, S., Weng, J.-K., Willats, W. W., Wipf, D., Wolf, P. G., Yang, L., Zimmer, A. D., Zhu, Q., Mitros, T., Hellsten, U., Loqu, D., Otilar, R., Salamov, A., Schmutz, J., Shapiro, H., Lindquist, E., Lucas, S., Rokhsar, D., and Grigoriev, I. V. (2011). The compact Selaginella genome identifies changes in gene content associated with the evolution of vascular plants. *Science (New York, N. Y.)*, 332(6032):960–963.

Baptiste, E., Charlebois, R. L., MacLeod, D., and Brochier, C. (2005). The two tempos of nuclear pore complex evolution: highly adapting proteins in an ancient frozen structure. *Genome Biology*, 6(10):R85.

Bass, H. W., Bordoli, S. J., and Foss, E. M. (2003). The desynaptic (dy) and desynaptic1 (dsy1) mutations in maize (*Zea mays L.*) cause distinct telomeremise-ment phenotypes during meiotic prophase. *Journal of Experimental Botany*, 54(380):39–46.

Baubec, T., Finke, A., Mittelsten Scheid, O., and Pecinka, A. (2014). Meristem-specific expression of epigenetic regulators safeguards transposon silencing in Arabidopsis. *EMBO reports*, 15(4):446–452.

Bauwens, S., Katsanis, K., Van Montagu, M., Van Oostveldt, P., and Engler, G. (1994). Procedure for whole mount *in situ* hybridization of interphase nuclei on Arabidopsis thaliana. *The Plant Journal*, 6(1):123–131.

Baye, L. M. and Link, B. A. (2008). Nuclear migration during retinal development. *Brain Research*, 1192:29–36.

- Benavente, R., Krohne, G., and Franke, W. W. (1985). Cell type-specific expression of nuclear lamina proteins during development of *Xenopus laevis*. *Cell*, 41(1):177–190.
- Benoit, M., Layat, E., Tourmente, S., and Probst, A. V. (2013). Heterochromatin dynamics during developmental transitions in *Arabidopsis* - a focus on ribosomal DNA loci. *Gene*, 526(1):39–45.
- Berr, A. and Schubert, I. (2007). Interphase chromosome arrangement in *Arabidopsis thaliana* is similar in differentiated and meristematic tissues and shows a transient mirror symmetry after nuclear division. *Genetics*, 176(2):853–863.
- Bian, Q. and Belmont, A. S. (2012). Revisiting higher-order and large-scale chromatin organization. *Current Opinion in Cell Biology*, 24(3):359–366.
- Bickmore, W. A. and van Steensel, B. (2013). Genome architecture: domain organization of interphase chromosomes. *Cell*, 152(6):1270–1284.
- Bolzer, A., Kreth, G., Solovei, I., Koehler, D., Saracoglu, K., Fauth, C., Müller, S., Eils, R., Cremer, C., Speicher, M. R., and Cremer, T. (2005). Three-dimensional maps of all chromosomes in human male fibroblast nuclei and prometaphase rosettes. *PLoS Biology*, 3(5).
- Bone, C. R., Tapley, E. C., Gorjánácz, M., and Starr, D. A. (2014). The *Caenorhabditis elegans* SUN protein UNC-84 interacts with lamin to transfer forces from the cytoplasm to the nucleoskeleton during nuclear migration. *Molecular Biology of the Cell*, 25(18):2853–2865.
- Bourbousse, C., Mestiri, I., Zabulon, G., Bourge, M., Formiggini, F., Koini, M. A., Brown, S. C., Fransz, P., Bowler, C., and Barneche, F. (2015). Light signaling controls nuclear architecture reorganization during seedling establishment. *Proceedings of the National Academy of Sciences of the United States of America*, 112(21):E2836–2844.
- Bowler, C., Benvenuto, G., Laflamme, P., Molino, D., Probst, A. V., Tariq, M., and Paszkowski, J. (2004). Chromatin techniques for plant cells. *The Plant Journal: For Cell and Molecular Biology*, 39(5):776–789.
- Brandt, A., Papagiannouli, F., Wagner, N., Wilsch-Bräuninger, M., Braun, M., Furlong, E. E., Loserth, S., Wenzl, C., Pilot, F., Vogt, N., Lecuit, T., Krohne, G., and Grohans, J. (2006). Developmental control of nuclear size and shape by kugelkern and kurzkern. *Current Biology*, 16(6):543–552.
- Brown, C. R., Kennedy, C. J., Delmar, V. A., Forbes, D. J., and Silver, P. A. (2008). Global histone acetylation induces functional genomic reorganization at mammalian nuclear pore complexes. *Genes & Development*, 22(5):627–639.
- Bupp, J. M., Martin, A. E., Stensrud, E. S., and Jaspersen, S. L. (2007). Telomere anchoring at the nuclear periphery requires the budding yeast Sad1-UNC-84 domain protein Mps3. *The Journal of Cell Biology*, 179(5):845–854.

- Burke, B. and Stewart, C. L. (2013). The nuclear lamins: finally in function. *Nature Reviews. Molecular Cell Biology*, 14(1):13–24.
- Cao, X. and Jacobsen, S. E. (2002). Locus-specific control of asymmetric and CpNpG methylation by the DRM and CMT3 methyltransferase genes. *Proceedings of the National Academy of Sciences of the United States of America*, 99 Suppl 4:16491–16498.
- Castleman, K. R. (1996). *Digital Image Processing*. Prentice Hall Press, Upper Saddle River, NJ, USA.
- Cavalier-Smith, T. (2005). Economy, speed and size matter: evolutionary forces driving nuclear genome miniaturization and expansion. *Annals of Botany*, 95(1):147–175.
- Chambliss, A. B., Khatau, S. B., Erdenberger, N., Robinson, D. K., Hodzic, D., Longmore, G. D., and Wirtz, D. (2013). The LINC-anchored actin cap connects the extracellular milieu to the nucleus for ultrafast mechanotransduction. *Scientific Reports*, 3:1087.
- Chen, C.-Y., Chi, Y.-H., Mutalif, R., Starost, M., Myers, T., Anderson, S., Stewart, C., and Jeang, K.-T. (2012). Accumulation of the inner nuclear envelope protein sun1 is pathogenic in progeric and dystrophic laminopathies. *Cell*, 149(3):565–577.
- Cheng, Z., Buell, C. R., Wing, R. A., Gu, M., and Jiang, J. (2001). Toward a cytological characterization of the rice genome. *Genome Research*, 11(12):2133–2141.
- Chi, Y.-H., Cheng, L. I., Myers, T., Ward, J. M., Williams, E., Su, Q., Faucette, L., Wang, J.-Y., and Jeang, K.-T. (2009). Requirement for Sun1 in the expression of meiotic reproductive genes and piRNA. *Development*, 136(6):965–973.
- Chi, Y.-H., Haller, K., Peloponese, J.-M., and Jeang, K.-T. (2007). Histone acetyltransferase halp and nuclear membrane protein hssun1 function in de-condensation of mitotic chromosomes. *Journal of Biological Chemistry*, 282(37):27447–27458.
- Chow, K.-H., Factor, R. E., and Ullman, K. S. (2012). The nuclear envelope environment and its cancer connections. *Nature reviews. Cancer*, 12(3):196–209.
- Ciska, M. and Moreno Diaz de la Espina, S. (2013). NMCP/LINC proteins: putative lamin analogs in plants? *Plant Signaling & Behavior*, 8(12):e26669.
- Ciska, M. and Moreno Diaz de la Espina, S. (2014). The intriguing plant nuclear lamina. *Frontiers in Plant Science*, 5.
- Cohen, M., Lee, K. K., Wilson, K. L., and Gruenbaum, Y. (2001). Transcriptional repression, apoptosis, human disease and the functional evolution of the nuclear lamina. *Trends in Biochemical Sciences*, 26(1):41–47.

- Cokus, S. J., Feng, S., Zhang, X., Chen, Z., Merriman, B., Haudenschild, C. D., Pradhan, S., Nelson, S. F., Pellegrini, M., and Jacobsen, S. E. (2008). Shotgun bisulphite sequencing of the Arabidopsis genome reveals DNA methylation patterning. *Nature*, 452(7184):215–219.
- Conklin, E. G. (1912). Cell size and nuclear size. *Journal of Experimental Zoology*, 12(1):1–98.
- Consortium, T. G. (2012). The tomato genome sequence provides insights into fl yfruit evolution. *Nature*, 485(7400):635–641.
- Cremer, M., von Hase, J., Volm, T., Brero, A., Kreth, G., Walter, J., Fischer, C., Solovei, I., Cremer, C., and Cremer, T. (2001). Non-random radial higher-order chromatin arrangements in nuclei of diploid human cells. *Chromosome Research: An International Journal on the Molecular, Supramolecular and Evolutionary Aspects of Chromosome Biology*, 9(7):541–567.
- Crisp, M., Liu, Q., Roux, K., Rattner, J. B., Shanahan, C., Burke, B., Stahl, P. D., and Hodzic, D. (2006). Coupling of the nucleus and cytoplasm role of the LINC complex. *The Journal of Cell Biology*, 172(1):41–53.
- Czechowski, T., Stitt, M., Altmann, T., Udvardi, M. K., and Scheible, W. (2005). Genome-wide identification and testing of superior reference genes for transcript normalization in Arabidopsis. *Plant Physiology*, 139(1):5–17.
- Dahl, K. N., Engler, A. J., Pajerowski, J. D., and Discher, D. E. (2005). Power-law rheology of isolated nuclei with deformation mapping of nuclear substructures. *Biophysical Journal*, 89(4):2855–2864.
- Dahl, K. N., Kahn, S. M., Wilson, K. L., and Discher, D. E. (2004). The nuclear envelope lamina network has elasticity and a compressibility limit suggestive of a molecular shock absorber. *Journal of Cell Science*, 117(20):4779–4786.
- de Nooijer, S., Wellink, J., Mulder, B., and Bisseling, T. (2009). Non-specific interactions are sufficient to explain the position of heterochromatic chromocenters and nucleoli in interphase nuclei. *Nucleic Acids Research*, 37(11):3558–3568.
- Dechat, T., Adam, S. A., Taimen, P., Shimi, T., and Goldman, R. D. (2010). Nuclear lamins. *Cold Spring Harbor Perspectives in Biology*, 2(11).
- DeGrasse, J. A., DuBois, K. N., Devos, D., Siegel, T. N., Sali, A., Field, M. C., Rout, M. P., and Chait, B. T. (2009). Evidence for a shared nuclear pore complex architecture that is conserved from the last common eukaryotic ancestor. *Molecular & Cellular Proteomics*, 8(9):2119–2130.
- Dekker, J., Marti-Renom, M. A., and Mirny, L. A. (2013). Exploring the three-dimensional organization of genomes: interpreting chromatin interaction data. *Nature Reviews. Genetics*, 14(6):390–403.
- Dey, P. (2010). Cancer nucleus: morphology and beyond. *Diagnostic Cytopathology*, 38(5):382–390.

- Ding, X., Xu, R., Yu, J., Xu, T., Zhuang, Y., and Han, M. (2007). Sun1 is required for telomere attachment to nuclear envelope and gametogenesis in mice. *Developmental Cell*, 12(6):863–872.
- Dittmer, T. A., Stacey, N. J., Sugimoto-Shirasu, K., and Richards, E. J. (2007). Little nuclei genes affecting nuclear morphology in *Arabidopsis thaliana*. *The Plant Cell*, 19(9):2793–2803.
- Dixon, J. R., Selvaraj, S., Yue, F., Kim, A., Li, Y., Shen, Y., Hu, M., Liu, J. S., and Ren, B. (2012). Topological domains in mammalian genomes identified by analysis of chromatin interactions. *Nature*, 485(7398):376–380.
- Douet, J., Blanchard, B., Cuvillier, C., and Tourmente, S. (2008). Interplay of RNA Pol IV and ROS1 During Post-Embryonic 5s rDNA Chromatin Remodeling. *Plant and Cell Physiology*, 49(12):1783–1791.
- Droc, G., Larivière, D., Guignon, V., Yahiaoui, N., This, D., Garsmeur, O., Dereeper, A., Hamelin, C., Argout, X., Dufayard, J.-F., Lengelle, J., Baurens, F.-C., Cenci, A., Pitollat, B., DHont, A., Ruiz, M., Rouard, M., and Bocs, S. (2013). The banana genome hub. *Database: The Journal of Biological Databases and Curation*, 2013.
- DuBois, K. N., Alsford, S., Holden, J. M., Buisson, J., Swiderski, M., Bart, J.-M., Ratushny, A. V., Wan, Y., Bastin, P., Barry, J. D., Navarro, M., Horn, D., Aitchison, J. D., Rout, M. P., and Field, M. C. (2012). Nup-1 is a large oiled-coil nucleoskeletal protein in trypanosomes with lamin-like functions. *PLoS Biology*, 10(3).
- Duc, C., Benoit, M., Le Goff, S., Simon, L., Poulet, A., Cotterell, S., Tatout, C., and Probst, A. V. (2015). The histone chaperone complex HIR maintains nucleosome occupancy and counterbalances impaired histone deposition in CAF-1 complex mutants. *The Plant Journal: For Cell and Molecular Biology*, 81(5):707–722.
- Duroc, Y., Lemhemdi, A., Larchevque, C., Hurel, A., Cuacos, M., Cromer, L., Horlow, C., Armstrong, S. J., Chelysheva, L., and Mercier, R. (2014). The kinesin atpss1 promotes synapsis and is required for proper crossover distribution in meiosis. *PLoS Genetics*, 10(10).
- Ea, V., Baudement, M.-O., Lesne, A., and Forn, T. (2015). Contribution of topological domains and loop formation to 3d chromatin organization. *Genes*, 6(3):734–750.
- Edens, L. J., White, K. H., Jevtic, P., Li, X., and Levy, D. L. (2013). Nuclear size regulation: from single cells to development and disease. *Trends in Cell Biology*, 23(4):151–159.
- Edgar, R. C. (2004). MUSCLE: a multiple sequence alignment method with reduced time and space complexity. *BMC Bioinformatics*, 5:113.

- Ellenberg, J., Siggia, E. D., Moreira, J. E., Smith, C. L., Presley, J. F., Worman, H. J., and Lippincott-Schwartz, J. (1997). Nuclear membrane dynamics and reassembly in living cells: targeting of an inner nuclear membrane protein in interphase and mitosis. *The Journal of Cell Biology*, 138(6):1193–1206.
- Esbelin, H.-A. and Malgouyres, R. (2014). Taylor optimal kernel for derivative estimation. In Barcucci, E., Frosini, A., and Rinaldi, S., editors, *Discrete Geometry for Computer Imagery*, number 8668 in Lecture Notes in Computer Science, pages 384–395. Springer International Publishing.
- Even-Faitelson, L., Hassan-Zadeh, V., Baghestani, Z., and Bazett-Jones, D. P. (2015). Coming to terms with chromatin structure. *Chromosoma*, pages 1–16.
- Fang, Y. (2005). Centromere positioning and dynamics in living arabidopsis plants. *Molecular Biology of the Cell*, 16(12):5710–5718.
- Feng, S., Cokus, S. J., Schubert, V., Zhai, J., Pellegrini, M., and Jacobsen, S. E. (2014). Genome-wide Hi-C analyses in wild-type and mutants reveal high-resolution chromatin interactions in Arabidopsis. *Molecular Cell*, 55(5):694–707.
- Ferrera, D., Canale, C., Marotta, R., Mazzaro, N., Gritti, M., Mazzanti, M., Capelari, S., Cortelli, P., and Gasparini, L. (2014). Lamin B1 overexpression increases nuclear rigidity in autosomal dominant leukodystrophy. *The FASEB Journal*, 28(9):3906–3918.
- Field, M. C., Horn, D., Alford, S., Koreny, L., and Rout, M. P. (2012). Telomeres, tethers and trypanosomes. *Nucleus*, 3(6):478–486.
- Fiserova, J., Kiseleva, E., and Goldberg, M. W. (2009). Nuclear envelope and nuclear pore complex structure and organization in tobacco BY-2 cells. *The Plant Journal: For Cell and Molecular Biology*, 59(2):243–255.
- Folker, E. S., Östlund, C., Luxton, G. W. G., Worman, H. J., and Gundersen, G. G. (2011). Lamin A variants that cause striated muscle disease are defective in anchoring transmembrane actin-associated nuclear lines for nuclear movement. *Proceedings of the National Academy of Sciences*, 108(1):131–136.
- Fourey, S. and Malgouyres, R. (2009). Normals estimation for digital surfaces based on convolutions. *Computers & Graphics*, 33(1):2–10.
- Fransz, P. and de Jong, H. (2011). From nucleosome to chromosome: a dynamic organization of genetic information. *The Plant Journal*, 66(1):4–17.
- Fransz, P., Soppe, W., and Schubert, I. (2003). Heterochromatin in interphase nuclei of *Arabidopsis thaliana*. *Chromosome Research: An International Journal on the Molecular, Supramolecular and Evolutionary Aspects of Chromosome Biology*, 11(3):227–240.
- Fransz, P. F., Armstrong, S., de Jong, J. H., Parnell, L. D., van Drunen, C., Dean, C., Zabel, P., Bisseling, T., and Jones, G. H. (2000). Integrated cytogenetic map

of chromosome arm 4s of *A. thaliana*: structural organization of heterochromatic knob and centromere region. *Cell*, 100(3):367–376.

Fransz, P. F. and de Jong, J. (2002). Chromatin dynamics in plants. *Current Opinion in Plant Biology*, 5(6):560–567.

Fridkin, A., Penkner, A., Jantsch, V., and Gruenbaum, Y. (2009). SUN-domain and KASH-domain proteins during development, meiosis and disease. *Cellular and Molecular Life Sciences*, 66(9):1518–1533.

Friederichs, J. M., Gardner, J. M., Smoyer, C. J., Whetstone, C. R., Gogol, M., Slaughter, B. D., and Jaspersen, S. L. (2012). Genetic analysis of mps3 sun domain mutants in *Saccharomyces cerevisiae* reveals an interaction with the sun-like protein slp1. *G3: Genes|Genomes|Genetics*, 2(12):1703–1718.

Fussner, E., Ching, R. W., and Bazett-Jones, D. P. (2011). Living without 30nm chromatin fibers. *Trends in Biochemical Sciences*, 36(1):1–6.

Gant, T. M., Harris, C. A., and Wilson, K. L. (1999). Roles of lap2 proteins in nuclear assembly and dna replication: truncated lap2 $\beta$  proteins alter lamina assembly envelope formation, nuclear size, and dna replication efficiency in xenopus laevis extracts. *The Journal of Cell Biology*, 144(6):1083–1096.

Gardner, J. M., Smoyer, C. J., Stensrud, E. S., Alexander, R., Gogol, M., Wiegraebe, W., and Jaspersen, S. L. (2011). Targeting of the SUN protein Mps3 to the inner nuclear membrane by the histone variant H2a.Z. *The Journal of Cell Biology*, 193(3):489–507.

Gaut, B. S. and Ross-Ibarra, J. (2008). Selection on major components of angiosperm genomes. *Science*, 320(5875):484–486.

Gerace, L. and Huber, M. D. (2012). Nuclear lamina at the crossroads of the cytoplasm and nucleus. *Journal of Structural Biology*, 177(1):24–31.

Gerlach, W. L. and Bedbrook, J. R. (1979). Cloning and characterization of ribosomal RNA genes from wheat and barley. *Nucleic Acids Research*, 7(7):1869–1885.

Gerlitz, G. and Bustin, M. (2011). The role of chromatin structure in cell migration. *Trends in cell biology*, 21(1):6–11.

Geyer, P. K., Vitalini, M. W., and Wallrath, L. L. (2011). Nuclear organization: taking a position on gene expression. *Current Opinion in Cell Biology*, 23(3):354–359.

Goldberg, M. W., Fiserova, J., Huttenlauch, I., and Stick, R. (2008a). A new model for nuclear lamina organization. *Biochemical Society Transactions*, 36(Pt 6):1339–1343.

Goldberg, M. W., Huttenlauch, I., Hutchison, C. J., and Stick, R. (2008b). Filaments made from A- and B-type lamins differ in structure and organization. *Journal of Cell Science*, 121(Pt 2):215–225.



- Gonzalez, D., Malgouyres, R., Esbelin, H.-A., and Samir, C. (2013). Convergence of level-wise convolution differential estimators. In Gonzalez-Diaz, R., Jimenez, M.-J., and Medrano, B., editors, *Discrete Geometry for Computer Imagery*, number 7749 in Lecture Notes in Computer Science, pages 335–346. Springer Berlin Heidelberg.
- Gonzalez, R. and Woods, R. (1992). *Digital image processing*. Addison-Wesley Longman Publishing Co., Inc., Boston, MA, USA.
- Görlich, D. and Kutay, U. (1999). Transport between the cell nucleus and the cytoplasm. *Annual Review of Cell and Developmental Biology*, 15:607–660.
- Goto, C., Tamura, K., Fukao, Y., Shimada, T., and Hara-Nishimura, I. (2014). The novel nuclear envelope protein kaku4 modulates nuclear morphology in arabidopsis. *The Plant Cell*, 26(5):2143–2155.
- Graumann, K. (2014). Evidence for LINC1-SUN associations at the plant nuclear periphery. *PLoS ONE*, 9(3):e93406.
- Graumann, K. and Evans, D. E. (2010). Plant SUN domain proteins: components of putative plant LINC complexes? *Plant Signaling & Behavior*, 5(2):154–156.
- Graumann, K. and Evans, D. E. (2011). Nuclear envelope dynamics during plant cell division suggest common mechanisms between kingdoms. *The Biochemical Journal*, 435(3):661–667.
- Graumann, K., Irons, S. L., Runions, J., and Evans, D. E. (2007). Retention and mobility of the mammalian lamin B receptor in the plant nuclear envelope. *Biology of the Cell / Under the Auspices of the European Cell Biology Organization*, 99(10):553–562.
- Graumann, K., Runions, J., and Evans, D. E. (2010). Characterization of SUN-domain proteins at the higher plant nuclear envelope. *The Plant Journal*, 61(1):134–144.
- Graumann, K., Vanrobays, E., Tutois, S., Probst, A. V., Evans, D. E., and Tatout, C. (2014). Characterization of two distinct subfamilies of SUN-domain proteins in Arabidopsis and their interactions with the novel KASH-domain protein AtTIK. *Journal of Experimental Botany*, page eru368.
- Gregory, T. R. (2005). The C-value enigma in plants and animals: a review of parallels and an appeal for partnership. *Annals of Botany*, 95(1):133–146.
- Grob, S., Schmid, M. W., and Grossniklaus, U. (2014). Hi-C analysis in Arabidopsis identifies the KNOT, a structure with similarities to the fl locus of Drosophila. *Molecular Cell*, 55(5):678–693.
- Guilak, F. (1995). Compression-induced changes in the shape and volume of the chondrocyte nucleus. *Journal of Biomechanics*, 28(12):1529–1541.

- Guilly, M. N., Kolb, J. P., Gosti, F., Godeau, F., and Courvalin, J. C. (1990). Lamins A and C are not expressed at early stages of human lymphocyte differentiation. *Experimental Cell Research*, 189(1):145–147.
- Guimil, S. and Dunand, C. (2007). Cell growth and differentiation in Arabidopsis epidermal cells. *Journal of Experimental Botany*, 58(14):3829–3840.
- Habermann, F. A., Cremer, M., Walter, J., Kreth, G., Von Hase, J., Bauer, K., Wienberg, J., Cremer, C., Cremer, T., and Solovei, I. (2001). Arrangements of macro- and microchromosomes in chicken cells. *Chromosome research an international journal on the molecular supramolecular and evolutionary aspects of chromosome biology*, 9(7):569–584.
- Hancock, R. (2004). A role for macromolecular crowding effects in the assembly and function of compartments in the nucleus. *Journal of Structural Biology*, 146(3):281–290.
- Haque, F., Mazzeo, D., Patel, J. T., Smallwood, D. T., Ellis, J. A., Shanahan, C. M., and Shackleton, S. (2010). Mammalian sun protein interaction networks at the inner nuclear membrane and their role in laminopathy disease processes. *Journal of Biological Chemistry*, 285(5):3487–3498.
- Harris, H. (1967). The reactivation of the red cell nucleus. *Journal of Cell Science*, 2(1):23–28.
- Heitz, E. (1928). Das heterochromatin der mause. *Jahrb Wiss Botanik* 69: 762818.
- Hildebrand, T. and Rügsegger, P. (1997). A new method for the model-independent assessment of thickness in three-dimensional images. *Journal of Microscopy*, 185(1):67–75.
- Hirochika, H., Okamoto, H., and Kakutani, T. (2000). Silencing of retrotransposons in Arabidopsis and reactivation by the ddm1 mutation. *The Plant Cell*, 12(3):357–369.
- Ho, C. Y. and Lammerding, J. (2012). Lamins at a glance. *Journal of Cell Science*, 125(Pt 9):2087–2093.
- Hoffmann, K., Sperling, K., Olins, A. L., and Olins, D. E. (2007). The granulocyte nucleus and lamin B receptor: avoiding the ovoid. *Chromosoma*, 116(3):227–235.
- Horn, H. F., Kim, D. I., Wright, G. D., Wong, E. S. M., Stewart, C. L., Burke, B., and Roux, K. J. (2013). A mammalian KASH domain protein coupling meiotic chromosomes to the cytoskeleton. *The Journal of Cell Biology*, 202(7):1023–1039.
- Horvitz, H. R. and Sulston, J. E. (1980). Isolation and genetic characterization of cell-lineage mutants of the nematode *Caenorhabditis elegans*. *Genetics*, 96(2):435–454.

Hu, T. T., Pattyn, P., Bakker, E. G., Cao, J., Cheng, J.-F., Clark, R. M., Fahlgren, N., Fawcett, J. A., Grimwood, J., Gundlach, H., Haberer, G., Hollister, J. D., Ossowski, S., Ottillar, R. P., Salamov, A. A., Schneeberger, K., Spannagl, M., Wang, X., Yang, L., Nasrallah, M. E., Bergelson, J., Carrington, J. C., Gaut, B. S., Schmutz, J., Mayer, K. F. X., Van de Peer, Y., Grigoriev, I. V., Nordborg, M., Weigel, D., and Guo, Y.-L. (2011). The *Arabidopsis lyrata* genome sequence and the basis of rapid genome size change. *Nature Genetics*, 43(5):476–481.

Husson, F., Josse, J., and Lê, P. (2009). FactoMineR, An R package dedicated to exploratory multivariate analysis.

Initiative, T. A. G. (2000). Analysis of the genome sequence of the flowering plant *Arabidopsis thaliana*. *Nature*, 408(6814):796–815.

International Rice Genome Sequencing Project (2005). The map-based sequence of the rice genome. *Nature*, 436(7052):793–800.

Iwabuchi, K. and Takagi, S. (2008). How and why do plant nuclei move in response to light? *Plant Signaling & Behavior*, 3(4):266–268.

Jacob, Y., Feng, S., LeBlanc, C. A., Bernatavichute, Y. V., Stroud, H., Cokus, S., Johnson, L. M., Pellegrini, M., Jacobsen, S. E., and Michaels, S. D. (2009). ATXR5 and ATXR6 are H3k27 monomethyltransferases required for chromatin structure and gene silencing. *Nature Structural & Molecular Biology*, 16(7):763–768.

Jacob, Y., Stroud, H., LeBlanc, C., Feng, S., Zhuo, L., Caro, E., Hassel, C., Gutierrez, C., Michaels, S. D., and Jacobsen, S. E. (2010). Regulation of heterochromatic DNA replication by histone H3 lysine 27 methyltransferases. *Nature*, 466(7309):987–991.

Jaillon, O., Aury, J.-M., Noel, B., Policriti, A., Clepet, C., Casagrande, A., Choisne, N., Aubourg, S., Vitulo, N., Jubin, C., Vezzi, A., Legeai, F., Huguency, P., Dasilva, C., Horner, D., Mica, E., Jublot, D., Poulain, J., Bruyère, C., Billault, A., Segurens, B., Gouyvenoux, M., Ugarte, E., Cattonaro, F., Anthouard, V., Vico, V., Fabbro, C. D., Alaux, M., Gaspero, G. D., Dumas, V., Felice, N., Paillard, S., Juman, I., Moroldo, M., Scalabrin, S., Canaguier, A., Clainche, I. L., Malacrida, G., Durand, E., Pesole, G., Laucou, V., Chatelet, P., Merdinoglu, D., Delledonne, M., Pezzotti, M., Lecharny, A., Scarpelli, C., Artiguenave, F., Pé, M. E., Valle, G., Morgante, M., Caboche, M., Adam-Blondon, A.-F., Weissenbach, J., Qutier, F., and Wincker, P. (2007). The grapevine genome sequence suggests ancestral hexaploidization in major angiosperm phyla. *Nature*, 449(7161):463–467.

Janesick, J. R. (2001). *Scientific charge-coupled devices*. SPIE Press.

Janski, N., Masoud, K., Batzenschlager, M., Herzog, E., Evrard, J.-L., Houlon, G., Bourge, M., Chabout, M.-E., and Schmit, A.-C. (2012). The GCP3-interacting proteins GIP1 and GIP2 are required for  $\gamma$ -tubulin complex protein localization, spindle integrity, and chromosomal stability. *The Plant Cell*, 24(3):1171–1187.

Jasencakova, Z., Meister, A., and Schubert, I. (2001). Chromatin organization and its relation to replication and histone acetylation during the cell cycle in barley. *Chromosoma*, 110(2):83–92.

Jeong, S. Y., Rose, A., Joseph, J., Dasso, M., and Meier, I. (2005). Plant-specific mitotic targeting of RanGAP requires a functional WPP domain. *The Plant Journal*, 42(2):270–282.

Jevtić, P., Edens, L. J., Vuković, L. D., and Levy, D. L. (2014). Sizing and shaping the nucleus: mechanisms and significance. *Current Opinion in Cell Biology*, 28:16–27.

Jevtić, P. and Levy, D. L. (2014). Mechanisms of nuclear size regulation in model systems and cancer. In Schirmer, E. C. and Heras, J. I. d. l., editors, *Cancer Biology and the Nuclear Envelope*, number 773 in Advances in Experimental Medicine and Biology, pages 537–569. Springer New York.

Jiao, Y., Leebens-Mack, J., Ayyampalayam, S., Bowers, J. E., McKain, M. R., McNeal, J., Rolf, M., Ruzicka, D. R., Wafula, E., Wickett, N. J., Wu, X., Zhang, Y., Wang, J., Zhang, Y., Carpenter, E. J., Deyholos, M. K., Kutchan, T. M., Chanderbali, A. S., Soltis, P. S., Stevenson, D. W., McCombie, R., Pires, J. C., Wong, G. K.-S., Soltis, D. E., and dePamphilis, C. W. (2012). A genome triplication associated with early diversification of the core eudicots. *Genome Biology*, 13(1):R3.

Jiao, Y., Wickett, N. J., Ayyampalayam, S., Chanderbali, A. S., Landherr, L., Ralph, P. E., Tomsho, L. P., Hu, Y., Liang, H., Soltis, P. S., Soltis, D. E., Clifton, S. W., Schlarbaum, S. E., Schuster, S. C., Ma, H., Leebens-Mack, J., and dePamphilis, C. W. (2011). Ancestral polyploidy in seed plants and angiosperms. *Nature*, 473(7345):97–100.

Jorgensen, P., Edgington, N. P., Schneider, B. L., Rupe, I., Tyers, M., and Futcher, B. (2007). The size of the nucleus increases as yeast cells grow. *Molecular Biology of the Cell*, 18(9):3523–3532.

Kasper, L. H., Brindle, P. K., Schnabel, C. A., Pritchard, C. E., Cleary, M. L., and van Deursen, J. M. (1999). CREB binding protein interacts with nucleoporin-specific FG repeats that activate transcription and mediate NUP98-HOXA9 oncogenicity. *Molecular and Cellular Biology*, 19(1):764–776.

Ketelaar, T., Faivre-Moskalenko, C., Esseling, J. J., de Ruijter, N. C. A., Grierson, C. S., Dogterom, M., and Emons, A. M. C. (2002). Positioning of nuclei in Arabidopsis root hairs: an actin-regulated process of tip growth. *The Plant Cell*, 14(11):2941–2955.

Khatau, S. B., Hale, C. M., Stewart-Hutchinson, P. J., Patel, M. S., Stewart, C. L., Searson, P. C., Hodzic, D., and Wirtz, D. (2009). A perinuclear actin cap regulates nuclear shape. *Proceedings of the National Academy of Sciences of the United States of America*, 106(45):19017–19022.

- Kim, D., Pertea, G., Trapnell, C., Pimentel, H., Kelley, R., and Salzberg, S. L. (2013). TopHat2: accurate alignment of transcriptomes in the presence of insertions, deletions and gene fusions. *Genome Biology*, 14(4):R36.
- Kim, D.-H., Li, B., Si, F., Phillip, J. M., Wirtz, D., and Sun, S. X. (2015). Volume regulation and shape bifurcation in the cell nucleus. *Journal of Cell Science*, 128(18):3375–3385.
- Kiseleva, E., Morozova, K. N., Voeltz, G. K., Allen, T. D., and Goldberg, M. W. (2007). Reticulon 4a/NogoA locates to regions of high membrane curvature and may have a role in nuclear envelope growth. *Journal of Structural Biology*, 160(2):224–235.
- Krüger, A., Batsios, P., Baumann, O., Luckert, E., Schwarz, H., Stick, R., Meyer, I., and Gräf, R. (2012). Characterization of NE81, the first lamin-like nucleoskeleton protein in a unicellular organism. *Molecular Biology of the Cell*, 23(2):360–370.
- Kyte, J. and Doolittle, R. F. (1982). A simple method for displaying the hydrophobic character of a protein. *Journal of Molecular Biology*, 157(1):105–132.
- Lammerding, J., Fong, L. G., Ji, J. Y., Reue, K., Stewart, C. L., Young, S. G., and Lee, R. T. (2006). Lamins A and C but not lamin b1 regulate nuclear mechanics. *Journal of Biological Chemistry*, 281(35):25768–25780.
- Layat, E., Sáez-Vásquez, J., and Tourmente, S. (2012). Regulation of Pol I-Transcribed 45s rDNA and Pol III-Transcribed 5s rDNA in Arabidopsis. *Plant and Cell Physiology*, 53(2):267–276.
- Lehner, C. F., Stick, R., Eppenberger, H. M., and Nigg, E. A. (1987). Differential expression of nuclear lamin proteins during chicken development. *The Journal of Cell Biology*, 105(1):577–587.
- Letunic, I. and Bork, P. (2011). Interactive Tree Of Life v2: online annotation and display of phylogenetic trees made easy. *Nucleic Acids Research*, 39(suppl 2):W475–W478.
- Levy, D. L. and Heald, R. (2010). Nuclear size is regulated by importin $\alpha$  and ntf2 in xenopus. *Cell*, 143(2):288–298.
- Li, B., Carey, M., and Workman, J. L. (2007). The role of chromatin during transcription. *Cell*, 128(4):707–719.
- Lin, F. and Worman, H. J. (1993). Structural organization of the human gene encoding nuclear lamin A and nuclear lamin C. *The Journal of Biological Chemistry*, 268(22):16321–16326.
- Lindeman, R. E. and Pelegri, F. (2012). Localized products of futile cycle/lrmp promote centrosome-nucleus attachment in the zebrafish zygote. *Current Biology*, 22(10):843–851.

- Liu, C. and Weigel, D. (2015). Chromatin in 3d: progress and prospects for plants. *Genome Biology*, 16(1):170.
- Louwers, M., Bader, R., Haring, M., van Driel, R., de Laat, W., and Stam, M. (2009). Tissue- and expression level-specific chromatin looping at maize b1 epialleles. *The Plant Cell*, 21(3):832–842.
- Lu, W., Schneider, M., Neumann, S., Jaeger, V.-M., Taranum, S., Munck, M., Cartwright, S., Richardson, C., Carthew, J., Noh, K., Goldberg, M., Noegel, A. A., and Karakesisoglou, I. (2012). Nesprin interchain associations control nuclear size. *Cellular and Molecular Life Sciences*, 69(20):3493–3509.
- Luger, K., Mäder, A. W., Richmond, R. K., Sargent, D. F., and Richmond, T. J. (1997). Crystal structure of the nucleosome core particle at 2.8 Å resolution. *Nature*, 389(6648):251–260.
- Lüke, Y., Zaim, H., Karakesisoglou, I., Jaeger, V. M., Sellin, L., Lu, W., Schneider, M., Neumann, S., Beijer, A., Munck, M., Padmakumar, V. C., Gloy, J., Walz, G., and Noegel, A. A. (2008). Nesprin-2 Giant (NUANCE) maintains nuclear envelope architecture and composition in skin. *Journal of Cell Science*, 121(11):1887–1898.
- Lukosz, W. and Marchand, M. (1963). Optischen abbildung unter überschreitung der beugungsbedingten auflösungsgrenze. *Optica Acta: International Journal of Optics*, 10(3):241–255.
- Luthra, R., Kerr, S. C., Harreman, M. T., Apponi, L. H., Fasken, M. B., Ramineni, S., Chaurasia, S., Valentini, S. R., and Corbett, A. H. (2007). Actively transcribed GAL genes can be physically linked to the nuclear pore by the SAGA chromatin modifying complex. *The Journal of Biological Chemistry*, 282(5):3042–3049.
- Mahy, N. L., Perry, P. E., Gilchrist, S., Baldock, R. A., and Bickmore, W. A. (2002). Spatial organization of active and inactive genes and noncoding DNA within chromosome territories. *The Journal of Cell Biology*, 157(4):579–589.
- Makova, K. D. and Hardison, R. C. (2015). The effects of chromatin organization on variation in mutation rates in the genome. *Nature Reviews Genetics*, 16(4):213–223.
- Malone, C. J., Fixsen, W. D., Horvitz, H. R., and Han, M. (1999). UNC-84 localizes to the nuclear envelope and is required for nuclear migration and anchoring during *C. elegans*. *Development*, 126(14):3171–3181.
- Maluszynska, J. and Heslop-Harrison, J. (1991). Localization of tandemly repeated DMA sequences in *Arabidopsis thaliana*. *The Plant Journal*, 1(2):159–166.
- Margalit, A., Brachner, A., Gotzmann, J., Foisner, R., and Gruenbaum, Y. (2007). Barrier-to-autointegration factor a BAFfling little protein. *Trends in Cell Biology*, 17(4):202–208.

Martinez-Zapater, J. M., Estelle, M. A., and Somerville, C. R. (1986). A highly repeated DNA sequence in *Arabidopsis thaliana*. *Molecular and General Genetics MGG*, 204(3):417–423.

Martini, F. J. and Valdeolmillos, M. (2010). Actomyosin contraction at the cell rear drives nuclear translocation in migrating cortical interneurons. *The Journal of Neuroscience*, 30(25):8660–8670.

Masoud, K., Herzog, E., Chabout, M.-E., and Schmit, A.-C. (2013). Microtubule nucleation and establishment of the mitotic spindle in vascular plant cells. *The Plant Journal*, 75(2):245–257.

Melaragno, J. E., Mehrotra, B., and Coleman, A. W. (1993). Relationship between endopolyploidy and cell size in epidermal tissue of arabidopsis. *The Plant Cell*, 5(11):1661–1668.

Merchant, S. S., Prochnik, S. E., Vallon, O., Harris, E. H., Karpowicz, S. J., Witman, G. B., Terry, A., Salamov, A., Fritz-Laylin, L. K., Marchal-Drouard, L., Marshall, W. F., Qu, L.-H., Nelson, D. R., Sanderfoot, A. A., Spalding, M. H., Kapitonov, V. V., Ren, Q., Ferris, P., Lindquist, E., Shapiro, H., Lucas, S. M., Grimwood, J., Schmutz, J., Cardol, P., Cerutti, H., Chanfreau, G., Chen, C.-L., Cognat, V., Croft, M. T., Dent, R., Dutcher, S., Fernández, E., Fukuzawa, H., González-Ballester, D., González-Halphen, D., Hallmann, A., Hanikenne, M., Hippler, M., Inwood, W., Jabbari, K., Kalanon, M., Kuras, R., Lefebvre, P. A., Lemaire, S. D., Lobanov, A. V., Lohr, M., Manuell, A., Meier, I., Mets, L., Mittag, M., Mittelmeier, T., Moroney, J. V., Moseley, J., Napoli, C., Nedelcu, A. M., Niyogi, K., Novoselov, S. V., Paulsen, I. T., Pazour, G., Purton, S., Ral, J.-P., Riaño-Pachón, D. M., Riekhof, W., Rymarquis, L., Schroda, M., Stern, D., Umen, J., Willows, R., Wilson, N., Zimmer, S. L., Allmer, J., Balk, J., Bisova, K., Chen, C.-J., Elias, M., Gendler, K., Hauser, C., Lamb, M. R., Ledford, H., Long, J. C., Minagawa, J., Page, M. D., Pan, J., Pootakham, W., Roje, S., Rose, A., Stahlberg, E., Terauchi, A. M., Yang, P., Ball, S., Bowler, C., Dieckmann, C. L., Gladyshev, V. N., Green, P., Jorgensen, R., Mayfield, S., Mueller-Roeber, B., Rajamani, S., Sayre, R. T., Brokstein, P., Dubchak, I., Goodstein, D., Hornick, L., Huang, Y. W., Jhaveri, J., Luo, Y., Martnez, D., Ngau, W. C. A., Otilar, B., Poliakov, A., Porter, A., Szajkowski, L., Werner, G., Zhou, K., Grigoriev, I. V., Rokhsar, D. S., and Grossman, A. R. (2007). The *Chlamydomonas* genome reveals the evolution of key animal and plant functions. *Science (New York, N.Y.)*, 318(5848):245–250.

Ming, R., Hou, S., Feng, Y., Yu, Q., Dionne-Laporte, A., Saw, J. H., Senin, P., Wang, W., Ly, B. V., Lewis, K. L. T., Salzberg, S. L., Feng, L., Jones, M. R., Skelton, R. L., Murray, J. E., Chen, C., Qian, W., Shen, J., Du, P., Eustice, M., Tong, E., Tang, H., Lyons, E., Paull, R. E., Michael, T. P., Wall, K., Rice, D. W., Albert, H., Wang, M.-L., Zhu, Y. J., Schatz, M., Nagarajan, N., Acob, R. A., Guan, P., Blas, A., Wai, C. M., Ackerman, C. M., Ren, Y., Liu, C., Wang, J., Wang, J., Na, J.-K., Shakirov, E. V., Haas, B., Thimmapuram, J., Nelson, D., Wang, X., Bowers, J. E., Gschwend, A. R., Delcher, A. L., Singh, R., Suzuki, J. Y., Tripathi, S., Neupane, K., Wei, H., Irikura, B., Paidi, M., Jiang, N., Zhang, W., Presting,

G., Windsor, A., Navajas-Prez, R., Torres, M. J., Feltus, F. A., Porter, B., Li, Y., Burroughs, A. M., Luo, M.-C., Liu, L., Christopher, D. A., Mount, S. M., Moore, P. H., Sugimura, T., Jiang, J., Schuler, M. A., Friedman, V., Mitchell-Olds, T., Shippen, D. E., dePamphilis, C. W., Palmer, J. D., Freeling, M., Paterson, A. H., Gonsalves, D., Wang, L., and Alam, M. (2008). The draft genome of the transgenic tropical fruit tree papaya (*Carica papaya* Linnaeus). *Nature*, 452(7190):991–996.

Ming, R., VanBuren, R., Liu, Y., Yang, M., Han, Y., Li, L.-T., Zhang, Q., Kim, M.-J., Schatz, M. C., Campbell, M., Li, J., Bowers, J. E., Tang, H., Lyons, E., Ferguson, A. A., Narzisi, G., Nelson, D. R., Blaby-Haas, C. E., Gschwend, A. R., Jiao, Y., Der, J. P., Zeng, F., Han, J., Min, X. J., Hudson, K. A., Singh, R., Grennan, A. K., Karpowicz, S. J., Watling, J. R., Ito, K., Robinson, S. A., Hudson, M. E., Yu, Q., Mockler, T. C., Carroll, A., Zheng, Y., Sunkar, R., Jia, R., Chen, N., Arro, J., Wai, C. M., Wafula, E., Spence, A., Han, Y., Xu, L., Zhang, J., Peery, R., Haus, M. J., Xiong, W., Walsh, J. A., Wu, J., Wang, M.-L., Zhu, Y. J., Paull, R. E., Britt, A. B., Du, C., Downie, S. R., Schuler, M. A., Michael, T. P., Long, S. P., Ort, D. R., Schopf, J. W., Gang, D. R., Jiang, N., Yandell, M., dePamphilis, C. W., Merchant, S. S., Paterson, A. H., Buchanan, B. B., Li, S., and Shen-Miller, J. (2013). Genome of the long-living sacred lotus (*Nelumbo nucifera* Gaertn.). *Genome Biology*, 14(5):R41.

Minguez, A. and Espina, S. M. D. d. l. (1993). Immunological characterization of lamins in the nuclear matrix of onion cells. *Journal of Cell Science*, 106(1):431–439.

Mitcham, J. L., Parnet, P., Bonnert, T. P., Garka, K. E., Gerhart, M. J., Slack, J. L., Gayle, M. A., Dower, S. K., and Sims, J. E. (1996). T1/ST2 signaling establishes it as a member of an expanding interleukin-1 receptor family. *Journal of Biological Chemistry*, 271(10):5777–5783.

Miyoshi, D. and Sugimoto, N. (2008). Molecular crowding effects on structure and stability of DNA. *Biochimie*, 90(7):1040–1051.

Mizuguchi, T., Fudenberg, G., Mehta, S., Belton, J.-M., Taneja, N., Folco, H. D., FitzGerald, P., Dekker, J., Mirny, L., Barrowman, J., and Grewal, S. I. S. (2014). Cohesin-dependent globules and heterochromatin shape 3d genome architecture in *S. pombe*. *Nature*, 516(7531):432–435.

Morimoto, A., Shibuya, H., Zhu, X., Kim, J., Ishiguro, K.-i., Han, M., and Watanabe, Y. (2012). A conserved KASH domain protein associates with telomeres, SUN1, and dynactin during mammalian meiosis. *The Journal of Cell Biology*, 198(2):165–172.

Murphy, S. P. and Bass, H. W. (2012). The maize (*Zea mays*) desynaptic (dy) mutation defines a pathway for meiotic chromosome segregation, linking nuclear morphology, telomere distribution and synapsis. *Journal of Cell Science*, 125(Pt 15):3681–3690.

Murphy, S. P., Simmons, C. R., and Bass, H. W. (2010). Structure and expression of the maize (*Zea mays* L.) SUN-domain protein gene family: evidence for the



existence of two divergent classes of SUN proteins in plants. *BMC Plant Biology*, 10(1):269.

Nagai, R. (1993). Regulation of intracellular movements in plant cells by environmental stimuli. in *International Review of Cytology* eds Jeon K. W., Jarvik J., editors. (San Diego, CA: Academic Press;) 251310.

Nagaki, K., Talbert, P. B., Zhong, C. X., Dawe, R. K., Henikoff, S., and Jiang, J. (2003). Chromatin immunoprecipitation reveals that the 180-bp satellite repeat is the key functional dna element of *Arabidopsis thaliana* centromeres. *Genetics*, 163(3):1221–1225.

Neil, M. A., Juskaitis, R., and Wilson, T. (1997). Method of obtaining optical sectioning by using structured light in a conventional microscope. *Optics Letters*, 22(24):1905–1907.

Neumann, F. R. and Nurse, P. (2007). Nuclear size control in fi yeast. *The Journal of Cell Biology*, 179(4):593–600.

Nora, E. P., Lajoie, B. R., Schulz, E. G., Giorgetti, L., Okamoto, I., Servant, N., Piolot, T., van Berkum, N. L., Meisig, J., Sedat, J., Gribnau, J., Barillot, E., Blüthgen, N., Dekker, J., and Heard, E. (2012). Spatial partitioning of the regulatory landscape of the X-inactivation centre. *Nature*, 485(7398):381–385.

Nyquist, H. (1928). Certain topics in telegraph transmission theory. *American Institute of Electrical Engineers, Transactions of the*, 47(2):617–644.

Nystedt, B., Street, N. R., Wetterbom, A., Zuccolo, A., Lin, Y.-C., Scofield, D. G., Vezzi, F., Delhomme, N., Giacomello, S., Alexeyenko, A., Vicedomini, R., Sahlin, K., Sherwood, E., Elfstrand, M., Gramzow, L., Holmberg, K., Hällman, J., Keech, O., Klasson, L., Koriabine, M., Kucukoglu, M., Källner, M., Luthman, J., Lysholm, F., Niittylä, T., Olson, A., Rilakovic, N., Ritland, C., Rosselló, J. A., Sena, J., Svensson, T., Talavera-López, C., Theien, G., Tuominen, H., Vanneste, K., Wu, Z.-Q., Zhang, B., Zerbe, P., Arvestad, L., Bhalerao, R., Bohlmann, J., Bousquet, J., Garcia Gil, R., Hvidsten, T. R., de Jong, P., MacKay, J., Morgante, M., Ritland, K., Sundberg, B., Lee Thompson, S., Van de Peer, Y., Andersson, B., Nilsson, O., Ingvarsson, P. K., Lundeberg, J., and Jansson, S. (2013). The Norway spruce genome sequence and conifer genome evolution. *Nature*, 497(7451):579–584.

Oda, Y. and Fukuda, H. (2011). Dynamics of Arabidopsis SUN proteins during mitosis and their involvement in nuclear shaping. *The Plant Journal*, 66(4):629–641.

Olins, A. L., Zwerger, M., Herrmann, H., Zentgraf, H., Simon, A. J., Monestier, M., and Olins, D. E. (2008). The human granulocyte nucleus: unusual nuclear envelope and heterochromatin composition. *European Journal of Cell Biology*, 87(5):279–290.

Otero, S., Desvoyes, B., and Gutierrez, C. (2014). Histone H3 dynamics in plant cell cycle and development. *Cytogenetic and Genome Research*, 143(1-3):114–124.

Otsu, N. (1979). A threshold selection method from gray-level histograms. *IEEE Transactions on Systems, Man, and Cybernetics: Systems*, 9 (1): 6266.

Palenik, B., Grimwood, J., Aerts, A., Rouz, P., Salamov, A., Putnam, N., Dupont, C., Jorgensen, R., Derelle, E., Rombauts, S., Zhou, K., Otilar, R., Merchant, S. S., Podell, S., Gaasterland, T., Napoli, C., Gendler, K., Manuell, A., Tai, V., Vallon, O., Piganeau, G., Jancek, S., Heijde, M., Jabbari, K., Bowler, C., Lohr, M., Robbens, S., Werner, G., Dubchak, I., Pazour, G. J., Ren, Q., Paulsen, I., Delwiche, C., Schmutz, J., Rokhsar, D., Van de Peer, Y., Moreau, H., and Grigoriev, I. V. (2007). The tiny eukaryote *Ostreococcus* provides genomic insights into the paradox of plankton speciation. *Proceedings of the National Academy of Sciences of the United States of America*, 104(18):7705–7710.

Parry, G. (2015). The plant nuclear envelope and regulation of gene expression. *Journal of Experimental Botany*, 66(6):1673–1685.

Pawar, V. (2015). *Novel plant nuclear envelope-associated coiled-coil proteins*. PhD thesis, Oxford Brookes University, Oxford.

Pawley, J. B. (2006). *Handbook Of Biological Confocal Microscopy*. Springer.

Pearson, C. G. and Bloom, K. (2004). Dynamic microtubules lead the way for spindle positioning. *Nature Reviews. Molecular Cell Biology*, 5(6):481–492.

Pecinka, A. and Mittelsten Scheid, O. (2012). Stress-Induced Chromatin Changes: A Critical View on Their Heritability. *Plant and Cell Physiology*, 53(5):801–808.

Pecinka, A., Schubert, V., Meister, A., Kreth, G., Klatter, M., Lysak, M. A., Fuchs, J., and Schubert, I. (2004). Chromosome territory arrangement and homologous pairing in nuclei of *Arabidopsis thaliana* are predominantly random except for NOR-bearing chromosomes. *Chromosoma*, 113(5):258–269.

Pilot, F., Philippe, J.-M., Lemmers, C., Chauvin, J.-P., and Lecuit, T. (2006). Developmental control of nuclear morphogenesis and anchoring by charleston, identified in a functional genomic screen of *Drosophila* cellularisation. *Development*, 133(4):711–723.

Poulet, A., Arganda-Carreras, I., Legland, D., Probst, A. V., Andrey, P., and Tatout, C. (2015). NucleusJ: an ImageJ plugin for quantifying 3d images of inter-phase nuclei. *Bioinformatics (Oxford, England)*, 31(7):1144–1146.

Price, M. N., Dehal, P. S., and Arkin, A. P. (2010). Fasttree 2 approximately maximum-likelihood trees for large alignments. *PLoS ONE*, 5(3):e9490.

Probst, A. V., Dunleavy, E., and Almouzni, G. (2009). Epigenetic inheritance during the cell cycle. *Nature Reviews Molecular Cell Biology*, 10(3):192–206.

Probst, A. V., Fransz, P. F., Paszkowski, J., and Mittelsten Scheid, O. (2003). Two means of transcriptional reactivation within heterochromatin. *The Plant Journal: For Cell and Molecular Biology*, 33(4):743–749.

Project, A. G., Albert, V. A., Barbazuk, W. B., dePamphilis, C. W., Der, J. P., Leebens-Mack, J., Ma, H., Palmer, J. D., Rounsley, S., Sankoff, D., Schuster, S. C., Soltis, D. E., Soltis, P. S., Wessler, S. R., Wing, R. A., Albert, V. A., Ammiraju, J. S. S., Barbazuk, W. B., Chamala, S., Chanderbali, A. S., dePamphilis, C. W., Der, J. P., Determann, R., Leebens-Mack, J., Ma, H., Ralph, P., Rounsley, S., Schuster, S. C., Soltis, D. E., Soltis, P. S., Talag, J., Tomsho, L., Walts, B., Wanke, S., Wing, R. A., Albert, V. A., Barbazuk, W. B., Chamala, S., Chanderbali, A. S., Chang, T.-H., Determann, R., Lan, T., Soltis, D. E., Soltis, P. S., Arikrit, S., Axtell, M. J., Ayyampalayam, S., Barbazuk, W. B., Burnette, J. M., Chamala, S., Paoli, E. D., dePamphilis, C. W., Der, J. P., Estill, J. C., Farrell, N. P., Harkess, A., Jiao, Y., Leebens-Mack, J., Liu, K., Mei, W., Meyers, B. C., Shahid, S., Wafula, E., Walts, B., Wessler, S. R., Zhai, J., Zhang, X., Albert, V. A., Carretero-Paulet, L., dePamphilis, C. W., Der, J. P., Jiao, Y., Leebens-Mack, J., Lyons, E., Sankoff, D., Tang, H., Wafula, E., Zheng, C., Albert, V. A., Altman, N. S., Barbazuk, W. B., Carretero-Paulet, L., dePamphilis, C. W., Der, J. P., Estill, J. C., Jiao, Y., Leebens-Mack, J., Liu, K., Mei, W., Wafula, E., Altman, N. S., Arikrit, S., Axtell, M. J., Chamala, S., Chanderbali, A. S., Chen, F., Chen, J.-Q., Chiang, V., Paoli, E. D., dePamphilis, C. W., Der, J. P., Determann, R., Fogliani, B., Guo, C., Harholt, J., Harkess, A., Job, C., Job, D., Kim, S., Kong, H., Leebens-Mack, J., Li, G., Li, L., Liu, J., Ma, H., Meyers, B. C., Park, J., Qi, X., Rajjou, L., Burtet-Sarramegna, V., Sederoff R., Shahid, S., Soltis, D. E., Soltis, P. S., Sun, Y.-H., Ulvskov, P., Villegente, M., Xue, J.-Y., Yeh, T.-F., Yu, X., Zhai, J., Acosta, J. J., Albert, V. A., Barbazuk, W. B., Bruenn, R. A., Chamala, S., Kochko, A. d., dePamphilis, C. W., Der, J. P., Herrera-Estrella, L. R., Ibarra-Laclette, E., Kirst, M., Leebens-Mack, J., Pissis, S. P., Poncet, V., Schuster, S. C., Soltis, D. E., Soltis, P. S., and Tomsho, L. (2013). The Amborella Genome and the Evolution of Flowering Plants. *Science*, 342(6165):1241089.

Prüfert, K., Vogel, A., and Krohne, G. (2004). The lamin CxxM motif promotes nuclear membrane growth. *Journal of Cell Science*, 117(25):6105–6116.

Qian, P., Hou, S., and Guo, G. (2009). Molecular mechanisms controlling pavement cell shape in Arabidopsis leaves. *Plant Cell Reports*, 28(8):1147–1157.

R Core Team (2013). R: A language and environment for statistical computing.

Rabl, C. (1885). Über zelltheilung.

rapa Genome Sequencing Project Consortium, T. B. (2011). The genome of the mesopolyploid crop species *Brassica rapa*. *Nature Genetics*, 43(10):1035–1039.

Reinsch, S. and Gonczy, P. (1998). Mechanisms of nuclear positioning. *Journal of Cell Science*, 111(16):2283–2295.

Rensing, S. A., Lang, D., Zimmer, A. D., Terry, A., Salamov, A., Shapiro, H., Nishiyama, T., Perroud, P.-F., Lindquist, E. A., Kamisugi, Y., Tanahashi, T., Sakakibara, K., Fujita, T., Oishi, K., Shin-I, T., Kuroki, Y., Toyoda, A., Suzuki, Y., Hashimoto, S.-i., Yamaguchi, K., Sugano, S., Kohara, Y., Fujiyama, A., Anterola, A., Aoki, S., Ashton, N., Barbazuk, W. B., Barker, E., Bennetzen, J. L.,

Blankenship, R., Cho, S. H., Dutcher, S. K., Estelle, M., Fawcett, J. A., Gundlach, H., Hanada, K., Heyl, A., Hicks, K. A., Hughes, J., Lohr, M., Mayer, K., Melkozernov, A., Murata, T., Nelson, D. R., Pils, B., Prigge, M., Reiss, B., Renner, T., Rombauts, S., Rushton, P. J., Sanderfoot, A., Schween, G., Shiu, S.-H., Stueber, K., Theodoulou, F. L., Tu, H., Peer, Y. V. d., Verrier, P. J., Waters, E., Wood, A., Yang, L., Cove, D., Cuming, A. C., Hasebe, M., Lucas, S., Mishler, B. D., Reski, R., Grigoriev, I. V., Quatrano, R. S., and Boore, J. L. (2008). The physcomitrella genome reveals evolutionary insights into the conquest of land by plants. *Science*, 319(5859):64–69.

Röber, R. A., Sauter, H., Weber, K., and Osborn, M. (1990). Cells of the cellular immune and hemopoietic system of the mouse lack lamins A/C: distinction versus other somatic cells. *Journal of Cell Science*, 95 ( Pt 4):587–598.

Ronneberger, O., Baddeley, D., Scheipl, F., Verweir, P. J., Burkhardt, H., Cremer, C., Fahrmeir, L., Cremer, T., and Joffe, B. (2008). Spatial quantitative analysis of fluorescently labeled nuclear structures: problems, methods, pitfalls. *Chromosome Research: An International Journal on the Molecular, Supramolecular and Evolutionary Aspects of Chromosome Biology*, 16(3):523–562.

Rosa, S., De Lucia, F., Mylne, J. S., Zhu, D., Ohmido, N., Pendle, A., Kato, N., Shaw, P., and Dean, C. (2013). Physical clustering of FLC alleles during Polycomb-mediated epigenetic silencing in vernalization. *Genes & Development*, 27(17):1845–1850.

Rose, A. and Meier, I. (2001). A domain unique to plant RanGAP is responsible for its targeting to the plant nuclear rim. *Proceedings of the National Academy of Sciences of the United States of America*, 98(26):15377–15382.

Rosin, F. M., Watanabe, N., Cacas, J.-L., Kato, N., Arroyo, J. M., Fang, Y., May, B., Vaughn, M., Simorowski, J., Ramu, U., McCombie, R. W., Spector, D. L., Martienssen, R. A., and Lam, E. (2008). Genome-wide transposon tagging reveals location-dependent effects on transcription and chromatin organization in Arabidopsis. *The Plant Journal: For Cell and Molecular Biology*, 55(3):514–525.

Rothballer, A. and Kutay, U. (2013). The diverse functional LINC s of the nuclear envelope to the cytoskeleton and chromatin. *Chromosoma*, 122(5):415–429.

Roudier, F., Teixeira, F. K., and Colot, V. (2009). Chromatin indexing in Arabidopsis: an epigenomic tale of tails and more. *Trends in Genetics*, 25(11):511–517.

Sáez-Vásquez, J. and Gadgil, O. (2010). Genome organization and function: a view from yeast and Arabidopsis. *Molecular Plant*, 3(4):678–690.

Saito, T. and Toriwaki, J.-I. (1994). New algorithms for euclidean distance transformation of an n-dimensional digitized picture with applications. *Pattern Recognition*, 27(11):1551–1565.

Sakamoto, Y. and Takagi, S. (2013). LITTLE NUCLEI 1 and 4 regulate nuclear morphology in *Arabidopsis thaliana*. *Plant and Cell Physiology*, 54(4):622–633.

Saksouk, N., Simboeck, E., and Djardin, J. (2015). Constitutive heterochromatin formation and transcription in mammals. *Epigenetics & Chromatin*, 8:3.

Santos, A. P. and Shaw, P. (2004). Interphase chromosomes and the Rab1 configuration: does genome size matter? *Journal of Microscopy*, 214(Pt 2):201–206.

Sasaki, Y., Miyoshi, D., and Sugimoto, N. (2006). Effect of molecular crowding on DNA polymerase activity. *Biotechnology Journal*, 1(4):440–446.

Sauer, F. C. (1935). Mitosis in the neural tube. *The Journal of Comparative Neurology*, 62(2):377–405.

Schatten, G., Maul, G. G., Schatten, H., Chaly, N., Simerly, C., Balczon, R., and Brown, D. L. (1985). Nuclear lamins and peripheral nuclear antigens during fertilization and embryogenesis in mice and sea urchins. *Proceedings of the National Academy of Sciences of the United States of America*, 82(14):4727–4731.

Schermelleh, L., Heintzmann, R., and Leonhardt, H. (2010). A guide to super-resolution fluorescence microscopy. *The Journal of Cell Biology*, 190(2):165–175.

Schmutz, J., Cannon, S. B., Schlueter, J., Ma, J., Mitros, T., Nelson, W., Hyten, D. L., Song, Q., Thelen, J. J., Cheng, J., Xu, D., Hellsten, U., May, G. D., Yu, Y., Sakurai, T., Umezawa, T., Bhattacharyya, M. K., Sandhu, D., Valliyodan, B., Lindquist, E., Peto, M., Grant, D., Shu, S., Goodstein, D., Barry, K., Futrell-Griggs, M., Abernathy, B., Du, J., Tian, Z., Zhu, L., Gill, N., Joshi, T., Libault, M., Sethuraman, A., Zhang, X.-C., Shinozaki, K., Nguyen, H. T., Wing, R. A., Cregan, P., Specht, J., Grimwood, J., Rokhsar, D., Stacey, G., Shoemaker, R. C., and Jackson, S. A. (2010). Genome sequence of the palaeopolyploid soybean. *Nature*, 463(7278):178–183.

Schnable, P. S., Ware, D., Fulton, R. S., Stein, J. C., Wei, F., Pasternak, S., Liang, C., Zhang, J., Fulton, L., Graves, T. A., Minx, P., Reily, A. D., Courtney, L., Kurchowski, S. S., Tomlinson, C., Strong, C., Delehaunty, K., Fronick, C., Courtney, B., Rock, S. M., Belter, E., Du, F., Kim, K., Abbott, R. M., Cotton, M., Levy, A., Marchetto, P., Ochoa, K., Jackson, S. M., Gillam, B., Chen, W., Yan, L., Higginbotham, J., Cardenas, M., Waligorski, J., Applebaum, E., Phelps, L., Falcone, J., Kanchi, K., Thane, T., Scimone, A., Thane, N., Henke, J., Wang, T., Ruppert, J., Shah, N., Rotter, K., Hodges, J., Ingenthron, E., Cordes, M., Kohlberg, S., Sgro, J., Delgado, B., Mead, K., Chinwalla, A., Leonard, S., Crouse, K., Collura, K., Kudrna, D., Currie, J., He, R., Angelova, A., Rajasekar, S., Mueller, T., Lomeli, R., Scara, G., Ko, A., Delaney, K., Wissotski, M., Lopez, G., Campos, D., Braidotti, M., Ashley, E., Golser, W., Kim, H., Lee, S., Lin, J., Dujmic, Z., Kim, W., Talag, J., Zuccolo, A., Fan, C., Sebastian, A., Kramer, M., Spiegel, L., Nascimento, L., Zutavern, T., Miller, B., Ambroise, C., Muller, S., Spooner, W., Narechania, A., Ren, L., Wei, S., Kumari, S., Faga, B., Levy, M. J., McMahan, L., Buren, P. V., Vaughn, M. W., Ying, K., Yeh, C.-T., Emrich, S. J., Jia, Y., Kalyanaraman, A., Hsia, A.-P., Barbazuk, W. B., Baucom, R. S., Brutnell, T. P., Carpita, N. C., Chapparro, C., Chia, J.-M., Deragon, J.-M., Estill, J. C., Fu, Y., Jeddalo, J. A., Han, Y., Lee, H., Li, P., Lisch, D. R., Liu, S., Liu, Z., Nagel, D. H., McCann, M. C.,

SanMiguel, P., Myers, A. M., Nettleton, D., Nguyen, J., Penning, B. W., Ponnala, L., Schneider, K. L., Schwartz, D. C., Sharma, A., Soderlund, C., Springer, N. M., Sun, Q., Wang, H., Waterman, M., Westerman, R., Wolfgruber, T. K., Yang, L., Yu, Y., Zhang, L., Zhou, S., Zhu, Q., Bennetzen, J. L., Dawe, R. K., Jiang, J., Jiang, N., Presting, G. G., Wessler, S. R., Aluru, S., Martienssen, R. A., Clifton, S. W., McCombie, W. R., Wing, R. A., and Wilson, R. K. (2009). The B73 Maize Genome: Complexity, Diversity, and Dynamics. *Science*, 326(5956):1112–1115.

Schneider, C. A., Rasband, W. S., and Eliceiri, K. W. (2012). NIH Image to ImageJ: 25 years of image analysis. *Nature Methods*, 9(7):671–675.

Schubert, V., Berr, A., and Meister, A. (2012). Interphase chromatin organisation in Arabidopsis nuclei: constraints versus randomness. *Chromosoma*, 121(4):369–387.

Seo, H.-S., Blus, B. J., Jankovic, N. Z., and Blobel, G. (2013). Structure and nucleic acid binding activity of the nucleoporin Nup157. *Proceedings of the National Academy of Sciences of the United States of America*, 110(41):16450–16455.

Sequeira-Mendes, J. and Gutierrez, C. (2015). Genome architecture: from linear organisation of chromatin to the 3d assembly in the nucleus. *Chromosoma*.

Serra, J. (1983). *Image Analysis and Mathematical Morphology*. Academic Press, Inc., Orlando, FL, USA.

Serra, J. P. and Soille, P. (1994). *Mathematical morphology and its applications to image processing*. Kluwer Academic Publishers, Dordrecht, Boston.

Shannon, C. (1949). Communication in the Presence of Noise. *Proceedings of the IRE*, 37(1):10–21.

She, C., Liu, J., Diao, Y., Hu, Z., and Song, Y. (2007). The distribution of repetitive DNAs along chromosomes in plants revealed by self-genomic in situ hybridization. *Journal of Genetics and Genomics*, 34(5):437–448.

Shumaker, D. K., Dechat, T., Kohlmaier, A., Adam, S. A., Bozovsky, M. R., Erdos, M. R., Eriksson, M., Goldman, A. E., Khuon, S., Collins, F. S., Jenuwein, T., and Goldman, R. D. (2006). Mutant nuclear lamin A leads to progressive alterations of epigenetic control in premature aging. *Proceedings of the National Academy of Sciences*, 103(23):8703–8708.

Shumaker, D. K., Lopez-Soler, R. I., Adam, S. A., Herrmann, H., Moir, R. D., Spann, T. P., and Goldman, R. D. (2005). Functions and dysfunctions of the nuclear lamin Ig-fold domain in nuclear assembly, growth, and EmeryDreifuss muscular dystrophy. *Proceedings of the National Academy of Sciences of the United States of America*, 102(43):15494–15499.

Simon, D. N. and Wilson, K. L. (2011). The nucleoskeleton as a genome-associated dynamic 'network of networks'. *Nature Reviews. Molecular Cell Biology*, 12(11):695–708.

- Simon, D. N. and Wilson, K. L. (2013). Partners and post-translational modifications of nuclear lamins. *Chromosoma*, 122(0):13–31.
- Simon, L., Voisin, M., Tatout, C., and Probst, A. V. (2015). Structure and function of centromeric and pericentromeric heterochromatin in *Arabidopsis thaliana*. *Frontiers in Plant Science*, 6.
- Slater, D. N., Rice, S., Stewart, R., Melling, S. E., Hewer, E. M., and Smith, J. H. F. (2005). Proposed Sheffi quantitative criteria in cervical cytology to assist the grading of squamous cell dyskaryosis, as the British Society for Clinical Cytology definitions require amendment. *Cytopathology*, 16(4):179–192.
- Sohaskey, M. L., Jiang, Y., Zhao, J. J., Mohr, A., Roemer, F., and Harland, R. M. (2010). Osteopotential regulates osteoblast maturation, bone formation, and skeletal integrity in mice. *The Journal of Cell Biology*, 189(3):511–525.
- Soppe, W. J. J., Jasencakova, Z., Houben, A., Kakutani, T., Meister, A., Huang, M. S., Jacobsen, S. E., Schubert, I., and Fransz, P. F. (2002). DNA methylation controls histone H3 lysine 9 methylation and heterochromatin assembly in Arabidopsis. *The EMBO journal*, 21(23):6549–6559.
- Sosa, B. A., Kutay, U., and Schwartz, T. U. (2013). Structural insights into LINC complexes. *Current Opinion in Structural Biology*, 23(2):285–291.
- Sosa, B. A., Rothballer, A., Kutay, U., and Schwartz, T. U. (2012). Linc complexes form by binding of three kash peptides to the interfaces of trimeric SUN proteins. *Cell*, 149(5):1035–1047.
- Starr, D. A. (2009). A nuclear-envelope bridge positions nuclei and moves chromosomes. *Journal of Cell Science*, 122(5):577–586.
- Steimer, A., Amedeo, P., Afsar, K., Fransz, P., Mittelsten Scheid, O., and Paszkowski, J. (2000). Endogenous targets of transcriptional gene silencing in Arabidopsis. *The Plant Cell*, 12(7):1165–1178.
- Sugimoto-Shirasu, K., Roberts, G. R., Stacey, N. J., McCann, M. C., Maxwell, A., and Roberts, K. (2005). RHL1 is an essential component of the plant DNA topoisomerase VI complex and is required for ploidy-dependent cell growth. *Proceedings of the National Academy of Sciences of the United States of America*, 102(51):18736–18741.
- Sullivan, T., Escalante-Alcalde, D., Bhatt, H., Anver, M., Bhat, N., Nagashima, K., Stewart, C. L., and Burke, B. (1999). Loss of a-Type lamin expression compromises nuclear envelope integrity leading to muscular dystrophy. *The Journal of Cell Biology*, 147(5):913–920.
- Sulston, J. E. and Horvitz, H. R. (1981). Abnormal cell lineages in mutants of the nematode *Caenorhabditis elegans*. *Developmental Biology*, 82(1):41–55.

- Taddei, A., Hediger, F., Neumann, F. R., Bauer, C., and Gasser, S. M. (2004). Separation of silencing from perinuclear anchoring functions in yeast Ku80, Sir4 and Esc1 proteins. *The EMBO journal*, 23(6):1301–1312.
- Talavera, G. and Castresana, J. (2007). Improvement of phylogenies after removing divergent and ambiguously aligned blocks from protein sequence alignments. *Systematic Biology*, 56(4):564–577.
- Tamura, K., Fukao, Y., Iwamoto, M., Haraguchi, T., and Hara-Nishimura, I. (2010). Identification and characterization of nuclear pore complex components in *Arabidopsis thaliana*. *The Plant Cell*, 22(12):4084–4097.
- Tamura, K., Goto, C., and Hara-Nishimura, I. (2015). Recent advances in understanding plant nuclear envelope proteins involved in nuclear morphology. *Journal of Experimental Botany*, 66(6):1641–1647.
- Tamura, K. and Hara-Nishimura, I. (2011). Involvement of the nuclear pore complex in morphology of the plant nucleus. *Nucleus*, 2(3):168–172.
- Tamura, K. and Hara-Nishimura, I. (2013). The molecular architecture of the plant nuclear pore complex. *Journal of Experimental Botany*, 64(4):823–832.
- Tamura, K., Iwabuchi, K., Fukao, Y., Kondo, M., Okamoto, K., Ueda, H., Nishimura, M., and Hara-Nishimura, I. (2013). Myosin XI-i links the nuclear membrane to the cytoskeleton to control nuclear movement and shape in *Arabidopsis*. *Current Biology*, 23(18):1776–1781.
- Tanabe, H., Müller, S., Neusser, M., von Hase, J., Calcagno, E., Cremer, M., Solovei, I., Cremer, C., and Cremer, T. (2002). Evolutionary conservation of chromosome territory arrangements in cell nuclei from higher primates. *Proceedings of the National Academy of Sciences*, 99(7):4424–4429.
- Tapley, E. C. and Starr, D. A. (2013). Connecting the nucleus to the cytoskeleton by SUNKASH bridges across the nuclear envelope. *Current Opinion in Cell Biology*, 25(1):57–62.
- Tariq, M., Saze, H., Probst, A. V., Lichota, J., Habu, Y., and Paszkowski, J. (2003). Erasure of CpG methylation in *Arabidopsis* alters patterns of histone H3 methylation in heterochromatin. *Proceedings of the National Academy of Sciences*, 100(15):8823–8827.
- Tatout, C., Evans, D. E., Vanrobays, E., Probst, A. V., and Graumann, K. (2014). The plant LINC complex at the nuclear envelope. *Chromosome Research*, 22(2):241–252.
- Tessadori, F., Chupeau, M.-C., Chupeau, Y., Knip, M., Germann, S., van Driel, R., Fransz, P., and Gaudin, V. (2007a). Large-scale dissociation and sequential re-assembly of pericentric heterochromatin in differentiated *Arabidopsis* cells. *Journal of Cell Science*, 120(Pt 7):1200–1208.



Tessadori, F., Schulkes, R. K., Driel, R. v., and Fransz, P. (2007b). Lightregulated largescale reorganization of chromatin during the fl transition in *Arabidopsis*. *The Plant Journal*, 50(5):848–857.

Tessadori, F., van Zanten, M., Pavlova, P., Clifton, R., Pontvianne, F., Snoek, L. B., Millenaar, F. F., Schulkes, R. K., van Driel, R., Voesenek, L. A. C. J., Spillane, C., Pikaard, C. S., Fransz, P., and Peeters, A. J. M. (2009). Phytochrome B and histone deacetylase 6 control light-induced chromatin compaction in *Arabidopsis thaliana*. *PLoS genetics*, 5(9):e1000638.

The International Peach Genome Initiative, Verde, I., Abbott, A. G., Scalabrin, S., Jung, S., Shu, S., Marroni, F., Zhebentyayeva, T., Dettori, M. T., Grimwood, J., Cattonaro, F., Zuccolo, A., Rossini, L., Jenkins, J., Vendramin, E., Meisel, L. A., Decroocq, V., Sosinski, B., Prochnik, S., Mitros, T., Policriti, A., Cipriani, G., Dondini, L., Ficklin, S., Goodstein, D. M., Xuan, P., Fabbro, C. D., Aramini, V., Copetti, D., Gonzalez, S., Horner, D. S., Falchi, R., Lucas, S., Mica, E., Maldonado, J., Lazzari, B., Bielenberg, D., Pirona, R., Miculan, M., Barakat, A., Testolin, R., Stella, A., Tartarini, S., Tonutti, P., Ars, P., Orellana, A., Wells, C., Main, D., Vizzotto, G., Silva, H., Salamini, F., Schmutz, J., Morgante, M., and Rokhsar, D. S. (2013). The high-quality draft genome of peach (*Prunus persica*) identifies unique patterns of genetic diversity, domestication and genome evolution. *Nature Genetics*, 45(5):487–494.

Thompson, H. L., Schmidt, R., and Dean, C. (1996). Identification and distribution of seven classes of middle-repetitive dna in the *Arabidopsis thaliana* genome. *Nucleic Acids Research*, 24(15):3017–3022.

Tirichine, L., Andrey, P., Biot, E., Maurin, Y., and Gaudin, V. (2009). 3d fl cent in situ hybridization using *Arabidopsis* leaf cryosections and isolated nuclei. *Plant Methods*, 5:11.

Towbin, B. D., Gonzalez-Sandoval, A., and Gasser, S. M. (2013). Mechanisms of heterochromatin subnuclear localization. *Trends in Biochemical Sciences*, 38(7):356–363.

Traas, J., Hülskamp, M., Gendreau, E., and Höfte, H. (1998). Endoreduplication and development: rule without dividing? *Current Opinion in Plant Biology*, 1(6):498–503.

True, L. D. and Jordan, C. D. (2008). The cancer nuclear microenvironment: interface between light microscopic cytology and molecular phenotype. *Journal of Cellular Biochemistry*, 104(6):1994–2003.

Turner, B. M. (2000). Histone acetylation and an epigenetic code. *BioEssays: News and Reviews in Molecular, Cellular and Developmental Biology*, 22(9):836–845.

Tuskan, G. A., DiFazio, S., Jansson, S., Bohlmann, J., Grigoriev, I., Hellsten, U., Putnam, N., Ralph, S., Rombauts, S., Salamov, A., Schein, J., Sterck, L., Aerts, A., Bhalerao, R. R., Bhalerao, R. P., Blaudez, D., Boerjan, W., Brun, A., Brunner, A., Busov, V., Campbell, M., Carlson, J., Chalot, M., Chapman, J., Chen,

G.-L., Cooper, D., Coutinho, P. M., Couturier, J., Covert, S., Cronk, Q., Cunningham, R., Davis, J., Degroeve, S., Djardin, A., dePamphilis, C., Detter, J., Dirks, B., Dubchak, I., Duplessis, S., Ehlting, J., Ellis, B., Gendler, K., Goodstein, D., Gribskov, M., Grimwood, J., Groover, A., Gunter, L., Hamberger, B., Heinze, B., Helariutta, Y., Henrissat, B., Holligan, D., Holt, R., Huang, W., Islam-Faridi, N., Jones, S., Jones-Rhoades, M., Jorgensen, R., Joshi, C., Kangasjärvi, J., Karlsson, J., Kelleher, C., Kirkpatrick, R., Kirst, M., Kohler, A., Kalluri, U., Larimer, F., Leebens-Mack, J., Lepl, J.-C., Locascio, P., Lou, Y., Lucas, S., Martin, F., Montanini, B., Napoli, C., Nelson, D. R., Nelson, C., Nieminen, K., Nilsson, O., Pereda, V., Peter, G., Philippe, R., Pilate, G., Poliakov, A., Razumovskaya, J., Richardson, P., Rinaldi, C., Ritland, K., Rouz, P., Ryaboy, D., Schmutz, J., Schrader, J., Segerman, B., Shin, H., Siddiqui, A., Sterky, F., Terry, A., Tsai, C.-J., Uberbacher, E., Unneberg, P., Vahala, J., Wall, K., Wessler, S., Yang, G., Yin, T., Douglas, C., Marra, M., Sandberg, G., Peer, Y. V. d., and Rokhsar, D. (2006). The genome of black cottonwood, *Populus trichocarpa* (Torr. & Gray). *Science*, 313(5793):1596–1604.

Tzur, Y. B., Margalit, A., Melamed-Book, N., and Gruenbaum, Y. (2006). Matefin/SUN-1 is a nuclear envelope receptor for CED-4 during *Caenorhabditis elegans* apoptosis. *Proceedings of the National Academy of Sciences of the United States of America*, 103(36):13397–13402.

Ulbert, S., Antonin, W., Platani, M., and Mattaj, I. W. (2006). The inner nuclear membrane protein Lem2 is critical for normal nuclear envelope morphology. *FEBS Letters*, 580(27):6435–6441.

Vaillant, I., Tutois, S., Jasencakova, Z., Douet, J., Schubert, I., and Tourmente, S. (2008). Hypomethylation and hypermethylation of the tandem repetitive 5S rRNA genes in Arabidopsis. *The Plant Journal: For Cell and Molecular Biology*, 54(2):299–309.

Van de Vosse, D. W., Wan, Y., Lapetina, D. L., Chen, W.-M., Chiang, J.-H., Aitchison, J. D., and Wozniak, R. W. (2013). A role for the nucleoporin Nup170p in chromatin structure and gene silencing. *Cell*, 152(5):969–983.

van Driel, R. and Fransz, P. (2004). Nuclear architecture and genome functioning in plants and animals: what can we learn from both? *Experimental Cell Research*, 296(1):86–90.

van Zanten, M., Koini, M. A., Geyer, R., Liu, Y., Brambilla, V., Bartels, D., Koornneef, M., Fransz, P., and Soppe, W. J. J. (2011). Seed maturation in *Arabidopsis thaliana* is characterized by nuclear size reduction and increased chromatin condensation. *Proceedings of the National Academy of Sciences of the United States of America*, 108(50):20219–20224.

Vanrobays, E., Thomas, M., and Tatout, C. (2013). Heterochromatin positioning and nuclear architecture. In Evans, D. E., Graumann, K., and Bryant, J. A., editors, *Annual Plant Reviews*, pages 157–190. John Wiley & Sons Ltd.

- Varas, J., Graumann, K., Osman, K., Pradillo, M., Evans, D. E., Santos, J. L., and Armstrong, S. J. (2015). Absence of SUN1 and SUN2 proteins in *Arabidopsis thaliana* leads to a delay in meiotic progression and defects in synapsis and recombination. *The Plant Journal*, 81(2):329–346.
- Vasnier, C., Muyt, A. d., Zhang, L., Tess, S., Kleckner, N. E., Zickler, D., and Espagne, E. (2014). Absence of SUN-domain protein Slp1 blocks karyogamy and switches meiotic recombination and synapsis from homologs to sister chromatids. *Proceedings of the National Academy of Sciences*, 111(38):E4015–E4023.
- Versaevel, M., Grevesse, T., and Gabriele, S. (2012). Spatial coordination between cell and nuclear shape within micropatterned endothelial cells. *Nature Communications*, 3:671.
- Vigouroux, C., Auclair, M., Dubosclard, E., Pouchelet, M., Capeau, J., Courvalin, J. C., and Buendia, B. (2001). Nuclear envelope disorganization in fibroblasts from lipodystrophic patients with heterozygous R482Q/W mutations in the lamin A/C gene. *Journal of Cell Science*, 114(Pt 24):4459–4468.
- Voeltz, G. K., Prinz, W. A., Shibata, Y., Rist, J. M., and Rapoport, T. A. (2006). A Class of Membrane Proteins Shaping the Tubular Endoplasmic Reticulum. *Cell*, 124(3):573–586.
- Wang, H., Dittmer, T. A., and Richards, E. J. (2013). Arabidopsis CROWDED NUCLEI (CRWN) proteins are required for nuclear size control and heterochromatin organization. *BMC Plant Biology*, 13(1):200.
- Wang, H., Liu, R., Wang, J., Wang, P., Shen, Y., and Liu, G. (2014). The Arabidopsis kinesin gene AtKin-1 plays a role in the nuclear division process during megagametogenesis. *Plant Cell Reports*, 33(5):819–828.
- Webster, M., Witkin, K. L., and Cohen-Fix, O. (2009). Sizing up the nucleus: nuclear shape, size and nuclear-envelope assembly. *Journal of Cell Science*, 122(10):1477–1486.
- Weiss, P. and Garber, B. (1952). Shape and movement of mesenchyme cells as functions of the physical structure of the medium: contributions to a quantitative morphology. *Proceedings of the National Academy of Sciences of the United States of America*, 38(3):264–280.
- Wright, S. I., Nowell, M. M., de Kloe, R., Camus, P., and Rampton, T. (2015). Electron imaging with an EBSD detector. *Ultramicroscopy*, 148:132–145.
- Wu, Q., Merchant, F., and Castleman, K. R. (2008). *Microscope Image Processing*. Academic Press.
- Xiang, X. and Fischer, R. (2004). Nuclear migration and positioning in filamentous fungi. *Fungal genetics and biology: FG & B*, 41(4):411–419.

Xiong, H., Rivero, F., Euteneuer, U., Mondal, S., Mana-Capelli, S., Larochelle, D., Vogel, A., Gassen, B., and Noegel, A. A. (2008). Dictyostelium Sun-1 connects the centrosome to chromatin and ensures genome stability. *Traffic (Copenhagen, Denmark)*, 9(5):708–724.

Yelagandula, R., Stroud, H., Holec, S., Zhou, K., Feng, S., Zhong, X., Muthurajan, U. M., Nie, X., Kawashima, T., Groth, M., Luger, K., Jacobsen, S. E., and Berger, F. (2014). The histone variant H2a.W defi heterochromatin and promotes chromatin condensation in Arabidopsis. *Cell*, 158(1):98–109.

Zhang, H. and Dawe, R. K. (2011). Mechanisms of plant spindle formation. *Chromosome Research*, 19(3):335–344.

Zhang, X., Clarenz, O., Cokus, S., Bernatavichute, Y. V., Pellegrini, M., Goodrich, J., and Jacobsen, S. E. (2007). Whole-genome analysis of histone H3 lysine 27 trimethylation in Arabidopsis. *PLOS Biol*, 5(5):e129.

Zhao, Q., Brkljacic, J., and Meier, I. (2008). Two distinct interacting classes of nuclear envelope-associated coiled-coil proteins are required for the tissue-specific nuclear envelope targeting of arabidopsis rangap. *The Plant Cell*, 20(6):1639–1651.

Zhou, X., Graumann, K., Evans, D. E., and Meier, I. (2012). Novel plant sun-kash bridges are involved in RanGAP anchoring and nuclear shape determination. *The Journal of Cell Biology*, 196(2):203–211.

Zhou, X., Graumann, K., and Meier, I. (2015a). The plant nuclear envelope as a multifunctional platform LINCed by SUN and KASH. *Journal of Experimental Botany*, 66(6):1649–1659.

Zhou, X., Graumann, K., Wirthmueller, L., Jones, J. D., and Meier, I. (2014). Identification of unique SUN-interacting nuclear envelope proteins with diverse functions in plants. *The Journal of Cell Biology*, 205(5):677–692.

Zhou, X., Groves, N. R., and Meier, I. (2015b). Plant nuclear shape is independently determined by the SUN-WIP-WIT2-myosin XI-i complex and CRWN1. *Nucleus (Austin, Tex.)*, 6(2):144–153.

Zhou, X. and Meier, I. (2014). Efficient plant male fertility depends on vegetative nuclear movement mediated by two families of plant outer nuclear membrane proteins. *Proceedings of the National Academy of Sciences of the United States of America*, 111(32):11900–11905.

Zink, D., Fischer, A. H., and Nickerson, J. A. (2004). Nuclear structure in cancer cells. *Nature Reviews Cancer*, 4(9):677–687.

# **Appendix A**

## **Quantitative analysis of nuclear parameters using 3D images**

### **A.1 NucleusJ: an ImageJ plugin for quantifying 3D images of interphase nuclei.**

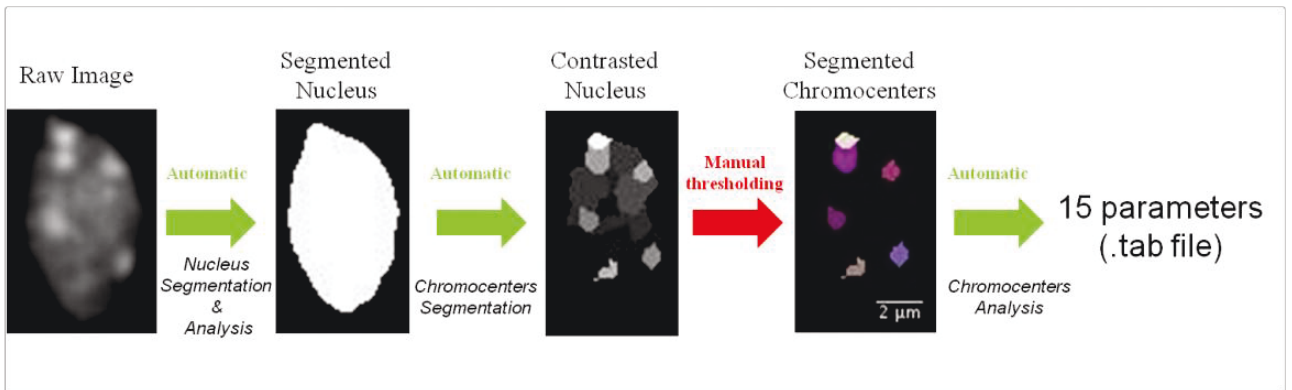
paper removed from electronic version: 3rd party copyright issue

## **A.2 NucleusJ documentation**

## NucleusJ

---

This plugin is dedicated to researchers interested in nuclear shape and chromatin organization. Starting from image stacks, the nuclear boundary as well as nuclear bodies are segmented. As output, NucleusJ automatically measures 15 parameters quantifying shape and size of nuclei as well as intra-nuclear objects and the positioning of the objects within the nuclear volume.



The plugin contains several methods to process and analyze 8 grey level image stacks of nuclei. For each method two versions are available, one version to analyze one image at a time and another for processing in batch mode.

NucleusJ paper : Poulet A, Arganda-Carreras I, Legland D, Probst AV, Andrey P, Tatout C. NucleusJ: an ImageJ plugin for quantifying 3D images of interphase nuclei. *Bioinformatics*. 2015 Apr 1;31(7):1144-6. doi: 10.1093/bioinformatics/btu774. Epub 2014 Nov 20. PubMed PMID: 25416749.

## Authors

---

Axel Poulet

- UMR CNRS 6293, INSERM U1103, [Genetic, Reproduction and Development](#), Clermont-Ferrand, France.
- [Department of Biological and Medical Sciences Faculty of Health and Life Sciences](#), Oxford Brookes University, Headington Campus, Oxford, United Kingdom

Philippe Andrey

- [Modeling and Digital Imaging Group](#), Institut Jean-Pierre Bourgin, INRA Versailles, France.

Contact: [axel.poulet@etudiant.univ-bpclermont.fr](mailto:axel.poulet@etudiant.univ-bpclermont.fr)

## Usage

---

This plugin aims to characterize the nucleus by nuclear morphology and chromatin organization parameters. It is divided into three main steps:

### A. First step: Nucleus Segmentation

The well known Otsu method has been combined with the optimization of a shape parameter called sphericity ( $36 \pi \times \text{Volume}^2 / \text{Surface Area}^3$ ). The threshold value provided by the standard Otsu method is used as a starting point to test a range of thresholds, which eventually leads to the selection of the value for which the sphericity is maximal. The selected threshold is subsequently used to segment the nucleus.

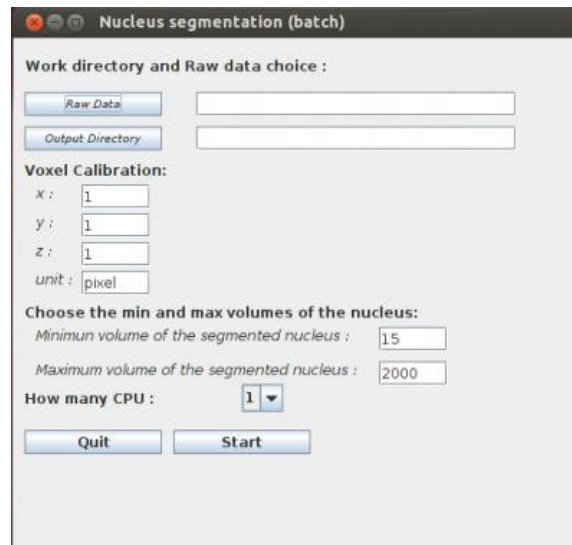
The user first needs to enter the minimal and maximal volume of the object to be segmented. If no object is found the program creates a log file (named: logErrorSeg.txt) when the program runs in batch mode. If the program runs in single opened image mode, a graphical window displaying this information appears. Two alternatives are possible: run the segmentation process only (A.1) or run the segmentation process and an analysis of the results (A.2).

#### A.1 Nucleus Segmentation

This method only performs the segmentation.

- Nucleus Segmentation: The process uses as input an opened image and the image result is displayed on the screen.
- Nucleus Segmentation (batch): before running the plugin, a WorkDirectory dedicated to a given analysis should be created by the user. Raw images have then to be saved in a new sub-directory created by the user and named hereafter RawDataNucleus. The result of the segmentation process is saved automatically in a new sub-directory created by the plugin and called SegmentedDataNucleus.

When the user is using one of these two methods, a pop up window appears:





The user has to inform the following parameters:

**Work directory and raw data choice:**

All the following steps are performed within the WorkDirectory

1. Raw Data: choose the WorkDirectory which contains the raw images saved in a single sub-directory. In this documentation this sub-directory is called **RawDataNucleus**.
2. Output Directory: choose the WorkDirectory the results are to be stored. This directory must contain the RawDataNucleus sub-directory containing the raw images.

**Voxel Calibration** corresponds to the voxel calibration used during the image acquisition..

1. x: width of voxel: *default value = 1*.
2. y: height of voxel: *default value = 1*.
3. z: depth of voxel: *default value = 1*.
4. unit: length unit ( $\mu\text{m}$ , ...): *default value = pixel*.

**Choose the minimum and maximum volume of the nucleus**: only objects with a volume between the minimum and the maximum allowed volume will be segmented.

1. minimum volume of the segmented nucleus: *default value = 15*.
2. maximum volume of the segmented nucleus: *default value = 2000*.

**How many CPU**: number of CPU (Central Processing Unit) used for image segmentation.

Once the START button is pressed, the program will create a new sub-directory called **SegmentedDataNucleus** which contains the image of the segmented nuclei.

## **A.2 Nucleus Segmentation & Analysis (2D and/or 3D)**

This part of the plugin first performs the segmentation and then the analysis of the segmented nucleus. Several nuclear morphology parameters listed below are computed.

### **Details of the 2D and 3D parameters generated by the plugin**

#### **The 2D nuclear morphology parameters are :**

1. *AspectRatio* = Major Axis / Minor Axis (source: imageJ documentation). This is the 2D equivalent of the elongation parameter above.
2. *Circularity* =  $(4\pi \times \text{Area} / \text{Perimeter}^2)$ , ranges from 0 (infinitely elongated polygon) to 1 (perfect circle) (source: imageJ documentation). This is the 2D equivalent of the sphericity parameter above.

These 2D parameters are computed on the slice where the nucleus reaches its largest area.

#### **The 3D nuclear morphology parameters are:**

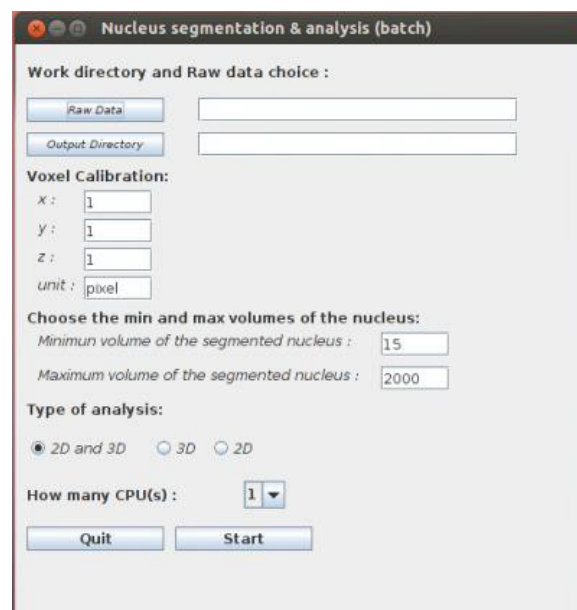
1. *Volume*: number of voxels in the nucleus x physical voxel size.
2. *Surface Area* : sum of the areas of the voxel faces at the nuclear boundary.
3. *Equivalent spherical radius*: radius of a sphere which has the same volume as the nucleus.

4. *Sphericity* =  $(36\pi \times \text{Volume}^2 / \text{Surface Area}^3)$ . This parameter takes its maximum value 1.0 for a sphere and decreases towards 0.0 as the shape surface becomes less regular.
5. *Flatness* = length of intermediate axis/length of shortest axis.
6. *Elongation* = length of longest axis/length of intermediate axis.

### Single image or batch analysis modes

- **Nucleus Segmentation & Analysis:** The process uses as input an opened image. The image results are displayed on the screen and results of the analysis are shown in the imageJ log window.
- **Nucleus Segmentation & Analysis (batch):** before running the plugin, a **WorkDirectory** dedicated to a given analysis should be created. Raw images have then to be saved in a new sub-directory created by the user and named hereafter **RawDataNucleus**. The image results of the segmented nuclei are automatically saved in the **SegmentedDataNucleus** sub-directory in the main **WorkDirectory**. The results of the analysis are saved in two tabulated files named **3DNucleiParameters.tab** and **2DNucleiParameters.tab**.

When the user is using one of these two methods, a pop up window appears:



The parameters are the same than for *Nucleus Segmentation*.

#### 2D or/and 3D analysis:

1. 2D and 3D: Two output files are created in the work directory **2DNucleiParameters.tab** and **3DNucleiParameters.tab**.
2. 3D: **3DNucleiParameters.tab** is created in the work directory.

3. 2D: **2DNucleiParameters.tab** is created in the work directory.

When you START, the program creates the sub-directory **SegmentedDataNucleus** which contains the image of the segmentation. This sub-directory, results file and log file are created in the main WorkDirectory (see also the example section of this documentation).

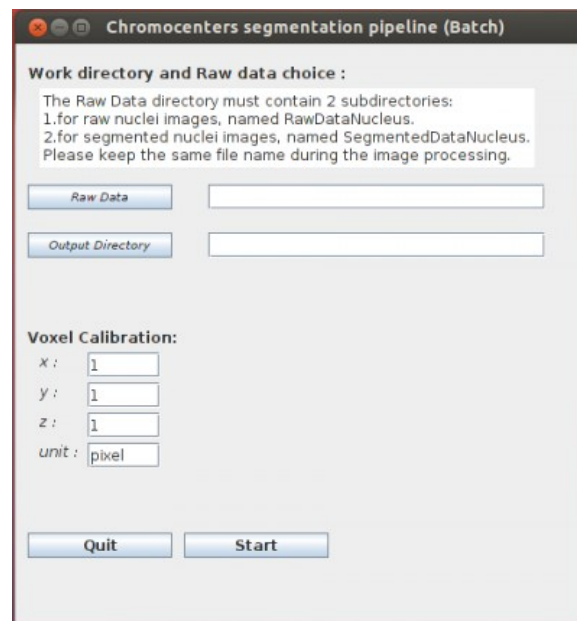
### **B.Second step: Chromocenter Segmentation**

This step is based on the watershed algorithm (source: Beucher and Lantuéjoul, 1979; Vincent et Soille, 1991; Beucher et Meyer, 1993) adapted in 3D (ijpb plugins). First the algorithm **automatically** computes the intensity contrast of the regions detected by the 3D watershed (see Andrey et al, 2010). Second chromocenters are then be extracted by **manual** thresholding. Thus the chromocenter segmentation requires two steps which are described below.

#### **Automatic Step**

- **Chromocenter Segmentation:** The process takes as input the opened image and the image results are displayed on the screen.
- **Chromocenter Segmentation (batch):** tbefore running the plugin, a WorkDirectory dedicated to a given analysis should be created. Raw images have then to be saved in a new sub-directory created by the user and named hereafter RawDataNucleus. The result is saved in the ConstrastDataNucleus sub-directory in the WorkDirectory, with the same name as the raw images.

When the user is using one of these two methods, a pop up window appears:



#### **Work directory and raw data choice**

1. Raw Data: The WorkDirectory should contain 2 sub-directories:
  - *RawDataNucleus*: containing the raw images of the nuclei.
  - *SegmentedDataNucleus*: containing the segmented images of the nuclei.

1. Output Directory: choose the WorkDirectory the results are to be stored. This directory must contain the **RawDataNucleus** and **SegmentedDataNucleus** sub-directories. Hereafter, this new sub-directory is called **ConstrastDataNucleus**.

**Voxel Calibration** which corresponds to the voxel calibration used during the image acquisition:

1. x: width of voxel: *default value = 1*.
2. y: height of voxel: *default value = 1*.
3. z: depth of voxel: *default value = 1*.
4. unit: unit of this calibration ( $\mu\text{m}$ , voxel...): *default value = pixel*.

When press START, the program creates the sub-directory ConstrastDataNucleus which contains the image of contrast regions. This sub-directory is created in the WorkDirectory.

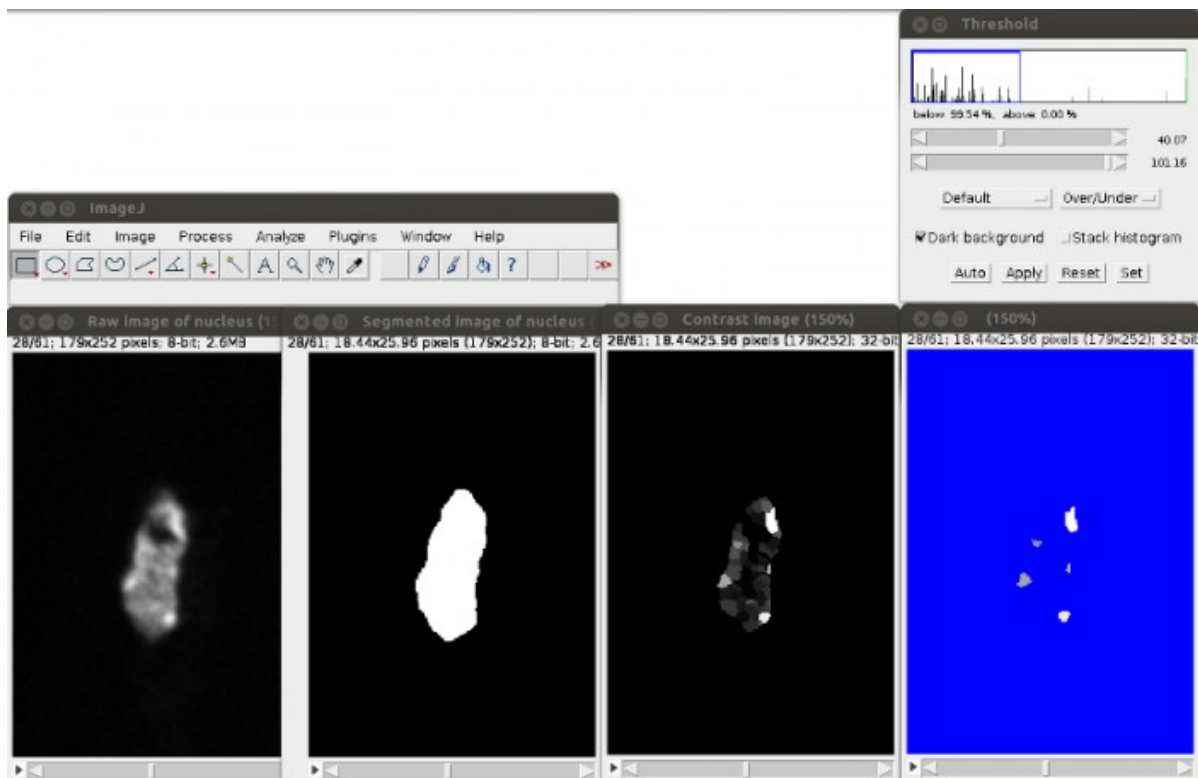
### Manual Step

First you have to create the **SegmentedDataCc** sub-directory in WorkDirectory.

Then to realize the segmented image of chromocenters, you can open three images on imageJ:

1. the raw image of nucleus.
2. the segmented image of nucleus.
3. the contrast image of the nucleus.

You can synchronize images with the ImageJ tool **Synchronize Windows** (Analyze>Tools>Synchronize Windows)



To define chromocenters, use the threshold tool (ImageJ menu: Image>Adjust>Threshold). Check the box Dark background and Stack histogram and chose the Over/Under option in the second drop-down list. Once you have chosen your threshold value push the button Apply.

Save the segmented chromocenters (Ctrl+S or ImageJ menu: File>Save or File>Save as) with the same name as the raw image of the nucleus in the directory **SegmentedDataCc**.

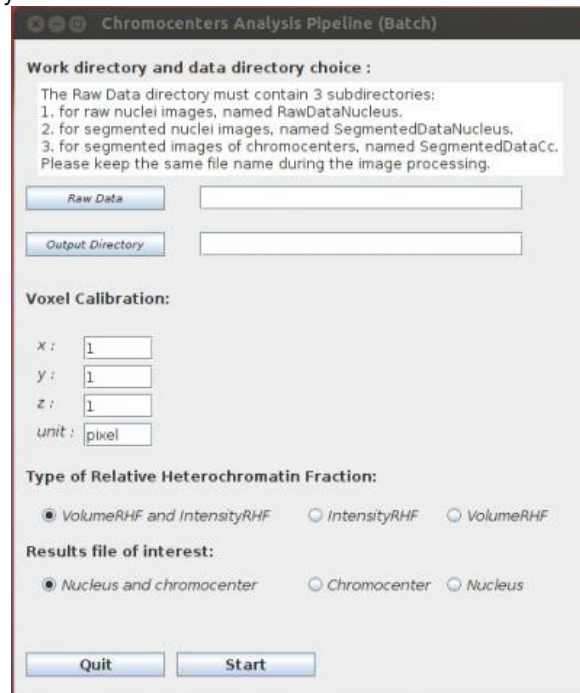
### C.Last step: Chromocenter Analysis

This step allows computing of nuclear morphology and chromatin organization parameters (see Usage). The plugin can generate 2 output files, one for the nuclear characterization (**NucAndCcParameters.tab**) and one for the chromocenters organization **CcParameters.tab**. \***Chromocenter Analysis**: The process uses as an input 3 opened images:

1. the raw image of the nucleus.
2. the segmented image of the nucleus.
3. the segmented image of the chromocenter(s).

The results of the analysis are displayed in the imageJ log window.

- **Chromocenters Analysis Pipeline (batch)**: the file(s) result(s) is (are) saved in the work directory.



#### Work directory and raw data choice

1. **Raw Data**: The main WorkDirectory must contain 3 sub-directories (a given image keeps the same name in all 3 sub-directories):
  - **RawDataNucleus** containing the raw images of the nuclei
  - **SegmentedDataNucleus** containing the segmented images of the nuclei

- **SegmentedDataCc** containing the segmented images of the chromocenters

2. Output Directory: choose the WorkDirectory the results are to be stored.

**Voxel Calibration** which corresponds to the voxel calibration used during the image acquisition:

1. x: width of voxel: *default value 1*.
2. y: height of voxel: *default value 1*.
3. z: depth of voxel: *default value 1*.
4. unit: unit of this calibration ( $\mu\text{m}$ , voxel...): *default value pixel*.

**Type of Relative Heterochromatin Fraction RHF (Fransz et al., 2002)**. This parameter determines the ratio of heterochromatin within the nucleus. This ratio can be computed with the volume (total chromocenter volume / nuclear volume) or the intensity (total chromocenter intensity / nuclear intensity).

1. VolumeRHF and IntensityRHF: computation of the 2 RHF parameters.
2. IntensityRHF: computation of RHF by the intensity.
3. VolumeRHF: computation of RHF by the volume.

**Result files of interest**

1. Nucleus and chromocenter: Two output files are created in the WorkDirectory **NucAndCcParameters.tab** and **CcParameters.tab**.
2. Chromocenter: **CcParameters.tab** is created in the WorkDirectory.
3. Nucleus: **NucAndCcParameters** is created in the WorkDirectory.

Once the START button is pressed, the program will create the results file(s) in the WorkDirectory.

**The nuclear characterization parameters contained in NucAndCcParameters.tab are:**

1. The 3D parameters listed in A.2 Nucleus Segmentation & Analysis..
2. The 2D parameters listed in A.2 Nucleus Segmentation & Analysis..
3. *NbCc*: number of chromocenters in the nucleus.
4. *VCcMean*: mean volume of the chromocenter(s) per nucleus.
5. *VCcTotal*: total volume of the chromocenter(s) per nucleus.
6. *DistanceBorderToBorderMean*: mean distance of chromocenter(s) border to nuclear periphery.
7. *DistanceBarycenterToBorderMean*: mean distance of chromocenter(s) barycenter to nuclear periphery.
8. *IntensityRHF* = total chromocenter intensity / nuclear intensity.
9. *VolumeRHF* = total chromocenter volume / nuclear volume.

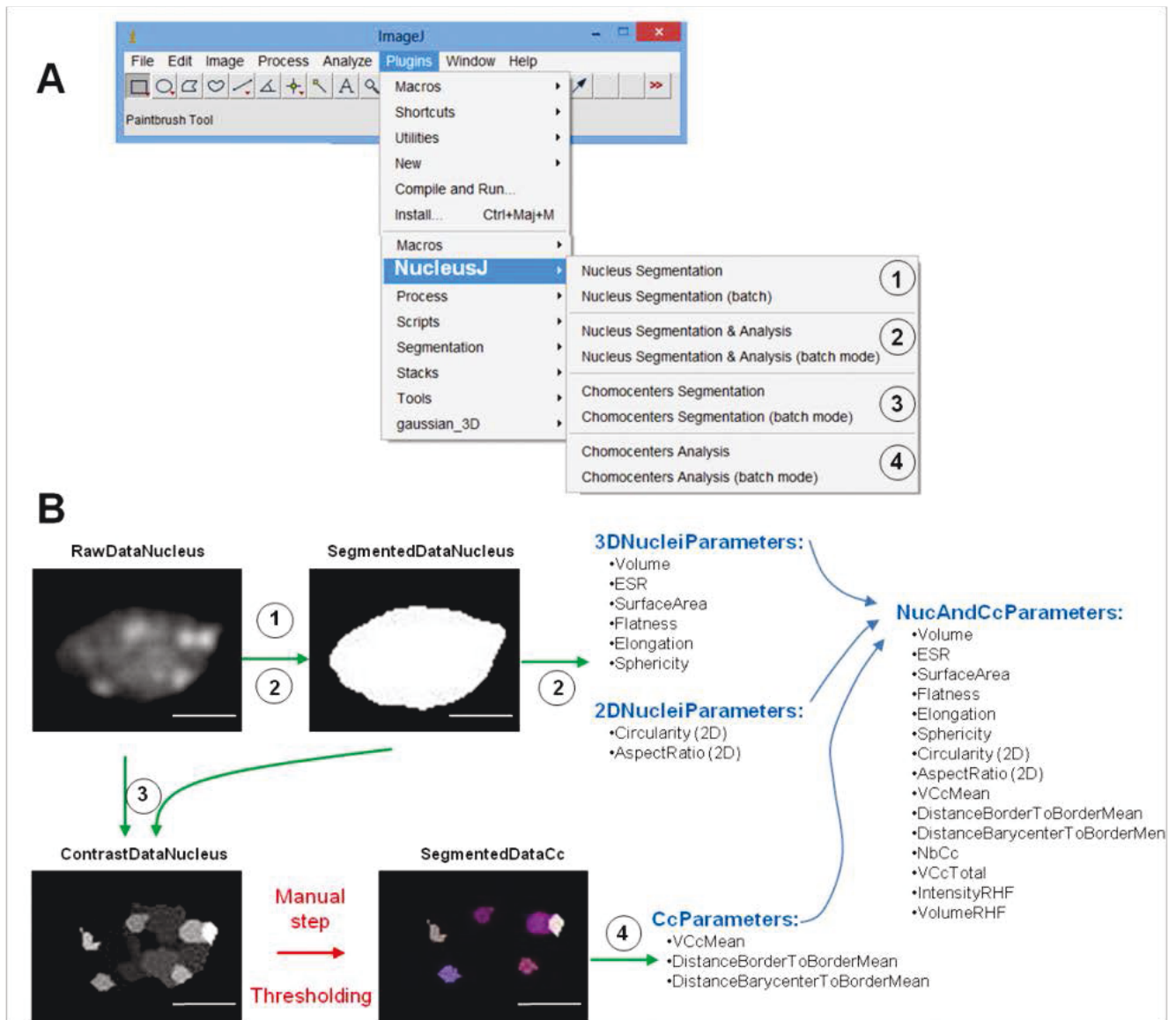
**The chromatin organization parameters in CcParameters.tab are:**

1. *Volume*: volume of chromocenter.
2. *DistanceBorderToBorder*: distance of the chromocenter border to nuclear periphery.
3. *DistanceBarycenterToBorder*: distance of the chromocenter barycenter to nuclear periphery.

## Example

### Example of image processing with NucleusJ

To analyze and characterize a raw image of a nucleus, you will have to run three different plugins.



#### The first step is the nuclear segmentation

At this step you can chose two plugins to detect the nucleus :

- 1. **Nucleus Segmentation or Nucleus Segmentation (batch)** : You obtain the image result of the segmentation.
- 2. **Nucleus Segmentation & Analysis or Nucleus Segmentation & Analysis (batch)**. If you run the *Nucleus Segmentation & Analysis (batch)* plugin you can have one or two result files, according to the option

chosen, **2DNucleiParameters.tab** and **3DNucleiParameters.tab**. With this plugin you can have a **log error file**, which contains the name of the unsegmented images.

#### **The second step is the detection of the chromocenter**

- 3. Plugin “**Chromocenter Segmentation**” generates an image representing the contrast of the analyzed regions. The results are stored in **ContrastDataNucleus** sub-directory. This image has to be thresholded manually to obtain the image of the segmented chromocenters and saved in the **SegmentedDatadCc** sub-directory with the same name as the raw image. This step could have been automatized but from our experience, automatic thresholding do not yield appropriate results. We kept that step as manual and relies on the expertise of the biologist. An example is given below: ImageJ menu at the top left, threshold tool on the right, 4 images at different stages of the process at the bottom. Green arrows indicate automatic processes while red arrow highlight the manual thresholding needed before the final analysis.

#### **The last step is the analysis of nucleus and chromocenter**

- 4. plugin “**Chromocenter Analysis**” creates one or two result files, according to the option chosen, **NucAndCcParameters.tab** and **CcParameters.tab**. This plugin can retrun a **log error file**, which contains the name of the images with a bad name.

### **Example of organization directory for batch analysis (recommended organization)**

When starting an analysis, first the user should create a main **WorkDirectory** as well as a **RawDataNucleus** sub-directory.

Raw data from **RawDataNucleus** are used by **Nucleus Segmentation** and **Nucleus Segmentation** to create a new sub-directory called **SegmentedDataNucleus**.

**Chromocenter Segmentation** uses the images contain within the **RawDataNucleus** and **SegmentedDataNucleus** to apply the 3D watershed transformation. Each new contrasted image are stored in a new sub-directory called **ContrastDataNucleus**.

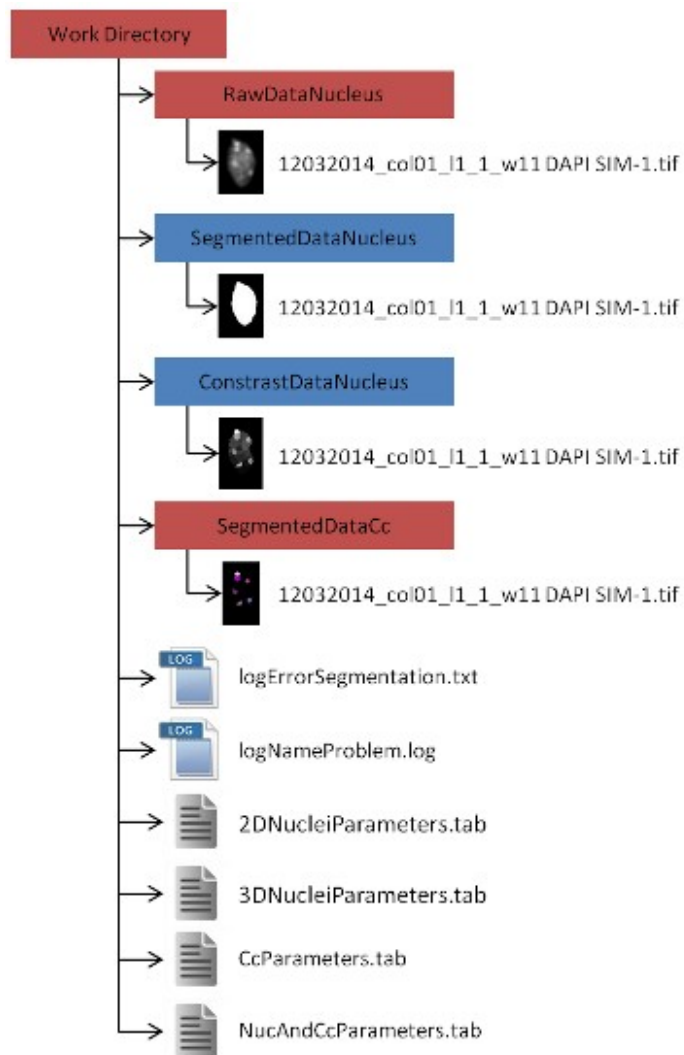
Manual thresholding should be performed on the contrasted images contained within **ContrastDataNucleus**. Once the threshold is applied, the image should be stored in a new sub-directory created by the user and called **SegmentedDatadCc**.

Finally **Chromocenter Analysis** is applied on the segmented chromocenters.

The complete plugin leads to 4 sub-directories and 4 logout files. 2 logError files may also be produced. To help the user, an example is given below where:

- directories and sub-directories created by the user are in red
- sub-directories automatically created by **NucleusJ** are in blue.
- All the files in the work directory are created by **NucleusJ** .





## Installation

Download ( [the latest NucleusJ .jar](#)) in your ImageJ plugins folder and then restart ImageJ or simply apply the command Help>Refresh Menus.

### Dependencies

- jama.jar : <http://math.nist.gov/javanumerics/jama/Jama-1.0.3.jar>
- MorphoLibJ\_ .jar:                   download                   the                   latest                   version  
from <https://github.com/ijpb/MorphoLibJ/releases>
- imagescience.jar  
: <http://www.imagescience.org/meijering/software/download/imagescience.jar>

## Download

The latest release (1.0.1) can be downloaded from here:

- [nucleusj\\_-1.0.1.jar](#)

The source code can be found [on GitHub](#).

## Citation

---

Andrey, P., Kiêu, K., Kress, C., Lehmann, G., Tirichine, L., Liu, Z., Biot, E., Adenot, P.-G., Hue-Beauvais, C., Houba-Hérin, N., Duranthon, V., Devinoy, E., Beaujean, N., Gaudin, V., Maurin, Y., Debey, P., 2010. Statistical Analysis of 3D Images Detects Regular Spatial Distributions of Centromeres and Chromocenters in Animal and Plant Nuclei. *PLoS Comput Biol* 6, e1000853.

Beucher, S., Lantuéjoul, C., 1979. Use of watersheds in contour detection. International workshop on image processing, real-time edge and motion detection.

Beucher, S., Meyer, F., 1993. The morphological approach to segmentation: the watershed transformation. *Mathematical Morphology in Image Processing*.

Fransz, P., de Jong, J.H., Lysak, M., Castiglione, M.R., Schubert, I., 2002. Interphase chromosomes in *Arabidopsis* are organized as well defined chromocenters from which euchromatin loops emanate. *Proceedings of the National Academy of Sciences* 99, 14584 –14589.

Otsu, N., 1979. A threshold selection method from gray-level histograms. *IEEE Trans. Sys., Man., Cyber.* 9, 62–66.

Vincent, L., Soille, P., 1991. Watersheds in digital spaces: an efficient algorithm based on immersion simulations. *IEEE Transactions on Pattern Analysis and Machine Intelligence* 13, 583–598.

.

## **Appendix B**

**Infl            of nuclear morphology  
on chromocentre organisation in  
*Arabidopsis thaliana***

## B.1 Primers for genotyping and RT-qPCR

Table B.1: Primers for RT-qPCR and genotyping.

Purpose	Gene	FORWARD (F) and REVERSE (R) PRIMERS (5' to 3')
Genotyping of <i>wit1-1</i> (GABI-Kat 470E06)	At5g11390	CT383_Wit1: TTCTTCCATGTAGACAACATCCTG
		CT384_Wit1: CACCATGGAACAGAACGGAACATGATAGA
		GK_o8409: ATATTGACCATCATACTCATTGC
Genotyping of <i>wit2-1</i> (SALK CS39986)	At1g68910	CT379_WIT2_RP127765: ATC TTC TCG GAT GGA AGA AGC
		CT380_WIT2_WIT21425R: GTTGAGTTCAGAGTTTGTGGTAGA
		Lbb1.3:ATTTTGCCGATTTCCGGAAC
Genotyping of <i>wip1-1</i> (SAIL_390_A08)	At4g26455	CT425_SAIL390_A08_Wip1-1_LB:CAA CAC AGT TAG CCT TCA AGA
		CT425_SAIL390_A08_Wip1-1_LB:CAA CAC AGT TAG CCT TCA AGA
		LBR Sail:TAGCATCTGAATTTTCATAACCAATCTCGATACAC
Genotyping of <i>wip2-1</i> (SALK_052226)	At5g56210	CT286_wip2-1_SALK_052226_LP: GACCCAAACCGTAAGAGAG
		CT287_wip2-1_SALK_052226_RP: TGGTCTTACTGGAATGGTGG
		Lbb1.3:ATTTTGCCGATTTCCGGAAC
Genotyping of <i>wip3-1</i> (GABI-Kat line 459H07)	At3g13360	CT288_wip3-1_GABI_459H07_LP: TTGATTTCGAGTCGCTTCTCTC
		CT289_wip3-1_GABI_459H07_RP: AATCAAGGTTTCGTGTGCAAAAC
		GK_o8409: ATATTGACCATCATACTCATTGC
Genotyping of <i>sun1-1</i> (SALK_123093c)	At5g04990	CT_SUN1_N668965_LP_5: CTGATCAAGATTCGTTCCAC
		CT_SUN1_N668965_RP_6: TACCAGAGGCTTTCACATTGG
		Lbb1.3:ATTTTGCCGATTTCCGGAAC
Genotyping of <i>sun4-1</i> (SALK_022028)	At1g71360	CT133_SALK022028_LP: TTGAACCGGACAAAACCTTG
		CT134_SALK022028_RP: GGGAAATTCACGGCTTTAAAC
		Lbb1.3:ATTTTGCCGATTTCCGGAAC
Genotyping of <i>sun5-1</i> (SALK_126070C)	At4g23950	CT139_SALK126070_LP: TAGCAGTATCATGACCCAGCC
		CT140_SALK126070_RP: GTCAGGGAGTCTGAGTTTCCC
		Lbb1.3:ATTTTGCCGATTTCCGGAAC
Genotyping of <i>crwn1-1</i> (SALK_023383)	At1g67230	CT_Linc1_N525347_LP_11: GCAACTTTGTCAAAGCAGAGG
		CT_Linc1_N525347_RP_12: AGTTTCCAATGCCTTCTCCTC
		Lbb1.3:ATTTTGCCGATTTCCGGAAC
Genotyping of <i>crwn2-1</i> (SALK_090952)	At1g13220	CT_Linc2_N658767_LP_15: CTCGAAGTTCGACCACTTCTGTC
		CT_Linc2_N658767_RP_16: AGCTCATTGCTAGAGAAGGGG
		Lbb1.3:ATTTTGCCGATTTCCGGAAC
Genotyping of <i>ddm1-10</i> (SALK_000590)	At5g66750	ddm1-10_For: CTCTCCCAATGGACGAAAC
		ddm1-10_Rev: TCAATGCCAAAATTGCAGA
		Lbb1.3:ATTTTGCCGATTTCCGGAAC
Genotyping of <i>atr5-1</i> (SALK_130607C)	At5g09790	ATXR5_LP: TTTCTCTTGTCCGGTGAATG
		ATXR5_RP: CCTGCAACAATCAGTGTGATG
		Lbb1.3:ATTTTGCCGATTTCCGGAAC
Genotyping of <i>atr6-1</i> (SAIL_181_D09)	At5g24340	ATXR6_LP: TTGAGATGAATCTGGAGACCG
		ATXR6_RP: AAACGACGACGATTTGGAGTG
		LBR Sail:TAGCATCTGAATTTTCATAACCAATCTCGATACAC
Genotyping of <i>atr-1</i> SALK_025687	At1g08600	ATRX_Salk025687_LP2: TCTTCTGGCAGTTGAGAGCA
		ATRX_Salk025687_RP: GTCAAGCTCAGATGTTCCAGC
		Lbb1.3:ATTTTGCCGATTTCCGGAAC
Genotyping of <i>atr-2</i> SAIL_861_B04	At1g08600	ATRX_Sail861B04_LP: AGGAACCTCACAGCTTCTTC
		ATRX_Sail861B04_RP: TCACATGATGGCTTCTTTTC
		LBR Sail:TAGCATCTGAATTTTCATAACCAATCTCGATACAC
Genotyping of <i>asf1b</i> SALK_105822	At5g38110	Lbb1.3:ATTTTGCCGATTTCCGGAAC
		At5g38110_LP: GTG AATCCATTCCAGTTCCGAG
		At5g38110_RP: CAAAACCTTGGTAGGAGGCTC
Genotyping of <i>asf1a</i> GABI_200G05	At1g66740	At1g66740_LP: ATCTTGTGGCAACTGTTGG
		At1g66740_RP: ATCTCCTTTTCTCCTTCCCC
		GK_o8409: ATATTGACCATCATACTCATTGC
qRT-PCR of 106B		AP394_106Bq-F: TCATTATGCTAGGTGGTTGA AP395_106Bq-R: GACAACAAGTTCATTAACCA
qRT-PCR of 180bp		180(all)-F: ACCATCAAAGCCTTGAGAGCA 180(all)-R: CCGTATGAGTCTTTGTCTTTGTATCTTCT
ChIP qPCR of <i>TSI</i>		TSIq-F: CTCTACCCTTTGCATTTCATGAATCCTT TSIq-R: GATGGGCAAAAGCCCTCGGTTTTAAAATG
ChIP qPCR of <i>UBC28</i>	At1g64230	At1g64230-ChIP-F: TCATTGTTAACGGACCCAAAC At1g64230-ChIP-R: CCAGCTTCTCGCAGTAGACTC
ChIP qPCR of <i>HXK1</i>	At4g29130	At4g29130_ChIP-F: AGGAGCTCGTCTCTCTGCTG At4g29130_ChIP-R: GCTCAAACAATCCACCATCC
ChIP qPCR of <i>UEV1C</i>	At2g36060	At2G36060_ChIP-F: GGTGACTGAAATGTGAATTTGC At2G36060_ChIP-R: ATGACGCCATCTCCTTCTTC
qRT-PCR of <i>SAND</i>	At2g28390	SA-F: AACTCTATGCAGCATTGATCCACT SA-R: TGATTGCATATCTTTATCGCCATC

## B.2 Results of statistical test between mutant and wild type

Table B.2: Guard cells comparison between wild type and LINC complex mutants.

3D parameters	col0_vs_crwn12		col0_vs_kaku4col0		vs_sun145col0_vs_wit12		col0_vs_wip123col0		vs_wifi	
Volume	<b>&lt; 2.2e-16</b>		<b>&lt; 2.2e-16</b>		0.1337		0.4354		<b>2.1e-05</b>	
	23.620	9.75189	25.29884	17.62202	25.29884	23.86394	25.29884	24.64538	23.62053	20.57520
Flatness	<b>0.0339</b>		<b>0.0001231</b>		<b>0.8198</b>		<b>0.5539</b>		<b>0.8187</b>	
	1.300625	1.240564	1.278113	1.195224	1.278113	1.284035	1.278113	1.263713	1.300625	1.293467
Elongation	<b>2.877e-10</b>		<b>0.00636</b>		<b>0.5756</b>		<b>0.02356</b>		<b>0.8374</b>	
	1.246970	1.405999	1.269409	1.211759	1.269409	1.257415	1.269409	1.221229	1.246970	1.242408
Sphericity	<b>&lt; 2.2e-16</b>		<b>&lt; 2.2e-16</b>		<b>0.0004957</b>		<b>4.931e-07</b>		<b>0.9067</b>	
	0.19573	0.25312	0.1764610	0.23568	0.1764610	0.1935486	0.1764610	0.196266	0.1957387	0.1952628
RHF <sub>i</sub>	<b>&lt; 2.2e-16</b>		<b>&lt; 2.2e-16</b>		<b>0.0022</b>		<b>0.008028</b>		<b>0.5351</b>	
	0.13844	0.25114	0.1345483	0.201730	0.1345	0.1540	0.1345483	0.1488698	0.1384451	0.1417610
RHF <sub>v</sub>	<b>&lt; 2.2e-16</b>		<b>1.864e-09</b>		<b>0.135</b>		<b>0.05486</b>		<b>0.00193</b>	
	0.07670	0.1274	0.07591	0.1075	0.07591	0.06976	0.075911	0.083254	0.07670329	0.065367
NbCc	<b>&lt; 2.2e-16</b>		<b>0.4943</b>		<b>0.04535</b>		<b>4.013e-08</b>		<b>0.02446</b>	
	4.991667	2.024390	4.834646	4.700935	4.834646	5.330357	4.834646	5.991228	4.991667	5.440000
Vcc Mean	<b>3.219e-15</b>		<b>0.3128</b>		<b>0.001845</b>		<b>2.462e-05</b>		<b>2.961e-16</b>	
	0.36258	0.643439	0.4021	0.3847	0.4021808	0.3316902	0.4021808	0.3339051	0.3625885	0.2462443
Vcc Total	<b>1.795e-15</b>		<b>0.2342</b>		<b>4.165e-07</b>		<b>0.1751</b>		<b>6.321e-11</b>	
	1.761801	1.185465	1.852214	1.754193	1.852214	1.475200	1.852214	1.966536	1.761801	1.284644
Distance Border	<b>0.0001248</b>		<b>0.002587</b>		<b>5.413e-13</b>		<b>0.3259</b>		<b>0.0002019</b>	
	0.24023	0.27640	0.23352	0.2601	0.2335268	0.3027251	0.2335268	0.2414045	0.2402300	0.2706634
Distance Barycenter	<b>8.704e-12</b>		<b>0.9763</b>		<b>0.01459</b>		<b>0.1546</b>		<b>0.0004821</b>	
	0.57248	0.680817	0.58851	0.58884	0.5885130	0.619497	0.5885130	0.5722164	0.5724800	0.5364228

Table B.3: Pavement cells comparison between wild type and LINC complex mutants.

3D parameters	col0_vs_crwn12		col0_vs_kaku4col0		vs_sun145col0_vs_wit12		col0_vs_wip123col0		vs_wifi	
Volume	<b>1.273e-08</b>		<b>1.324e-07</b>		<b>8.752e-05</b>		0.3678		<b>0.0001078</b>	
	138.63486	76.71158	130.5478	85.32168	130.5478	95.1263	130.5478	121.7815	138.63486	100.3537
Flatness	<b>&lt; 2.2e-16</b>		<b>2.489e-10</b>		<b>0.6924</b>		<b>0.01676</b>		<b>0.2336</b>	
	1.545358	1.227230	1.555794	1.311155	1.555794	1.536931	1.555794	1.679347	1.545358	1.59659
Elongation	<b>&lt; 2.2e-16</b>		<b>&lt; 2.2e-16</b>		<b>8.016e-09</b>		<b>1.297e-13</b>		<b>&lt; 2.2e-16</b>	
	1.946777	1.205465	1.706213	1.212176	1.706213	1.348038	1.706213	1.260208	1.946777	1.252297
Sphericity	<b>&lt; 2.2e-16</b>		<b>4.798e-15</b>		<b>1.261e-05</b>		<b>0.0001934</b>		<b>3.482e-07</b>	
	0.1140521	0.2047111	0.11512	0.16613	0.1151289	0.1448511	0.1151289	0.139731	0.1140521	0.14236
RHF <sub>i</sub>	<b>&lt; 2.2e-16</b>		<b>&lt; 2.2e-16</b>		<b>4.323e-11</b>		<b>0.003998</b>		<b>0.005026</b>	
	0.056180	0.150098	0.06905	0.114650	0.06905356	0.105753	0.06905	0.08388	0.05618	0.06724
RHF <sub>v</sub>	<b>&lt; 2.2e-16</b>		<b>4.154e-09</b>		<b>0.002003</b>		<b>0.02582</b>		<b>0.2444</b>	
	0.027335	0.068622	0.033893	0.053604	0.03389372	0.044250	0.03389	0.04168	0.02733	0.03003
NbCc	<b>0.09906</b>		<b>0.001534</b>		<b>0.1006</b>		<b>0.1814</b>		<b>0.6378</b>	
	6.928058	7.848739	8.633333	10.4049	8.633333	9.435484	8.633333	9.359375	6.928058	7.13846
Vcc Mean	<b>3.157e-06</b>		<b>0.3482</b>		<b>0.3055</b>		<b>0.5103</b>		<b>6.036e-08</b>	
	0.4534476	0.5590714	0.4237	0.40477	0.4237292	0.4001207	0.4237292	0.4376171	0.4534476	0.35799
Vcc Total	<b>2.916e-05</b>		<b>0.01116</b>		<b>0.513</b>		<b>0.05459</b>		<b>0.002448</b>	
	3.005797	4.261573	3.487691	4.1115	3.487691	3.640923	3.487691	3.969125	3.005797	2.44406
Distance Border	<b>0.4231</b>		<b>0.2467</b>		<b>0.0002074</b>		<b>0.04475</b>		<b>0.009524</b>	
	0.3781535	0.3892068	0.3620	0.37735	0.3620513	0.4074372	0.3620513	0.390895	0.3781535	0.41371
Distance Barycenter	<b>0.7203</b>		<b>0.09442</b>		<b>0.5237</b>		<b>0.0247</b>		<b>0.8852</b>	
	0.8052116	0.8123	0.78504	0.75752	0.7850434	0.7952824	0.7850434	0.82728	0.805211	0.80800

Table B.4: Root hair cells comparison between wild type and LINC complex mutants.

3D parameters	col0_vs_crwn12		col0_vs_kaku4col0		_vs_sun145col0_vs_wit12		col0_vs_wip123col0		_vs_wifi	
Volume	<b>8.125e-08</b>		0.6672		0.71		0.25		0.9316	
	109.08868	59.79314	113.93981	107.235	113.93981	107.584	113.93981	131.2783	109.08868	109.9967
Flatness	<b>0.491</b>		<b>0.2633</b>		<b>0.6335</b>		<b>0.7572</b>		<b>0.8654</b>	
	1.456240	1.414238	1.558837	1.716006	1.558837	1.623213	1.558837	1.525579	1.456240	1.467172
Elongation	<b>1.151e-08</b>		<b>1.497e-08</b>		<b>4.981e-05</b>		<b>7.311e-09</b>		<b>0.5731</b>	
	3.022610	1.298324	3.569873	1.451435	3.569873	2.174565	3.569873	1.338134	3.022610	2.837785
Sphericity	<b>6.117e-15</b>		<b>2.481e-10</b>		<b>8.973e-05</b>		<b>2.2e-16</b>		<b>0.8407</b>	
	0.09587	0.18519	0.06558	0.14746	0.06558	0.11416	0.06558	0.13781	0.095870	0.09400
RHFv	<b>0.001497</b>		<b>1.124e-05</b>		<b>0.003564</b>		<b>0.511</b>		<b>0.8983</b>	
	0.08932	0.12784	0.08783	0.12720	0.08783	0.11660	0.08783	0.08379	0.08932	0.08835
RHFv	<b>0.0005455</b>		<b>0.008733</b>		<b>0.3422</b>		<b>0.1664</b>		<b>0.8131</b>	
	0.04065	0.06722	0.04646	0.06086	0.04646	0.05191	0.04646	0.04094	0.04065	0.03954
NbCc	<b>2.509e-12</b>		<b>0.5859</b>		<b>0.9519</b>		<b>0.5175</b>		<b>0.288</b>	
	9.477273	6.153846	10.52	11.17647	10.52	10.44444	10.52	11.4717	9.477273	10.333333
Vcc Mean	<b>0.0005726</b>		<b>0.1045</b>		<b>0.8899</b>		<b>0.6863</b>		<b>0.09043</b>	
	0.42936	0.6014365	0.4878	0.56145	0.4878226	0.4950	0.48782	0.47227	0.42936	0.3752561
Vcc Total	<b>0.8625</b>		<b>0.009206</b>		<b>0.9801</b>		<b>0.3984</b>		<b>0.8552</b>	
	3.666760	3.604775	4.607616	6.0390	4.607616	4.617901	4.607616	5.064176	3.666760	3.713527
Distance Border	<b>0.5286</b>		<b>0.0003698</b>		<b>0.01238</b>		<b>0.006716</b>		<b>0.4763</b>	
	0.351012	0.36502	0.29744	0.38934	0.2974407	0.3687	0.2974	0.3592208	0.351012	0.3367211
Distance Barycenter	<b>0.01283</b>		<b>0.009523</b>		<b>0.07837</b>		<b>0.02648</b>		<b>0.09904</b>	
	0.747509	0.81812	0.7256	0.8097	0.7256872	0.7814	0.7256	0.7891	0.7475097	0.7037618

Table B.5: Guard cells comparison between wild type and chromatin mutants.

3D parameters	col0_vs_atrx56col0		_vs_ddm1-10		col0_vs_asflacol0		_vs_asf1b		col0_vs_asflab		col0_vs_atrx1		col0_vs_atrx2	
Volume	<b>0.3647</b>		<b>0.0007572</b>		<b>0.03212</b>		<b>0.3925</b>		<b>0.1508</b>		<b>5.001e-05</b>		<b>0.151</b>	
	23.62053	24.41771	23.62053	27.24945	25.29884	27.13723	25.29884	26.01476	22.67206	24.29808	25.29884	29.90898	25.29884	26.48214
Flatness	<b>0.104</b>		<b>0.1641</b>		<b>0.3564</b>		<b>0.2627</b>		<b>0.2553</b>		<b>0.8187</b>		<b>0.4152</b>	
	1.300625	1.355335	1.300625	1.344536	1.278113	1.301279	1.278113	1.305912	1.357740	1.390266	1.278113	1.272340	1.278113	1.259179
Elongation	<b>3.443e-05</b>		<b>0.03153</b>		<b>0.4811</b>		<b>0.1666</b>		<b>0.5604</b>		<b>0.4094</b>		<b>0.368</b>	
	1.246970	1.370809	1.246970	1.29561	1.269409	1.253162	1.269409	1.303215	1.288062	1.300288	1.269409	1.250939	1.269409	1.247838
Sphericity	<b>0.006946</b>		<b>0.6563</b>		<b>0.2093</b>		<b>0.01048</b>		<b>0.6526</b>		<b>0.8634</b>		<b>6.325e-12</b>	
	0.1957387	0.1833705	0.1957	0.1938	0.1764810	0.17157	0.1764810	0.1869995	0.1806061	0.1823172	0.1764810	0.1771685	0.1764810	0.204670
RHFv	<b>0.0671</b>		<b>9.225e-07</b>		<b>0.118</b>		<b>0.6763</b>		<b>3.27e-05</b>		<b>0.06304</b>		<b>0.6212</b>	
	0.1384451	0.1286374	0.1384451	0.1092	0.1345483	0.1267905	0.1345483	0.1366440	0.14875	0.1297756	0.1345483	0.1256446	0.1345483	0.1372910
RHFv	<b>1.193e-07</b>		<b>0.0003887</b>		<b>4.468e-07</b>		<b>0.0163</b>		<b>0.0009348</b>		<b>2.625e-09</b>		<b>0.3771</b>	
	0.076703	0.058402	0.076703	0.06256	0.0759118	0.057739	0.075911	0.06785974	0.090560	0.079196	0.075911	0.055868	0.075911	0.07231
NbCc	<b>0.6503</b>		<b>0.1974</b>		<b>0.006484</b>		<b>0.04437</b>		<b>6.178e-06</b>		<b>1.369e-05</b>		<b>0.09426</b>	
	4.991667	5.093458	4.991667	4.712963	4.834646	5.369748	4.834646	5.254386	5.217822	6.074074	4.834646	5.750000	4.834646	5.194175
Vcc Mean	<b>1.757e-10</b>		<b>0.8909</b>		<b>9.522e-13</b>		<b>0.0004617</b>		<b>7.77e-11</b>		<b>3.736e-11</b>		<b>0.03135</b>	
	0.3625885	0.2749329	0.3625	0.3595	0.4021808	0.2837223	0.4021808	0.3413096	0.3821204	0.3094122	0.4021808	0.2872365	0.4021808	0.3642014
Vcc Total	<b>2.069e-09</b>		<b>0.01605</b>		<b>1.252e-07</b>		<b>0.0226</b>		<b>0.2191</b>		<b>0.0003186</b>		<b>0.529</b>	
	1.761801	1.323408	1.761801	1.564690	1.852214	1.464399	1.852214	1.685919	1.901185	1.822626	1.852214	1.586863	1.852214	1.799266
Distance Border	<b>2.532e-06</b>		<b>0.02609</b>		<b>4.858e-13</b>		<b>2.046e-07</b>		<b>0.1913</b>		<b>9.698e-11</b>		<b>0.0003337</b>	
	0.2402300	0.2801826	0.24023	0.2626	0.2335268	0.300213	0.23352	0.2789642	0.2049523	0.2136914	0.23352	0.29422	0.2335268	0.2690453
Distance Barycenter	<b>0.6767</b>		<b>0.004804</b>		<b>0.04285</b>		<b>0.01776</b>		<b>0.168</b>		<b>0.3011</b>		<b>0.1493</b>	
	0.5724800	0.5680153	0.57248	0.61120	0.5885130	0.6120676	0.5885130	0.6160257	0.55609	0.5430570	0.5885130	0.6010828	0.5885130	0.6061067

Table B.6: Pavement cells comparison between wild type and chromatin mutants.

3D parameters	col0_vs_atrx56col0		vs_ddm1-10		col0_vs_asf1acol0		vs_asf1b		col0_vs_asf1ab		col0_vs_atrx1		col0_vs_atrx2	
Volume	0.9463		0.3209		0.2402		0.1585		0.0503		0.7647		0.9169	
	138.63486	137.8170	138.63486	127.5575	130.5478	119.8178	130.5478	146.0286	144.6653	122.607	130.5478	133.5611	130.5478	129.5747
Flatness	0.6296		0.001717		0.3226		0.3991		0.02561		0.08889		0.3601	
	1.545358	1.525124	1.545358	1.683673	1.555794	1.600264	1.555794	1.593407	1.519047	1.608679	1.555794	1.637099	1.555794	1.595746
Elongation	0.9132		0.3657		0.01186		0.1094		3.111e-06		0.7416		0.0793	
	1.946777	1.937282	1.946777	1.865705	1.706213	1.901396	1.706213	1.820757	1.939331	2.45254	1.706213	1.730258	1.706213	1.827882
Sphericity	0.7815		0.501		0.0447		0.5884		0.01723		0.6296		0.4571	
	0.1140521	0.11582	0.1140521	0.11798	0.1151289	0.10236	0.11512	0.11180	0.1109684	0.0972797	0.1151289	0.1121536	0.1151	0.1198145
RHF <sub>i</sub>	< 2.2e-16		0.07718		0.09325		0.1079		0.002244		9.139e-06		0.1559	
	0.05618	0.08858	0.05618	0.06169	0.06905	0.076266	0.069053	0.075489	0.057733	0.073418	0.06905	0.088110	0.06905	0.07512
RHF <sub>v</sub>	0.008617		0.2699		0.4362		0.4828		0.03196		0.6629		0.93	
	0.027335	0.032688	0.027335	0.02938	0.033893	0.031630	0.033893	0.031942	0.032154	0.039848	0.03389	0.03516	0.033893	0.034155
NbCc	9.5e-08		0.04353		0.1709		0.001908		1.633e-05		2.02e-08		0.04172	
	6.928058	9.909091	6.928058	7.858268	8.633333	9.290323	8.633333	10.59285	7.096491	10.052023	8.633333	12.223077	8.633333	9.717391
Vcc Mean	6.722e-06		0.001187		0.002111		0.01582		2.287e-09		2.96e-06		0.2391	
	0.4534476	0.3712485	0.4534476	0.3966973	0.4237292	0.3613817	0.4237292	0.37719	0.5357140	0.39402	0.4237292	0.3346647	0.42372	0.4007175
Vcc Total	0.009553		0.7001		0.3342		0.06424		0.2586		0.02127		0.131	
	3.005797	3.636733	3.005797	3.085715	3.487691	3.290090	3.487691	3.996031	3.506740	3.840078	3.487691	4.039711	3.487691	3.852174
Distance Border	0.01114		0.02022		2.662e-06		6.532e-08		0.2463		0.0001385		0.0003749	
	0.3781535	0.4129641	0.3781535	0.4094587	0.3620513	0.4259574	0.3620513	0.43734	0.32398	0.30908	0.3620513	0.4121648	0.36205	0.40823
Distance Barycenter	0.01493		0.1066		0.0001593		3.001e-05		0.008135		0.3011		0.01104	
	0.8052116	0.7594037	0.8052116	0.83728	0.7850434	0.85128	0.7850434	0.8613155	0.7707453	0.7214821	0.7850434	0.7845950	0.78504	0.8307762

Table B.7: Root hair cells comparison between wild type and chromatin mutants.

3D parameters	col0_vs_atrx56col0		vs_ddm1-10		col0_vs_asf1acol0		vs_asf1b		col0_vs_asf1ab		col0_vs_atrx1		col0_vs_atrx2	
Volume	0.2725		0.0622		0.1026		0.7298		0.002721		0.3865		0.4938	
	109.088	119.0924	109.08868	131.5833	113.93981	88.97238	113.93981	109.0374	140.4610	177.2373	113.93981	128.2701	113.93981	123.5519
Flatness	0.03587		0.2144		0.2635		0.9401		0.3902		0.6421		0.77	
	1.456240	1.623033	1.456240	1.548614	1.558837	1.695697	1.558837	1.567275	1.384106	1.435291	1.558837	1.504086	1.558837	1.588995
Elongation	0.2225		0.9686		0.1732		0.7921		0.1207		0.729		0.3765	
	3.022610	2.585807	3.022610	3.036336	3.569873	2.963744	3.569873	3.466858	4.689416	5.371079	3.569873	3.760412	3.569873	3.212451
Sphericity	0.9583		0.1111		0.1085		0.2952		0.000901		0.05086		0.01566	
	0.095870	0.095375	0.09587	0.08176	0.065588	0.080780	0.065588	0.07286462	0.065427	0.04726	0.06558	0.08112	0.065588	0.08880
RHF <sub>i</sub>	0.05895		0.01126		0.1544		0.3034		0.275		0.4567		0.3378	
	0.08932	0.07586	0.08932	0.071134	0.087838	0.106266	0.087838	0.09516678	0.07322	0.068558	0.08783	0.09341	0.087838	0.09476
RHF <sub>v</sub>	0.05272		0.01889		0.5438		0.8831		0.2826		0.3103		0.1765	
	0.04065	0.03246	0.04065	0.030797	0.046462	0.050980	0.046462	0.045823	0.037618	0.035033	0.046462	0.041595	0.04646	0.04099
NbCc	0.7734		0.6989		0.4912		0.653		1.372e-05		0.7609		0.9214	
	9.477273	9.23684	9.477273	9.145833	10.52	9.50	10.52	9.914286	9.983051	14.2553	10.52	10.88462	10.52	10.63265
Vcc Mean	0.9001		0.8112		0.7147		0.4563		0.008166		0.5847		0.6221	
	0.42936	0.42477	0.42936	0.42077	0.4878226	0.4698343	0.4878226	0.5276994	0.5175131	0.43606	0.4878226	0.46357	0.4878226	0.4677270
Vcc Total	0.8119		0.7713		0.2264		0.6571		0.009682		0.527		0.8559	
	3.666760	3.604547	3.666760	3.580361	4.607616	4.018159	4.607616	4.842796	4.864101	5.86790	4.607616	4.944610	4.607616	4.685887
Distance Border	0.1697		0.8543		0.229		0.6531		0.8311		0.01352		0.006544	
	0.351012	0.38140	0.351012	0.3548071	0.2974407	0.3294780	0.2974407	0.3083612	0.2734905	0.276843	0.2974407	0.36139	0.2974407	0.3595537
Distance Barycenter	0.2544		0.6811		0.3599		0.8668		0.7573		0.2529		0.2938	
	0.74750	0.78304	0.7475097	0.7360807	0.7256872	0.7574000	0.7256872	0.7206487	0.6655588	0.67207	0.7256872	0.76207	0.7256872	0.7595695

## B.3 Nuclear morphology of the chromatin mutants

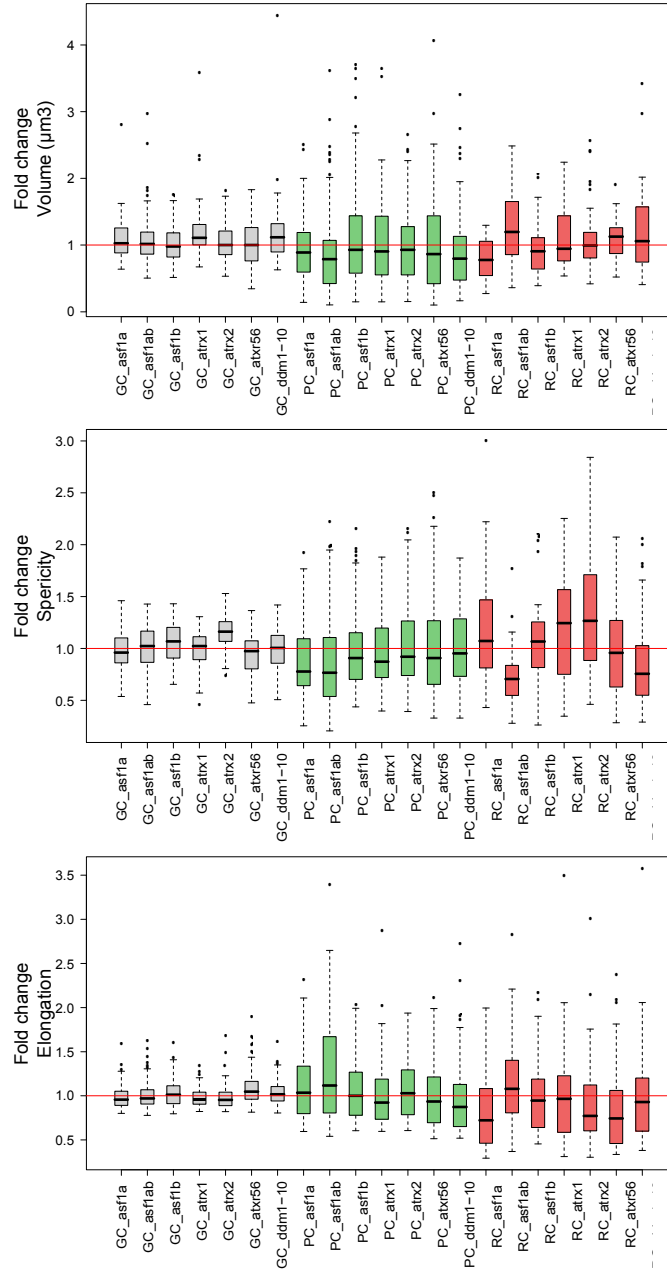


Figure B.1: Alteration of nuclear morphology in heterochromatin mutant nuclei from guard cells, pavement cells and root cells. Boxplots of nuclear morphology parameters generated by *NucleusJ* highlighting the phenotypic variations in three types of nuclei (GC in gray, PC in green and RC in red) for seven mutant backgrounds. Samples and Statistical analysis are available respectively in Table 3.2 and Appendix B.2. All parameters recorded for mutant backgrounds were standardised using Col-o (WT) set as 1 (red line).



## B.4 FISH-3D

Table B.8: Sample of nuclei in GC and PC.

	Number GC nuclei	Number PC nuclei	Total of nuclei
Col-o	56	46	102
<i>kaku4-2</i>	32	51	83
<i>crwn1 crwn2</i>	35	41	76
<i>wifi</i>	44	29	73
<i>sun1 sun4 sun5</i>	27	32	59
<i>ddm1-10</i>	47	43	90
<i>atxr5 atxr6</i>	41	48	89

Table B.9: Proportion of condensed nuclei in GC and PC.

	GC condensed	PC condensed	Total condensed
Col-o	35.71	34.78	35.29
<i>kaku4-2</i>	40.62	13.72	24.10
<i>crwn1 crwn2</i>	31.43	48.78	40.79
<i>wifi</i>	25	13.79	20.55
<i>sun1 sun4 sun5</i>	18.52	21.87	20.34
<i>ddm1-10</i>	12.76	16.28	14.44
<i>atxr5 atxr6</i>	24.39	22.91	23.60

## B.5 Quantitative RT-PCR analysis of the chromatin mutants

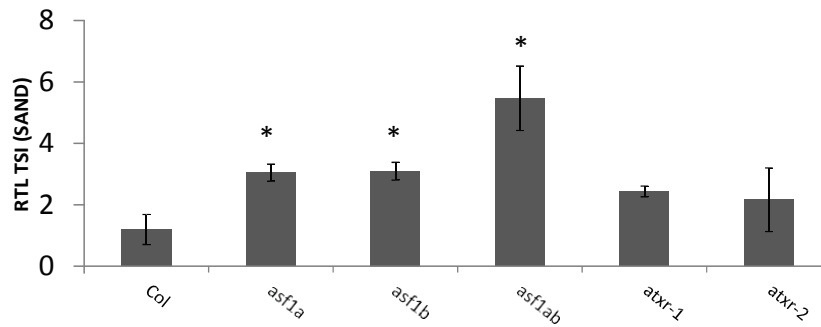


Figure B.2: **Quantitative RT-PCR analysis of TSI expression in WT and chromatin mutants.** Transcription level of TSI scored by RT-qPCR. Histograms show means of transcript level  $\pm$  SEM obtained for two independent PCR amplifications of three biological replicates. The y axis shows the fold change relative to WT (WT set to 1) after normalisation to expression of At2g28390 (*AtSAND*). (\*:  $p \leq 0.05$ )

## **Appendix C**

### **Exploring of the proteins of the plant nuclear envelope**

# C.1 KASH proteins detected with the Perl script

## C.1.1 Results of finding KASH homologues

Table C.1: KASH results from the Perl script.

Gene name	Organism	Gene id	Homologues	e-value	Score
AtWIP1	<i>Arabidopsis thaliana</i>	AT4G26455	no	no	no
AtWIP2	<i>Arabidopsis thaliana</i>	AT5G56210	no	no	no
AtSINE4	<i>Arabidopsis thaliana</i>	AT4G24950	no	no	no
AtSINE2	<i>Arabidopsis thaliana</i>	AT3G03970	no	no	no
AtTIK	<i>Arabidopsis thaliana</i>	AT5G44920	no	no	no
AtSINE1	<i>Arabidopsis thaliana</i>	AT1G54385	no	no	no
AtWIP3	<i>Arabidopsis thaliana</i>	AT3G13360	no	no	no
AtSINE3	<i>Arabidopsis thaliana</i>	AT3G06600	no	no	no
Aly478787	<i>Arabidopsis lyrata</i>	478787.v1	no	no	no
Aly492343	<i>Arabidopsis lyrata</i>	492343.v1	no	no	no
AlySINE2	<i>Arabidopsis lyrata</i>	340556.v1	AtSINE2	0	929
AlySINE1	<i>Arabidopsis lyrata</i>	474709.v1	AtSINE1	0	964
AlyWIP3	<i>Arabidopsis lyrata</i>	904239.v1	AtSINE3	0	730
Bra.E03268.1.p	<i>Brassica rapa</i>	Brara.E03477.v1.3	no	no	no
BraSINE2-a	<i>Brassica rapa</i>	Brara.E03477.v1.3	AtSINE2	0	763
BraSINE3	<i>Brassica rapa</i>	Brara.A03650.v1.3	AtSINE3	1e-83	246
Bra.A01491.1.p	<i>Brassica rapa</i>	Brara.A01491.v1.3	no	no	no
BraWIP1	<i>Brassica rapa</i>	Brara.A01633.v1.3	AtWIP1	0	555
BraSINE2-b	<i>Brassica rapa</i>	Brara.A03794.v1.3	AtSINE2	5e-169	487
Bra.K01474.1.p	<i>Brassica rapa</i>	Brara.K01474.v1.3	no	no	no
BraWIP2	<i>Brassica rapa</i>	Brara.J01056.v1.3	AtWIP2	3e-88	272
BraWIP3-a	<i>Brassica rapa</i>	Brara.A03268.v1.3	AtWIP3	1e-134	393
BraSINE1	<i>Brassica rapa</i>	Brara.I00153.v1.3	AtSINE1	0	823
Cpa_CP00117G00040	<i>Carica papaya</i>	CP00117G00040	no	no	no
CpaSINE1/2	<i>Carica papaya</i>	CP00051G01090	AtSINE1 2	0	642
CpaWIP	<i>Carica papaya</i>	CP00012G000680	ATWIP	3e-76	250
Cpa_CP00009G00390	<i>Carica papaya</i>	CP00009G00390	no	no	no
Gma.13G045900.2.p	<i>Glycine max</i>	Glyma.13G045900	no	no	no
GmaSINE1/2-a	<i>Glycine max</i>	Glyma.02G071700	AtSINE1 2	0	547
GmaSINE1/2-b	<i>Glycine max</i>	Glyma.16G152900	AtSINE1 2	0	550
Gma.17G035100.1.p	<i>Glycine max</i>	Glyma.17G035100	no	no	no
GmaSINE1/2-c	<i>Glycine max</i>	Glyma.19G110600	AtSINE1 2	0	540
Gma.06G321400.1.p	<i>Glycine max</i>	Glyma.06G321400	no	no	no
GmaSINE1/2-d	<i>Glycine max</i>	Glyma.16G041800	AtSINE1 2	0	525
GmaWIP-b	<i>Glycine max</i>	Glyma.04G113700	ATWIP	1e-41	157
Sly_Solyc03g083980	<i>Solanum lycopersicum</i>	Solyc03g083980.1	no	no	no
Sly_Solyc12g089020	<i>Solanum lycopersicum</i>	Solyc12g089020.1	no	no	no
Sly_Solyc03g019740	<i>Solanum lycopersicum</i>	Solyc03g019740.1	no	no	no
Sly_Solyc03g093980	<i>Solanum lycopersicum</i>	Solyc03g093980.1	no	no	no
Sly_Solyc07g066170	<i>Solanum lycopersicum</i>	Solyc07g066170.2	no	no	no
SlySINE1/2	<i>Solanum lycopersicum</i>	Solyc03g062700.2	AtSINE1 2	3e-176	509
MacSINE1/2-b	<i>Musa acuminata</i>	103993855	AtSINE1 2	3e-156	459
NnuSINE1/2-b	<i>Nelumbo nucifera</i>	104597698	AtSINE1 2	0	538
NnuSINE1/2-a	<i>Nelumbo nucifera</i>	104611165	AtSINE1 2	0	587
Os04g46790.1	<i>Oryza sativa</i>	LOC Os04g46790	no	no	no
Os04g39540.1	<i>Oryza sativa</i>	LOC Os04g39540	no	no	no
Os12g42960.1	<i>Oryza sativa</i>	LOC Os12g42960	no	no	no
Os04g31720.1	<i>Oryza sativa</i>	LOC Os04g31720	no	no	no
OsaSINE1/2	<i>Oryza sativa</i>	LOC Os11g37100	AtSINE1 2	6e-151	447
PabSINE-c	<i>Picea abies</i>	MA_395650g0010	AtSINE	8e-94	303
Ppa_Phpat.005G028200.1.p	<i>Physcomitrella patens</i>	Phpat.005G028200.v3.0	no	no	no
PpaSINE-a	<i>Physcomitrella patens</i>	Phpat.006G062300.v3.0	AtSINE	9e-48	177
Ppa_Phpat.003G109500.1.p	<i>Physcomitrella patens</i>	Phpat.003G109500.v3.0	no	no	no
Ppa_Phpat.005G024400.3.p	<i>Physcomitrella patens</i>	Phpat.005G024400.v3.0	no	no	no
Ppa_Phpat.018G064200.2.p	<i>Physcomitrella patens</i>	Phpat.018G064200.v3.0	no	no	no
Ppa_Phpat.006G062300.1.p	<i>Physcomitrella patens</i>	Phpat.006G062300.v3.0	no	no	no
PpaSINE-b	<i>Physcomitrella patens</i>	Phpat.022G009100.v3.0	AtSINE	2e-50	186
PpeSINE1/2	<i>Prunus persica</i>	ppa020856m	AtSINE1 2	0	575
Ppe_ppa000468m	<i>Prunus persica</i>	ppa000468m	no	no	no
Ppe_ppa003004m	<i>Prunus persica</i>	ppa003004m	no	no	no
Ppe_ppa020688m	<i>Prunus persica</i>	ppa020688m	no	no	no
Ppe_ppa015988m	<i>Prunus persica</i>	ppa015988m	no	no	no
Ppe_ppa1027141m	<i>Prunus persica</i>	ppa1027141m	no	no	no
AtrSINE	<i>Amborella trichopoda</i>	evm 27.TU.AmTr v1.0 scaffold000004.62	AtSINE	1e-135	407
Atr 00070G00090	<i>Amborella trichopoda</i>	evm 27.TU.AmTr v1.0 scaffold00070.9	no	no	no
Atr 00079G00540	<i>Amborella trichopoda</i>	evm 27.TU.AmTr v1.0 scaffold00079.55	no	no	no
Atr 00061G00420	<i>Amborella trichopoda</i>	evm 27.TU.AmTr v1.0 scaffold00061.45	no	no	no
Ptr Potri.012G102300.1	<i>Populus trichocarpa</i>	Potri.012G102300	no	no	no
Ptr Potri.017G115200.1	<i>Populus trichocarpa</i>	Potri.017G115200	no	no	no
Ptr Potri.008G152700.2	<i>Populus trichocarpa</i>	Potri.008G152700	no	no	no
Ptr WIP-b	<i>Populus trichocarpa</i>	Potri.011G169000	ATWIP	8e-59	205
Smo 432042	<i>Selaginella moellendorffii</i>	432042.v1	no	no	no
TcaSINE1/2	<i>Theobroma cacao</i>	TC0005G29190	AtSINE1 2	2e-121	370
TcaWIP	<i>Theobroma cacao</i>	TC0007G00130	ATWIP	2e-73	244
Tca Thecc1EG029977t1	<i>Theobroma cacao</i>	Thecc1EG029977t1	no	no	no
VviWIP	<i>Vitis vinifera</i>	VV19G06810	ATWIP	5e-157	46
VviSINE1/2	<i>Vitis vinifera</i>	VV08G08350	AtSINE1 2	0	534
Zma GRMZM2G034882	<i>Zea mays</i>	GRMZM2G034882	no	no	no
Zma GRMZM2G162319	<i>Zea mays</i>	GRMZM2G162319	no	no	no
Zma GRMZM2G370707	<i>Zea mays</i>	GRMZM2G370707	no	no	no
Zma GRMZM2G094850	<i>Zea mays</i>	GRMZM2G094850	no	no	no
Zma GRMZM2G151418	<i>Zea mays</i>	GRMZM2G151418	no	no	no
ZmaSINE1/2	<i>Zea mays</i>	GRMZM2G000608	AtSINE1 2	5e-143	427
Zma GRMZM2G112187	<i>Zea mays</i>	GRMZM2G112187	no	no	no

### C.1.2 KASH proteins clustered using Perl script results

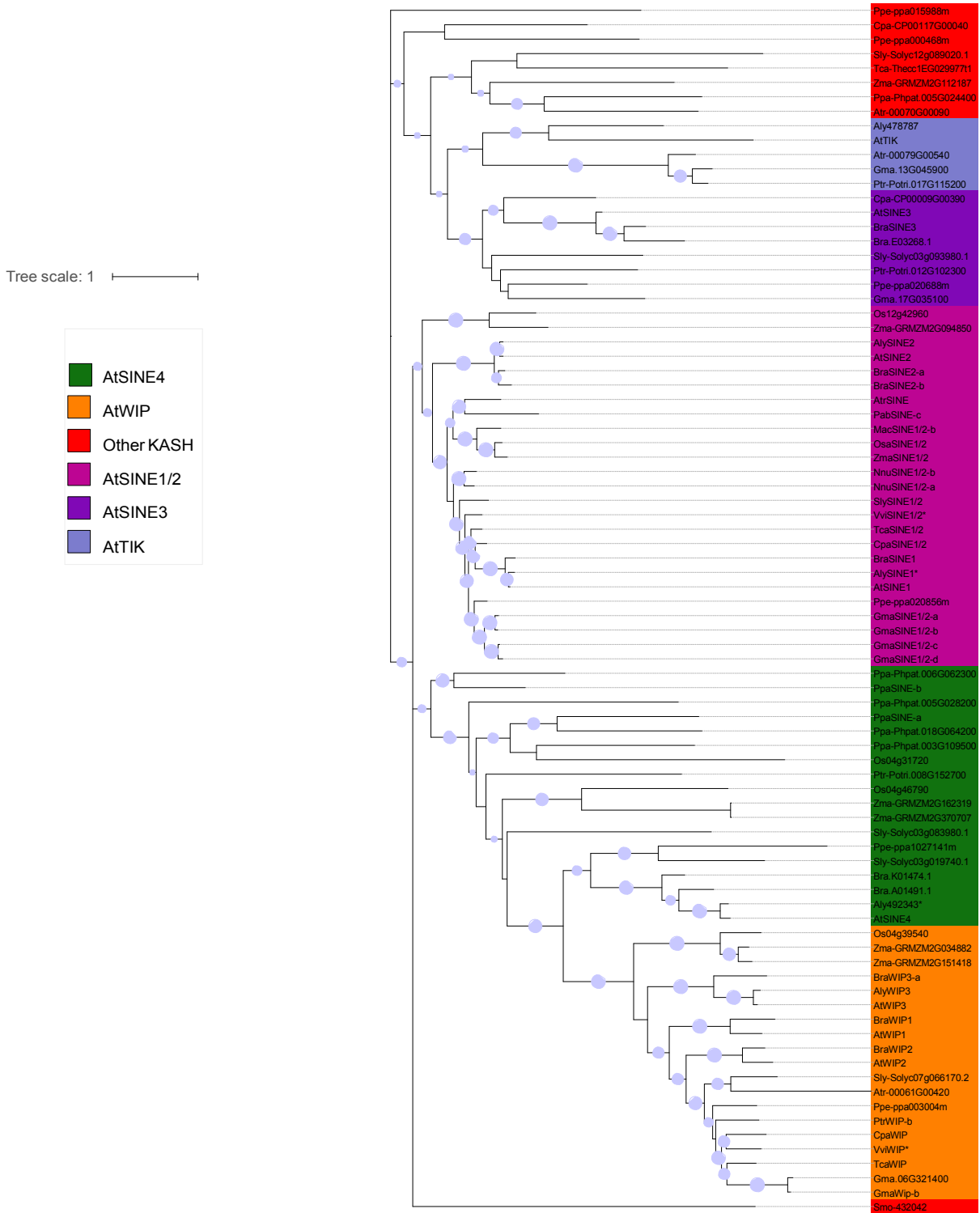


**Figure C.1: KASH protein clustering.** A maximum likelihood tree of KASH protein homologues constructed from an alignment. Bootstrap values are represented by the diameter of the pale blue circle. If the bootstrap is below 0.5 the bootstrap is not indicated. The colour of the label shows the cluster to which the KASH protein belongs. The gene label is constructed from the three letters from the species name (see Table 4.1) and the gene name of the *A. thaliana*.

## C.2 Homologue protein results obtain with BLASTp

### C.2.1 CRWN homologue results

Table C.2: CRWN results.

Gene name	Organism	Gene id	Homologues	e-value	Score
AlyCRWN3	<i>Arabidopsis lyrata</i>	476006.v1	AtCRWN3	0	573
AlyCRWN2	<i>Arabidopsis lyrata</i>	471477.v1	AtCRWN2	0	1676
BraCRWN1-a	<i>Brassica rapa</i>	Brara.B01707.v1.3	AtCRWN1	0	1527
BraCRWN1-b	<i>Brassica rapa</i>	Brara.G02692.v1.3	AtCRWN1	0	1516
BraCRWN3	<i>Brassica rapa</i>	Brara.B01814.v1.3	AtCRWN3	0	1006
BraCRWN2	<i>Brassica rapa</i>	Brara.F00805.v1.3	AtCRWN2	0	1347
BraCRWN4	<i>Brassica rapa</i>	Brara.I00831.v1.3	AtCRWN4	0	1415
CpaCRWN23	<i>Cpa</i>	CP00001G02270	AtCRWN2 3	0	544
CpaCRWN1	<i>Carica papaya</i>	CP00179G00320	AtCRWN1	0	607
CpaCRWN4	<i>Carica papaya</i>	CP00129G00560	AtCRWN4	0	653
GmaCRWN1-a	<i>Glycine max</i>	Glyma.08G256300.Wm82.a2.v1	AtCRWN1	0	802
GmaCRWN1-b	<i>Glycine max</i>	Glyma.18G280500.Wm82.a2.v1	AtCRWN1	0	791
GmaCRWN2/3-a	<i>Glycine max</i>	Glyma.02G101800.Wm82.a2.v1	AtCRWN2 3	1e-153	491
GmaCRWN2/3-b	<i>Glycine max</i>	Glyma.01G090100.Wm82.a2.v1	AtCRWN2 3	2e-130	423
GmaCRWN4-a	<i>Glycine max</i>	Glyma.05G109300.Wm82.a2.v1	AtCRWN4	0	699
GmaCRWN4-b	<i>Glycine max</i>	Glyma.17G157900.Wm82.a2.v1	AtCRWN4	0	696
GmaCRWN4-c	<i>Glycine max</i>	Glyma.11G045200.Wm82.a2.v1	AtCRWN4	6e-156	481
MacCRWN1/2/3-a	<i>Musa acuminata</i>	103971466	AtCRWN1 2 3	5e-160	504
MacCRWN1/2/3-b	<i>Musa acuminata</i>	103987369	AtCRWN1 2 3	5e-141	457
MacCRWN1/2/3-c	<i>Musa acuminata</i>	103994553	AtCRWN1 2 3	1e-137	444
MacCRWN4	<i>Musa acuminata</i>	103989600	AtCRWN4	3e-176	546
NnuCRWN2/3-a	<i>Nelumbo nucifera</i>	104603075	AtCRWN2 3	0	761
NnuCRWN2/3-b	<i>Nelumbo nucifera</i>	104601026	AtCRWN2 3	0	739
NnuCRWN4	<i>Nelumbo nucifera</i>	104591220	AtCRWN4	0	679
OsaCRWN1/2/3	<i>Oryza sativa</i>	LOC_Os02g48010	AtCRWN1 2 3	8e-129	422
OsaCRWN4	<i>Oryza sativa</i>	LOC_Os01g56140	AtCRWN4	9e-139	442
PabCRWN4-b	<i>Picea abies</i>	MA_10432363g0010	AtCRWN4	2e-83	294
PabCRWN4-a	<i>Picea abies</i>	MA_10432363g0010	AtCRWN4	4e-129	426
PpeCRWN1	<i>Prunus persica</i>	PPE003G21990	AtCRWN1	0	862
PpeCRWN2/3	<i>Prunus persica</i>	PPE001G31400	AtCRWN2 3	0	566
PpeCRWN4	<i>Prunus persica</i>	PPE006G22330	AtCRWN4	0	781
PtrCRWN1	<i>Populus trichocarpa</i>	Potri.017G111400.v3.0	AtCRWN1	0	860
PtrCRWN2/3	<i>Populus trichocarpa</i>	Potri.008G114800.v3.0	AtCRWN2 3	0	576
PtrCRWN4	<i>Populus trichocarpa</i>	Potri.012G034300.1.v3.0	AtCRWN4	0	780
TcaCRWN1	<i>Theobroma cacao</i>	TC0004G14630	AtCRWN1	0	926
TcaCRWN2/3	<i>Theobroma cacao</i>	TC0002G36050	AtCRWN2 3	0	660
TcaCRWN4	<i>Theobroma cacao</i>	TC0001G07580	AtCRWN4	0	795
ZmaCRWN1/2/3	<i>Zea mays</i>	GRMZM2G015875	AtCRWN1 2 3	4e-126	416
ZmaCRWN4	<i>Zea mays</i>	GRMZM2G320013.v6a	AtCRWN4	2e-119	390
SmoCRWN	<i>Selaginella moellendorffii</i>	45495.v1	AtCRWN	5e-47	170
SlyCRWN1-a	<i>Solanum lycopersicum</i>	Solyc03g045050.2	AtCRWN1	0	698
SlyCRWN1-b	<i>Solanum lycopersicum</i>	Solyc02g089800.2	AtCRWN1	0	671
SlyCRWN4	<i>Solanum lycopersicum</i>	Solyc02g091960.2	AtCRWN4	4e-88	291
VviCRWN2/3	<i>Vitis vinifera</i>	GSVIVT01011972001	AtCRWN2 3	0	633
VviCRWN1	<i>Vitis vinifera</i>	GSVIVT01031076001	AtCRWN1	1e-130	422
VviCRWN4	<i>Vitis vinifera</i>	GSVIVT01007428001	AtCRWN4	0	780
AtrCRWN1/2/3	<i>Amborella trichopoda</i>	evm_27.TU.AmTr_v1.0 scaffold00024.349	AtCRWN1 2 3	6e-160	508
AtrCRWN4	<i>Amborella trichopoda</i>	evm_27.TU.AmTr_v1.0 scaffold00044.217	AtCRWN4	4e-134	433
PpaCRWN	<i>Physcomitrella patens</i>	Phpat.002G143000.v3.0	AtCRWN	6e-41	165
PpaCRWN	<i>Physcomitrella patens</i>	Phpat.001G006400.v3.0	AtCRWN	2e-18	91.7

## C.2.2 NEAP homologue results

Table C.3: NEAP results.

Gene name	Organism	Gene id	Homologues	e-value	Score
AlyNEAP3	<i>Arabidopsis lyrata</i>	471040.v1	AtNEAP3	0	585
AlyNEAP1	<i>Arabidopsis lyrata</i>	340760.v1	AtNEAP1	0	541
AlyNEAP2	<i>Arabidopsis lyrata</i>	326902.v1	AtNEAP2	0	560
BraNEAP3	<i>Brassica rapa</i>	Brara.F00604.v1.3	AtNEAP3	2e-168	471
BraNEAP1	<i>Brassica rapa</i>	Brara.E03339.v1.3	AtNEAP1	2e-171	480
BraNEAP2-a	<i>Brassica rapa</i>	Brara.F02817.v1.3	AtNEAP2	0	514
BraNEAP2-b	<i>Brassica rapa</i>	Brara.I00491.v1.3	AtNEAP2	0	504
CpaNEAP	<i>Carica papaya</i>	CP00048G02160	AtNEAP1 2 3	9e-141	401
GmaNEAP-a	<i>Glycine max</i>	Glyma.10G144000.Wm82.a2.v1	AtNEAP1 2 3	4e-141	404
GmaNEAP-b	<i>Glycine max</i>	Glyma.20G092900.Wm82.a2.v1	AtNEAP1 2 3	4e-139	399
MacNEAP-a	<i>Musa acuminata</i>	103970415	AtNEAP1 2 3	1e-107	318
MacNEAP-b	<i>Musa acuminata</i>	103993307	AtNEAP1 2 3	5e-99	296
NnuNEAP-a	<i>Nelumbo nucifera</i>	104611262	AtNEAP1 2 3	1e-126	366
NnuNEAP-b	<i>Nelumbo nucifera</i>	104607137	AtNEAP1 2 3	7e-122	354
OsaNEAP	<i>Oryza sativa</i>	LOC Os05g04530	AtNEAP1 2 3	3e-113	332
PabNEAP-a	<i>Picea abies</i>	MA_136804g0010	AtNEAP1 2 3	7e-80	244
PabNEAP-b	<i>Picea abies</i>	MA_902507g0010	AtNEAP1 2 3	5e-47	158
PpeNEAP-a	<i>Prunus persica</i>	PPE006G31130	AtNEAP1 2 3	1e-131	379
PpeNEAP-b	<i>Prunus persica</i>	Potri.005G003600.v3.0	AtNEAP1/2/3	8e-105	309
PtrNEAP-a	<i>Populus trichocarpa</i>	Potri.013G003400.v3.0	AtNEAP1 2 3	2e-135	389
TcaNEAP	<i>Theobroma cacao</i>	TC0005G32630	AtNEAP1 2 3	1e-144	412
ZmaNEAP-a	<i>Zea mays</i>	GRMZM2G042593	AtNEAP1 2 3	2e-111	328
ZmaNEAP-b	<i>Zea mays</i>	GRMZM2G061728	AtNEAP1 2 3	1e-107	318
SlyNEAP	<i>Solanum lycopersicum</i>	Solyc01g101130.2	AtNEAP1 2 3	2e-127	367
VvibNEAP-a	<i>Vitis vinifera</i>	GSVIVT01031318001	AtNEAP1 2 3	9e-134	384
VviNEAP-b	<i>Vitis vinifera</i>	GSVIVT01028212001	AtNEAP1 2 3	2e-118	344
AtrNEAP	<i>Amborella trichopoda</i>	evm_27.TU.AmTr_v1.0_scaffold00045.73	AtNEAP1 2 3	2e-119	347

## C.2.3 KAKU4 homologue results

Table C.4: KAKU4 results.

Gene name	Organism	Gene id	Homologues	e-value	Score
AlyKAKU4	<i>Arabidopsis lyrata</i>	888976.v1	AtKAKU4	0	810
BraKAKU4-a	<i>Brassica rapa</i>	Brara.H01351.v1.3	AtKAKU4	2e-168	485
BraKAKU4-b	<i>Brassica rapa</i>	Brara.A00629.v1.3	AtKAKU4	2e-122	366
NnuKAKU4	<i>Nelumbo nucifera</i>	104603165	AtKAKU4	6e-32	131
PpeKAKU4	<i>Prunus persica</i>	PPE Q01G46440	AtKAKU4	8e-49	177
PtrKAKU4	<i>Populus trichocarpa</i>	Potri.018G006200.v3.0	AtKAKU4	1e-38	148
TcaKAKU4	<i>Theobroma cacao</i>	TC0009G00640	AtKAKU4	4e-53	191
SlyKAKU4	<i>Solanum lycopersicum</i>	Solyc08g006480.2	AtKAKU4	5e-33	132
VviKAKU4	<i>Vitis vinifera</i>	GSVIVT01035528001	AtKAKU4	7e-39	149
CpaKAKU4	<i>Carica papaya</i>	CP00023G00050	AtKAKU4	3e-21	93.6
GmaKAKU4-a	<i>Glycine max</i>	Glyma.04G074900.Wm82.a2.v1	AtKAKU4	8e-38	149
GmaKAKU4-b	<i>Glycine max</i>	Glyma.06G075900.Wm82.a2.v1	AtKAKU5	1e-35	142
OsaKAKU4	<i>Oryza sativa</i>	LOC Os04g56140	AtKAKU4	2e-11	66.6
MacKAKU4	<i>Musa acuminata</i>	695024736	AtKAKU4	2e-15	80.1
ZmaKAKU4	<i>Zea mays</i>	GRMZM2G104199.v6a	AtKAKU4	2e-11	67.4

## C.2.4 SINE homologue results

Table C.5: SINE results.

Gene name	Organism	Gene id	Homologues	e-value	Score
AlySINE3	<i>Arabidopsis lyrata</i>	928307.v1	AtSINE3	2e-122	343
AlySINE2	<i>Arabidopsis lyrata</i>	340556.v1	AtSINE2	0	929
AlySINE1	<i>Arabidopsis lyrata</i>	474709.v1	AtSINE1	0	964
BraSINE2-a	<i>Brassica rapa</i>	Brara.E03477.v1.3	AtSINE2	0	763
BraSINE3	<i>Brassica rapa</i>	Brara.A03650.v1.3	AtSINE3	1e-83	246
BraSINE2-b	<i>Brassica rapa</i>	Brara.A03794.v1.3	AtSINE2	5e-169	487
BraSINE1	<i>Brassica rapa</i>	Brara.I00153.v1.3	AtSINE1	0	823
CpaSINE1/2	<i>Carica papaya</i>	CP00051G01090	AtSINE1 2	0	642
GmaSINE1/2-a	<i>Glycine max</i>	Glyma.02G071700.Wm82.a2.v1	AtSINE1 2	0	547
GmaSINE1/2-b	<i>Glycine max</i>	Glyma.16G152900.Wm82.a2.v1	AtSINE1 2	0	550
GmaSINE1/2-c	<i>Glycine max</i>	Glyma.19G110600.Wm82.a2.v1	AtSINE1 2	0	540
GmaSINE1/2-d	<i>Glycine max</i>	Glyma.16G041800.Wm82.a2.v1	AtSINE1 2	0	525
MacSINE1/2-a	<i>Musa acuminata</i>	103978817	AtSINE1 2	5e-145	431
MacSINE1/2-b	<i>Musa acuminata</i>	103993855	AtSINE1 2	3e-156	459
NnuSINE1/2-a	<i>Nelumbo nucifera</i>	104611165	AtSINE1 2	0	587
NnuSINE1/2-b	<i>Nelumbo nucifera</i>	104597698	AtSINE1 2	0	538
OsaSINE1/2	<i>Oryza sativa</i>	LOC Os11g37100	AtSINE1 2	6e-151	447
PabSINE-a	<i>Picea abies</i>	MA 10351739g0010	AtSINE	9e-76	254
PabSINE-b	<i>Picea abies</i>	MA 162159g0010	AtSINE	2e-75	255
PabSINE-c	<i>Picea abies</i>	MA 395650g0010	AtSINE	8e-94	303
PpeSINE1/2	<i>Prunus persica</i>	PPE007G03120	AtSINE1 2	0	575
PtrSINE1/2-a	<i>Populus trichocarpa</i>	Potri.019G033900.v3.0	AtSINE1 2	0	620
PtrSINE1/2-b	<i>Populus trichocarpa</i>	Potri.013G058700.v3.0	AtSINE1 2	0	632
TcaSINE1/2	<i>Theobroma cacao</i>	TC0005G29190	AtSINE1 2	2e-121	370
ZmaSINE1/2	<i>Zea mays</i>	GRMZM2G000608	AtSINE1 2	5e-143	427
SlySINE1/2	<i>Solanum lycopersicum</i>	Solyc03g062700.2	AtSINE1 2	3e-176	509
VviSINE1/2	<i>Vitis vinifera</i>	GSVIVT01033391001	AtSINE1 2	0	534
AtrSINE	<i>Amborella trichopoda</i>	evm 27.TU.AmTr v1.0 scaffold00004.62	AtSINE	1e-135	407
PpaSINE-a	<i>Physcomitrella patens</i>	Phpat.006G062300.v3.0	AtSINE	9e-48	177
PpaSINE-b	<i>Physcomitrella patens</i>	Phpat.022G009100.v3.0	AtSINE	2e-50	186
PpaSINE-c	<i>Physcomitrella patens</i>	Phpat.005G028100.v3.0	AtSINE	2e-58	196
SmoSINE	<i>Selaginella moellendorffii</i>	410901.v1	AtSINE	2e-46	175

## C.2.5 WIP homologue results

Table C.6: WIP results.

Gene name	Organism	Gene id	Homologues	e-value	Score
AlyWIP1	<i>Arabidopsis lyrata</i>	492167.v1	AtWIP1	0	843
AlyWIP2	<i>Arabidopsis lyrata</i>	950278.v1	AtWIP2	0	652
AlyWIP3	<i>Arabidopsis lyrata</i>	904239.v1	AtWIP3	0	730
BraWIP3-b	<i>Brassica rapa</i>	Brara.C03463.v1.3	AtWIP3	5e-140	409
BraWIP1	<i>Brassica rapa</i>	Brara.A01633.v1.3	AtWIP1	0	555
BraWIP2	<i>Brassica rapa</i>	Brara.J01056.v1.3	AtWIP2	3e-88	272
BraWIP3-a	<i>Brassica rapa</i>	Brara.A03268.v1.3	AtWIP3	1e-134	393
CpaWIP	<i>Carica papaya</i>	CP00012G00680	ATWIP	3e-76	250
GmaWIP-a	<i>Glycine max</i>	Glyma.06G321400.Wm82.a2.v1	ATWIP	7e-44	164
GmaWIP-b	<i>Glycine max</i>	Glyma.04G113700.Wm82.a2.v1	ATWIP	1e-41	157
MacWIP	<i>Musa acuminata</i>	104594339	ATWIP	3e-29	121
NnuWIP	<i>Nelumbo nucifera</i>	719990236	ATWIP	1e-47	175
PtrWIP-a	<i>Populus trichocarpa</i>	Potri.001G472000.v3.0	ATWIP	1e-60	210
PtrWIP-b	<i>Populus trichocarpa</i>	Potri.011G169000.v3.0	ATWIP	8e-59	205
TcaWIP	<i>Theobroma cacao</i>	TC0007G00130	ATWIP	2e-73	244
VviWIP	<i>Vitis vinifera</i>	GSVIVT01014846001	ATWIP	5e-157	46



## C.2.6 TIK homologues results

Table C.7: NEAP results.

Gene name	Organism	Gene id	Homologues	e-value	Score
AlyTIK-a	<i>Arabidopsis lyrata</i>	948593.v1	AtTIK	5e-45	151
AlyTIK-b	<i>Arabidopsis lyrata</i>	356572.v1	AtTIK	1e-44	149
BraTIK	<i>Brassica rapa</i>	Brara.F01121.v1.3	AtTIK	3e-41	145
GmaTIK	<i>Glycine max</i>	Glyma.U008300.Wm82.a2.v1	AtTIK	2e-25	106
NnuTIK	<i>Nelumbo nucifera</i>	104587523	AtTIK	3e-e28	113
PabTIK	<i>Picea abies</i>	MA.10437230g0040	AtTIK	3e-21	89.4
PpeTIK	<i>Prunus persica</i>	MA.10437230g0040	AtTIK	2e-27	110
PtrTIK	<i>Populus trichocarpa</i>	Potri.T039900.v3.0	AtTIK	2e-27	111
SlyTIK	<i>Solanum lycopersicum</i>	Solyc01g102840.2	AtTIK	2e-25	104
VviTIK	<i>Vitis vinifera</i>	GSVIVT01022984001	AtTIK	2e-27	108
AtrTIK	<i>Amborella trichopoda</i>	evm.27.TU.AmTr.v1.0.scaffold00085.75	AtTIK	2e-20	89.0
TcaTIK	<i>Theobroma cacao</i>	TC0028G00020	AtTIK	5e-25	104

## C.2.7 Cter SUN homologue results

Table C.8: Cter-SUN results.

Gene name	Organism	Gene id	Homologues	e-value	Score
AlySUN1	<i>Arabidopsis lyrata</i>	939904.v1	AtSUN1	0	804
AlySUN2-a	<i>Arabidopsis lyrata</i>	478408.v1	AtSUN2	0	791
AlySUN2-b	<i>Arabidopsis lyrata</i>	497464.v1	AtSUN2	0	786
BraSUN1	<i>Brassica rapa</i>	Brara.J02691.v1.3	AtSUN1	0	683
BraSUN2	<i>Brassica rapa</i>	Brara.E02993.v1.3	AtSUN2	0	533
CpaCterSUN	<i>Carica papaya</i>	CP00033G01210	AtCterSUN	1e-154	446
GmaCterSUN-a	<i>Glycine max</i>	Glyma.15G223100	AtCterSUN	2e-134	397
GmaCterSUN-b	<i>Glycine max</i>	Glyma.13G185300	AtCterSUN	2e-131	389
MacCterSUN-a	<i>Musa acuminata</i>	10399728	AtCterSUN	8e-120	358
MacCterSUN-b	<i>Musa acuminata</i>	103998202	AtCterSUN	1e-118	355
MacCterSUN-c	<i>Musa acuminata</i>	103971044	AtCterSUN	3e-107	326
NnuCterSUN	<i>Nelumbo nucifera</i>	104611507	AtCterSUN	8e-127	376
OsaCterSUN-a	<i>Oryza sativa</i>	LOC.Os05g18770	AtCterSUN	2e-96	298
OsaCterSUN-b	<i>Oryza sativa</i>	LOC.Os01g16220	AtCterSUN	3e-90	282
PabCterSUN-a	<i>Picea abies</i>	MA.10431452g0010	AtCterSUN	2e-71	232
PabCterSUN-b	<i>Picea abies</i>	MA.633971g0010	AtCterSUN	3e-48	171
PpeCterSUN	<i>Prunus persica</i>	PPE002G04740	AtCterSUN	5e-157	456
PtrCterSUN-a	<i>Populus trichocarpa</i>	Potri.010G247900.v3.0	AtCterSUN	5e-134	395
PtrCterSUN-b	<i>Populus trichocarpa</i>	Potri.008G010900.v3.0	AtCterSUN	3e-125	373
TcaCterSUN	<i>Theobroma cacao</i>	TC0010G12940	AtCterSUN	1e-130	386
ZmaCterSUN-a	<i>Zea mays</i>	GRMZM2G109818	AtCterSUN	2e-97	301
ZmaCterSUN-b	<i>Zea mays</i>	GRMZM2G440614	AtCterSUN	3e-80	256
SmoCterSUN-a	<i>Selaginella moellendorffii</i>	138182.v1	AtCterSUN	6e-79	248
SmoCterSUN-b	<i>Selaginella moellendorffii</i>	122417.v1	AtCterSUN	6e-79	248
SmoCterSUN-c	<i>Selaginella moellendorffii</i>	64465.v1	AtCterSUN	1e-69	223
SmoCterSUN-d	<i>Selaginella moellendorffii</i>	89851.v1	AtCterSUN	8e-68	218
SlyCterSUN	<i>Solanum lycopersicum</i>	Solyc01g096780.2	AtCterSUN	3e-110	328
VviCterSUN	<i>Vitis vinifera</i>	GSVIVT01001935001	AtCterSUN	3e-65	206
AtrCterSUN	<i>Amborella trichopoda</i>	evm.27.TU.AmTr.v1.0.scaffold00101.65	AtCterSUN	3e-97	300
PpaCterSUN-a	<i>Physcomitrella patens</i>	Phpat.007G018800.v3.0	AtCterSUN	3e-66	221
PpaCterSUN-b	<i>Physcomitrella patens</i>	Phpat.011G086200.v3.0	AtCterSUN	6e-64	214
OluCterSUN	<i>Ostreococcus lucimarinus</i>	24577	AtCterSUN	3e-30	122

## C.2.8 MidSUN homologue results

Table C.9: Mid-SUN results.

Gene name	Organism	Gene id	Homologues	e-value	Score
AlySUN3	<i>Arabidopsis lyrata</i>	335524.v1	AtSUN3	0	977
AlySUN4	<i>Arabidopsis lyrata</i>	339371.v1	AtSUN4	0	1009
AlySUN5	<i>Arabidopsis lyrata</i>	354376.v1	AtSUN5	0	1001
BraSUN3	<i>Brassica rapa</i>	Brara.I03282.v1.3	AtSUN3	0	654
BraSUN4-a	<i>Brassica rapa</i>	Brara.G03043.v1.3	AtSUN4	0	754
BraSUN4-b	<i>Brassica rapa</i>	Brara.G02411.v1.3	AtSUN4	0	729
BraSUN5	<i>Brassica rapa</i>	Brara.A01400.v1.3	AtSUN5	0	823
CpaSUN3/4-a	<i>Carica papaya</i>	CP00142G00130	AtSUN3 4	9e-133	402
CpaSUN3/4-b	<i>Carica papaya</i>	CP00006G00590	AtSUN3 4	3e-155	456
CpaSun5	<i>Carica papaya</i>	CP00079G00080	AtSUN5	9e-113	346
GmaSUN3/4-a	<i>Glycine max</i>	Glyma.12G242200.Wm82.a2.v1	AtSUN3 4	6e-128	389
GmaSUN3/4-b	<i>Glycine max</i>	Glyma.04G110900.Wm82.a2.v1	AtSUN3 4	5e-124	382
GmaSUN3/4-c	<i>Glycine max</i>	Glyma.09G002200.Wm82.a2.v1	AtSUN3 4	2e-129	388
GmaSUN3/4-d	<i>Glycine max</i>	Glyma.06G323600.Wm82.a2.v1	AtSUN3 4	2e-142	427
GmaSun5-a	<i>Glycine max</i>	Glyma.11G016300.Wm82.a2.v1	AtSUN5	8e-124	377
GmaSun5-b	<i>Glycine max</i>	Glyma.01G226400.Wm82.a2.v1	AtSUN5	1e-123	376
MacSUN3/4	<i>Musa acuminata</i>	103979160	AtSUN3 4	4e-137	411
MacSUN5	<i>Musa acuminata</i>	103996105	AtSUN5	6e-108	334
NnuSUN3/4	<i>Nelumbo nucifera</i>	104610179	AtSUN3 4	3e-146	435
NnuSUN5	<i>Nelumbo nucifera</i>	104604783	AtSUN5	1e-133	402
OsaSUN3/4	<i>Oryza sativa</i>	LOC Os01g65520	AtSUN3 4	6e-126	384
OsaSUN5	<i>Oryza sativa</i>	LOC Os01g41600	AtSUN5	6e-97	305
PabMidSUN	<i>Picea abies</i>	MA_3228g0010	AtMidSUN	4e-120	367
PpeSUN3/4	<i>Prunus persica</i>	PPE008G00470	AtSUN3 4	7e-160	470
PpeSUN5	<i>Prunus persica</i>	PPE005G13080	AtSUN5	1e-131	397
PtrSUN3/4	<i>Populus trichocarpa</i>	Potri.019G068900.v3.0	AtSUN3 4	1e-170	498
PtrSUN5-a	<i>Populus trichocarpa</i>	Potri.003G141500.v3.0	AtSUN5	7e-132	394
PtrSUN5-b	<i>Populus trichocarpa</i>	Potri.001G089700.v3.0	AtSUN5	8e-126	382
TcaSUN3/4	<i>Theobroma cacao</i>	POPTR_0019s09690.1	AtSUN3 4	2e-154	456
TcaSUN5	<i>Theobroma cacao</i>	TC0003G29550	AtSUN5	7e-136	407
ZmaSUN3/4	<i>Zea mays</i>	GRMZM2G005483	AtSUN3 4	3e-120	370
ZmaSUN5	<i>Zea mays</i>	AC194341.4_FGP003	AtSUN5	5e-98	310
SmoMidSUN-a	<i>Selaginella moellendorffii</i>	441228.v1	AtMidSUN	1e-69	234
SmoMidSUN-b	<i>Selaginella moellendorffii</i>	440338.v1	AtMidSUN	5e-69	231
SmoMidSUN-c	<i>Selaginella moellendorffii</i>	411384.v1	AtMidSUN	6e-57	199
SmoMidSUN-d	<i>Selaginella moellendorffii</i>	440339.v1	AtMidSUN	7e-55	193
SmoMidSUN-e	<i>Selaginella moellendorffii</i>	409314.v1	AtMidSUN	6e-49	176
SmoMidSUN-f	<i>Selaginella moellendorffii</i>	409317.v1	AtMidSUN	3e-42	158
SlySUN5	<i>Solanum lycopersicum</i>	Solyc08g082540.2	AtSUN5	1e-120	367
VviSUN3/4	<i>Vitis vinifera</i>	GSVIVT01037194001	AtSUN3 4	5e-157	461
VviSUN5	<i>Vitis vinifera</i>	GSVIVT01019558001	AtSUN5	1e-62	214
AtrSUN3/4	<i>Amborella trichopoda</i>	evm_27.TU.AmTr_v1.0_scaffold000099.66	AtSUN3 4	1e-118	365
AtrSUN5	<i>Amborella trichopoda</i>	evm_27.TU.AmTr_v1.0_scaffold000021.233	AtSUN5	5e-118	360
PpaMidSUN-a	<i>Physcomitrella patens</i>	Phpat.021G008400.v3.0	AtMidSUN	1e-72	244
PpaMidSUN-b	<i>Physcomitrella patens</i>	Phpat.018G065400.v3.0	AtMidSUN	6e-69	239
CreMidSUN	<i>Chlamydomonas reinhardtii</i>	Cre12.g517300.t1.1	AtMidSUN	1e-24	110
OluMidSUN	<i>Ostreococcus lucimarinus</i>	32403	AtMidSUN	9e-31	126

## C.3 Tissue expression of the LINC complex protein homologues

### C.3.1 Eudicot expression results

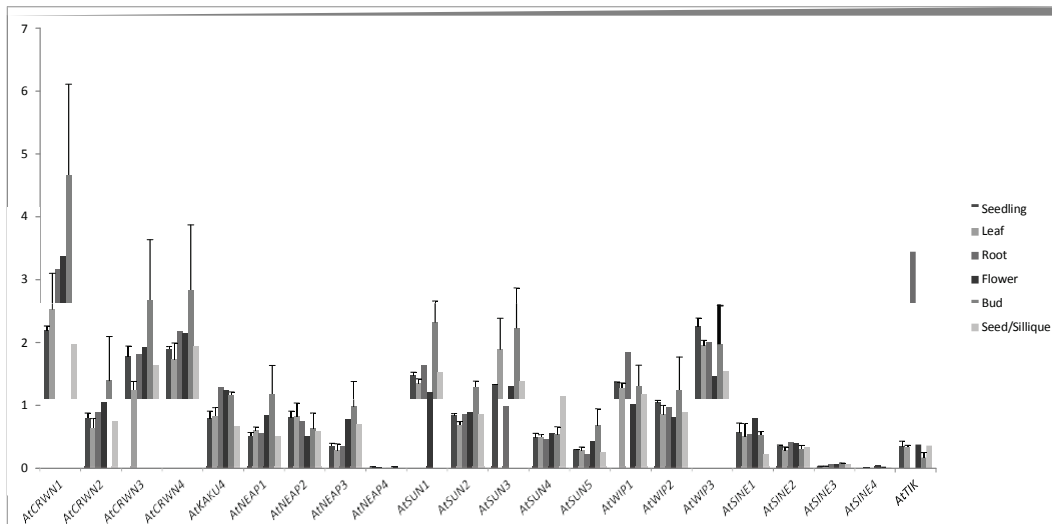


Figure C.2: *Arabidopsis thaliana* results. Data Table 4.3 were used in order to monitor the expression of candidate genes investigated in this study. Histograms show means of transcription levels expressed in  $RPKM \pm SEM$ . *SAND* gene was used as a reference and set at 1 RPKM (Table 4.4).

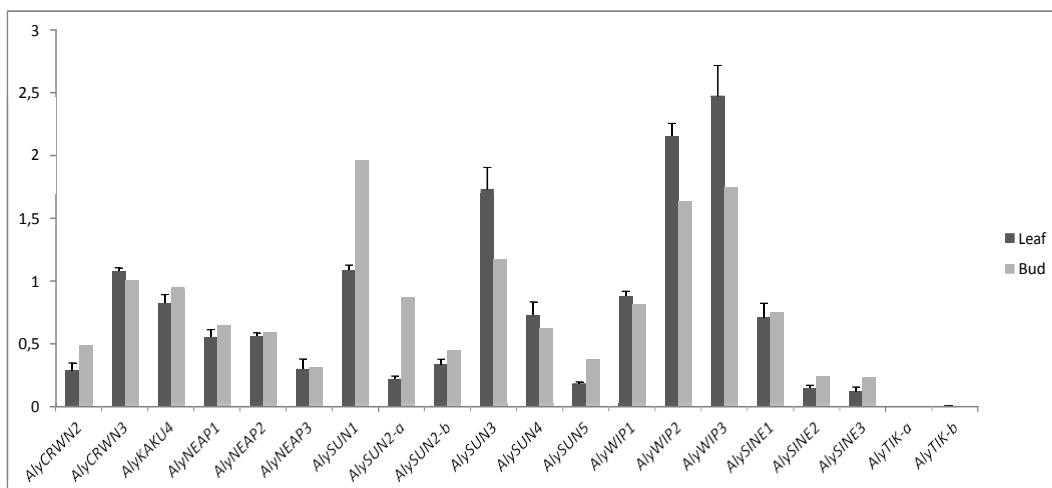


Figure C.3: *Arabidopsis lyrata* results. Data Table 4.3 were used in order to monitor the expression of candidate genes investigated in this study. Histograms show means of transcription levels expressed in  $RPKM \pm SEM$ . *SAND* gene was used as a reference and set at 1 RPKM (Table 4.4).

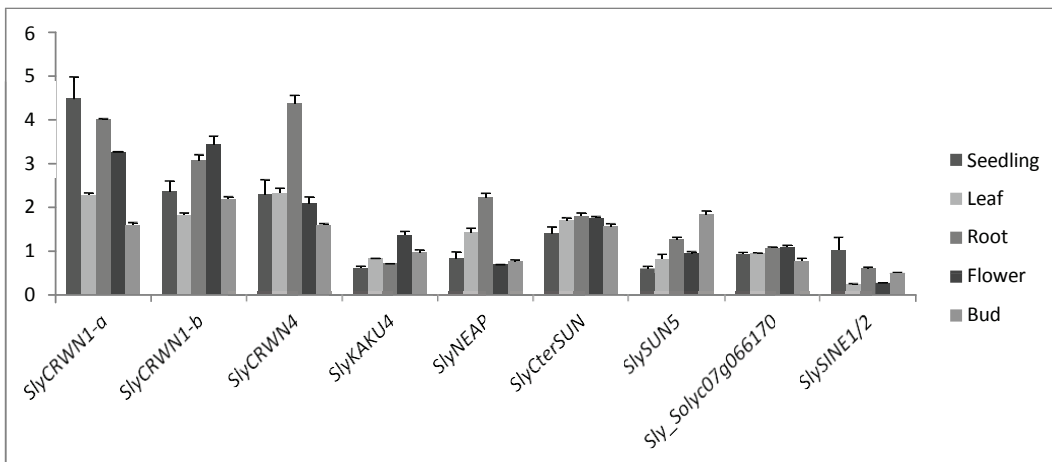


Figure C.4: *Solanum lycopersicum* results. Data Table 4.3 were used in order to monitor the expression of candidate genes investigated in this study. Histograms show means of transcription levels expressed in *RPKM*  $\pm$  *SEM*. *SAND* gene was used as a reference and set at 1 *RPKM* (Table 4.4).

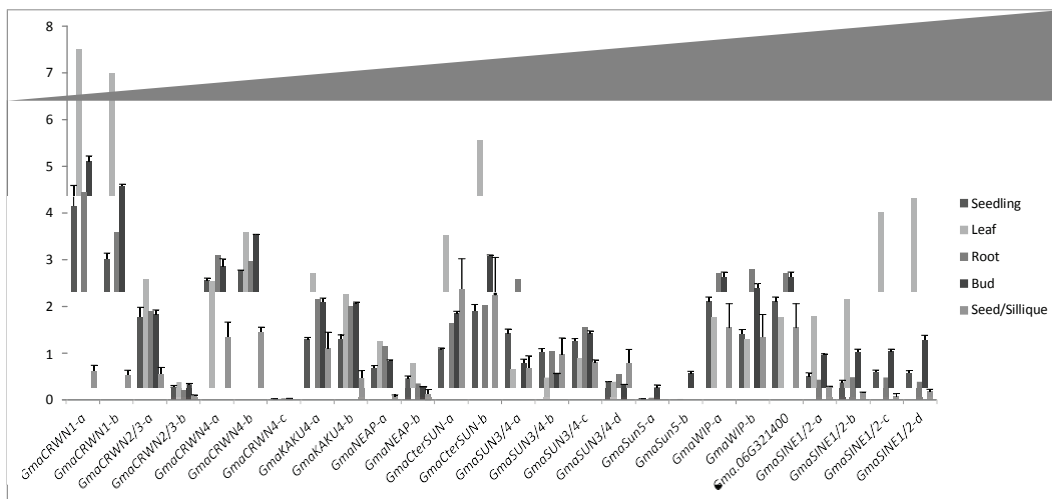
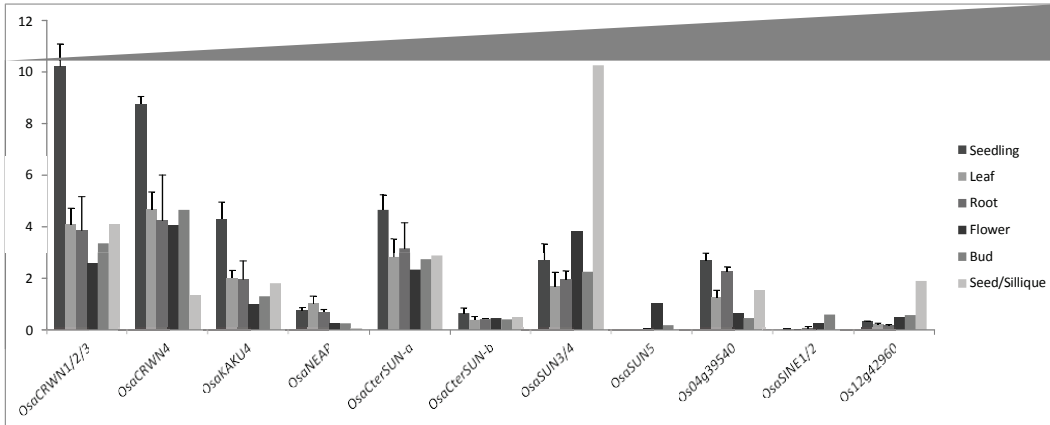
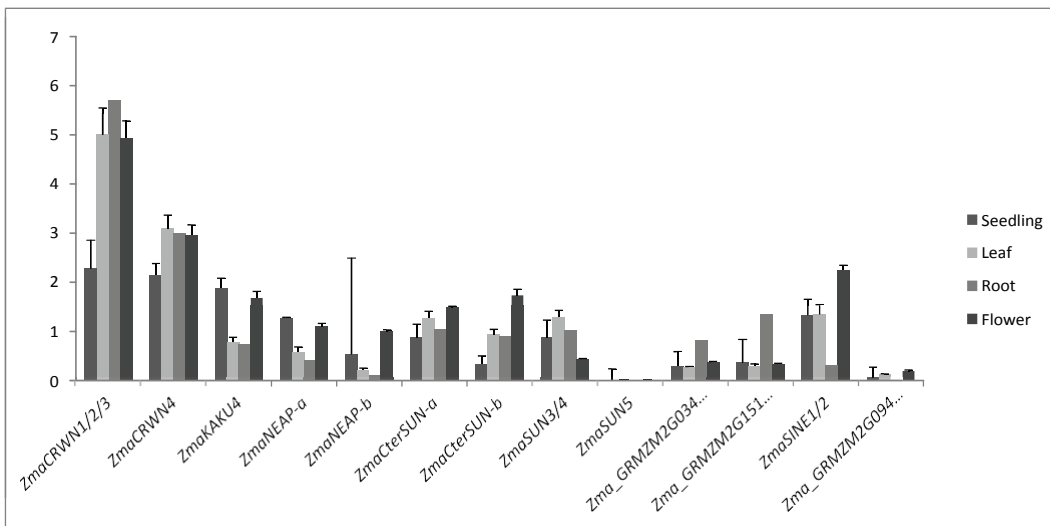


Figure C.5: *Glycine max* results. Data Table 4.3 were used in order to monitor the expression of candidate genes investigated in this study. Histograms show means of transcription levels expressed in *RPKM*  $\pm$  *SEM*. *SAND* gene was used as a reference and set at 1 *RPKM* (Table 4.4).

### C.3.2 Monocot expression results



**Figure C.6: *Oryza sativa* results.** Data Table 4.3 were used in order to monitor the expression of candidate genes investigated in this study. Histograms show means of transcription levels expressed in  $RPKM \pm SEM$ . *SAND* gene was used as a reference and set at 1 RPKM (Table 4.4).



**Figure C.7: *Zea Mays* results.** Data Table 4.3 were used in order to monitor the expression of candidate genes investigated in this study. Histograms show means of transcription levels expressed in  $RPKM \pm SEM$ . *SAND* gene was used as a reference and set at 1 RPKM (Table 4.4).

### C.3.3 Basal angiosperm and moss expression results

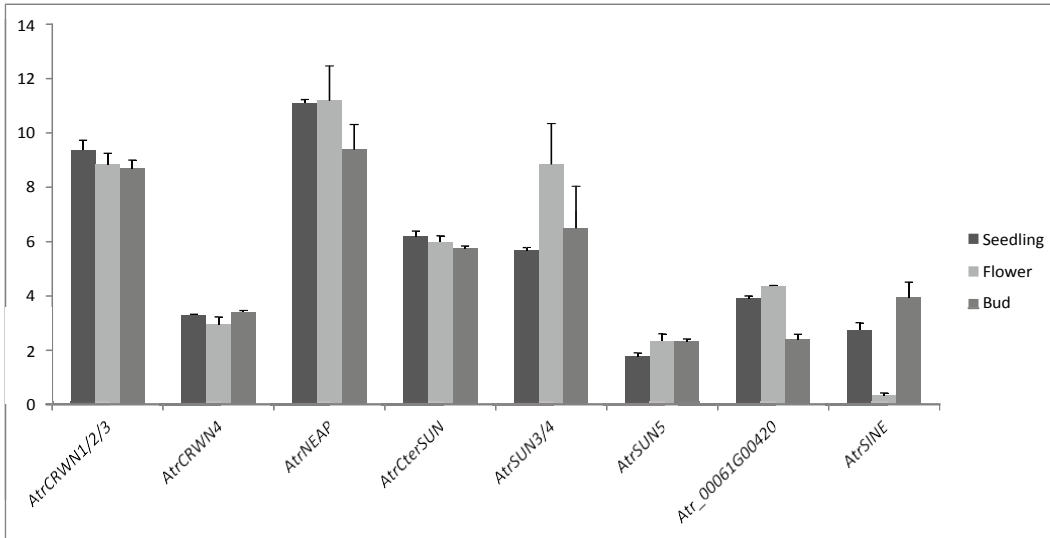


**Figure C.8: *Amborella trichopoda* results.** Data Table 4.3 were used in order to monitor the expression of candidate genes investigated in this study. Histograms show means of transcription levels expressed in  $RPKM \pm SEM$ . *SAND* gene was used as a reference and set at 1 RPKM (Table 4.4).

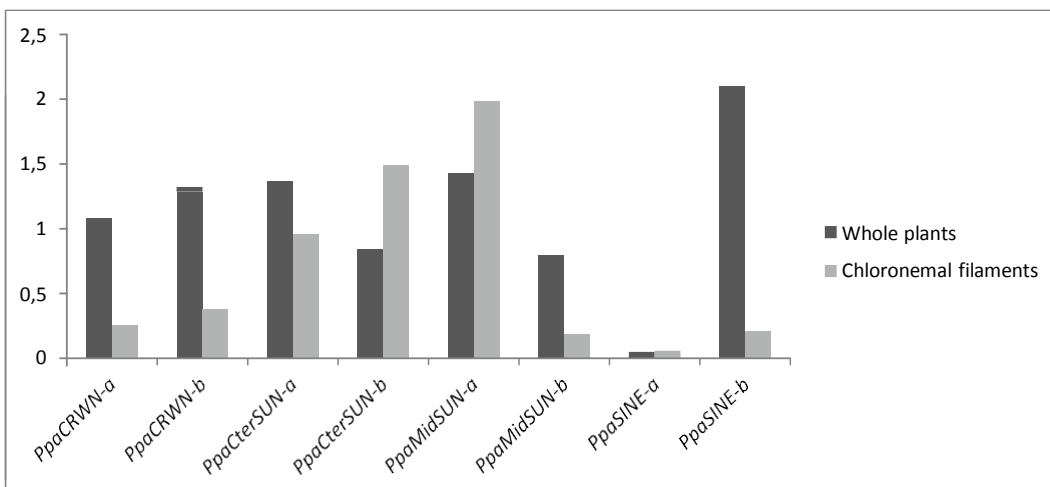


**Figure C.9: *Physcomitrella patens* results.** Data Table 4.3 were used in order to monitor the expression of candidate genes investigated in this study. Histograms show means of transcription levels expressed in  $RPKM \pm SEM$ . *SAND* gene was used as a reference and set at 1 RPKM (Table 4.4).



# ELSEVIER LICENSE TERMS AND CONDITIONS

Feb 29, 2016

This is an Agreement between Axel Poulet ("You") and Elsevier ("Elsevier"). It consists of your order details, the terms and conditions provided by Elsevier, and the payment terms and conditions.

**All payments must be made in full to CCC. For payment instructions, please see information listed at the bottom of this form.**

Supplier	Elsevier Limited The Boulevard,Langford Lane Kidlington,Oxford,OX5 1GB,UK
Registered Company Number	1982084
Customer name	Axel Poulet
Customer address	Faculty of Health and Life Sciences, Oxford, None OX3 0BP
License number	3797270610253
License date	Jan 27, 2016
Licensed content publisher	Elsevier
Licensed content publication	Trends in Biochemical Sciences
Licensed content title	Mechanisms of heterochromatin subnuclear localization
Licensed content author	Benjamin D. Towbin,Adriana Gonzalez-Sandoval,Susan M. Gasser
Licensed content date	July 2013
Licensed content volume number	38
Licensed content issue number	7
Number of pages	8
Start Page	356
End Page	363
Type of Use	reuse in a thesis/dissertation
Intended publisher of new work	other
Portion	figures/tables/illustrations
Number of figures/tables/illustrations	1
Format	both print and electronic
Are you the author of this Elsevier article?	No
Will you be translating?	No
Original figure numbers	Figure 1
Title of your thesis/dissertation	Chromatin organisation at the interphase in Arabidopsis Thaliana
Expected completion date	Apr 2016
Estimated size (number of pages)	100
Elsevier VAT number	GB 494 6272 12
Price	0.00 GBP



VAT/Local Sales Tax 0.00 GBP / 0.00 GBP

**Total 0.00 GBP**

[Terms and Conditions](#)

### INTRODUCTION

1. The publisher for this copyrighted material is Elsevier. By clicking "accept" in connection with completing this licensing transaction, you agree that the following terms and conditions apply to this transaction (along with the Billing and Payment terms and conditions established by Copyright Clearance Center, Inc. ("CCC"), at the time that you opened your Rightslink account and that are available at any time at <http://myaccount.copyright.com>).

### GENERAL TERMS

2. Elsevier hereby grants you permission to reproduce the aforementioned material subject to the terms and conditions indicated.

3. Acknowledgement: If any part of the material to be used (for example, figures) has appeared in our publication with credit or acknowledgement to another source, permission must also be sought from that source. If such permission is not obtained then that material may not be included in your publication/copies. Suitable acknowledgement to the source must be made, either as a footnote or in a reference list at the end of your publication, as follows:

"Reprinted from Publication title, Vol /edition number, Author(s), Title of article / title of chapter, Pages No., Copyright (Year), with permission from Elsevier [OR APPLICABLE SOCIETY COPYRIGHT OWNER]." Also Lancet special credit - "Reprinted from The Lancet, Vol. number, Author(s), Title of article, Pages No., Copyright (Year), with permission from Elsevier."

4. Reproduction of this material is confined to the purpose and/or media for which permission is hereby given.

5. Altering/Modifying Material: Not Permitted. However figures and illustrations may be altered/adapted minimally to serve your work. Any other abbreviations, additions, deletions and/or any other alterations shall be made only with prior written authorization of Elsevier Ltd. (Please contact Elsevier at [permissions@elsevier.com](mailto:permissions@elsevier.com))

6. If the permission fee for the requested use of our material is waived in this instance, please be advised that your future requests for Elsevier materials may attract a fee.

7. Reservation of Rights: Publisher reserves all rights not specifically granted in the combination of (i) the license details provided by you and accepted in the course of this licensing transaction, (ii) these terms and conditions and (iii) CCC's Billing and Payment terms and conditions.

8. License Contingent Upon Payment: While you may exercise the rights licensed immediately upon issuance of the license at the end of the licensing process for the transaction, provided that you have disclosed complete and accurate details of your proposed use, no license is finally effective unless and until full payment is received from you (either by publisher or by CCC) as provided in CCC's Billing and Payment terms and conditions. If full payment is not received on a timely basis, then any license preliminarily granted shall be deemed automatically revoked and shall be void as if never granted. Further, in the event that you breach any of these terms and conditions or any of CCC's Billing and Payment terms and conditions, the license is automatically revoked and shall be void as if never granted. Use of materials as described in a revoked license, as well as any use of the materials beyond the scope of an unrevoked license, may constitute copyright infringement and publisher reserves the right to take any and all action to protect its copyright in the materials.

9. Warranties: Publisher makes no representations or warranties with respect to the licensed material.

10. Indemnity: You hereby indemnify and agree to hold harmless publisher and CCC, and their respective officers, directors, employees and agents, from and against any and all claims arising out of your use of the licensed material other than as specifically authorized pursuant to this license.

11. No Transfer of License: This license is personal to you and may not be sublicensed, assigned, or transferred by you to any other person without publisher's written permission.

12. No Amendment Except in Writing: This license may not be amended except in a writing signed by both parties (or, in the case of publisher, by CCC on publisher's behalf).

13. Objection to Contrary Terms: Publisher hereby objects to any terms contained in any purchase order, acknowledgment, check endorsement or other writing prepared by you, which terms are inconsistent with these terms and conditions or CCC's Billing and Payment terms and conditions. These terms and conditions, together with CCC's Billing and Payment terms and conditions (which are incorporated herein), comprise the entire agreement between you and publisher (and CCC) concerning this licensing transaction. In the event of any conflict between your obligations established by these terms and conditions and those established by CCC's Billing and Payment terms and conditions, these terms and conditions shall control.

14. Revocation: Elsevier or Copyright Clearance Center may deny the permissions described in this License at their sole discretion, for any reason or no reason, with a full refund payable to you. Notice of such denial will be made using the contact information provided by you. Failure to receive such notice will not alter or invalidate the denial. In no event will Elsevier or Copyright Clearance Center be responsible or liable for any costs, expenses or damage incurred by you as a result of a denial of your permission request, other than a refund of the amount(s) paid by you to Elsevier and/or Copyright Clearance Center for denied permissions.

### LIMITED LICENSE

The following terms and conditions apply only to specific license types:

15. **Translation:** This permission is granted for non-exclusive world **English** rights only unless your license was granted for translation rights. If you licensed translation rights you may only translate this content into the languages you requested. A professional translator must perform all translations and reproduce the content word for word preserving the integrity of the article.

16. **Posting licensed content on any Website:** The following terms and conditions apply as follows: Licensing material from an Elsevier journal: All content posted to the web site must maintain the copyright information line on the bottom of each image; A hyper-text must be included to the Homepage of the journal from which you are licensing at <http://www.sciencedirect.com/science/journal/xxxxx> or the Elsevier homepage for books at <http://www.elsevier.com>; Central Storage: This license does not include permission for a scanned version of the material to be stored in a central repository such as that provided by Heron/XanEdu.

Licensing material from an Elsevier book: A hyper-text link must be included to the Elsevier homepage at <http://www.elsevier.com>. All content posted to the web site must maintain the copyright information line on the bottom of each image.

**Posting licensed content on Electronic reserve:** In addition to the above the following clauses are applicable: The web site must be password-protected and made available only to bona fide students registered on a relevant course. This permission is granted for 1 year only. You may obtain a new license for future website posting.

17. **For journal authors:** the following clauses are applicable in addition to the above:

**Preprints:**

A preprint is an author's own write-up of research results and analysis, it has not been peer-reviewed, nor has it had any other value added to it by a publisher (such as formatting, copyright, technical enhancement etc.).

Authors can share their preprints anywhere at any time. Preprints should not be added to or enhanced in any way in order to appear more like, or to substitute for, the final versions of articles however authors can update their preprints on arXiv or RePEc with their Accepted Author Manuscript (see below).

If accepted for publication, we encourage authors to link from the preprint to their formal publication via its DOI. Millions of researchers have access to the formal publications on ScienceDirect, and so links will help users to find, access, cite and use the best available version. Please note that Cell Press, The Lancet and some society-owned have different preprint policies. Information on these policies is available on the journal homepage.

**Accepted Author Manuscripts:** An accepted author manuscript is the manuscript of an article that has been accepted for publication and which typically includes author-incorporated changes suggested during submission, peer review and editor-author communications.

Authors can share their accepted author manuscript:

- immediately
  - via their non-commercial person homepage or blog
  - by updating a preprint in arXiv or RePEc with the accepted manuscript
  - via their research institute or institutional repository for internal institutional uses or as part of an invitation-only research collaboration work-group
  - directly by providing copies to their students or to research collaborators for their personal use
  - for private scholarly sharing as part of an invitation-only work group on commercial sites with which Elsevier has an agreement
- after the embargo period
  - via non-commercial hosting platforms such as their institutional repository
  - via commercial sites with which Elsevier has an agreement

In all cases accepted manuscripts should:

- link to the formal publication via its DOI
- bear a CC-BY-NC-ND license - this is easy to do
- if aggregated with other manuscripts, for example in a repository or other site, be shared in alignment with our hosting policy not be added to or enhanced in any way to appear more like, or to substitute for, the published journal article.

**Published journal article (JPA):** A published journal article (PJA) is the definitive final record of published research that appears or will appear in the journal and embodies all value-adding publishing activities including peer review co-ordination, copy-editing, formatting, (if relevant) pagination and online enrichment.

Policies for sharing publishing journal articles differ for subscription and gold open access articles:

**Subscription Articles:** If you are an author, please share a link to your article rather than the full-text. Millions of researchers have access to the formal publications on ScienceDirect, and so links will help your users to find, access, cite, and use the best available version.

Theses and dissertations which contain embedded PJAs as part of the formal submission can be posted publicly by the



[Creative Commons](#)

## Creative Commons License Deed

---

Attribution 4.0 International (CC BY 4.0)

This is a human-readable summary of (and not a substitute for) the [license](#).

[Disclaimer](#)



### You are free to:



**Share** — copy and redistribute the material in any medium or format



**Adapt** — remix, transform, and build upon the material for any purpose, even commercially.

The licensor cannot revoke these freedoms as long as you follow the license terms.

### Under the following terms:



**Attribution** — You must give [appropriate credit](#), provide a link to the license, and [indicate if changes were made](#). You may do so in any reasonable manner, but not in any way that suggests the licensor endorses you or your use.

**No additional restrictions** — You may not apply legal terms or [technological measures](#) that legally restrict others from doing anything the license permits.

### Notices:

You do not have to comply with the license for elements of the material in the public domain or where your use is permitted by an applicable [exception or limitation](#).

No warranties are given. The license may not give you all of the permissions necessary for your intended use. For example, other rights such as [publicity, privacy, or moral rights](#) may limit how you use the material.

## Proprietary Rights Notice for *MBoC*

*Molecular Biology of the Cell (MBoC)* ©2013 by The American Society for Cell Biology (ASCB). Individual articles are distributed by The American Society for Cell Biology under license from the author(s), who retain copyright. Two months after being published at [www.molbiolcell.org](http://www.molbiolcell.org), the material in *MBoC* is available for non-commercial use by the general public under an Attribution-Noncommercial-Share Alike 3.0 Unported Creative Commons License (<http://creativecommons.org/licenses/by-nc-sa/3.0>). Under this license, the content may be used at no charge for noncommercial purposes by the general public, provided that: the authorship of the materials is attributed to the author(s) (in a way that does not suggest that the authors endorse the users or any user's use); users include the terms of this license in any use or distribution they engage in; users respect the fair use rights, moral rights, and rights that the authors and any others have in the content.

For permissions to copy beyond the terms stated above and that permitted by Section 107 or 108 of the U.S. Copyright Law and for reprints, contact the [Copyright Clearance Center](#) or the ASCB ([mboc@ascb.org](mailto:mboc@ascb.org)).

ASCB®, The American Society for Cell Biology®, and Molecular Biology of the Cell® are registered trademarks of The American Society for Cell Biology.

---

## Warranties

In no event shall the ASCB or Stanford University be liable for any damages, including direct, special, incidental, indirect or consequential damages of any kind, or any damages whatsoever resulting from loss of use, data or profits, whether or not advised of the possibility of damage, and on any theory of liability, arising out of or in connection with the use or performance of this information.

This publication is provided "as is" without warranty of any kind, either expressed or implied, including, but not limited to, the implied warranties of merchantability, fitness for a particular purpose, or non-infringement.

Descriptions of, or references to, products or publications does not imply endorsement of that product or publication.

*MBoC* is under development and changes may be made in these publications and programs at any time.

---

**THE AMERICAN ASSOCIATION FOR THE ADVANCEMENT OF SCIENCE ORDER DETAILS**

Jan 18, 2016

---

---

Order Number	501099505
Order date	Jan 18, 2016
Licensed content publisher	The American Association for the Advancement of Science
Licensed content publication	Science
Licensed content title	The Amborella Genome and the Evolution of Flowering Plants
Licensed content author	Amborella Genome Project, Victor A. Albert, W. Bradley Barbazuk, Claude W. dePamphilis, Joshua P. Der, James Leebens-Mack, Hong Ma, Jeffrey D. Palmer, Steve Rounsley, David Sankoff, Stephan C. Schuster, Douglas E. Soltis, Pamela S. Soltis, Susan R. Wessler, Rod A. Wing, Victor A. Albert, Jetty S. S. Ammiraju, W. Bradley Barbazuk, Srikar Chamala, Andre S. Chanderbali, Claude W. dePamphilis, Joshua P. Der, Ronald Determann, James Leebens-Mack, Hong Ma, Paula Ralph, Steve Rounsley, Stephan C. et al.
Licensed content date	Dec 20, 2013
Volume number	342
Issue number	6165
Type of Use	Thesis / Dissertation
Requestor type	Scientist/individual at a research institution
Format	Print and electronic
Portion	Not specified
Order reference number	None
Title of your thesis / dissertation	Chromatin organisation at the interphase in Arabidopsis Thaliana
Expected completion date	Apr 2016
Estimated size(pages)	100
Requestor Location	Axel Poulet Faculty of Health and Life Sciences, Oxford Brookes University Headington Campus Oxford OX3 0BP UK Oxford, United Kingdom OX3 0BP Attn: Axel Poulet
Total	Not Available
Total	Not Available

---

---